Evanescent Wave And Cavity Enhanced Absorption Spectroscopy For Trace Molecule Sensing Using Diode And Quantum Cascade Lasers.

A thesis submitted for the degree of

Doctor of Philosophy (Science)

in

Physics (Experimental)

by

Sanchi Maithani

August, 2020

Department of Physics
University of Calcutta
Kolkata, India

Dedicated to my Family and my Supervisor…

Acknowledgements

Here, I would like to thank all those whose support made this thesis possible. First, I would like to express my sincere thanks and gratitude to my supervisor Dr. Manik Pradhan for his guidance, support and the immense resources that he made available for research work. I also thank him for providing interesting research topics for work and for always being ready to help whenever we needed. I also feel deep gratitude to my senior Dr. Abhijit Maity who helped me all throughout my Ph.D. with his unique ideas and thorough discussions. He not only inspired me with his own brilliant endeavours in research but also provided his best support and friendship at all times. I would also thank my seniors Mithun Pal, Dr. Chiranjit Ghosh, Dr. Gourab Dutta Banik, Dr. Suman Som and my earlier lab member Santanu Mandal who helped me in the early years of my PhD. I also thank my lab members Sayoni Bhattacharya, Biswajit Panda, Ardhendu Pal and Akash Das for helping me with my work and all lab members for providing a pleasant atmosphere in lab and giving me the opportunity to work alongside them. I would also thank our collaborator Dr. Sujit Chaudhuri who provided the participants and helped in the breath analysis work.

It is beyond words the amount of gratitude that I feel towards my parents who have worked hard and provided endless love and support in my life and work. I also owe sincere gratitude to my late grandparents whose love and wisdom made my childhood truly blessed. I also feel blessed to have my sister whose presence and affection has always made my life joyful.

I feel happy to have met my dear friends Debalina, Riddhi, my IPhD batchmates and other friends with whom I spent lots of happy moments. I also give my heartfelt thanks to my old teachers who inspired and encouraged me early in my life.

Finally, I want to acknowledge DST-INSPIRE Fellowship for doctoral work and S. N. Bose National Centre for Basic Sciences, Kolkata for giving me the opportunity to carry out Ph.D. work and providing excellent research facilities.

- Sanchi Maithani

Abstract

Trace molecule detection finds its applications in various fields such as environmental monitoring, biomedical analysis, chemical and industrial sensing. To detect low concentrations of molecules in gaseous and in condensed phase, high-sensitive techniques are required. One such technique is cavity enhanced absorption spectroscopy (CEAS), in which the interaction of light with the sample is increased to enhance the sensitivity. In this thesis, the development and applications of different variants of the CEAS technique are described for trace molecule analysis. Initially, the development of a quantum cascade laser (QCL) based cavity ring-down spectroscopy (CRDS) setup in the 6.2 μm region is described for gas-phase analysis. The system was used to probe rotational-vibrational spectra of ammonia (NH_3) molecule wherein interference-free spectral lines of NH_3 were analyzed. Subsequently, NH_3 was measured in air and human breath to demonstrate the ability of the setup for real-world applications.

Further, the above setup was employed to study the A/B hybrid type rotational-vibrational band of 1,3-butadiene in the 6.2 μm region and ~ 924 spectral lines were identified. We performed Gaussian and PGOPHER simulations to simulate the spectra of 1,3-butadiene and assign the experimental spectral lines. Next, we utilized another QCL-CRDS system at 7.8 μm to investigate deuterated isotopologues of water in the gas-phase where their relative fractionations were studied in the H-D exchange reaction between H_2O and D_2O. We further developed a setup combining evanescent wave (EW) with CRDS to study trace molecules in condensed phase. The system was utilized to study the interfacial kinetics of salt-induced aggregation of gold and silver nanoparticles on the prism surface and the effect of protein binding of urease on the aggregation of nanoparticles.

Eventually, we employed a CO_2 isotope analyzer based on the CEAS technique to explore the response of the urease enzyme towards isotopes of

CO_2. We observed a strong isotopic preference of urease towards $^{12}CO_2$ in comparison to $^{13}CO_2$, for its activation during the urea hydrolysis reaction. We also validated this behaviour in presence of isotopically varied bicarbonate ions. Thus, we developed and implemented the different variants of the CEAS technique for a variety of applications.

List of publications related to Thesis work

[1] **Sanchi Maithani**, Santanu Mandal, Abhijit Maity, Mithun Pal and Manik Pradhan. "High-resolution spectral analysis of ammonia near 6.2 μm using a cw EC-QCL coupled with cavity ring-down spectroscopy." ***Analyst*** 143, no. 9 (2018): 2109-2114.

[2] **Sanchi Maithani**, Abhijit Maity and Manik Pradhan. "High-resolution spectral analysis of hybrid A/B-type band of 1, 3-butadiene at 6.2 μm using an EC-QCL coupled with cavity ring-down spectroscopy." ***Chemical Physics*** 522, (2019): 123-128.

[3] **Sanchi Maithani**, Biswajit Panda, Abhijit Maity and Manik Pradhan. "Gas-Phase Isotopic Fractionation Study of Singly and Doubly Deuterated Isotopologues of Water in the H–D Exchange Reaction by Cavity Ring-Down Spectroscopy." ***The Journal of Physical Chemistry A*** 124, no. 6 (2020): 1104-1111.

[4] **Sanchi Maithani**, Abhijit Maity and Manik Pradhan. "A prototype evanescent wave-coupled cavity ring-down spectrometer for probing real-time aggregation kinetics of gold and silver nanoparticles." ***Analytical Chemistry*** 92, no. 5 (2020): 3998-4005.

[5] **Sanchi Maithani**, Mithun Pal, Abhijit Maity and Manik Pradhan. "Isotope selective activation: a new insight into the catalytic activity of urease." ***RSC advances*** 7, no. 50 (2017): 31372-31376.

[6] **Sanchi Maithani**, Abhijit Maity, Mithun Pal, Sayoni Bhattacharya, Gourab Dutta Banik, Chiranjit Ghosh, Sujit Chaudhuri and Manik Pradhan. "Isotopic evidences of the preferential coordination between $^{12}CO_2$ and urease enzyme." ***Chemical Physics*** 520, (2019): 21-26.

[7] **Sanchi Maithani**, Abhijit Maity and Manik Pradhan. "High-sensitive detection of ammonia in exhaled breath using cavity ring-down spectroscopy." ***Asian Journal of Physics*** 28, no. 4 (2019): 219-224.

List of publications apart from Thesis work

[1] Biswajit Panda, **Sanchi Maithani** and Manik Pradhan. "High-resolution investigation of temperature and pressure-induced spectroscopic parameters of ^{13}C-isotopomer of CH_4 in the v_4 band using cavity ring-down spectroscopy." ***Chemical Physics*** 535, (2020): 110769.

[2] Mithun Pal, **Sanchi Maithani**, Abhijit Maity and Manik Pradhan. "Simultaneous monitoring of ^{32}S, ^{33}S and ^{34}S isotopes of H_2S using cavity ring-down spectroscopy with a mid-infrared external-cavity quantum cascade laser." ***Journal of Analytical Atomic Spectrometry*** 34, no. 5 (2019): 860-866.

[3] Mithun Pal, **Sanchi Maithani**, Abhijit Maity, Sujit Chaudhuri and Manik Pradhan. "Exploring the physiological link of breath N_2O through nitrification and denitrification processes in human gastric juice." ***Journal of Breath Research*** 13, no. 1 (2018): 016002.

[4] Abhijit Maity, Mithun Pal, **Sanchi Maithani**, Gourab Dutta Banik and Manik Pradhan. "Wavelength modulation spectroscopy coupled with an external-cavity quantum cascade laser operating between 7.5 and 8 μm." ***Laser Physics Letters*** 15, no. 4 (2018): 045701.

[5] Abhijit Maity, Mithun Pal, Gourab Dutta Banik, **Sanchi Maithani** and Manik Pradhan. "Cavity ring-down spectroscopy using an EC-QCL operating at 7.5 μm for direct monitoring of methane isotopes in air." ***Laser Physics Letters*** 14, no. 11 (2017): 115701.

[6] Gourab Dutta Banik, Suman Som, Abhijit Maity, Mithun Pal, **Sanchi Maithani**, Santanu Mandal and Manik Pradhan. "An EC-QCL based N_2O sensor at 5.2 μm using cavity ring-down spectroscopy for environmental applications." ***Analytical Methods*** 9, no. 15 (2017): 2315-2320.

[7] Abhijit Maity, Mithun Pal, Suman Som, **Sanchi Maithani**, Sujit Chaudhuri and Manik Pradhan**.** "Natural ^{18}O and ^{13}C-urea in gastric juice:

a new route for non-invasive detection of ulcers." ***Analytical and Bioanalytical Chemistry*** 409, no. 1 (2017): 193-200.

[8] Abhijit Maity, Mithun Pal, **Sanchi Maithani**, Barnali Ghosh, Sujit Chaudhuri and Manik Pradhan. "Molecular hydrogen in human breath: a new strategy for selectively diagnosing peptic ulcer disease, non-ulcerous dyspepsia and *Helicobacter pylori* infection." ***Journal of Breath Research*** 10, no. 3 (2016): 036007.

List of conference proceedings, patent, review and book chapters

Conference proceeding

[1] **Sanchi Maithani**, Abhijit Maity, Mithun Pal and Manik Pradhan. "Ro-vibrational analysis of ammonia at 6.2 μm using high-precision cavity ring-down spectroscopy." In ***Optics and Photonics for Energy and the Environment*, Optical Society of America**, (2018), pp. EW3A.1.

Patent-Filed and published

[1] **Sanchi Maithani**, Abhijit Maity, Chandan Samanta, Kaustuv Das, Barnali Ghosh, Manik Pradhan and Arup Kumar Raychaudhuri. "A gas-sensing system for selective detection of (Nitric Oxide) NO gas and a method for fabricating the same." File no. 201731038036 A, (2017).

Review article

[1] **Sanchi Maithani** and Manik Pradhan. "Cavity ring-down spectroscopy and its applications to environmental, chemical and biomedical systems." ***Journal of Chemical Sciences*** (accepted) (2020).

Book chapters

[1] **Sanchi Maithani**, Abhijit Maity and Manik Pradhan. "Quantum Cascade Laser Spectroscopy for Atmospheric Sensing and Biomedical Diagnostics." In ***Advances in Spectroscopy: Molecules to Materials*, Springer, Singapore** (ISBN: 978-981-15-0201-9), (2019): 67-82.

[2] Abhijit Maity, **Sanchi Maithani** and Manik Pradhan. "Cavity Ring-Down Spectroscopy: Recent Technological Advances and Applications." In ***Molecular and Laser Spectroscopy: Advances and Applications, Volume 2*, Elsevier** (ISBN: 978-0-12-818870-5), (2020): 83-120.

Table of Contents

Thesis title: "Evanescent Wave And Cavity Enhanced Absorption Spectroscopy For Trace Molecule Sensing Using Diode And Quantum Cascade Lasers."

Thesis Abstract:

Trace molecule detection finds its applications in various fields such as environmental monitoring, biomedical analysis, chemical and industrial sensing. To detect low concentrations of molecules in gaseous and in condensed phase, high-sensitive techniques are required. One such technique is cavity enhanced absorption spectroscopy (CEAS), in which the interaction of light with the sample is increased to enhance the sensitivity. In this thesis, the development and applications of different variants of the CEAS technique are described for trace molecule analysis. Initially, the development of a quantum cascade laser (QCL) based cavity ring-down spectroscopy (CRDS) setup in the 6.2 μm region is described for gas-phase analysis. The system was used to probe rotational-vibrational spectra of ammonia (NH_3) molecule wherein interference-free spectral lines of NH_3 were analyzed. Subsequently, NH_3 was measured in air and human breath to demonstrate the ability of the setup for real-world applications.

Further, the above setup was employed to study the A/B hybrid type rotational-vibrational band of 1,3-butadiene in the 6.2 μm region and ~ 924 spectral lines were identified. We performed Gaussian and PGOPHER simulations to simulate the spectra of 1,3-butadiene and assign the experimental spectral lines. Next, we utilized another QCL-CRDS system at 7.8 μm to investigate deuterated isotopologues of water in the gas-phase where their relative fractionations were studied in the H-D exchange reaction between H_2O and D_2O. We further developed a setup combining evanescent wave (EW) with CRDS to study trace molecules in condensed phase. The system was utilized to study the interfacial kinetics of salt-induced aggregation of gold and silver nanoparticles on the prism surface and the effect of protein binding of urease on the aggregation of nanoparticles.

Eventually, we employed a CO_2 isotope analyzer based on the CEAS technique to explore the response of the urease enzyme towards isotopes of CO_2. We observed a strong isotopic preference of urease towards $^{12}CO_2$ in comparison to $^{13}CO_2$, for its activation during the urea hydrolysis reaction. We also validated this behaviour in presence of isotopically varied bicarbonate ions. Thus, we developed and implemented the different variants of the CEAS technique for a variety of applications.

Self-attested
Maithani
(SANCHI MAITHANI)

Chapter 1

The importance of trace molecule detection and its spectroscopic aspects: an introduction

1.1 Introduction to trace gas detection

Numerous inorganic and organic molecules such as carbon dioxide (CO_2), water vapour (H_2O), ammonia (NH_3), nitric oxide (NO), methane (CH_4), acetylene (C_2H_2) etc. are present in the environment and many of them are in trace quantities such as parts per million by volume (ppmv, 10^{-6}), parts per billion by volume (ppbv, 10^{-9}) and even parts per trillion by volume (pptv, 10^{-12}) levels. Even in such low concentrations, these molecules play significant roles in the environment by affecting the chemistry of atmosphere, soil, and oceans, and hence influence the overall climate. Moreover, the emergence of pollution and global warming have made the monitoring of such molecules further crucial. Table 1.1 provides the typical concentrations of few trace gases and their importance in the atmosphere. However, the exact gas concentrations vary from place to place depending on their sources of origin like biogenic (vegetation, microbial activity, volcanoes etc.) or anthropogenic (industrial, vehicular emission, agricultural activity etc.) sources. Besides the geological significance, many molecules and radicals are also of immense astrophysical interest and their study helps to reveal various processes in interstellar space.

Table 1.1: *Typical concentrations of trace gases in the atmosphere and their importance* [1-11].

Trace gas	Concentration ppbv (10^{-9})	Importance
Ammonia (NH_3)	0.01 - 50	Produced from fertilizer use, helps in the formation of particulate matter
Methane (CH_4)	1500-2000	Greenhouse gas, emitted from fossil fuels, main constituent of natural gas
Nitrous oxide (N_2O)	300-340	Greenhouse gas, causes ozone depletion, produced from various biogenic and anthropogenic sources
Nitrogen dioxide (NO_2)	0.01-200	Produced by combustion, lightning, volcanoes. Regulates atmospheric chemistry and effects ozone concentrations
Tropospheric ozone (O_3)	10-200	Greenhouse gas, air pollutant and produced through photochemical reactions of other precursor molecules.
Carbon monoxide (CO)	50-200	Toxic gas generated during incomplete combustion of fossil fuels and biomass.
1,3-butadiene (C_4H_6)	< 5	Carcinogenic gas emitted by vehicular exhaust, industries and cigarette smoke.

Another field where trace molecule detection has gained importance is biomedical diagnostics. For instance, several inorganic and organic trace gas molecules are exhaled from the human breath which can be analyzed to diagnose a disease or provide information about the health and

metabolic activities of an individual. This technique is commonly referred to as human breath analysis and is emerging as a non-invasive method in medical diagnostics. In some cases, the concentration of a molecule in exhaled breath can be correlated to a disease condition, for example the amount of H_2S in breath is linked to airway diseases [12]. In other cases, the breath molecule is analyzed in response to a suitable test meal that is provided to an individual, such as the monitoring of enriched $^{13}CO_2$ isotope in breath after a ^{13}C-enriched urea test meal to detect the presence of *Helicobacter Pylori (H. Pylori)* bacteria in stomach [13]. Table 1.2 enlists the concentrations of molecules in exhaled breath associated with various diseases.

Table 1.2: *Concentrations of molecules in human breath linked to various disease conditions* [12-21].

Trace gas	**Concentration in exhaled breath**	**Diseases/Condition**
Ammonia (NH_3)	0.05-2 ppmv	Kidney diseases, liver cirrhosis
Methane (CH_4)	2-10 ppmv	Fermentation by gut microbes, intestinal diseases
Carbon dioxide and its isotopes (CO_2)	3-5 %	*H. Pylori* infection in stomach, diabetes mellitus
Hydrogen sulphide (H_2S)	0.2–2 ppmv	Halitosis, Airway diseases
Nitric oxide (NO)	5-60 ppbv	Asthma, cystic fibrosis, lung cancer
Acetone (CH_3COCH_3)	0.2-4 ppmv	Diabetes mellitus, heart failure
1,3-butadiene (C_4H_6)	0.8-25 ppbv	Present in breath of smokers, carcinogenic

Many other volatile organic compounds (VOCs) such as ethane, propanol, acetonitrile etc. present in few tens of ppbv or sub-ppbv amounts are also known to be linked to certain malfunctions in the human body [22]. Thus, by exploring these trace constituents in breath, routine health analysis can be performed in a non-invasive way.

Trace gas sensing also presents many applications in other fields such as public security systems where organic vapours of explosives can be identified with concentrations as low as pptv [23]. Furthermore, certain organic compounds such as ethylene (C_2H_4) are linked to the growth of plants and can be an indicator for over-ripening of fruits, vegetables etc. in food processing and storage sites [23]. Some inorganic gases like NH_3, H_2S, and carbonyl sulphide (OCS) can react and cause surface damage in materials. Hence, the concentrations of these gases need to be monitored for industrial process control such as in semiconductor manufacturing sites. However, the trace sensing of such low concentrations of molecules requires high-sensitive and molecule selective techniques, some of which are discussed in section 1.5.

1.2 Importance of trace sensing in condensed phase

Trace species in the condensed phase (solid and liquid) such as colloids, radicals, trace elements and impurities are present all around us in the environment, water bodies, soil, man-made materials and also in human body. Even in low quantities, many such species are toxic to life and are severe pollutants such as heavy metal ions, acidic radicals, inorganic and organic industrial wastes, microplastics and so on. Hence, their presence in the environment needs to be regularly monitored. Again, in the biomedical field, the assessment of health parameters through testing of several species in body fluids (blood, urine, saliva etc.) is a common procedure. However, owing to the complexity and variety of the different

biomolecules present, the measurement systems are always in need of improvement.

Moreover, it is also crucial to understand the role of various chemical species in the environment, biological systems or in industrial processes by probing their interactions and identifying their specific behaviours. This can be achieved by studying their physical properties such as refractive indices, electrical and magnetic behaviour, their interactions with light (spectroscopy), chemical kinetics, reaction chemistry and so on. Numerous techniques and sensors have been devised to detect such trace species and examine their chemical characteristics. Few such techniques using the concept of evanescent wave have been described in section 1.6 of this chapter.

1.3 Importance of isotope analysis

Low abundant isotopes of molecules are another type of trace species as their natural abundances are very less in comparison to the main isotope of a molecule. However, isotopes are very useful indicators of various processes and deviations in physical and chemical systems over time. Moreover, it is also interesting to investigate reaction chemistry involving isotopes as it provides a deeper understanding of the fundamentals of chemical interactions. In the context of isotope analysis, the isotope ratio is more frequently used parameter than the exact isotope concentration. Stable isotope ratios in atmosphere, oceans, glaciers etc. are widely used to determine paleoclimatic information, climatic models and atmospheric chemistry [24, 25]. Such ratios, particularly the D/H ratio of water and $\delta^{13}C$ ratio of CH_4 and carbonates in planetary objects, interstellar clouds and meteorites provide valuable information about their formation and other processes occurring in them [26, 27]. Similarly, the study of isotopes has enabled effective detection and analysis of diseases such as the use of $^{13}C/^{12}C$ ratio of CO_2 to detect *H. Pylori* infection in stomach. Furthermore,

deuterated solvents (such as D_2O) and isotopic labeling of ^{13}C are used to identify and study compounds using Fourier transform infrared spectroscopy (FTIR) and nuclear magnetic resonance (NMR) spectroscopy, respectively [28]. Thus, the study of isotopes is used in a range of fields to explore the behavior of molecules and for many practical applications. Table 1.3 provides the significance of isotopes in various disciplines.

Table 1.3: *Significance and applications of less abundant stable isotopes of molecules in different fields*.

Molecule	Isotope/s	Significance
H_2O	$H_2{}^{18}O$, $H_2{}^{17}O$,HDO	Its measurement in oceans, glaciers, atmosphere provides paleoclimatic information [24, 25]
	D_2O	Used as coolant in heavy water nuclear reactors [29], used in FTIR analysis as a solvent to avoid H_2O absorption
	HDO	Used to detect leakage in heavy water reactors [29], to compute D/H ratio of water in astrophysical environments [27]
CO_2	$^{13}CO_2$	$^{13}C/^{12}C$ ratio of CO_2 is utilized in breath analysis to detect various diseases like *H. Pylori* infection [13], diabetes [30], irritable bowel syndrome [31] etc.
	$C^{18}O^{16}O$	^{18}O exchange in isotopes is linked to enzymatic activity and subsequently to disease detection [16]
CH_4	$^{13}CH_4$, CH_3D	$^{13}C/^{12}C$ and D/H ratios of CH_4 are used to study planetary atmospheres and surfaces [27], also used to

		compare organic and inorganic sources in nature [27]
N_2O	$N^{15}NO(^{\alpha}N)$, ^{15}NNO ($^{\beta}N$), $N_2{}^{18}O$	Site-specific $^{\alpha}N$ or $^{\beta}N$ and $N_2{}^{18}O$ are linked to mechanisms of N_2O production by microbes in soil [32]
H_2S	$H_2{}^{33}S$, $H_2{}^{34}S$, $H_2{}^{36}S$	Analysis of sulphur isotopes is used to understand astrophysical systems [33]

The isotope ratio is usually defined as the ratio of the heavier isotope of a molecule with respect to its main isotope (most abundant). The delta (δ) notation in units of ‰ (per mil) is used to express the isotope ratio of an atom in a molecule, as shown in equation 1.1 [13] for $^{13}C/^{12}C$ isotope ratios of carbon.

$$\delta^{13}C(‰) = \frac{\left(\frac{^{13}C}{^{12}C}\right)_{sample} - \left(\frac{^{13}C}{^{12}C}\right)_{standard}}{\left(\frac{^{13}C}{^{12}C}\right)_{standard}} \times 1000 \qquad (1.1)$$

The above equation is applicable to other atoms (N, O, H etc.) as well where the carbon isotopes above can be replaced with the isotopes of that atom. The ‰ symbol indicates multiplication by 1000, which is used to enhance the readability of the delta values since the ratio values are very small. The standard ratio value (denominator in equation 1.1) is used to provide a reference value with respect to which other values would be evaluated and hence the δ value for the standard is 0‰. The standard ratio value varies from one isotope to the other and is internationally accepted, although it may be updated from time to time. A list of the standards for the isotope ratios of various molecules is given in Table 1.4.

Table 1.4: *List of standard isotope ratio values for commonly used isotopes* [34, 35].

Isotope	Isotope ratio	Standard Used	Standard isotope ratio value
D (^{2}H)	D/H	Vienna Standard Mean Ocean Water (VSMOW)	1.5575×10^{-4}
^{17}O	$^{17}O/^{16}O$	Vienna Standard Mean Ocean Water (VSMOW)	3.799×10^{-4}
^{18}O	$^{18}O/^{16}O$	Vienna Standard Mean Ocean Water (VSMOW)	2.0052×10^{-3}
^{13}C	$^{13}C/^{12}C$	Vienna Pee Dee Belemnite (VPDB)	1.12372×10^{-2}
^{15}N	$^{15}N/^{14}N$	Atmospheric nitrogen (N_2)	3.677×10^{-3}
^{34}S	$^{34}S/^{32}S$	Vienna Canyon Diablo Troilite (VCDT)	4.5005×10^{-2}
^{37}Cl	$^{37}Cl/^{35}Cl$	Standard Mean Ocean Chloride (SMOC)	3.24×10^{-1}

In chapters 4, 6 and 7 of this thesis, works on isotope analysis have been described to study the interaction between different isotopes of a molecule (water) and the isotope-selective response of an enzyme.

1.4 Spectroscopic aspects of trace molecule sensing

1.4.1 Basic types of molecular spectroscopy

Spectroscopy is one of the most powerful ways which extracts information about molecules and their behaviors by exploiting the interaction between molecules and electromagnetic radiation. Although several different types of spectroscopy exist, here only few key types are described those have been utilized in this thesis work. Different electromagnetic regions induce different types of effects on the molecules. For instance, the transitions between the electronic energy levels in molecules occur in the ultraviolet (UV) and the visible light regions. The conventional method mostly used in UV-visible spectroscopy is to allow the incident light through a sample and collect the light intensity change after the sample. The absorption of light by the sample is given by the Beer-Lambert's law depicted in equation 1.2.

$$A = \log_{10}\frac{I_0}{I} = \varepsilon c l \qquad (1.2)$$

Here, A is the absorbance due to the sample, I and I_0 are the detected intensities of light with and without the sample, respectively, c is the concentration of the sample, l is the path length of light inside the sample and ε is the molar attenuation coefficient which depicts the ability of a sample to attenuate the light at a particular wavelength. A plot of the intensity of extinction of light by a sample against the wavelength or wavenumber is termed as a spectrum. The UV-visible spectroscopy is mainly used for quantitative determination of liquid and solid analytes, although few gases and radicals are also analyzed in the near-UV region. Figure 1.1 illustrates the conventional single pass absorption spectroscopy system.

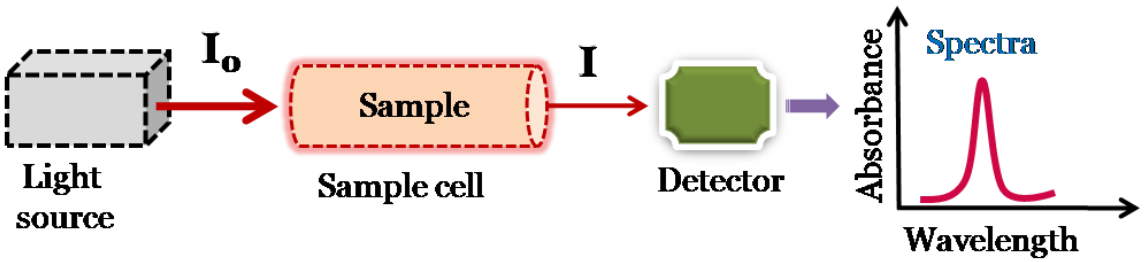

Figure 1.1 *A schematic illustration of the single pass absorption spectroscopy setup.*

The infrared (IR) region, on the other hand, induces molecular motion of vibration in the molecule. The criterion for a vibrational transition in a molecule is the variation in the molecule's dipole moment while undergoing a vibration. The vibration of a bond in a molecule can be expressed as a simplified model of a simple harmonic oscillator where the displacement potential energy V and the energy levels (ε_v) are given by equations 1.3 and 1.4, respectively.

$$V = \frac{1}{2}k(r - r_e)^2 \qquad (1.3)$$

where r depicts the internuclear distance of the atoms, r_e is the equilibrium distance at which the energy is minimum and k is the force constant.

$$\varepsilon_v = \left(v + \frac{1}{2}\right)\omega'; \quad \text{where } \omega' = \frac{1}{2\pi c}\sqrt{\frac{k}{\mu}} \qquad (1.4)$$

Here, v is the vibrational quantum number and can only take integral values, ω′ is the vibrational frequency (in cm^{-1}) and μ is the reduced mass of the atoms forming the bond. This results in a transition selection rule of $\Delta v = \pm 1$. However, in reality molecular bonds do not undergo perfect simple harmonic motion but involve anharmonicity. The anharmonic energy profile E with respect to the internuclear distance is expressed by the Morse function (equation 1.5).

$$E = D_e[1 - e^{(a(r_e - r))}]^2 \qquad (1.5)$$

where D_e is the dissociation energy for the molecule and a is a constant for a specific molecule. Subsequently, the vibrational energy levels are given

by equation 1.6 [28]. The equation takes into account the dissociation of a molecule into atoms as the bonds are stretched beyond a certain limit.

$$\varepsilon_v = \left(v + \frac{1}{2}\right)\omega'_e - \left(v + \frac{1}{2}\right)^2 \omega'_e x_e \qquad (1.6)$$

Here x_e is the anharmonicity constant and ω_e' is the equilibrium vibration frequency. From equation 1.6, the selection rules are extended to $\Delta v = \pm 1, \pm 2, \pm 3$ and so on. While $\Delta v = \pm 1$ represents a fundamental transition, $\Delta v = \pm 2, \pm 3$ etc. refer to first, second and subsequent overtone transitions. The fundamental and overtone transitions originate in the ground state v=0 whereas transitions originating from v=1 and above are called hot band transitions. The hot bands are of weaker intensities, though their strength can be increased by increasing the temperature. Since the IR spectroscopy involves bond vibrations, it provides a multitude of information on bond length, bond angles of a molecule and the interactions of a molecule with other molecules in its environment. More importantly, the characteristic frequency at which the transitions occur enables the identification of a molecule or the functional group present in a compound.

The vibrational transitions in the infrared region are mostly accompanied by rotational transitions as well since it requires less energy for molecular rotation than that for vibration. However, pure rotational spectrum can be observed in the microwave region. A molecule must have a permanent dipole moment to show the rotational spectrum. The energy of molecular rotation can be simply described by the energy of a rigid rotor system E_J (in cm^{-1}) as given in equation 1.7.

$$E_J = BJ(J+1); \quad \text{where } B = \frac{h}{8\pi^2 cI} \qquad (1.7)$$

Here, B is the rotational constant, J is the rotational quantum number, h is the Planck's constant, c is the speed of light and I is the moment of inertia of the molecule. It is to be noted that I and B are defined along each of the three dimensional axis of a molecule. However, when molecules rotate, the centrifugal force tends to pull the atoms away and it increases as the molecule rotates faster. This non-rigid behaviour can be incorporated in the above relation as (equation 1.8):

$$E_J = BJ(J+1) - DJ^2(J+1)^2 \text{; where } D = \frac{h^3}{32\pi^4 I^2 r^2 kc} \qquad (1.8)$$

where D is the centrifugal distortion constant, r is the internuclear distance and k is the force constant. The magnitude of D is far smaller than that of B and hence the contribution of D becomes relevant at higher values (>10) of J [28]. Nevertheless, the selection rule for a rotational transition is $\Delta J = \pm 1$.

The smaller rotational energy levels are present inside each vibrational level and give rise to the fine rotational-vibrational (ro-vibrational) spectrum in the infrared region. Depending on the selection rule, the ro-vibrational bands consist of different branches where $\Delta J = -1$, $\Delta J = 0$, and $\Delta J = +1$ represent P, Q and R branches, respectively. The presence of these fine ro-vibrational spectral bands provides the opportunity for probing the molecules in different spectral regions. The fundamental ro-vibrational transitions of molecules occur in the mid-IR region (~ 3-25 μm) which is aptly known as the molecular fingerprint region. On the other hand, the overtone transitions are observed in the near-infrared region (~0.85-3 μm) and have lower spectral line intensities than the fundamental bands. A significant advantage of ro-vibrational spectroscopy is that isotopes of the same molecule have distinct transition frequencies due to the difference in reduced mass μ, as evident from equation 1.4. Moreover, the moment of inertia I and rotational constant B will also be different and hence allowing the isotopes to be distinguished. Figure 1.2 shows a HITRAN simulation [36] of the absorption bands of trace molecules in the mid-infrared region

and also demonstrates the capability of ro-vibrational spectroscopy to distinguish between the isotopes of a molecule (as shown for CO_2 and water isotopes). HITRAN (high-resolution transmission) is a simulated spectroscopic database of trace molecules in the atmosphere.

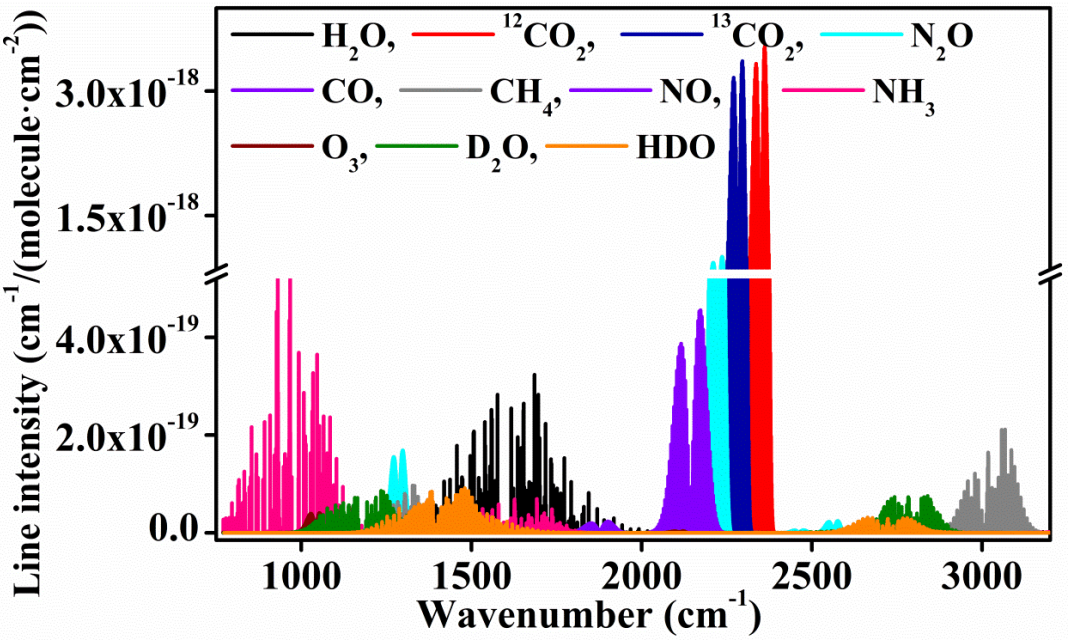

Figure 1.2 *HITRAN simulation of the absorption spectra of trace gases in the mid-infrared region. The shift in the spectra for different isotopes of a molecule can be seen for water (H_2O, HDO, D_2O) and CO_2 ($^{12}CO_2$ and $^{13}CO_2$).*

Thus, the ro-vibrational spectroscopy in the mid-infrared region is very much suited for trace sensing of gas molecules and their isotopes due to the strong fundamental bands in this region. However, collisional broadening of the spectra occurs for liquids and there is increased possibility of spectral overlap with other molecules. Still, oftentimes infrared spectroscopy is used to detect functional group frequencies in liquid state compounds. In contrast, in the UV-visible region, few gases have absorption bands while many liquids, colloids, nanoparticles and biological compounds possess specific absorption bands and hence the UV-visible spectroscopy is used as a common characterization technique in chemistry. Nevertheless, in the current thesis work, we have utilized ro-vibrational

and the UV-visible region for trace detection of gas phase and liquid phase molecules, respectively.

1.4.2 Spectral linewidth

Every spectral transition line possesses a certain linewidth, i.e. a range of frequencies around the line centre due to the finite lifetime of the transition. This fundamentally comes from the Heisenberg's uncertainty relation between the energy of a state and the lifetime in that state. Hence, the uncertainty or the width of the transition frequency ($\Delta\nu$) can be stated as equation 1.9 and is referred to as the natural broadening of the spectral line.

$$\Delta\nu = \frac{\Delta E}{h} \approx \frac{1}{2\pi\Delta t} \qquad (1.9)$$

where ΔE and Δt are the uncertainties in the energy and the lifetime, respectively.

Random molecular motions in liquids and gases also produce Doppler effect in the transition frequencies, thereby causing a broadening in the spectral lines. This is known as Doppler broadening and can be expressed using a Gaussian line shape function where the width or full width half maximum (FWHM) $\Delta\nu_{FWHM}$ of the spectral line is given by equation 1.10.

$$\Delta\nu_{FWHM} = \frac{2\nu_0}{c}\sqrt{\frac{2k_B T \ln 2}{m}} \qquad (1.10)$$

Here, ν_0 is the transition line centre, c is the speed of light, k_B is the Boltzmann's constant, T is the temperature and m is the mass of the molecule or the moving particle.

Another significant cause of spectral broadening is the collision among the molecules or particles. The collisions reduce the lifetime of the transitions and hence cause a widening of the spectral line. This collisional broadening

is also called pressure broadening as increase in pressure increases the collisional probability and is more pronounced in liquids and gases at high pressures. The pressure broadening is represented using a Lorentzian spectral line shape. However, in cases when both Doppler and collisional broadening are dominant, then the Voigt profile, which is a convolution of the Gaussian and the Lorentzian line profile, is used to express the spectral line shape.

1.5 An overview of techniques for trace gas detection

1.5.1 Single and multi-pass absorption spectroscopy

As discussed in section 1.4.1, the conventional technique of absorption spectroscopy involves the comparing of light intensity in the presence and absence of a sample. But, the intensity fluctuations of the light source create a background noise which is reflected in the detected intensity. Hence, the absorbance due to low concentration of a sample (equation 1.2) will be indistinguishable from the background noise in the conventional single pass absorption technique. According to equation 1.2, the absorption of such trace concentrations can be made substantial by increasing the path length through the sample. This has led to the use of multi-pass cells such as White cell and Herriott cell where focusing mirrors are used to allow numerous passes of the light beam inside the sample cell, thus increasing the path length through the sample of interest. Holes or slits in the mirrors allow the entry and exit of the light. Although the path length in these cells can go up to tens of metres, it is difficult to achieve larger path lengths due to interference between the beams which limits the detection sensitivity [37-39].

1.5.2 Fourier Transform Infrared Spectroscopy (FTIR)

In the IR region, Fourier transform infrared spectroscopy (FTIR) is one of the most commonly used techniques for characterization of molecules and compounds. In FTIR, light beam with a range of frequencies is passed through the sample and data is collected multiple times by modulating the input beam using an interferometer. The resultant data is Fourier transformed to obtain the spectrum of the sample [40]. FTIR is more commonly used for solid and liquid samples than for gas phase molecules. For gases, multi-pass absorption cells are used where sufficient concentration or pressure of the gas is required to obtain the spectra. Such conditions increase the spectral broadening, thereby lowering the resolution and making the selective detection of a molecule difficult. Nevertheless, since FTIR spectroscopy covers a wide spectral range in IR, it is still utilized for the detection of multiple gas species in low-resolution [41], or in combination with other spectroscopic techniques [42].

1.5.3 Gas chromatography based mass spectrometry (GC-MS) technique

The GC-MS technique has long been used for specific and quantitative detection of gaseous and volatile compounds. It involves the passage of a sample through a capillary column and utilizes the time it requires for a compound to pass through the column which is called the retention time. The various components of a compound emerging from the column are detected using a mass spectrometer which detects the component species according to their mass to charge (m/z) ratio [43]. GC-MS is widely used in pharmaceutical, forensic, environmental and many other chemical analysis applications [44, 45]. Yet, there are some limitations of GC-MS such as the difficulty in detection of non-volatile, polar and thermally unstable compounds.

1.5.4 Photoacoustic spectroscopy (PAS)

In PAS technique, the interaction of light with the molecules is observed indirectly using the acoustic detection. The input light is modulated, which changes the sample temperature if any absorption occurs and consequently produces an output of a modulated acoustic wave. The output is measured using a sensitive microphone or a quartz tuning fork in quartz-enhanced PAS (QEPAS) which provides high-sensitivity of detection. QEPAS has been utilized for trace molecular detection in various fields [46, 47]. The acoustic signal in QEPAS can be enhanced by increasing the power of the light source. This can be advantageous as there is scope of better performance when using a high power source.

1.5.5 Cavity enhanced absorption spectroscopy (CEAS) technique

As discussed in section 1.4.1, the enhancement in the path length through a sample can directly increase the absorbance. In CEAS technique, the path length is markedly enhanced by trapping the input light in an optical cavity created by two very high-reflectivity mirrors. After entering the cavity, the light makes multiple reflections inside the cavity owing to the high-reflective mirrors. A part of the light intensity is leaked from the mirrors after every trip of the light. The intensity of the output light after each pass decays exponentially and the decay time constant of this signal is measured. The decay rate of the light is noted in the presence and absence of the sample and is directly proportional to the absorption due to the sample. Here, the path length can be enhanced to several kilometers and thus the sensitivity is greatly increased. Since the measurement parameter is the decay time and not the intensity, the technique is immune to the intensity fluctuations of the source. The CEAS technique and many of its variants such as cavity ring-down spectroscopy (CRDS), off-axis integrated cavity output spectroscopy (OA-ICOS), broad-band cavity enhanced absorption spectroscopy (BB-CEAS) etc. are widely used in trace detection

of species such as gases, aerosols, radicals etc. and the technique can also be extended to probe condensed phase molecules [48, 49]. In this thesis work, the CEAS technique has been utilized in the mid-infrared, near-infrared and the visible spectral regions to probe molecules in the gas as well as condensed phase. The principles have been described in detail in further chapters.

1.6 Evanescent-wave based spectroscopy in the condensed phase

Spectroscopy in the condensed phases comes with its own set of considerations. Particularly, for the liquid phase, the UV-visible region is one of the most favourable choices as many chemical species such as dyes, nanoparticles, biological and inorganic compounds possess strong absorption bands in this region. The fluorescent properties of dyes and the plasmon absorption bands of nanoparticles are frequently exploited in different types of sensors for detection of chemical and biological species [50]. Nowadays, there is an ever increasing demand for compact and fast chemical detection methods [50] such as fibre-optic based sensing, surface plasmon resonance (SPR), attenuated total internal reflectance (ATR) spectroscopy, plasmonic and nano-chip based sensors and so on. These sensors usually rely on the interaction of the target molecules with the sensor surface for their detection. Thus, it is vital that surface interactions are characterized properly for better performance. It is also crucial to determine the kinetics of such surface interactions to work out the response times and the corresponding mechanisms of the interactions.

Many of these sensors utilize the phenomenon of total internal reflection (TIR) of light which occurs when light passes from a denser to a rarer medium at an angle above the critical angle. Since the light is totally reflected, the incident energy is equal to the reflected light energy and no power is carried in the second medium. Figure 1.3 depicts the total internal

reflection phenomenon between two interfaces. However, due to the discontinuity at the interfacial boundary of the two media, the Maxwell's equations on the boundary conditions give an exponentially decaying field in the second medium. This field is called the evanescent wave (EW) and it extends in a sub-wavelength region above the interface. The expression for EW can be derived from the total internal reflection theory as follows [51, 52]:

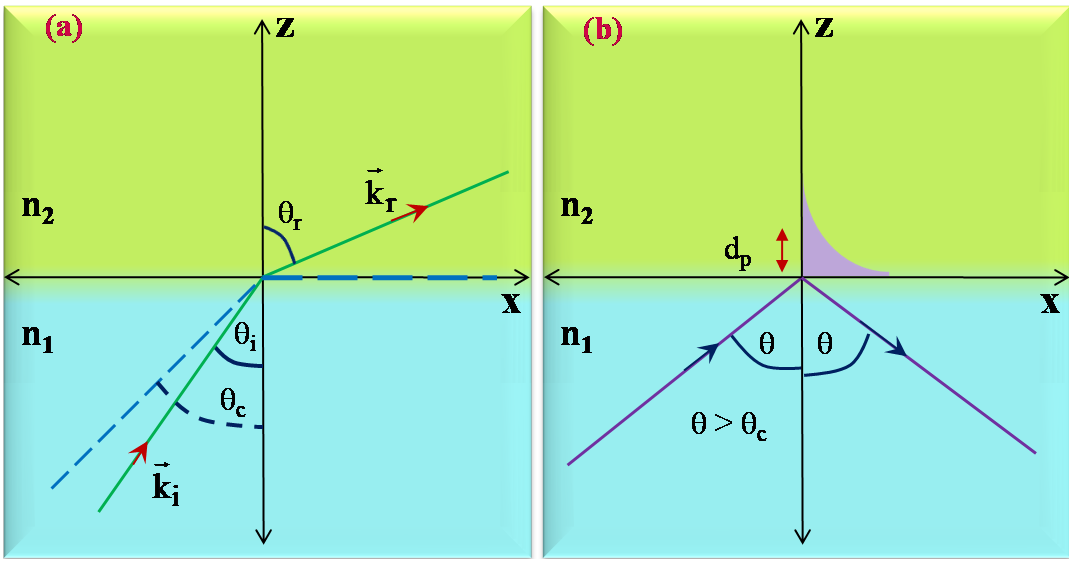

Figure 1.3 a) *shows the refraction of light from higher (n_1) to lower (n_2) refractive index medium. θ_c is the critical angle at which the light is refracted parallel to the interface of the two media.* ***b)*** *At angles greater than the critical angle, the light reflects in the same medium (n_1) with an exponentially decaying evanescent wave in the second medium.*

Let a plane wave of electric field $E_i(\mathbf{r},t)$ be incident on the x-z plane with a wave vector k_i as shown in Figure 1.3. The form of $E_i(\mathbf{r},t)$ and the corresponding refracted beam $E_r(\mathbf{r},t)$ with wave vector k_r is given in equation 1.11 below:

$$E_i(\vec{\mathbf{r}},t) = E_{i0}\, e^{i(\vec{k}_i.\vec{\mathbf{r}}-\omega t)},\ E_r(\vec{\mathbf{r}},t) = E_{r0}\, e^{i(\vec{k}_r.\vec{\mathbf{r}}-\omega t)} \quad (1.11)$$

$$E_{r0}e^{i(\vec{k}_r.\vec{\mathbf{r}})} = E_{r0}e^{i(\sin\theta_r\, k_x x+\cos\theta_r k_z z)} \qquad (1.12)$$

where ω is the wave frequency, E_{i0} and E_{r0} are the amplitudes of the fields and **r** is the position vector.

By law of refraction:
$$\sin\theta_i = \frac{n_2}{n_1}\sin\theta_r \qquad (1.13)$$

Here, n_1 and n_2 are the refractive indices of the two media and θ_i and θ_r are the incidence and refracted angles, respectively.

Since critical angle $\theta_c = \sin^{-1}(n_2/n_1)$, at incidence angle $\theta_i > \theta_c$,

$$\Rightarrow \cos\theta_r = i\sqrt{\frac{\sin^2\theta_i}{(n_2/n_1)^2}-1} \qquad (1.14)$$

Using equations 1.14 in 1.12, we get

$$\Rightarrow E_{r0}\, e^{i\sin\theta_r k_{rx}x}\, e^{-\alpha k_{rz}z} \qquad (1.15)$$

where α is the decay constant given by:

$$\alpha = \sqrt{\frac{\sin^2\theta_i}{(n_2/n_1)^2}-1} \qquad (1.16)$$

The above equation 1.15 shows a propagating wave in the x direction and an exponentially decaying wave in the z-direction. This decaying component constitutes the evanescent wave. The intensity of the EW can be expressed as equation 1.17 below:

$$I = I_0 e^{-\frac{z}{d_p}} \qquad (1.17)$$

where d_p is the extent of the decay or the penetration of the EW in the second medium and is known as the penetration depth (equation 1.18) of the EW.

$$d_p = \frac{\lambda}{2\pi\sqrt{n_1^2 \sin^2\theta_i - n_2^2}} \qquad (1.18)$$

Here λ is the wavelength of the light beam used.

When molecules enter the penetration depth of the EW and interact with the EW field, the EW is perturbed and draws light from the incident light beam. The resultant change in the reflected light can be measured and thus the small extent of the EW allows molecular species to be detected with high surface sensitivity. A diagram illustrating the perturbation of evanescent wave through particle scattering is shown in Figure 1.4 where TIR is realized in a prism-water interface. This property of the EW is utilized in many surface sensors as mentioned before. Few such techniques are described below:

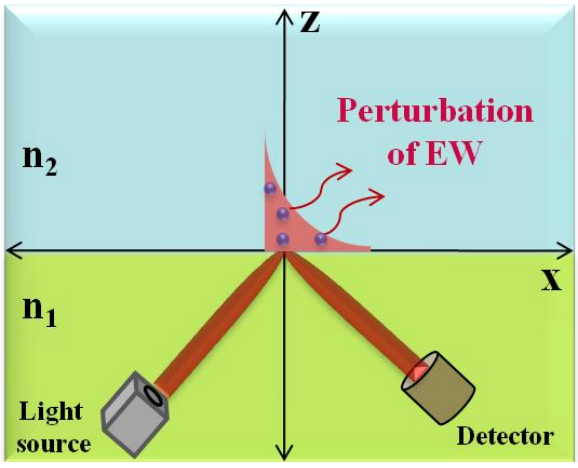

Figure 1.4 *depicts the perturbation of the evanescent wave where interaction of evanescent wave with particles or molecular species results in the propagation of light in the second medium.*

1.6.1 Fibre optic based sensors

An optical fibre consists of a high refractive index core material covered with a lower refractive index cladding. When light enters at a suitable angle in an optical fibre, such that the angle of incidence from the core to the cladding is more than the critical angle, the light experiences TIR at the core-cladding interface and travels through the entire fibre length with repeated TIR events. To utilize the fibre optic as a sensor, part of the cladding length on the fibre is removed to expose the core which in turn creates another high to low index medium interface. Thus, repeated TIR events create EW at multiple positions. This exposed layer is usually chemically coated to sense specific molecular species. The multiple events increase the sensitivity of the sensor while the small size allows the sensor to be compact. These features have enabled optical fibres to be used frequently in chemical sensing [53-55].

1.6.2 Surface plasmon resonance (SPR) based sensors

Plasmons are the free electron oscillations in a metal which can be generated by optical frequencies at certain conditions. In SPR, a thin film of a noble metal (silver, gold etc.) is coated on a dielectric to create a metal-dielectric interface on top of which the EW is generated using the TIR condition. At a particular angle greater than the critical angle, the wave vector of the incident light matches the wave vector of the plasmon oscillations which results in surface plasmon resonance [56, 57]. In SPR, both the intensity and the penetration depth of the resultant EW field get enhanced and therefore SPR offers a sensitive sensing surface. The SPR phenomenon depends on both the wavelength and the angle of incident light used and so SPR can be achieved either by varying the incident angle at constant wavelength or by changing the wavelength at a constant angle. In SPR, the particular SPR angle or wavelength is sensitive to the refractive index of the medium above the dielectric-metal interface. To utilize this

property in sensing, the metal surface is coated or functionalized chemically with a receptor which can sense or get attached to another target molecule. A change in the surface coating or a surface interaction causes a change in the SPR angle or wavelength and thus the system is used as a surface-sensitive sensor. Due to the increased field sensitivity in SPR, it is widely utilized as a biosensor for detecting biomolecules and to study their interactions [50, 56-58].

Another form of plasmon resonance known as localized surface plasmon resonance (LSPR) is seen in metal nanoparticles where the particle size is smaller or comparable to the wavelength of light. The field near the particle is significantly increased and large absorption is observed at the plasmon resonant frequency. This frequency mainly lies in the visible light region and is sensitive to the immediate environment and the interactions of the nanoparticles. Hence, the plasmon absorptions are used to detect and study interactions of chemical species with the nanoparticles [59, 60] and have enabled the use of nanoparticles in various colorimetric and surface based sensor chips [59-62].

1.6.3 Attenuated total internal reflectance (ATR) spectroscopy

The ATR spectroscopy utilizes the evanescent wave through TIR in a high refractive index crystal and is mainly used in the infrared region. The crystal is generally chosen to be long so as to allow EW at multiple spots to increase the sensitivity. Moreover, the penetration depth of the EW for the infrared beam can possess a range about ~ 0.4-5 μm which is greater than those in the visible region (ranging from tens to few hundred nanometres). ATR is utilized in combination with Fourier transform infrared spectroscopy to analyze the infrared spectra of solid and liquid samples and probe analyte interactions in the infrared region [63-65].

1.6.4 Evanescent wave-cavity enhanced absorption spectroscopy

Although EW can be a useful tool for studying interfacial activity of molecules, direct use of EW is limited due to the difficulty in accurate measurement of very minute changes in the reflected intensity against the background intensity noise of the light beam. This limitation has been overcome by combining the EW with CEAS technique where the measurement of the decay time eliminates the noise due to intensity fluctuations from the light source. The EW is typically created on top of a prism which is kept inside the optical cavity in CEAS. Moreover, the multiple passes in the optical cavity provides high-sensitivity and allows the analysis of liquid and solid molecular species using the CEAS technique. This technique has been employed for numerous applications to probe interfacial kinetics, surface adsorption of molecules, thin-film analysis, surface electrochemistry and so on [66-68]. The technical details of EW-CEAS are discussed in Chapter 5 of this thesis where an EW-CEAS setup has been developed to investigate the interfacial kinetics of nanoparticles in the visible light region.

1.7 References

[1] Carmichael, G. R., M. Ferm, N. Thongboonchoo, J. -H. Woo, L. Y. Chan, K. Murano, P. H. Viet *et al.* "Measurements of sulfur dioxide, ozone and ammonia concentrations in Asia, Africa, and South America using passive samplers." *Atmospheric Environment* 37, no. 9-10 (2003): 1293-1308.

[2] von Bobrutzki, K., C. F. Braban, D. Famulari, S. K. Jones, T. Blackall, T. E. L. Smith, M. Blom *et al.* "Field inter-comparison of eleven atmospheric ammonia measurement techniques." *Atmospheric Measurement Techniques* 3, (2010): 91-112.

[3] Blasing, T. J. "Recent Greenhouse Gas Concentrations". United States. doi:10.3334/CDIAC/atg.032. https://www.osti.gov/servlets/purl/1394398. (2016).

[4] Turner, A. J., C. Frankenberg, P. O. Wennberg and D. J. Jacob. "Ambiguity in the causes for decadal trends in atmospheric methane and hydroxyl." *Proceedings of the National Academy of Sciences* 114, no. 21 (2017): 5367-5372.

[5] Schreiber, F., P. Wunderlin, K. M. Udert and G. F. Wells. "Nitric oxide and nitrous oxide turnover in natural and engineered microbial communities: biological pathways, chemical reactions, and novel technologies." *Frontiers in microbiology* 3, (2012): 372.

[6] Syakila, A. and C. Kroeze. "The global nitrous oxide budget revisited." *Greenhouse Gas Measurement and Management* 1, no. 1 (2011): 17-26.

[7] Kharol, S. K., R. V. Martin, S. Philip, B. Boys, L. N. Lamsal, M. Jerrett, M. Brauer, D. L. Crouse, C. McLinden and R. T. Burnett. "Assessment of the magnitude and recent trends in satellite-derived ground-level nitrogen dioxide over North America." *Atmospheric Environment* 118, (2015): 236-245.

[8] Cooper, O. R., D. D. Parrish, J. Ziemke, M. Cupeiro, I. E. Galbally, S. Gilge, L. Horowitz *et al.* "Global distribution and trends of tropospheric ozone: An observation-based review." *Elementa: Science of the Anthropocene* 2, (2014): p.000029.

[9] U.S. EPA. 2017b. History of the national ambient air quality standards for carbon monoxide. Accessed 2017. https://www.epa.gov/co-pollution/table-historical-carbon-monoxide-co-national-ambient-air-quality-standards-naaqs.

[10] Duffy, B. L. and P. F. Nelson. "Exposure to emissions of 1, 3-butadiene and benzene in the cabins of moving motor vehicles and buses in Sydney, Australia." *Atmospheric Environment* 31, no. 23 (1997): 3877-3885.

[11] Kim, Y. M., S. Harrad and R. M. Harrison. "Concentrations and sources of VOCs in urban domestic and public microenvironments." *Environmental science & technology* 35, no. 6 (2001): 997-1004.

[12] Chen, Y. H., W. Z. Yao, B. Geng, Y. L. Ding, M. Lu, M. W. Zhao and C. S. Tang. "Endogenous hydrogen sulfide in patients with COPD." *Chest* 128, no. 5 (2005): 3205-3211.

[13] Crosson, E. R., K. N. Ricci, B. A. Richman, F. C. Chilese, T. G. Owano, R. A. Provencal, M. W. Todd *et al.* "Stable isotope ratios using cavity ring-down spectroscopy: determination of 13C/12C for carbon dioxide in human breath." *Analytical Chemistry* 74, no. 9 (2002): 2003-2007.

[14] Hibbard, T. and A. J. Killard. "Breath ammonia analysis: Clinical application and measurement." *Critical Reviews in Analytical Chemistry* 41, no. 1 (2011): 21-35.

[15] Pimentel, M., R. P. Gunsalus, S. S. C. Rao and H. Zhang. "Methanogens in human health and disease." *The American Journal of Gastroenterology Supplements* 1, no. 1 (2012): 28.

[16] Ghosh, C., S. Mandal, G. D. Banik, A. Maity, P. Mukhopadhyay, S. Ghosh and M. Pradhan. "Targeting erythrocyte carbonic anhydrase and 18O-isotope of breath CO2 for sorting out type 1 and type 2 diabetes." *Scientific reports* 6, (2016): 35836.

[17] Suarez, F. L., J. K. Furne, J. Springfield and M. D. Levitt. "Morning breath odor: influence of treatments on sulfur gases." *Journal of dental research* 79, no. 10 (2000): 1773-1777.

[18] Ojoo, J. C., S. A. Mulrennan, J. A. Kastelik, A. H. Morice and A. E. Redington. "Exhaled breath condensate pH and exhaled nitric oxide in allergic asthma and in cystic fibrosis." *Thorax* 60, no. 1 (2005): 22-26.

[19] Wang, C., A. Mbi and M. Shepherd. "A study on breath acetone in diabetic patients using a cavity ringdown breath analyzer: exploring correlations of breath acetone with blood glucose and glycohemoglobin A1C." *IEEE Sensors Journal* 10, no. 1 (2009): 54-63.

[20] Marcondes-Braga, F. G., I. G. R. Gutz, G. L. Batista, P. H. N. Saldiva, S. M. Ayub-Ferreira, V. S. Issa, S. Mangini, E. A. Bocchi and F. Bacal. "Exhaled acetone as a new biomarker of heart failure severity." *Chest* 142, no. 2 (2012): 457-466.

[21] Gordon, S. M., L. A. Wallace, M. C. Brinkman, P. J. Callahan and D. V. Kenny. "Volatile organic compounds as breath biomarkers for active and passive smoking." *Environmental health perspectives* 110, no. 7 (2002): 689-698.

[22] Konvalina, G. and H. Haick. "Sensors for breath testing: from nanomaterials to comprehensive disease detection." *Accounts of chemical research* 47, no. 1 (2014): 66-76.

[23] Fidric, B. G., R. A. Provencal, S. M. Tan, E. R. Crosson, A. A. Kachanov and B. A. Paldus. "Bananas, explosives and the future of cavity ring-down spectroscopy." *Optics and photonics news* 14, no. 7 (2003): 24-29.

[24] Van Trigt, R., H. A. J. Meijer, A. E. Sveinbjörnsdóttir, S. J. Johnsen and E. R. Th. Kerstel. "Measuring stable isotopes of hydrogen and oxygen in ice by means of laser spectrometry: the Bølling transition in the Dye-3 (south Greenland) ice core." *Annals of Glaciology* 35, (2002): 125-130.

[25] Hanisco, T. F., E. J. Moyer, E. M. Weinstock, J. M. St. Clair, D. S. Sayres, J. B. Smith, R. Lockwood *et al.* "Observations of deep convective influence on stratospheric water vapor and its isotopic composition." *Geophysical research letters* 34, no. 4 (2007).

[26] McKay, D. S., E. K. Gibson, K. L. Thomas-Keprta, H. Vali, C. S. Romanek, S. J. Clemett, X. D. F. Chillier, C. R. Maechling and R. N. Zare. "Search for past life on Mars: possible relic biogenic activity in Martian meteorite ALH84001." *Science* 273, no. 5277 (1996): 924-930.

[27] Webster, C. R. and P. R. Mahaffy. "Determining the local abundance of Martian methane and its' 13C/12C and D/H isotopic ratios for comparison with related gas and soil analysis on the 2011 Mars Science Laboratory (MSL) mission." *Planetary and Space Science* 59, no. 2-3 (2011): 271-283.

[28] Banwell, C. N. and E. M. McCash. *Fundamentals of molecular spectroscopy*. 5th Edition. McGraw-Hill, (1994).

[29] Kim, T. S., H. Park, K. Ko, G. Lim, Y. H. Cha, J. Han and D. Y. Jeong. "Laser-based sensor for a coolant leak detection in a nuclear reactor." *Applied Physics B* 100, no. 2 (2010): 437-442.

[30] Ghosh, C., A. Maity, G. D. Banik, S. Som, A. Chakraborty, C. Selvan, S. Ghosh, B. Ghosh, S. Chowdhury and M. Pradhan. "Non-invasive 13C-glucose breath test using residual gas analyzer-mass spectrometry: a novel tool for screening individuals with pre-diabetes and type 2 diabetes." *Journal of Breath research* 8, no. 3 (2014): 036001.

[31] Banik, G. D., A. Maity, S. Som, C. Ghosh, S. B. Daschakraborty, S. Chaudhuri, S. Ghosh and M. Pradhan. "Diagnosis of small intestinal bacterial overgrowth in irritable bowel syndrome patients using high-precision stable 13CO2/12CO2 isotope ratios in exhaled breath." *Journal of Analytical Atomic Spectrometry* 29, no. 10 (2014): 1918-1924.

[32] Park, S., T. Pérez, K. A. Boering, Susan E. Trumbore, J. Gil, S. Marquina and S. C. Tyler. "Can N2O stable isotopes and isotopomers be useful tools to characterize sources and microbial pathways of N2O production and consumption in tropical soils?" *Global Biogeochemical Cycles* 25, no. 1 (2011).

[33] Chakraborty, S., T. L. Jackson, M. Ahmed and M. H. Thiemens. "Sulfur isotopic fractionation in vacuum UV photodissociation of hydrogen sulfide and its potential relevance to meteorite analysis." *Proceedings of the National Academy of Sciences* 110, no. 44 (2013): 17650-17655.

[34] Kendall, C. and E. A. Caldwell. "Fundamentals of isotope geochemistry." In *Isotope tracers in catchment hydrology*, pp. 51-86. Elsevier, (1998).

[35] Sharp, Z. "Principles of stable isotope geochemistry 2nd Edition", (2017). doi: https://doi.org/10.25844/h9q1-0p82

[36] Gordon, I. E., L. S. Rothman, C. Hill, R. V. Kochanov, Y. Tan, P. F. Bernath, M. Birk *et al.* "The HITRAN2016 molecular spectroscopic database." *Journal of Quantitative Spectroscopy and Radiative Transfer* 203, (2017): 3-69.

[37] McManus, J. B., D. D. Nelson, S. C. Herndon, J. H. Shorter, M. S. Zahniser, S. Blaser, L. Hvozdara, A. Muller, M. Giovannini and J. Faist. "Comparison of cw and pulsed operation with a TE-cooled quantum cascade infrared laser for detection of nitric oxide at 1900 cm-1." *Applied Physics B* 85, (2006): 235-241.

[38] Waechter, H. and M. W. Sigrist. "Mid-infrared laser spectroscopic determination of isotope ratios of N2O at trace levels using wavelength modulation and balanced path length detection." *Applied Physics B* 87, no. 3 (2007): 539-546.

[39] Lancaster, D. G., D. Richter, R. F. Curl and F. K. Tittel. "Real-time measurements of trace gases using a compact difference-frequency-based sensor operating at 3.5 μm." *Applied Physics B: Lasers & Optics* 67, no. 3 (1998): 339-345.

[40] Doyle, W. M. "Principles and applications of Fourier transform infrared (FTIR) process analysis." *Process Control Qual* 2, no. 1 (1992): 11-41.

[41] Toon, G. C., C. C. Liebe, B. Nemati, I. Harris, A. Kleinböhl, M. Allen, V. Hipkin *et al.* "Solar occultation FTIR spectrometry at Mars for trace gas detection: A sensitivity study." *Earth and Space Science* 6, no. 5 (2019): 836-860.

[42] Liu, L., A. Mandelis, A. Melnikov, K. Michaelian, H. Huan and C. Haisch. "Step-Scan T-Cell Fourier Transform Infrared Photoacoustic Spectroscopy (FTIR-PAS) for

Monitoring Environmental Air Pollutants." *International Journal of Thermophysics* 37, no. 7 (2016): 64.

[43] Clement, R. E. and V. Y. Taguchi. "Techniques for the gas chromatography-mass spectrometry identification of organic compounds in effluents." (1991).

[44] Yang, X., H. Zhang, Y. Liu, J. Wang, Y. C. Zhang, A. J. Dong, H. T. Zhao, C. H. Sun and J. Cui. "Multiresidue method for determination of 88 pesticides in berry fruits using solid-phase extraction and gas chromatography–mass spectrometry: Determination of 88 pesticides in berries using SPE and GC–MS." *Food chemistry* 127, no. 2 (2011): 855-865.

[45] Fiehn, O. "Metabolomics by gas chromatography–mass spectrometry: Combined targeted and untargeted profiling." *Current protocols in molecular biology* 114, no. 1 (2016): 30-4.

[46] Wojtas, J., Z. Bielecki, T. Stacewicz, J. Mikołajczyk and M. Nowakowski. "Ultrasensitive laser spectroscopy for breath analysis." *Opto-electronics review* 20, no. 1 (2012): 26-39.

[47] Ma, Y. "Review of recent advances in QEPAS-based trace gas sensing." *Applied Sciences* 8, no. 10 (2018): 1822.

[48] Mazurenka, M., A. J. Orr-Ewing, R. Peverall and G. A. D. Ritchie. "4 cavity ring-down and cavity enhanced spectroscopy using diode lasers." *Annual Reports Section" C" (Physical Chemistry)* 101, (2005): 100-142.

[49] Berden, G., R. Peeters and G. Meijer. "Cavity ring-down spectroscopy: Experimental schemes and applications." *International reviews in physical chemistry* 19, no. 4 (2000): 565-607.

[50] Li, M., S. K. Cushing and N. Wu. "Plasmon-enhanced optical sensors: a review." *Analyst* 140, no. 2 (2015): 386-406.

[51] Novotny, L. and B. Hecht. *Principles of nano-optics*. Cambridge university press, (2012).

[52] Prieve, D. C. and J. Y. Walz. "Scattering of an evanescent surface wave by a microscopic dielectric sphere." *Applied optics* 32, no. 9 (1993): 1629-1641.

[53] Wang, Xu-D. and O. S. Wolfbeis. "Fiber-optic chemical sensors and biosensors (2008–2012)." *Analytical chemistry* 85, no. 2 (2013): 487-508.

[54] Srivastava, S. K., V. Arora, S. Sapra and B. D. Gupta. "Localized surface plasmon resonance-based fiber optic U-shaped biosensor for the detection of blood glucose." *Plasmonics* 7, no. 2 (2012): 261-268.

[55] Leung, A., P. M. Shankar and R. Mutharasan. "A review of fiber-optic biosensors." *Sensors and Actuators B: Chemical* 125, no. 2 (2007): 688-703.

[56] Caucheteur, C., T. Guo and J. Albert. "Review of plasmonic fiber optic biochemical sensors: improving the limit of detection." *Analytical and bioanalytical chemistry* 407, no. 14 (2015): 3883-3897.

[57] Homola, J. "Surface plasmon resonance sensors for detection of chemical and biological species." *Chemical reviews* 108, no. 2 (2008): 462-493.

[58] Nivedha, S., P. R. Babu and K. Senthilnathan. "Surface plasmon resonance: physics and technology." *Current Science (00113891)* 115, no. 1 (2018).

[59] Mayer, K. M. and J. H. Hafner. "Localized surface plasmon resonance sensors." *Chemical reviews* 111, no. 6 (2011): 3828-3857.

[60] Fan, X., W. Zheng and D. J. Singh. "Light scattering and surface plasmons on small spherical particles." *Light: Science & Applications* 3, no. 6 (2014): e179-e179.

[61] Szunerits, S. and R. Boukherroub. "Sensing using localised surface plasmon resonance sensors." *Chemical Communications* 48, no. 72 (2012): 8999-9010.

[62] Huang, C., K. Bonroy, G. Reekman, K. Verstreken, L. Lagae and G. Borghs. "An on-chip localized surface plasmon resonance-based biosensor for label-free monitoring of antigen–antibody reaction." *Microelectronic engineering* 86, no. 12 (2009): 2437-2441.

[63] Kiefer, J., K. Frank and H. P. Schuchmann. "Attenuated total reflection infrared (ATR-IR) spectroscopy of a water-in-oil emulsion." *Applied spectroscopy* 65, no. 9 (2011): 1024-1028.

[64] Ribeiro da Luz, B. "Attenuated total reflectance spectroscopy of plant leaves: a tool for ecological and botanical studies." *New Phytologist* 172, no. 2 (2006): 305-318.

[65] Pengel, S., B. Schönberger, S. Nayak and A. Erbe. "Attenuated total reflection mid-IR-spectroscopy for electrochemical applications using a QCL." In *Laser Applications to Chemical, Security and Environmental Analysis*, pp. LT6B-1. Optical Society of America, (2012).

[66] Schnippering, M., S. R. T. Neil, S. R. Mackenzie and P. R. Unwin. "Evanescent wave cavity-based spectroscopic techniques as probes of interfacial processes." *Chemical Society Reviews* 40, no. 1 (2011): 207-220.

[67] Van der Sneppen, L., F. Ariese, C. Gooijer and W. Ubachs. "Liquid-phase and evanescent-wave cavity ring-down spectroscopy in analytical chemistry." *Annual Review of Analytical Chemistry* 2, (2009): 13-35.

[68] Van der Sneppen, L., G. Hancock, C. Kaminski, T. Laurila, S. R. Mackenzie, S. R. T. Neil, R. Peverall, G. A. D. Ritchie, M. Schnippering and P. R. Unwin. "Following interfacial kinetics in real time using broadband evanescent wave cavity-enhanced absorption spectroscopy: a comparison of light-emitting diodes and supercontinuum sources." *Analyst* 135, no. 1 (2010): 133-139.

Chapter 2

Development of a cavity enhanced absorption spectroscopy (CEAS) setup using a quantum cascade laser (QCL) and its application to trace analysis of ammonia molecule

2.1 Introduction

As discussed in section 1.5.5 of the previous chapter, CEAS is a high-sensitive technique that is used for molecular detection. In CEAS, the drastic enhancement in the optical path length is achieved by several reflections of light in an optical cavity that leads to ultra-high sensitivities of the order of pptv. In some variants of CEAS, the decay time of the light leaking from the cavity is measured and is denoted as the ring-down time. Since the measurement parameter is time, the resultant measurement is not sensitive to the light intensity fluctuations of the source. This noise reduction feature provides a high signal to noise ratio for the measurements and therefore leads to the accurate detection of molecules. Furthermore, the rate of decay of the leaked light is directly proportional to the absorption or extinction of light by the sample inside the cavity and hence secondary calibration is not required. CEAS is a general term used for the increased path length of light due to an optical cavity arrangement and thus different terms are used according to the setup arrangements.

Although the CEAS technique has many variants, one of the most basic variant is cavity ring-down spectroscopy (CRDS) where the light is incident along the central axis of the optical cavity and the back and forth reflections take place along this axis. On the other hand, if the light is incident on an off-axis position such that the light retraces its path after some reflections inside the cavity, the technique is called off-axis CEAS (OA-CEAS) or off-axis integrated cavity output spectroscopy (OA-ICOS) [1, 2]. In this chapter, a setup development for the CRDS variant of CEAS has been described using a quantum cascade laser in the mid-infrared region of 6.2 μm and the system has been utilized for the spectral analysis of ammonia (NH_3) molecule.

2.2 Basic principles of CRDS technique

The basic element of a CRDS system is the creation of a stable optical cavity using high-reflectivity mirrors (Reflectivity: R>99.9%) [2]. Figure 2.1 depicts the basic principle of CRDS. In CRDS, the light is injected along the central axis of the mirrors and owing to the high-reflectivity of the mirrors, the entered light undergoes several back and forth reflections inside the cavity. At every pass, very small fraction of light is leaked from the cavity and is detected behind the second mirror. The intensity of the leaked light (I) decays exponentially and can be expressed as equation 2.1 below [3, 4]:

$$
\begin{aligned}
I &= I_0.\exp\left[-\left(\frac{\text{No.of reflections}}{\text{round trip}}\right)\left(\frac{\text{Loss}}{\text{Reflection}}\right)(\text{No. of round trips})\right] \\
&= I_0.\exp\left[-(2)(1-R)\left(\frac{tc}{2L}\right)\right] \\
&= I_0.\exp\left[-\frac{(1-R)\,c}{L}t\right] \\
&= I_0.\exp\left[-\frac{t}{\tau_0}\right]; \quad \text{where } \tau_0 = \frac{L}{c\,(1-R)}
\end{aligned}
\tag{2.1}
$$

Here, I_0 is the incident light intensity, R is the reflectivity of the mirrors, c is the speed of light and L is the length of the cavity. τ_0 is the decay time constant or the time taken by the light intensity to fall to 1/e of its initial value in the absence of a sample and is known as the empty cavity ring-down time. τ_0 is a characteristic parameter of a CRDS system and a higher value of τ_0 indicates more retention of light inside the cavity which in turn means greater optical path length and hence greater sensitivity of the system.

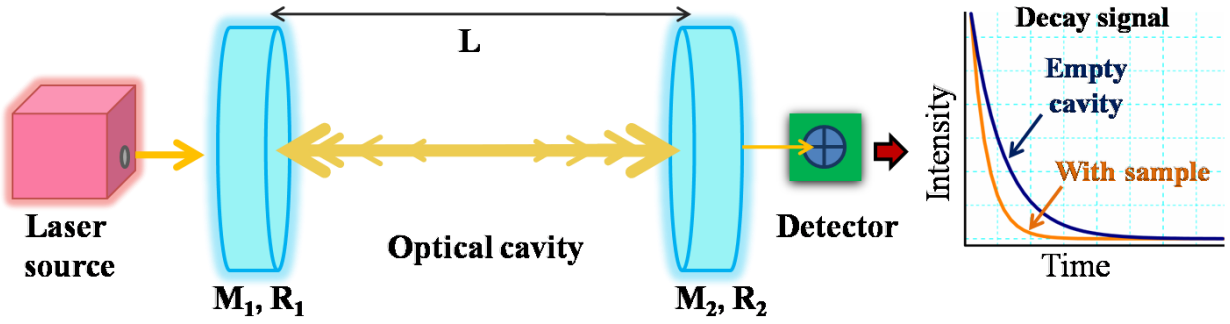

Figure 2.1 *depicts the basic principle of CRDS. A stable cavity is built using high-reflectivity mirrors M_1 and M_2 with radii of curvature R_1 and R_2. The arrows indicate the back and forth path of light, with lesser intensity after each pass. The output decays faster in presence of a sample inside the cavity than in empty cavity condition.*

When a sample is present inside the cavity, absorption due to the sample causes the light to decay faster and the resultant ring-down time decreases. Now, in addition to the natural decay of light, there is contribution from the sample as well. Equation 2.1 can be modified to incorporate the absorption as (equation 2.2) [3]:

$$I = I_0 \exp\left[-(1-R)\left(\frac{tc}{L}\right)+\left(\frac{\text{Absorption loss}}{\text{round trip}}\right)(\text{No. of round trips})\right]$$

$$= I_0 \exp\left[-(1-R)\left(\frac{tc}{L}\right)+(2.\alpha d)\left(\frac{tc}{2L}\right)\right]$$

$$= I_0 \exp\left[-\frac{tc}{L}((1-R)+\alpha.d)\right]$$

$$= I_0 \exp\left[-\frac{t}{\tau}\right]; \qquad \text{where } \tau = \frac{1}{c}\left[\frac{L}{(1-R)+\alpha.d}\right] \qquad (2.2)$$

Here, τ is the ring-down time in the presence of the sample and d is the length of the sample which is equal to L when the sample fills the cavity. α is the absorption coefficient of the sample and can be expressed as (equation 2.3) [5]:

$$\alpha = \sigma.[X] \qquad (2.3)$$

where σ is the wavelength dependent absorption cross-section of the sample and [X] is the concentration of the sample.

The inverse of the ring-down time is the decay rate (k in second^{-1}) of the light inside the cavity (equation 2.4).

$$k = \frac{1}{\tau} \qquad (2.4)$$

Using equations 2.1, 2.2 and 2.3, we can write,

$$\frac{k - k_0}{c} = \frac{\Delta k}{c} = \alpha = \sigma.[X] \qquad (2.5)$$

Thus, the change in the decay rate Δk is directly proportional to the absorption due to the sample. To obtain the spectra of a sample, the decay

rate can be plotted against the wavelength (or wavenumber) of the light. The curve can be fitted using an appropriate line shape function and the concentration of the sample can be evaluated using the area under the fitted curve of the 'k versus wavenumber plot' and the value of the absorption cross-section of the spectral line of the sample [6].

The CRDS system is also characterized by many other parameters which provide an overview for different technical features of the system. For instance, the optical path length L_{op} traversed by the light in cavity can be given as (equation 2.6):

$$L_{op} = c.\tau_0 \qquad (2.6)$$

where c is the speed of light. For a typical value of τ_0 =10 μs, L_{op} = 3 kilometres which is a significantly enhanced value in comparison to a typical sample length of few tens of centimetres.

Furthermore, the time required for light to complete one round trip (to and fro pass) in the cavity is called the round trip time (t_r) (equation 2.7) [5]:

$$t_r = \frac{2L}{c} \qquad (2.7)$$

For a cavity length L=50 cm, t_r=3.33 ns. Also, the number of passes can be calculated by dividing the optical path length by the cavity length.

The sensitivity of CRDS can be defined in terms of the minimum absorption that can be distinguished from noise. This parameter is known as the minimum absorption coefficient α_{min} (measured in cm^{-1}) (equation 2.8) [2, 5]:

$$\alpha_{min} = \frac{1}{c\tau_0}\frac{\Delta\tau_{min}}{\tau_0} \qquad (2.8)$$

where $\Delta\tau_{min}$ is the minimum detectable change in the ring-down time and

$\Delta\tau_{min}/\tau_0$ is the relative error in the measurements. Typical values of α_{min} in CRDS range from 10^{-8}-10^{-10} cm^{-1} and can go up to 10^{-12} cm^{-1} in some variants of CRDS, thus making CRDS a very high-sensitive technique [5]. The sensitivity can also be described by the noise equivalent absorption (NEA) coefficient as (equation 2.9) [7]:

$$NEA = \sqrt{\frac{2}{f_{rep}}}\,\alpha_{min} \qquad (2.9)$$

Here, f_{rep} is the acquisition rate of the ring-down data and the units for NEA comes out to be cm^{-1} $Hz^{-1/2}$. Lower value of α_{min} and NEA indicate higher sensitivity of the system. Since NEA takes into account the data acquisition rate of the observations, higher acquisition rates would improve the NEA and also the overall sensitivity.

If the absorption cross-section σ of a molecular spectral line is known, the α_{min} value can also be translated to obtain the minimum number of molecules that can be detected $[X_{min}]$, using equation 2.10.

$$[X_{min}] = \frac{\alpha_{min}}{\sigma} \qquad (2.10)$$

For gas-phase molecules, $[X_{min}]$ is usually expressed in terms of the mixing ratio (ppmv, ppbv etc.) of a molecule in a mixture.

2.3 Advantages and limitations of the CRDS technique

Advantages:

- The enormous optical path length in CRDS leads to very high sensitivities through which pptv order concentrations can also be measured.
- The measurement of decay time as the output parameter eliminates the noise due to source intensity fluctuations.

- If the absorption cross-section of a transition is known, no secondary calibration is required since the decay rate is directly proportional to the sample absorption.

Limitations:

- The availability of high-reflectivity mirrors for narrow wavelength ranges makes the technique expensive.
- The alignment of the cavity is critical and needs to be precise to achieve the mode-matching condition. Hence, cavity stability is an issue.

2.4 Role and features of a stable optical cavity in CRDS

A stable optical cavity (stable resonator) is one of the most essential components of a CRDS system which traps the incoming light, leading to an enhanced optical path length. For this to occur, appropriate cavity geometry and proper alignment are necessary. Therefore, it is important to understand the features and requirements to form a stable cavity which are discussed below.

2.4.1 Modes in an optical cavity

Similar to waves in a stationary string, a stable optical cavity supports certain modes (frequencies) of its own as shown in Figure 2.2. For a longitudinal mode to exist in the cavity, the phase change in a round trip must be an integral multiple of 2π or the length L of the cavity should be an integer multiple of half wavelength λ as given in equation 2.11 [1, 5].

$$L = m\frac{\lambda}{2} \qquad \Rightarrow \nu = m\frac{c}{2L} \tag{2.11}$$

where ν is the frequency of the longitudinal mode and m is an integer.

Subsequently, the frequency spacing between the modes Δν can be given as equation 2.12 and is inverse of the round-trip time of light in the cavity. This spacing is also known as the free spectral range (FSR) of the cavity which depends on the length L of the cavity.

$$\mathrm{FSR} = \Delta\nu = \frac{c}{2L} \qquad (2.12)$$

In CRDS, a resonance is established between the cavity and the laser modes as shown in Figure 2.2. Generally the cavity mode linewidths are much smaller than the laser linewidths. Thus, for a particular laser linewidth the FSR determines how many cavity modes fall inside a single laser mode (Figure 2.2). For typical continuous lasers with a narrow linewidth, the mode matching is performed using additional components while for pulsed lasers where linewidths are large and cover many FSRs of the cavity, several hundreds of modes might fall inside a laser linewidth and no additional mode matching tools are necessary [1]. However, continuous or pulsed laser sources are used according to the need of a particular system and will be discussed in section 2.5.

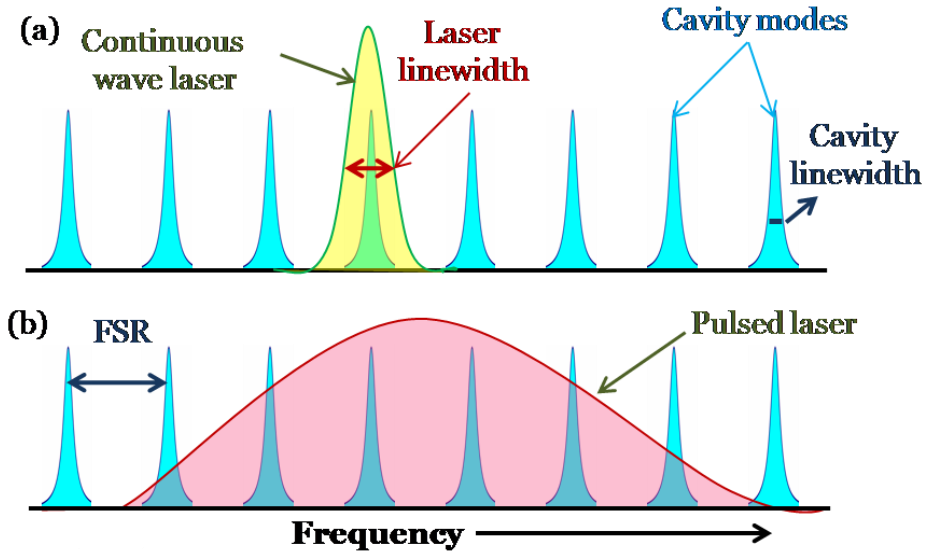

Figure 2.2 *shows cavity modes in a stable optical cavity.* ***a)*** *and* ***b)*** *depict the mode-matching case for continuous wave laser and pulsed laser, respectively.*

The ability of an optical cavity to trap or sustain the light inside it depends on the quality factor of the cavity and the input light. For an optical cavity, the quality factor is more commonly known as the finesse (F) which depends on the reflectivity (R) of the mirrors (equation 2.13). Higher the reflectivity, greater will be the finesse and lesser will the transmission through the mirrors at each pass of light, resulting in better trapping of light inside the cavity [1,5].

$$\text{Finesse } (F) = \frac{\pi\sqrt{R}}{(1-R)} \qquad (2.13)$$

The finesse and the FSR can also be used to calculate the linewidth (full width at half maximum) of the cavity modes (ν_{FWHM}) using equation 2.14.

$$\nu_{FWHM} = \frac{\Delta\nu}{F} \qquad (2.14)$$

2.4.2 Criteria for a stable optical cavity

For resonance to occur in a stable cavity, the input light beam characteristics should match with the cavity geometry. For instance, a highly divergent beam would not follow a specified path inside the cavity and would lead to beam divergence losses. For proper matching of laser modes with the longitudinal modes in a cavity, low divergence Gaussian beams are utilized. Figure 2.3 shows the propagation of such a Gaussian beam along the z-axis.

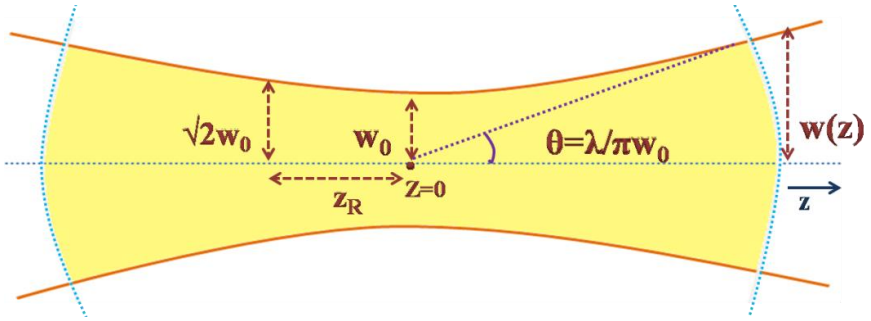

***Figure* 2.3** *Propagation of a Gaussian beam from the point of focus at z=0. w(z) represents the beam spot size at different points along the z axis. Adapted from Ref. [8]*

The point at which the beam width is lowest is the focusing point of the beam (at z=0) and the beam width at this point is called the beam waist w_0. The beam spot size at any point along the propagation w(z) can be written as (equation 2.15) [8]:

$$w(z) = w_0\sqrt{1+(\frac{z}{z_R})} \qquad (2.15)$$

Here, z_R is the distance from w_0 where the beam area is twice and the beam diameter is √2 times than that at the beam waist and is given by:

$$\text{Rayleigh range}(z_R) = \frac{\pi w_0^2}{\lambda} \qquad (2.16)$$

At points far from the beam waist ($z>>z_R$), the beam wavefront increases linearly with an angular divergence θ given by (equation 2.17):

$$\theta = \frac{\lambda}{\pi w_0} \qquad (2.17)$$

Hence, a well collimated (less divergent) beam would possess a large beam waist for a particular wavelength.

For the propagation of a Gaussian beam inside a stable optical cavity in a two mirror resonator cavity system, the curvature of the beam wavefronts should match the radii of curvature R_1 and R_2 of the mirrors (M_1 and M_2) [1]. The stability of the cavity can be expressed in terms of the g parameters as described in equation 2.18 [1,5].

$$g_1 = 1-\frac{L}{R_1} \text{ and } g_2 = 1-\frac{L}{R_2} \qquad (2.18)$$

The g parameters form the condition for a stable optical cavity, that is $0<g_1g_2<1$. The beam waist and the beam spot sizes on the mirrors w_1 and w_2 can also be expressed using the g parameters as:

$$w_0^2 = \frac{L\lambda}{\pi}\sqrt{\frac{g_1g_2(1-g_1g_2)}{(g_1+g_2-2g_1g_2)^2}} \qquad (2.19)$$

$$w_1^2 = \frac{L\lambda}{\pi}\sqrt{\frac{g_2}{g_1(1-g_1g_2)}} \quad \text{and} \quad w_2^2 = \frac{L\lambda}{\pi}\sqrt{\frac{g_1}{g_2(1-g_1g_2)}} \qquad (2.20)$$

The curvature and proper alignment of the mirrors are also crucial elements for a stable cavity in order to retain the light and prevent divergence losses and beam walk-off. For instance, aligning two plane mirrors ($R_1=R_2=\infty$) exactly parallel to each other is very difficult which makes the cavity very susceptible to instability. The stability condition for different mirror curvatures and geometries can be depicted by a stability diagram shown in Figure 2.4 [8]. The shaded region in the diagram indicates the possible geometries and combinations of L and R using which a stable cavity can be formed.

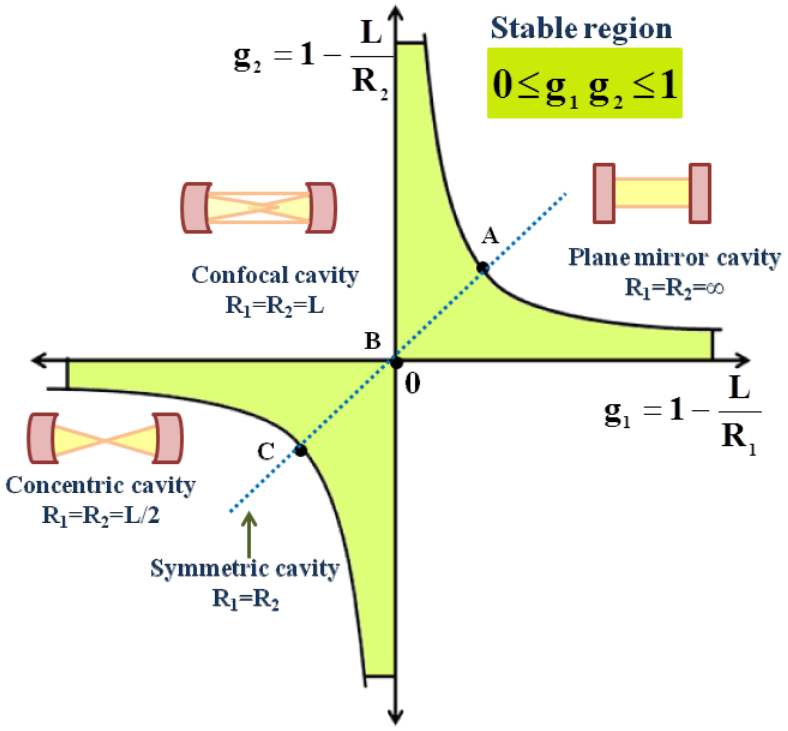

Figure 2.4 *Diagram illustrating the stability condition for a two mirror cavity. The shaded region depicts values of g_1 and g_2 for which the two mirror cavities would be stable. Points A, B and C represent three symmetric (R_1=R_2) type mirror cavities. Adapted from Ref. [8].*

2.5 Continuous wave and pulsed laser sources in CRDS

Since CRDS involves trapping the light and observing the decay time, the use of continuous or pulsed laser source includes different arrangements for the two cases. In continuous laser sources, it is intended to have a single mode, narrow linewidth, Gaussian beam profile (Figure 2.2a) so as to excite or mode-match with a single mode in the optical cavity. For such a case in CRDS, the decay of this resonant mode is observed. Usually, a well-aligned optical cavity mode might not match naturally with the laser mode and thus, an external component is needed to achieve this. One common way is to modulate the cavity length at a certain frequency by using piezo-electric transducers attached to the mirrors, which allows the repeated mode-

matching of the laser and the cavity modes. Thus, the resonance spikes are achieved and the input light is cut-off when resonance occurs and the decay is observed [1].

On the other hand, pulsed sources have a comparatively larger linewidth (Figure 2.2b) and will excite many modes in a stable cavity. Thus, generally external mode-matching components are not required in this case. Here, the fall time of the laser pulse exiting from the cavity is utilized to obtain the decay time of the light in the cavity. However, the inherent rise and fall time of the laser pulse should be far lower than the cavity decay time so that the inherent fall time of the laser should not hinder the decay (ring-down) time measurements [7, 9].

2.6 Quantum Cascade Laser (QCL) as a mid-infrared laser source

Quantum Cascade Lasers (QCLs) operate in the infrared region and have improved the study of ro-vibrational spectroscopy of molecules [10]. Not only it provides the access to the molecular "finger-print" region in the mid-infrared but also allows high-resolution spectral study due to their narrow linewidths (<0.0003 cm^{-1}) [6, 11]. QCLs differ from the diode lasers in their structure and mechanism as diode lasers utilize the interband transition of electrons to produce photons while QCLs exploit the intersubband transitions in thin layers of semiconductor materials [10, 12]. Figure 2.5 shows the basic mechanism of photon generation in a QCL where alternative thin (nanometre order) layers of semiconductors are arranged which act as quantum wells. On applying a suitable electric field bias, the electron transition occurs between the subbands and a photon is emitted [13]. The electrons tunnel through the barrier and reach another subband to undergo a transition. This generates another photon and the process carries on, thus giving a cascade of photon output. One of the biggest advantages of QCL is that the output wavelength depends on the

thickness of the layers and hence the same materials can produce different wavelengths by changing the layer thicknesses. Moreover, QCLs can have broad tuning range (>100 cm^{-1}), high power outputs and can function at room temperatures [14]. Therefore, these features of QCLs have facilitated their use in spectroscopic and molecular sensor based applications [10, 15]. In this thesis, we have utilized QCLs in combination with the CRDS technique to study high-resolution spectra of various molecules.

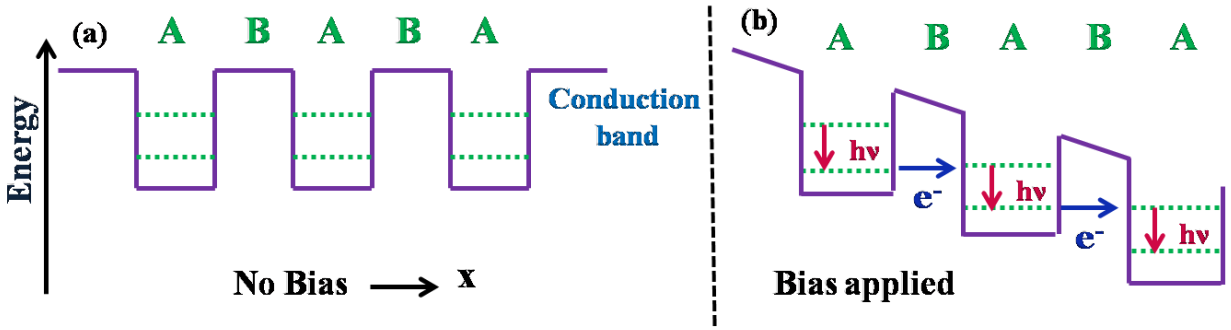

Figure 2.5 *Diagram indicating the bands in the quantum wells in the absence* ***(a)*** *and presence* ***(b)*** *of external bias. 'A' represents the active region of the well where the electron transition occurs while 'B' is the tunnelling barrier for the electron. Adapted from Ref. [13, 16]*

2.7 Development of the CRDS setup: Experimental details

We developed a CRDS based experimental setup for spectroscopic detection of gas-phase molecules [17]. The schematic of the setup is shown in Figure 2.6. The light source used was a continuous wave external-cavity quantum cascade laser (*cw* EC-QCL, MHF-41062, Daylight Solutions, USA) emitting at a centre wavelength around 6.2 µm with a mode-hop free (MHF) tuning range of 6.0-6.3 µm (1590-1650 cm^{-1}) and a high power (~ 90 mW) output. The QCL was capable of operating at room-temperature and had a narrow linewidth (<0.0004 cm^{-1}) which enabled the high-resolution spectral study of molecules. The output beam from the QCL was well-

collimated and Gaussian in nature. To avoid any back-reflection of light towards the QCL from other optics, an optical isolator (FIO-5-(6.0-6.5); Innovation Photonics) was utilized. The light was then incident on an acousto-optic modulator (AOM, AGM-405B11M; IntraAction Corp., USA) wherein a radio-frequency driver produces a sound wave in a non-linear crystal that modulates its refractive index. This causes the crystal to diffract the input light into different orders [18].

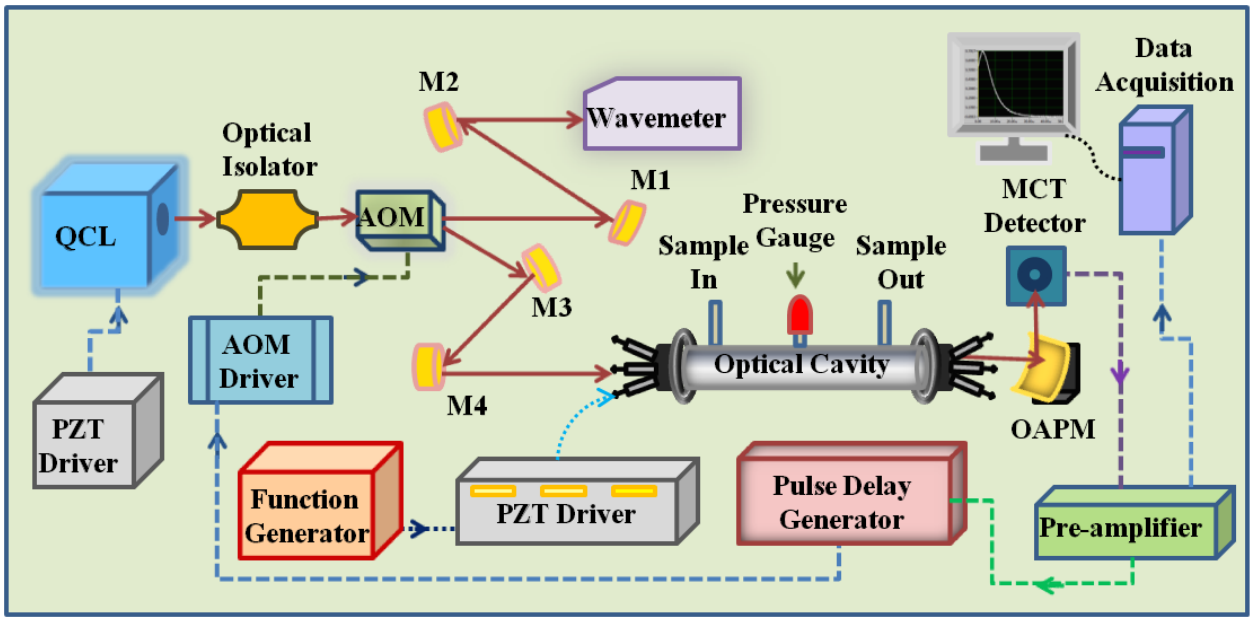

Figure 2.6 *A schematic diagram illustrating the developed CRDS setup. Here M_1, M_2, M_3 and M_4 are plane, gold-coated mirrors to direct light towards the required components.*

In the present setup, the incoming light was diffracted by the AOM into zeroth and first orders. The zeroth order was directed to a wavemeter (621B-MIR; Bristol Instruments) to measure the wavelength of light with an accuracy of 0.001 cm^{-1}. The first order was directed and properly aligned to the central axis of the optical cavity. A quartz-coated ring-down cell of ~ 50 cm length was used to hold two very high-reflectivity mirrors (CRD Optics Inc., USA) at its two ends, which comprised the optical cavity. The mirrors were plano-concave with reflectivity R > 99.98% at 6.2 μm and with radii of

curvature (ROC) of 1 metre. Thus, the g parameters for the cavity were $g_1=g_2=0.5$ which indicated a stable, symmetric optical cavity. The ring-down cell also consisted of outlets with valves to allow entry and exit of gases and an outlet valve for pressure gauge (Pfeiffer Vacuum) to determine the pressure of gas inside the cavity.

The output light was collected behind the second mirror and focused on a mid-IR, thermoelectrically-cooled mercury-cadmium-telluride (MCT) detector (PVI-4TE-6-1X1, Vigo Systems S.A.) using a gold-coated 90^0 off-axis parabolic mirror (OAPM, Newport Corporation). The signal obtained from the detector was amplified using a pre-amplifier (SR560; Stanford Research Systems). As was described in sections 2.4.1 and 2.5, since the linewidth of the QCL is narrow, the cavity modes do not naturally match with the laser modes. Hence, the cavity length was modulated using piezo-electric transducers (PZT, Thorlabs PE4) attached to the mirror mounts. The PZT were driven by applying a periodic triangular ramp voltage ($V_{peak\ to\ peak}$=57 V, Frequency=50 Hz) to them such that for a forward movement they covered a distance more than half the wavelength of input light. This ensured the possibility of mode-matching for every cycle of the applied voltage. Figure 2.7a shows a National Instruments (NI)-scope picture of the resonant modes and the applied triangular voltage. Hence, periodic resonance due to mode-matching was observed. Since the cavity mirrors were aligned straight and parallel to each other with the incident light passing through the central axis of the cavity, the resultant modes were longitudinal TEM_{00} as has been described in section 2.4.1.

In order to achieve ring-down decay of these resonant modes, the output of the pre-amplifier was connected to a pulse delay generator (DG645, Stanford Research Systems) which sent a timed pulse to the AOM whenever a threshold value of the resonance occurred. Here, the AOM behaves as a fast switching device, which cuts the first order input towards the cavity and thus the decay of the resonant mode is observed. Figure 2.7b shows a typical ring-down decay event. The data was collected using a fast

data-acquisition card (PCI 5122, 14-bit, 100 MHz bandwidth, National Instruments) and was further analyzed by a custom-made LabVIEW program. In order to acquire the spectra, the laser was tuned using a piezo-electric transducer (PZT, Thorlabs PE4).

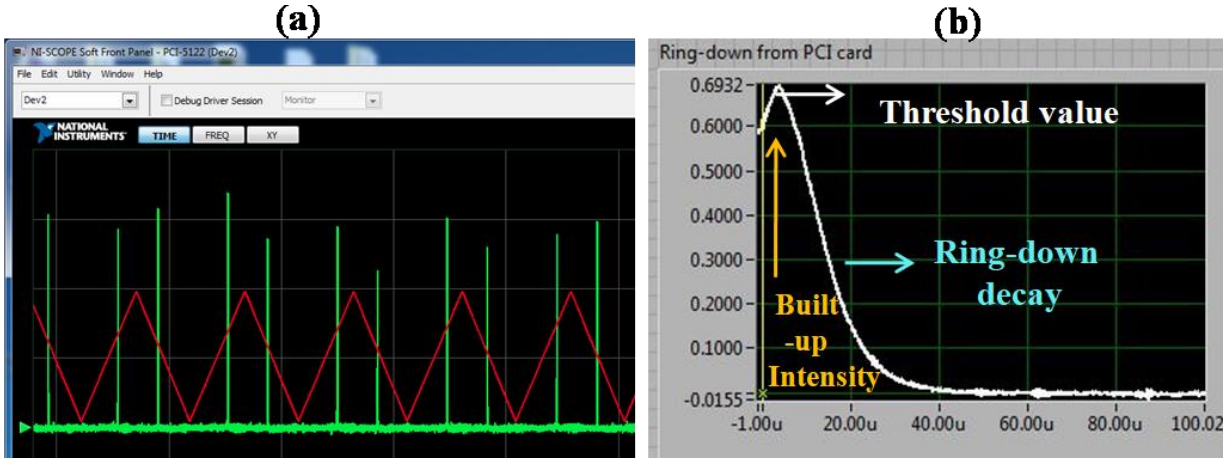

Figure 2.7 a) *NI-scope image of the resonant intensity modes (TEM_{00}) (green) in the CRDS setup. The triangular signal (red) is the voltage applied to the PZTs for cavity length modulation.* ***b)*** *A typical ring-down event showing the built-up of resonant intensity up to a threshold value and the subsequent exponential decay.*

2.7.1 CRDS setup parameters

An empty cavity ring-down time (τ_0) of 7.8 μs was obtained for the present setup with a standard deviation (1 SD) of 0.35 % after averaging 10 ring-down time values [17]. Figure 2.8 shows the distribution of ring-down values (τ_0) at a fixed wavenumber. The distribution was fitted using a Gaussian function and the resultant values of τ_0 and SD were evaluated. Using τ_0 in equation 2.6, the optical path length was calculated to be ~2.34 km for a cavity length of 50 cm, which demonstrated the significant enhancement of path length in the CRDS technique. Further, the round-trip time and the FSR of the cavity were evaluated to be 3.33 ns and 300 MHz,

respectively. The τ_0 was also utilized to obtain the experimental value for the reflectivity of the cavity mirrors which was ~ 99.978 %.

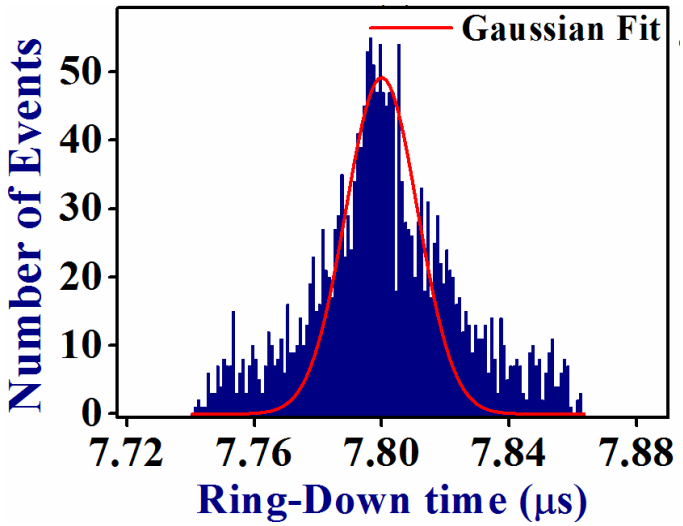

Figure 2.8 *shows a histogram distribution of the τ_0 values with number of events depicting the frequency or occurrence of a particular value of τ_0 in the distribution. A Gaussian function has been used to fit the values [17].*

The reflectivity was subsequently used to calculate the finesse F ~ 14,680 using equation 2.13. Interestingly, by using the experimental time scale values of the FSR and the width of the resonant modes, we could also evaluate the experimental linewidth of the QCL by using the relation $\Delta\gamma_{QCL}$ / FSR = Δt_{TEM00} / Δt_{FSR}, where Δt_{TEM00} and Δt_{FSR} are the observed time scale values of resonant mode and the FSR, respectively. The experimental linewidth of the QCL was ~ 0.00035 cm^{-1} (~10.62 MHz) which complied with the manufacturer specified value of < 0.0004 cm^{-1}. On the other hand, the cavity mode linewidth $\Delta\gamma_{cavity}$ was evaluated using $\Delta\gamma_{cavity}=1/2\pi\tau_0$ which resulted in $\Delta\gamma_{cavity}$=20.44 kHz. Furthermore, the minimum absorption coefficient α_{min} for the current setup was evaluated to be 1.49 × 10^{-8} cm^{-1} whereas a noise-equivalent absorption coefficient (NEA) of 2.11 × 10^{-9} cm^{-1} $Hz^{-1/2}$ was obtained for the data acquisition rate of 100 Hz.

2.7.2 Stability analysis of the cavity

To estimate the stability of the optical cavity, Allan variance analysis [19] was used which also expressed the noise characteristics of the system and provided the optimum time for the measurements. Figure 2.9 shows the Allan variance analysis of the τ_0 values measured against the integration time (time taken for completing n number of measurements) at a data acquisition rate of 100 Hz. Allan variance is a log-log plot for the variance calculated by grouping the data values.

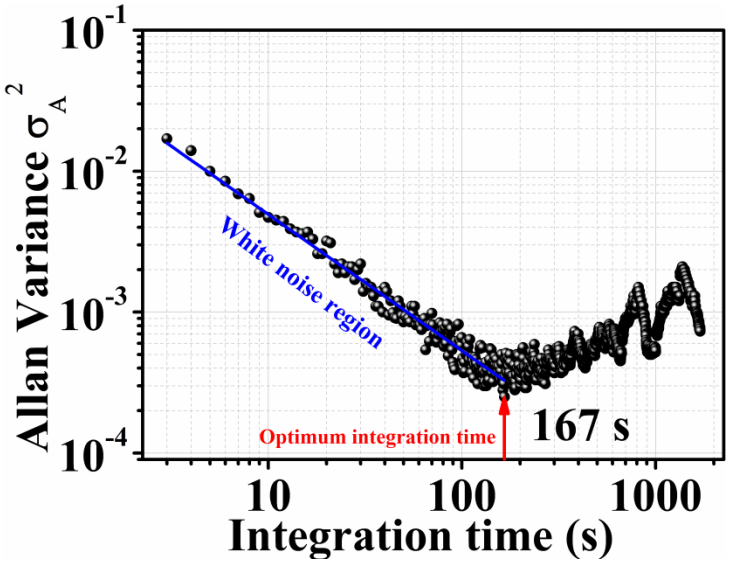

Figure 2.9 *shows the Allan variance plot of the empty cavity ring-down time with respect to the integration time of the measurements [17].*

As is evident from Figure 2.9, when the integration time is increased, by averaging more and more data, the Allan variance decreases up to a certain point and then increases. The initial linear region represents the white noise region with the decreasing variance. Further on, the Allan variance increases due to various fluctuations in the system. The Allan variance provides the optimum integration time for completing the measurements, which was ~167 seconds for the present setup.

2.8 Probe molecule: Ammonia (NH_3)

2.8.1 Importance of ammonia molecule

Ammonia is a significant trace gas molecule that is normally found in ppbv levels in the atmosphere (0.01 – 50 ppbv) [20, 21] and human breath (50-2000 ppbv). In the environment, it is released from the use of fertilizers, livestock, industrial emissions etc. and takes part in the formation of particulate matter in the atmosphere [22-24]. It also causes acidification and is toxic to animals and therefore NH_3 levels need to be monitored in the atmosphere. Moreover, NH_3 concentrations in exhaled human breath have also been linked to malfunctions and diseases in humans such as liver cirrhosis and kidney malfunction which has led to the application of breath NH_3 analysis for disease diagnosis [25-27]. In case of kidney malfunctions, breath NH_3 levels are enhanced in individuals. Since NH_3 is excreted by the kidneys through urine, impaired kidney function results in excess NH_3 build-up in the blood and hence increased NH_3 in the breath [28]. Also, individuals suffering from diabetes mellitus are prone to kidney malfunction which leads to the condition of diabetic nephropathy [29, 30]. However, kidney dysfunction does not become evident in early stages and eventually leads to kidney failure. Thus, it is crucial that kidney malfunction is detected in early stages. In this chapter, the spectral detection and analysis of NH_3 using the developed CRDS setup has been described along with the measurement of NH_3 in an atmospheric and human breath sample. Further, a preliminary study was performed to investigate the levels of NH_3 in the breath of diabetic and non-diabetic individuals.

2.8.2 Rotational-vibrational spectroscopy of NH_3

NH_3 is a symmetric top molecule with a pyramidal shape as shown in Figure 2.10. Since it is a non-linear molecule, it possesses 3N-6 (N=number of atoms) modes i.e. 3x4-6=6 modes of vibration.

Out of these, 2 modes are degenerate in nature which results in 4 different types of vibrational modes as shown in Figure 2.10a [31, 32].

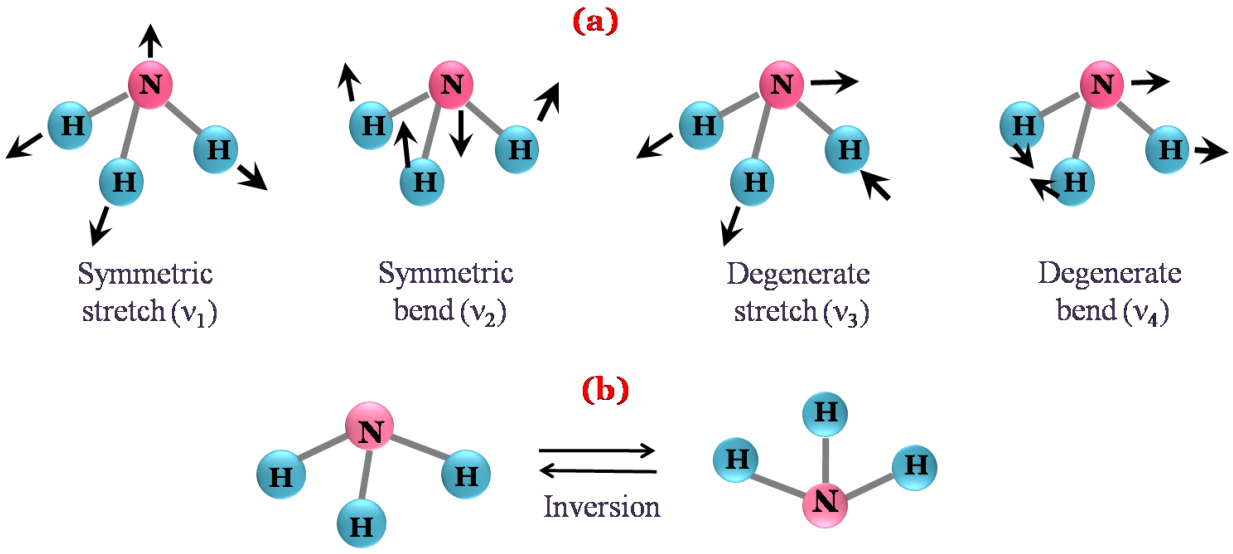

Figure 2.10 a) *shows the normal modes of ammonia molecule. The arrows indicate the direction of vibration.* ***b)*** *The two inverted forms of* NH_3.

A HITRAN simulation [33] of the infrared (500-5500 cm^{-1} range) spectra (ro-vibrational) for NH_3 is shown in Figure 2.11. The spectral line intensities for the fundamental vibrations (normal modes) are observed to be comparably higher than that of the combination bands ($\nu_2+\nu_4$, $\nu_2+\nu_3$). Thus, it is advantageous to work in the mid-infrared region since the spectral line intensities of molecules are higher. We have therefore probed the ν_4 band in the 6.2 μm region which has high line intensity than most other bands of NH_3. The rotational transitions in NH_3 are expressed in terms of the rotational quantum numbers J and K where J is the total angular

momentum quantum number and K is the projection of J on the molecular axis [34].

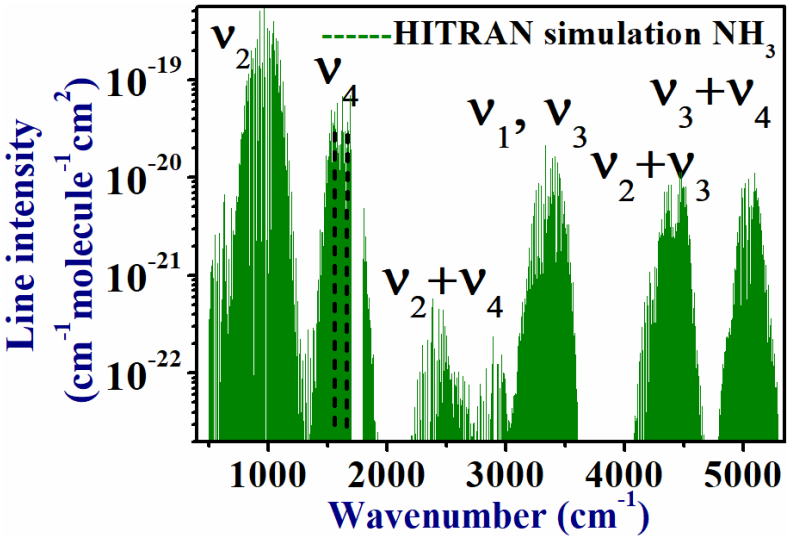

Figure 2.11 *HITRAN simulation for the ro-vibrational spectral bands of NH_3 in the infrared region. Modes like $\nu_2+\nu_4$ refer to the combinations bands which arise when two or more modes are excited together. The dotted lines depict the region around 6.2 μm used in the current work [17].*

NH_3 molecule also shows an inversion symmetry which indicates the upward or the downward positions of the hydrogen atoms with respect to the nitrogen atom as shown in Figure 2.10b. The interchange in these positions causes the doubling of the ro-vibrational spectral lines [35, 36] also called inversion doubling of NH_3.

2.9 Results and Discussion

We initially performed a HITRAN simulation [33] to explore the spectral lines of NH_3 in the mode-hop free range of the QCL (1590-1650 cm^{-1}) as shown in Figure 2.12a. The simulation was carried out with the experimental parameters of NH_3 (27.2 ppm), 1 Torr pressure, 296K

temperature and 2.34 km sample path length. The spectra of 5% (50,000 ppmv) H_2O and 5% CO_2 were also simultaneously simulated as these are major molecules in real samples of atmosphere and human breath. For selective measurement of NH_3 in a real sample, it is crucial to avoid the interference of spectral line features of such major gas components. It is noteworthy to mention that the 6.2 µm region contains strong water absorption band and hence the region is less investigated. However, it is free from CO_2 absorption. Nevertheless, the use of QCL allows high-resolution tuning of the wavenumber and therefore the region can be investigated for NH_3 with minimum overlap from other molecules.

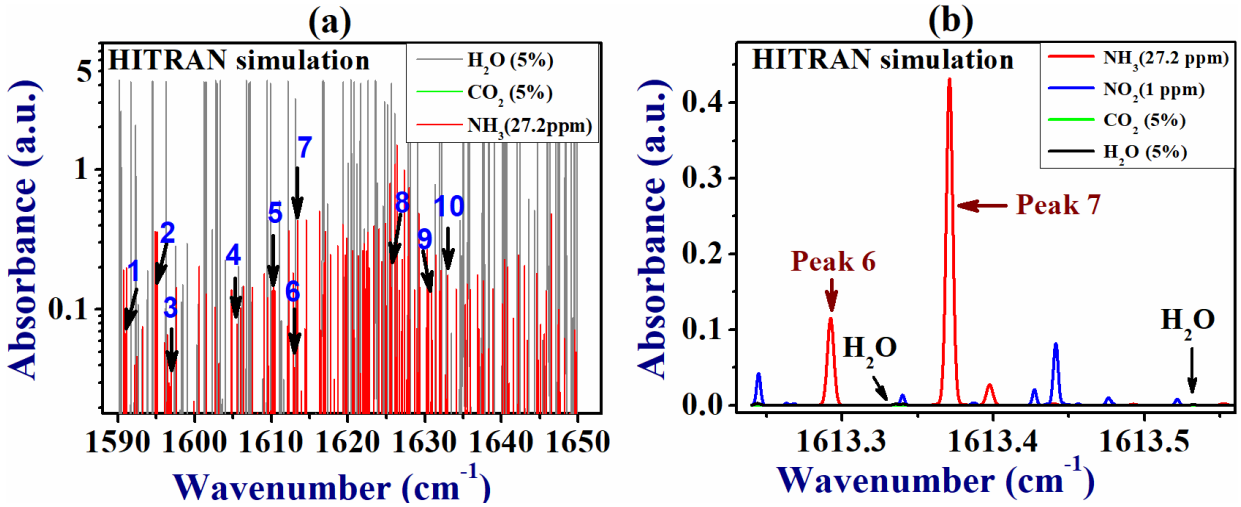

Figure 2.12 a) *HITRAN simulation for NH_3 spectral lines in the MHF range of the laser around 6.2 µm. The numbers indicate 10 selected interference-free spectral peaks of NH_3.* ***b)*** *HITRAN simulation for the strongest interference-free peak (Peak 7) in the region near 1613.370 cm^{-1} [17]. a. u. indicates arbitrary units.*

From the simulation, we selected ten spectral lines of NH_3 which were interference-free from the direct overlap of spectral peaks of other molecular species. However, it may be noted that at pressures > 30 Torr the trailing feet of the profiles of H_2O peaks started to interfere with the spectral lines of NH_3. An expanded view of the HITRAN simulation is

shown (Figure 2.12b) for the strongest interference-free peak in the region at 1613.370 cm^{-1} which does not contain strong H_2O peaks in its neighbourhood and is thus best suited for selective NH_3 detection.
Subsequently, we experimentally investigated the high-resolution spectra of the ten above mentioned spectral lines of NH_3 using the QCL based CRDS technique. Among the ten lines, eight lines belonged to the fundamental v_4 band (degenerate bending) and two lines were originated from the first overtone transitions in the v_2 band (symmetric bending). Within these vibrational bands, all the lines emerged from the Q-branch transitions ($\Delta J=0$). The CRDS spectra of NH_3 was attained by plotting the decay rate with respect to the wavenumber for a calibrated gas mixture of 27.20 ± 0.06 ppmv of NH_3 in nitrogen (N_2) (Air Liquide, UK) at 1 Torr pressure (Figure 2.13).

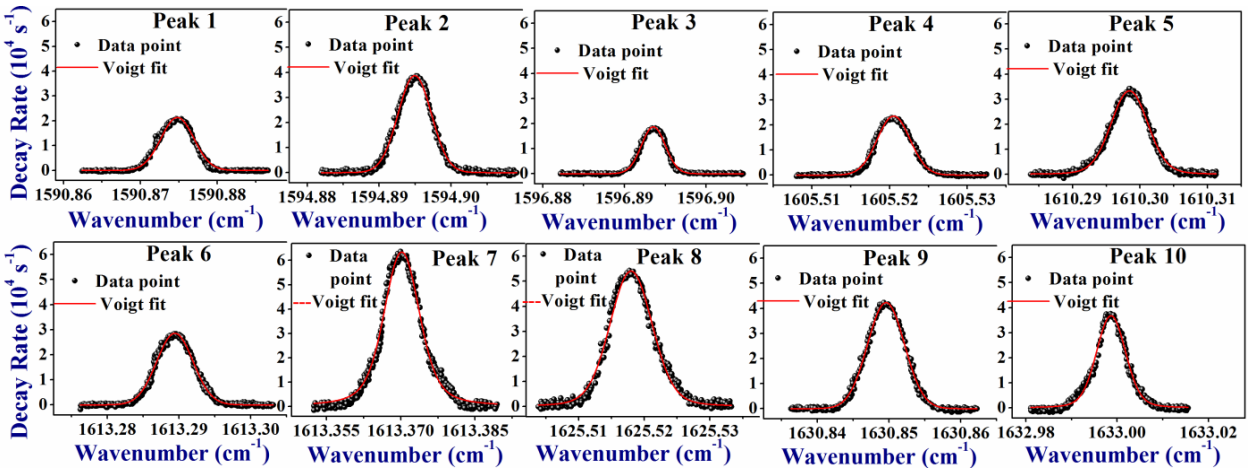

Figure 2.13 *High-resolution CRDS spectra of NH_3 in the region 1590-1634 cm^{-1}. The peaks 1 to 10 indicate the peak numbers in Figure 2.12a and Table 2.1 [17].*

The data were fitted with Voigt profiles and the area under the fitted curve was used to determine the line intensity, more specifically referred to as the line-integrated absorption cross-section for a spectral line. Table 2.1 provides the experimental and simulated values for the spectral peak positions, absorption cross-sections and the line assignments for the ten lines of NH_3. The assignments were obtained from the HITRAN simulation.

Table 2.1 *Experimental CRDS and HITRAN simulated values of peak positions and absorption cross-sections for the ten transition lines of NH_3. The assignments are given in the notation ${}^{\Delta K}\Delta J(J'', K'')$, where J″ and K″ are the ground state rotational quantum numbers while the 's' and 'a' are symmetric and anti-symmetric for the inversion symmetries. In the experimental positions, the last digit is in the brackets as the wavemeter resolution is 0.001 cm^{-1} and so this value is uncertain [17].*

Peak No.	**Line Centre Wavenumber (cm^{-1}) (HITRAN)**	**Line Centre Wavenumber (cm^{-1}) (Experimental)**	**Line Integrated absorption cross-section (cm^{-1} $molecule^{-1}cm^2$) (HITRAN)**	**Line Integrated absorption cross-section ($cm^{-1}molecule^{-1}cm^2$) (Experimental)**	**Band and Line Assignment**	**Inversion Symmetry Lower state→ Upper State**
1.	1590.8807	1590.874(8)	4.009×10^{-21}	$(4.20\pm0.02) \times 10^{-21}$	ν_2 $^{Q}Q(5,5)$	a→s
2.	1594.8991	1594.894(9)	8.227×10^{-21}	$(8.48\pm0.04) \times 10^{-21}$	ν_2 $^{Q}Q(3,3)$	a→s
3.	1596.8961	1596.893(5)	2.206×10^{-21}	$(2.37\pm0.04) \times 10^{-21}$	ν_4 $^{R}Q(9,7)$	s→s
4.	1605.5258	1605.520(5)	4.638×10^{-21}	$(4.69\pm0.02) \times 10^{-21}$	ν_4 $^{R}Q(9,6)$	s→s
5.	1610.3023	1610.298(4)	9.155×10^{-21}	$(9.08\pm0.04) \times 10^{-21}$	ν_4 $^{R}Q(6,4)$	s→s
6.	1613.2922	1613.289(4)	6.856×10^{-21}	$(6.82\pm0.03) \times 10^{-21}$	ν_4 $^{R}Q(7,4)$	s→s
7.	1613.3708	1613.370(1)	2.585×10^{-20}	$(2.48\pm0.03) \times 10^{-20}$	ν_4 $^{R}Q(4,3)$	a→a

8.	1625.5170	1625.517(9)	1.904×10^{-20}	$(1.87\pm0.01) \times 10^{-20}$	ν_4 $^{R}Q(5,1)$	s→s
9.	1630.8509	1630.849(5)	1.032×10^{-20}	$(1.02\pm0.03) \times 10^{-20}$	ν_4 $^{P}Q(1,1)$	a→a
10.	1632.9991	1632.998(6)	1.057×10^{-20}	$(1.19\pm0.02) \times 10^{-20}$	ν_4 $^{P}Q(3,1)$	s→s

Since the above ten lines of NH_3 are interference-free from substantial overlap from other molecules, they can be utilized for sensing NH_3 in real life samples. Furthermore, from Table 2.1, it is evident that the spectral lines have a wide range of absorption cross-sections which will allow the measurement of a broad range of concentrations of NH_3.

Further, we utilized the strongest spectral line in the region at 1613.370 cm^{-1} with an absorption cross-section of $\sigma = 2.585 \times 10^{-20}$ cm^{-1} $molecule^{-1}$ cm^2 and performed a detailed analysis. The CRDS spectra of a calibrated mixture of 2.55 ppmv of NH_3 at 1613.370 cm^{-1} and with 10 Torr pressure is shown in Figure 2.14a. At the same position, the spectra of 5% CO_2 and 5% H_2O were also taken since NH_3 shows chemical affinity to CO_2 and H_2O and so any interference due to these molecules should be investigated. However, no such interference was observed as seen from Figure 2.14a where the baseline of the spectra is not altered in presence of these molecules. Since NH_3 is a sticky molecule, a quartz-coated ring-down cell was utilized to minimize the sticking of NH_3 on the inner lining of the cavity cell. In order to examine the accuracy of measurements, we observed the above concentration of NH_3 (2.55 ppmv) continuously for 15 minutes (Figure 2.14b) and noted a drift of 11 ppbv in the concentration value after 15 minutes. We also evaluated the minimum detection sensitivity of 2.78×10^9 molecules cm^{-3} for the spectral line at 1613.370 cm^{-1} which resulted in a detection limit of 112 pptv at 760 Torr (1 atmosphere) pressure. However, at such a high pressure, the spectra would broaden and there is high

probability of overlap with other molecular spectra. Hence, to investigate the actual effect of pressure on the spectra and to find the optimum pressure value, the pressure broadening effect was observed. A particular NH_3 concentration was inserted into the cavity and pressure was further increased by adding zero air. It was found (Figure 2.14c) that with increase in pressure the peak height decreased while the full-width at half maxima (FWHM) of the peak increased due to the pressure broadening effect. To calculate the air-broadened pressure coefficient (γ_{air}), we plotted the half-width half maxima (HWHM) against the pressure and obtained the value of 0.098±0.003 cm^{-1} atm^{-1} for γ_{air} from the slope of the linear fitting curve (Figure 2.14d). This value agreed with the HITRAN value of γ_{air} =0.100 cm^{-1} atm^{-1} for the transition line. Further, up to 115 Torr pressure, no overlapping was found from the spectra of other molecules and hence the detection limit of 740 pptv at a pressure of 115 Torr was evaluated for an integration time of ~167 seconds.

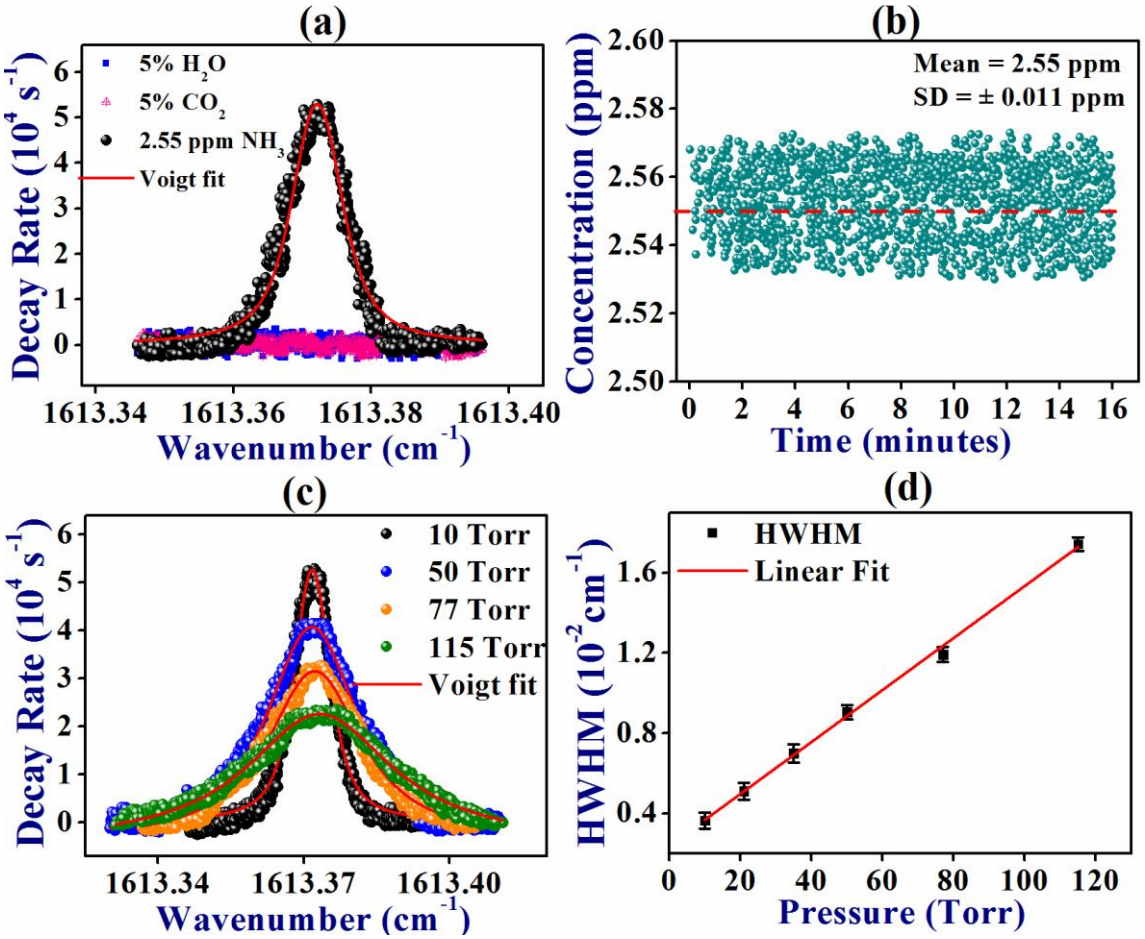

Figure 2.14 a) *CRDS spectra for 2.55 ppmv of NH_3 at 1613.370 cm^{-1}. Spectra of 5% CO_2 and 5% H_2O is also shown to examine the interference-free nature of the spectral region.* ***b)*** *Data for 2.55 ppmv of NH_3 taken for 15 minutes to observe the measurement drift.* ***c)*** *Pressure broadening effect observed for the peak at 1613.370 cm^{-1}.* ***d)*** *Plot of HWHM versus pressure shows a linear increase in the HWHM with increase in pressure for spectral peak at 1613.370 cm^{-1} [17].*

We eventually utilized the QCL-CRDS system to detect trace concentrations of NH_3 selectively in real sample mixtures of atmospheric air and human breath for practical field applications. The spectra for an outdoor air and a human breath sample are shown in Figure 2.15a and b, respectively. The spectra were obtained at 25 Torr pressure and the measured concentrations of NH_3 in air and breath were found to be 44.0 ± 0.7 ppbv and 89.7 ± 0.8 ppbv, respectively which are typical values for outdoor air in India [37] and a normal human breath sample [38].

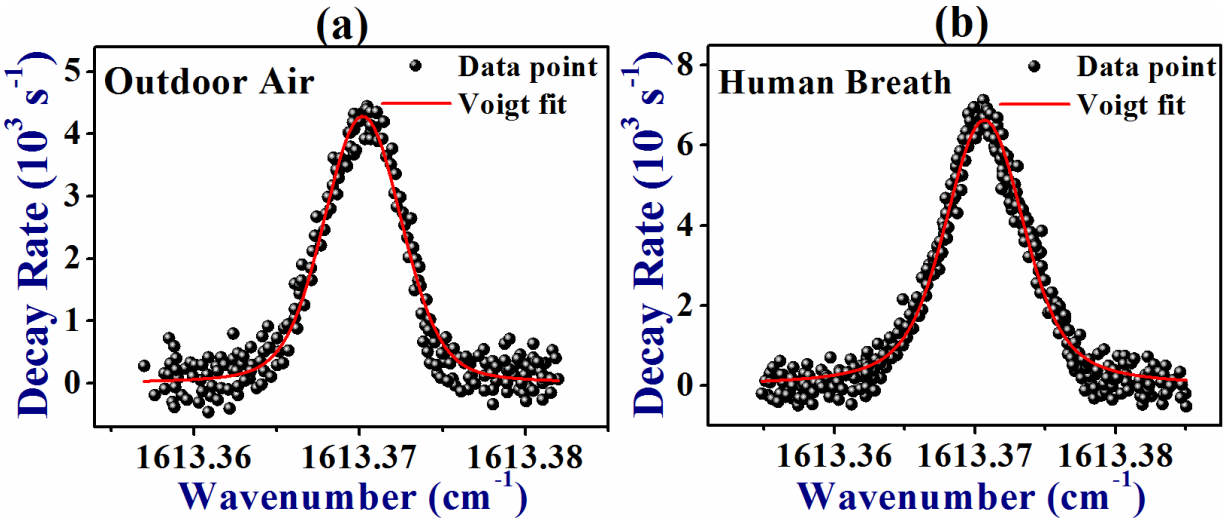

Figure 2.15 a) *and* ***b)*** *depict the CRDS spectra for NH_3 in an outdoor air and a human breath sample, respectively. The spectra have been fitted using a Voigt profile [17].*

In another work, we performed a preliminary study using the QCL-CRDS setup at 6.2 µm to explore the breath NH_3 levels in diabetic individuals with indications of kidney malfunction [39]. For this experiment, another strong peak was chosen at 1579.360(9) cm^{-1} with an absorption cross-section of 5.8008 x 10^{-20} cm^2 mol^{-1} cm^{-1} due to its large line intensity and its interference-free nature (Figure 2.16a). The line position of 1579.360(9) cm^{-1} matched well with the HITRAN value of 1579.3615 cm^{-1}. The experimental CRDS spectra of 1 ppmv of NH_3 taken at 0.72 Torr pressure is shown in Figure 2.16b. The detection limit at this transition line was evaluated as ~1.49 ppbv at a pressure of 25 Torr.

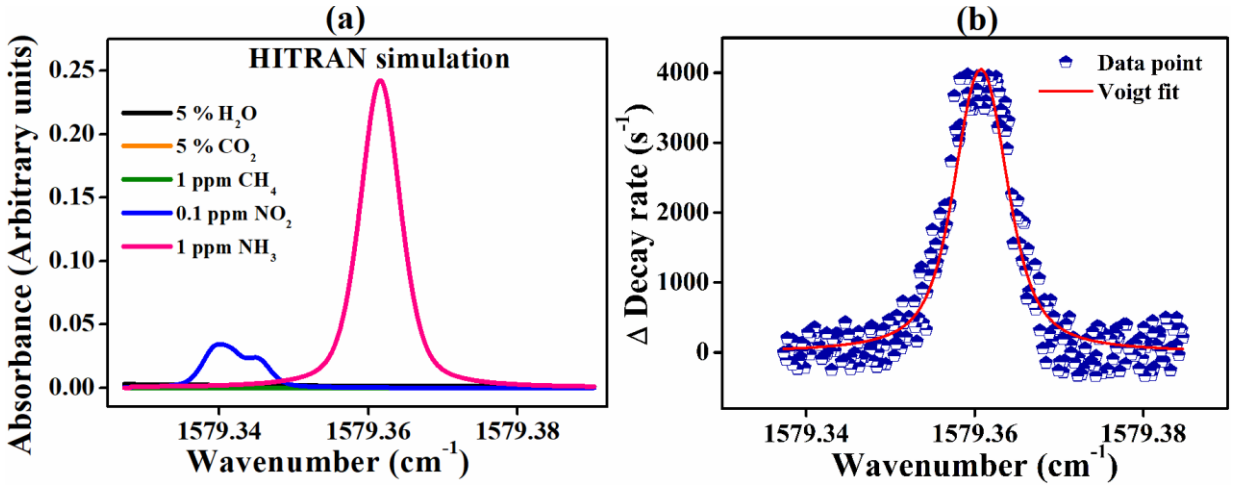

Figure 2.16 a) *depict the HITRAN simulation for transition line at 1579.360(9) cm^{-1} demonstrating the interference-free nature of the line.* ***b)*** *CRDS spectra of 1 ppmv of NH_3 with Voigt profile as the fitting function [39].*

We subsequently measured NH_3 in the fasting exhaled breath of three healthy individuals and three type-II diabetic patients with indications of early stage chronic kidney disease. The individuals were categorized as healthy or diabetic as per their glycosylated haemoglobin (HbA1c) levels in blood which is a standard test for diabetes in accordance with the American Diabetes Association [40]. An HbA1c $\geq$ 6.5 in blood was regarded as diabetic while a value of HbA1c $\leq$ 5.7 was considered as non-diabetic

[40]. The kidney function was assessed on the basis of the level of glomerular filtration rate (GFR) which is the rate of clearance of a filtration marker molecule (such as creatinine) from the kidney [41-43]. A GFR ≥ 90 mL per minute (min) is taken to be normal while a GFR ≤ 90 mL per min signals a decreased kidney function. Further, kidney malfunction can be categorized into five stages on the basis of GFR values as: Stage 1-GFR ≥ 90 mL per min (normal), Stage 2-GFR 60 to 89 mL per min (mild), Stage 3a-GFR 45 to 59 mL per min (mild to moderate), Stage 3b-GFR 30 to 44 mL per min (moderate to severe), Stage 4-GFR 15 to 29 mL per min (severe) and Stage 5-GFR ≤ 15 mL per minute (kidney failure) [39, 41]. In this work, the diabetic patients had a mean GFR of 66.9 ± 8.7 mL per min which indicated stage 2 of the kidney malfunction in which individuals generally do not show any symptoms. Thus, such patients run the risk of developing kidney failure with time and require early detection for timely treatment.

The exhaled breath NH_3 measurements for the subjects were made by initially collecting their fasting breath in breath collection bags (QUINTRON, USA, QT00892) and then measuring the breath using the QCL-CRDS setup. Written consent was taken from all individuals taking part in the study. The NH_3 concentration in the exhaled breath of all subjects is provided in Table 2.2. For samples of diabetic subjects, the sample pressure was kept at 12 Torr while it was 25 Torr for samples of healthy individuals to optimize the measurement. As is evident from Table 2.2, the breath NH_3 values for diabetic subjects are much larger than that for non-diabetics, indicating that even in an early stage breath NH_3 could distinguish between normal and mild dysfunction of the kidney. Since diabetic individuals are more prone to kidney disease, breath NH_3 can become a non-invasive biomarker for detection of kidney malfunction in diabetics and such individuals could routinely undergo breath NH_3 analysis non-invasively. However, this was a preliminary study and studies with larger groups of subjects are required to quantitatively classify the breath NH_3 for different stages of kidney malfunction in diabetics.

***Table* 2.2** *Exhaled breath NH_3 concentrations for diabetic and non-diabetic individuals, measured using QCL-CRDS setup [39].*

Condition	Non-diabetic			Diabetic		
Individual Subjects	1	2	3	4	5	6
Ammonia concentration (ppbv)	112 ± 5	109 ± 15	107 ± 11	1625 ± 25	1784 ± 31	2446 ± 46

2.10 Conclusion

We developed an experimental setup based on the CRDS technique using a QCL operating around 6.2 μm in the mid-infrared region. The setup parameters were characterized in detail and the system performance was tested using NH_3 as a probe molecule. Further, through simulation and experiment, ten spectral lines of NH_3 were selected and analysed that had minimal overlap with other molecular species so as to detect NH_3 selectively in a real sample mixture. The detection limit for NH_3 in the current setup was found to be few ppbv and even pptv level by increase of pressure, thus demonstrating the potential for high-sensitive NH_3 detection. Subsequently, the spectra of the strongest transition line in the region was studied in detail and further utilized for the measurement of NH_3 in outdoor air and human breath samples to validate the capability of the CRDS system to sensitively detect NH_3 for real life applications. We also performed a preliminary study for the measurement of NH_3 in exhaled breath samples of healthy individuals and diabetic patients with signs of early stage kidney disease. The study showed enhanced breath NH_3 levels for diabetics, thus indicating that breath NH_3 could act as a biomarker for early diagnosis of kidney malfunction in diabetic patients.

2.11 References

[1] Mazurenka, M., A. J. Orr-Ewing, R. Peverall and G. A. D. Ritchie. "4 cavity ring-down and cavity enhanced spectroscopy using diode lasers." *Annual Reports Section" C"(Physical Chemistry)* 101, (2005): 100-142.

[2] Wheeler, M. D., S. M. Newman, A. J. Orr-Ewing and M. N. R. Ashfold. "Cavity ring-down spectroscopy." *Journal of the Chemical Society, Faraday Transactions* 94, no. 3 (1998): 337-351.

[3] von Koch B. "Atmospheric traces monitoring using cavity ring-down spectroscopy", PhD Thesis, Technischen Universitat zur, Germany, (2003).

[4] O'Keefe, A. and D. A. G. Deacon. "Cavity ring-down optical spectrometer for absorption measurements using pulsed laser sources." *Review of Scientific Instruments* 59, no. 12 (1988): 2544-2551.

[5] Berden, G. and R. Engeln, eds. *Cavity ring-down spectroscopy: techniques and applications*. John Wiley & Sons, (2009).

[6] Maity, A., M. Pal, G. D. Banik, S. Maithani and M. Pradhan. "Cavity ring-down spectroscopy using an EC-QCL operating at 7.5 μm for direct monitoring of methane isotopes in air." *Laser Physics Letters* 14, no. 11 (2017): 115701.

[7] Van Zee, R. D., J. T. Hodges and J. Patrick Looney. "Pulsed, single-mode cavity ringdown spectroscopy." *Applied optics* 38, no. 18 (1999): 3951-3960.

[8] Demtröder, W. *Laser spectroscopy*. Vol. 1. Springer-Verlag, Fourth edition, (2008).

[9] Scherer, J. J., J. B. Paul, A. O'keefe and R. J. Saykally. "Cavity ringdown laser absorption spectroscopy: history, development, and application to pulsed molecular beams." *Chemical reviews* 97, no. 1 (1997): 25-52.

[10] Kosterev, A., G. Wysocki, Y. Bakhirkin, S. So, R. Lewicki, M. Fraser, F. Tittel and R. F. Curl. "Application of quantum cascade lasers to trace gas analysis." *Applied Physics B* 90, no. 2 (2008): 165-176.

[11] Mukherjee, N. and C. K. N. Patel. "Molecular fine structure and transition dipole moment of NO2 using an external cavity quantum cascade laser." *Chemical Physics Letters* 462, no. 1-3 (2008): 10-13.

[12] Faist, J., F. Capasso, D. L. Sivco, C. Sirtori, A. L. Hutchinson and A. Y. Cho. "Quantum cascade laser." *Science* 264, no. 5158 (1994): 553-556.

[13] Welzel, S., R. Engeln and J. Röpcke. “Quantum cascade laser based chemical sensing using optically resonant cavities.” In: G. Gagliardi, & H. P. Loock (Eds.) *Cavity-Enhanced Spectroscopy and Sensing*, pp. 93-142. Springer, Berlin, Heidelberg (2014).

[14] Hugi, A., R. Terazzi, Y. Bonetti, A. Wittmann, M. Fischer, M. Beck, J. Faist and E. Gini. "External cavity quantum cascade laser tunable from 7.6 to 11.4 μ m." *Applied Physics Letters* 95, no. 6 (2009): 061103.

[15] Wysocki, G., R. F. Curl, F. K. Tittel, R. Maulini, J. M. Bulliard and J. Faist. "Widely tunable mode-hop free external cavity quantum cascade laser for high resolution spectroscopic applications." *Applied Physics B* 81, no. 6 (2005): 769-777.

[16] Maithani, S., A. Maity and M. Pradhan. "Quantum Cascade Laser Spectroscopy for Atmospheric Sensing and Biomedical Diagnostics." In *Advances in Spectroscopy: Molecules to Materials*, pp. 67-82. Springer, Singapore, (2019).

[17] Maithani, S., S. Mandal, A. Maity, M. Pal and M. Pradhan. "High-resolution spectral analysis of ammonia near 6.2 μm using a cw EC-QCL coupled with cavity ring-down spectroscopy." *Analyst* 143, no. 9 (2018): 2109-2114.

[18] Paldus, B. A., J. S. Harris Jr, J. Martin, J. Xie and R. N. Zare. "Laser diode cavity ring-down spectroscopy using acousto-optic modulator stabilization." *Journal of applied physics* 82, no. 7 (1997): 3199-3204.

[19] Werle, P., R. Mucke and F. Slemr. “The limits of signal averaging in atmospheric trace-gas monitoring by tunable diode-laser absorption spectroscopy (TDLAS).” *Applied Physics B* 57, (1993): 131-139.

[20] Carmichael, G. R., M. Ferm, N. Thongboonchoo, J. H. Woo, L. Y. Chan, K. Murano, P. H. Viet *et al.* "Measurements of sulfur dioxide, ozone and ammonia concentrations in Asia, Africa, and South America using passive samplers." *Atmospheric Environment* 37, no. 9-10 (2003): 1293-1308.

[21] von Bobrutzki, K., C. F. Braban, D. Famulari, S. K. Jones, T. Blackall, T. E. L. Smith, M. Blom *et al.* "Field inter-comparison of eleven atmospheric ammonia measurement techniques." *Atmospheric Measurement Techniques* 3, (2010): 91-112.

[22] Koerkamp, P. W. G. G., J. H. M. Metz, G. H. Uenk, V. R. Phillips, M. R. Holden, R. W. Sneath, J. L. Short *et al.* "Concentrations and emissions of ammonia in livestock buildings in Northern Europe." *Journal of Agricultural Engineering Research* 70, no. 1 (1998): 79-95.

[23] Pushkarsky, M. B., M. E. Webber and C. K. N. Patel. "Ultra-sensitive ambient ammonia detection using CO2-laser-based photoacoustic spectroscopy." *Applied Physics B* 77, no. 4 (2003): 381-385.

[24] Heald, C. L., J. L. Collett Jr, T. Lee, K. B. Benedict, F. M. Schwandner, Y. Li, L. Clarisse *et al.* "Atmospheric ammonia and particulate inorganic nitrogen over the United States." *Atmospheric Chemistry and Physics*, European Geosciences Union 12, no. 21 (2012): 10295-10312.

[25] Hibbard, T. and A. J. Killard. "Breath ammonia analysis: Clinical application and measurement." *Critical Reviews in Analytical Chemistry* 41, no. 1 (2011): 21-35.

[26] Narasimhan, L. R., W. Goodman and C. K. N. Patel. "Correlation of breath ammonia with blood urea nitrogen and creatinine during hemodialysis." *Proceedings of the National Academy of Sciences* 98, no. 8 (2001): 4617-4621.

[27] Bhatia, V., R. Singh and S. K. Acharya. "Predictive value of arterial ammonia for complications and outcome in acute liver failure." *Gut* 55, no. 1 (2006): 98-104.

[28] Demirjian, S., K. M. Paschke, X. Wang, D. Grove, R. J. Heyka and R. A. Dweik. "Molecular breath analysis identifies the breathprint of renal failure." *Journal of Breath research* 11, no. 2 (2017): 026009.

[29] Gross, J. L., M. J. De Azevedo, S. P. Silveiro, L. H. Canani, M. L. Caramori and T. Zelmanovitz. "Diabetic nephropathy: diagnosis, prevention, and treatment." *Diabetes care* 28, no. 1 (2005): 164-176.

[30] American Diabetes Association. "Nephropathy in diabetes." *Diabetes care* 27, no. suppl 1 (2004): s79-s83.

[31] Azzawi, M. M., M. J. Hussein, N. K. Jebur and H. F. Saad. "Design and Construction of Optical System to Detect of Ammonia Gas." *International Journal of Structural Glass and Advanced Materials Research, 3,* (2019): 56-61.

[32] Yurchenko, S. N., M. Carvajal, H. Lin, J. Zheng, W. Thiel and P. Jensen. "Dipole moment and rovibrational intensities in the electronic ground state of NH3: bridging the gap between ab initio theory and spectroscopic experiment." *The Journal of chemical physics* 122, no. 10 (2005): 104317.

[33] Rothman, L. S., I. E. Gordon, Y. Babikov, A. Barbe, D. C. Benner, P. F. Bernath, M. Birk *et al*. "The HITRAN2012 molecular spectroscopic database." *Journal of Quantitative Spectroscopy and Radiative Transfer* 130, (2013): 4-50.

[34] Down, M. J., C. Hill, S. N. Yurchenko, J. Tennyson, L. R. Brown and I. Kleiner. "Re-analysis of ammonia spectra: Updating the HITRAN 14NH3 database." *Journal of Quantitative Spectroscopy and Radiative Transfer* 130, (2013): 260-272.

[35] Bethlem, H. L., M. Kajita, B. Sartakov, G. Meijer and W. Ubachs. "Prospects for precision measurements on ammonia molecules in a fountain." *The European Physical Journal Special Topics* 163, no. 1 (2008): 55-69.

[36] Harris, D. C. and M. D. Bertolucci. *Symmetry and spectroscopy: an introduction to vibrational and electronic spectroscopy*. Courier Corporation, (1989).

[37] Sharma, S. K., M. Kumar, N. C. Gupta, M. Saxena and T. K. Mandal. "Characteristics of ambient ammonia over Delhi, India." *Meteorology and Atmospheric Physics* 124, no. 1-2 (2014): 67-82.

[38] Manne, J., O. Sukhorukov, W. Jäger and J. Tulip. "Pulsed quantum cascade laser-based cavity ring-down spectroscopy for ammonia detection in breath." *Applied optics* 45, no. 36 (2006): 9230-9237.

[39] Maithani, S., A. Maity and M. Pradhan. "High-sensitive detection of ammonia in exhaled breath using cavity ring-down spectroscopy." *Asian Journal of Physics* 28, no. 4 (2019): 219-224.

[40] http://www.diabetes.org/diabetes-basics/diagnosis/?loc=db-slabnav

[41] Van Der Velde, M., K. Matsushita, J. Coresh, B. C. Astor, M. Woodward, A. S. Levey, P. E. de Jong, R. T. Gansevoort and Chronic Kidney Disease Prognosis Consortium. "Lower estimated glomerular filtration rate and higher albuminuria are associated with all-cause and cardiovascular mortality. A collaborative meta-analysis of high-risk population cohorts." *Kidney international* 79, no. 12 (2011): 1341-1352.

[42] Schwartz, G. J. and S. L. Furth. "Glomerular filtration rate measurement and estimation in chronic kidney disease." *Pediatric nephrology* 22, no. 11 (2007): 1839-1848.

[43] Stevens, L. A., J. Coresh, T. Greene and A. S. Levey. "Assessing kidney function—measured and estimated glomerular filtration rate." *New England Journal of Medicine* 354, no. 23 (2006): 2473-2483.

Chapter 3

High-resolution analysis of 1,3-butadiene spectral band at 6.2 μm using QCL based CRDS system

3.1 Introduction

In the previous chapter, the utilization of the developed QCL-CRDS setup at 6.2 μm to probe the NH_3 molecule was discussed. In this chapter, the use of the same setup to study a larger molecule, 1,3-butadiene (C_4H_6) is described. 1,3-butadiene is an unsaturated gaseous hydrocarbon which is carcinogenic and regarded as an air pollutant [1]. It is mainly released from the rubber and polymer industries, vehicular exhaust and smoke from cigarettes [2-4]. The concentration of 1,3-butadiene is roughly < 5ppbv in ambient air [5,6] while it is ~ 0.8-25 ppbv in human breath [7]. It is also a spectroscopically significant molecule as it is the smallest conjugate hydrocarbon with alternate double and single bonds and therefore its spectra would be prototype spectra for higher conjugate molecules. Moreover, 1,3-butadiene does not exhibit a microwave spectra due to its lack of a permanent dipole moment. Hence, the determination of its ro-vibrational spectra is of further importance and its high-resolution infrared spectra would assist in understanding the structure, bond properties and obtaining the spectroscopic constants of the molecule. However, the fine ro-vibrational spectra of molecules become closely spaced and overlapped

due to increased molecular motions as the number of atoms and bonds in a molecule increase. Although the ro-vibrational spectra of such large molecules are important, such measurements are difficult to perform.

Many studies in the past have investigated the infrared spectra of 1,3-butadiene including assignment of vibrational and spectroscopic parameters of the rotamers of 1,3-butadiene [8-12]. Yet, the fine ro-vibrational spectra of 1,3-butadiene has remained largely unexplored. Moreover, the fine ro-vibrational line by line parameters are unavailable in the HITRAN database [13]. Figure 3.1 shows the HITRAN simulation for 1,3-butadiene along with other smaller molecules around the 6.2 μm region. The simulation of 1,3-butadiene shows a broad spectra in comparison to other small molecules in the region for which high-resolution spectral lines can be seen, thus depicting the congested nature of the spectra of 1,3-butadiene. Such spectra would also lack selectivity in detection due to its broad nature and the overlap with other molecules.

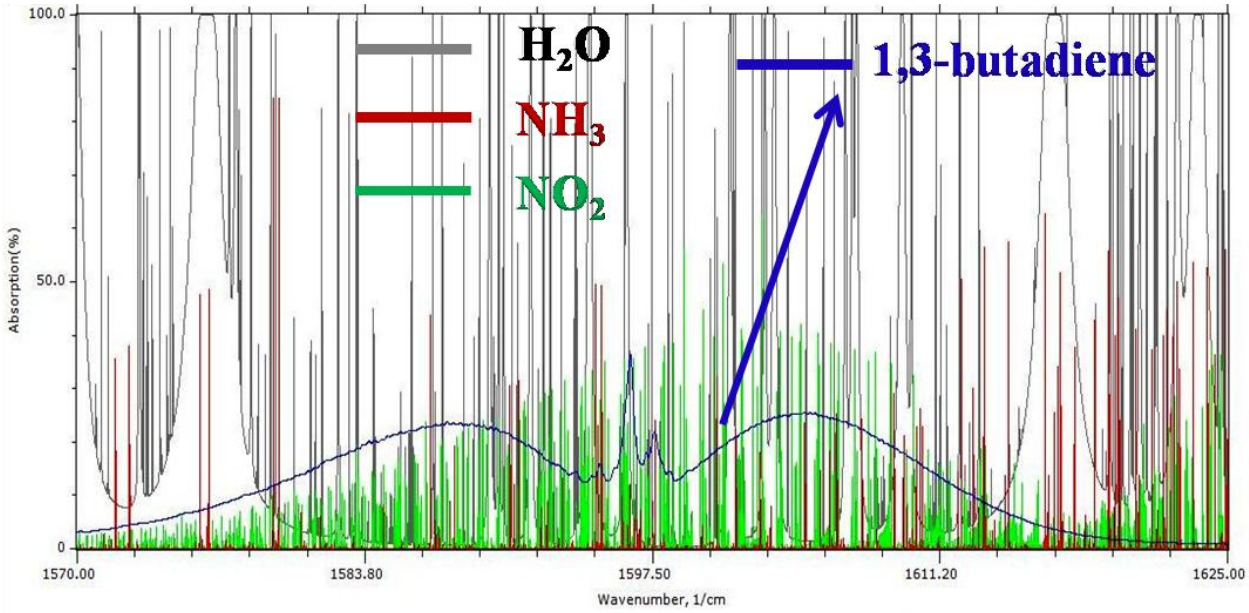

Figure 3.1 *Snapshot of the HITRAN simulation of 1,3-butadiene and its comparison to the ro-vibrational spectra of other small molecules in the 6.2 μm region.*

In this chapter, the applicability of the QCL-CRDS (at 6.2 μm) system to obtain high-resolution spectra of 1,3-butadiene molecule is discussed wherein other simulations (Gaussian 16 and PGOPHER) were performed to compute the high-resolution spectra and a comparison between the simulation and the experiment was made. Experimentally, more than 900 spectral lines were identified and assigned using the Gaussian and PGOPHER simulations. Simultaneously, spectroscopic parameters were also evaluated for the ro-vibrational band studied in the 6.2 μm region. Furthermore, we aimed to find an interference-free region among the 1,3-butadiene spectra for selective detection of this molecule in future.

3.2 1,3-butadiene molecule: Structure and symmetry

1,3-butadiene molecule possesses alternate double and single bonds between the carbon atoms making it a conjugate molecule (Figure 3.2). It is a near-prolate symmetric top (slightly asymmetric top) i.e. the moment of inertia (I) values follow $I_b \approx I_c > I_a$ [11, 14] where a, b and c are the axes of rotation (Figure 3.2).

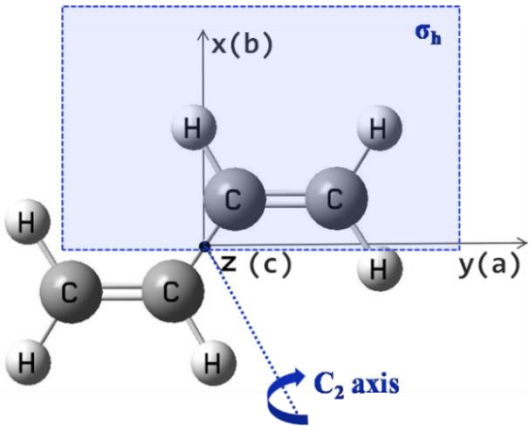

Figure 3.2 *Diagram of 1,3-butadiene showing the Cartesian axes (x, y and z) and the principle axes of rotation (a, b and c) of the molecule. Here z is out of the plane of the paper towards the observer. C_2 is the axis of rotation symmetry while σ_h is the horizontal mirror plane of symmetry. The plane of paper is taken to be horizontal.*

For a prolate top $I_b=I_c>I_a$ and the slight asymmetry of 1,3-butadiene with respect to the pure prolate top can be represented by the Ray's asymmetry parameter (κ) (equation 3.1) [14,15]:

$$\kappa = \frac{2B - A - C}{A - C} \qquad (3.1)$$

where A, B and C are the rotational constants for the three axes a, b and c, respectively. κ varies from $-1 \leq \kappa \leq 1$ where -1 refers to the prolate symmetric top and 1 refers to the oblate symmetric top. For 1,3-butadiene, $\kappa \sim -0.97$ which makes it a near-prolate symmetric top.

1,3-butadiene also possesses C_{2h} point group symmetry where z axis is the C_2 axis of rotation and a mirror plane symmetry (σ_h) lies in the x-y plane [14].

3.3 Spectroscopy of 1,3-butadiene in the 6.2 μm region

The ro-vibrational band of 1,3-butadiene in the 6.2 μm region (centred around 1596 cm^{-1}) arises from the anti-symmetric stretching of the C=C bonds as shown in Figure 3.3. The vibration belongs to the ν_{20} mode of the fundamental band of 1,3-butadiene. Now, if a mode of vibration is symmetric with regard to the C_2 rotation symmetry axis, the mode is referred as 'A' type while if the vibrational mode is anti-symmetric to the C_2 axis, then it is designated as 'B' type. These letters are further subscribed with 'g' or 'u' depending on whether the motion is symmetric (g) or anti-symmetric (u) with respect to the inversion operation. The vibrational mode around 1596 cm^{-1} has B_u symmetry while the ground state is A_g type. For B_u type modes the dipole moment changes may occur along both the 'a' and 'b' rotation axes, which indicate A/B type hybrid bands in the infrared spectra [12, 14]. For an asymmetric top such as 1,3-butadiene, although the total angular momentum J can be used to define the state of the rotating

molecule, K (projection of J on a symmetry axis) cannot define the state any more due to the asymmetry. Rather than K, K_a (projection of J on 'a' axis) and K_c (projection of J on 'c' axis) are used which are the defining quantum numbers for the pure oblate and pure prolate cases, respectively. For the A and B type bands, the following selection rules apply as $\Delta J=0, \pm1, \Delta K_a=0, \Delta K_c=\pm1$ for A type bands and $\Delta J=0, \pm1, \Delta K_a=\pm1, \Delta K_c=\pm1$ for B type bands [12,15].

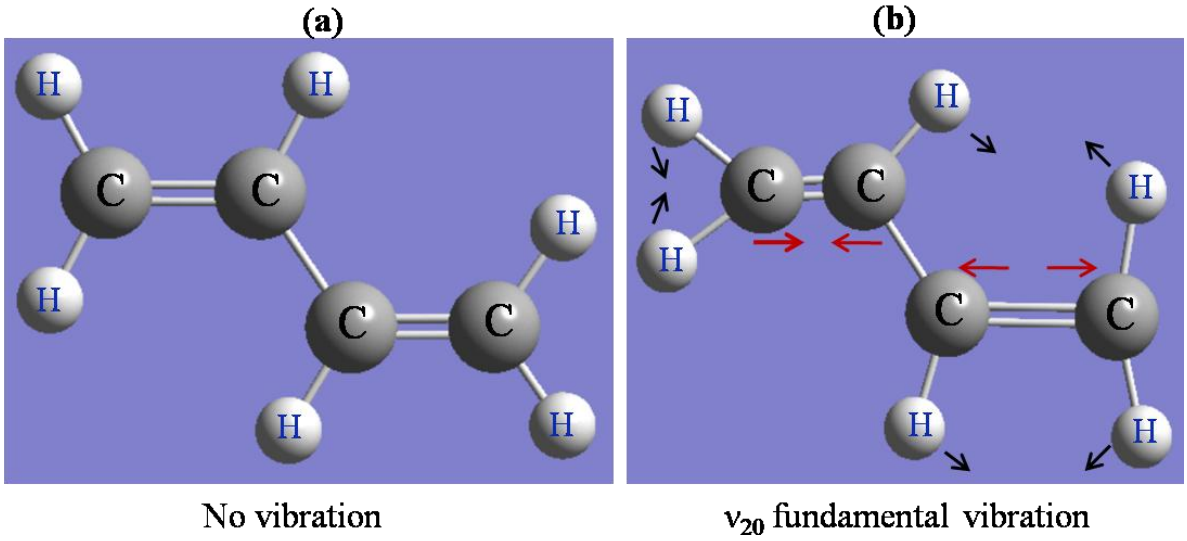

Figure 3.3 a) *Structure of 1,3-butadiene molecule without any motion.* ***b)*** *Diagram depicting the vibrational motions (arrows) in 1,3-butadiene during the C=C anti-symmetric stretching of the ν_{20} fundamental vibration. Diagrams* ***a)*** *and* ***b)*** *were made with the help of Gauss view [16,17].*

3.4 Experimental details

The developed CRDS setup with QCL operating around 6.2 μm as described in Chapter 2, was utilized to measure the high-resolution (with an accuracy of 0.001 cm^{-1}) spectra of 1,3-butadiene molecule. It is noteworthy to mention that the narrow linewidth of the QCL allowed the separation of the fine ro-vibrational spectra. On the other hand, the high-sensitivity of CRDS enabled the observation of spectra at low pressure and

low concentration and hence minimized the spectral overlap among the lines due to pressure broadening. To obtain the CRDS spectra, a calibrated mixture of 1000±23 ppmv of 1,3-butadiene gas in N_2 (Air Liquide, UK) was inserted into the cavity at a pressure of 1 Torr and at room temperature (~296 K). The ro-vibrational spectra of 1,3-butadiene in the ν_{20} fundamental mode centred around ~1596 cm^{-1} was probed as mentioned in Section 3.3 above.

3.5 Results and discussion

In order to compare and assign the experimentally obtained spectra, the theoretical spectra was evaluated using Gaussian 16 [16, 17] and the PGOPHER [18-20] simulations. PGOPHER is a simulation package which computes and performs fitting of high-resolution spectra of molecules. It requires various spectroscopic parameters and symmetry information about the molecule as inputs to simulate the spectra. On the other hand, Gaussian is a well-known software package used to perform vibrational frequency analysis and for calculation of spectroscopic parameters. Thus, in order to calculate the required parameters we used Gaussian 16 [16] which utilized Gauss View [17] as the graphical user interface to build the molecule and symmetrize the basic molecular structure. In Gaussian 16, the DFT-RB3YLP (Density Functional Theory-Becke, three-parameter, Lee-Yang-Parr) method [21] was utilized for the vibrational frequency and spectroscopic calculation by using the 6-311++G(3df,2p) basis set [22] which provided an optimized approximation of the molecular wave functions. From calculations using Gaussian, we obtained the band origin of the ν_{20} band at 1596.412 cm^{-1} along with other rotational parameters such as the ground state and the excited state rotational constants (A, B, C), the dipole moment derivatives (dd_a, dd_b, dd_c) and the moments of inertia (I_a, I_b and I_c). The simulation also provided the symmetry information i.e. the C_{2h} point group and the Ray's asymmetry parameter (κ) value. The values of

the parameters from Gaussian are provided in Table 3.1 [23]. The rotational constants allow the determination of the finer rotational spectral features whereas the dipole moment derivatives are crucial to estimate the relative line intensities of the transitions.

Table 3.1 *Spectroscopic parameters for 1,3-butadiene evaluated with Gaussian 16 [23].*

Evaluated Parameter	**Value**
Ground State A (cm^{-1})	1.398087
Ground State B (cm^{-1})	0.147648
Ground State C (cm^{-1})	0.133440
Excited State A (cm^{-1})	1.395653
Excited State B (cm^{-1})	0.147366
Excited State C (cm^{-1})	0.133123
dd_a (Debye)	3.19784
dd_b (Debye)	-3.62452
dd_c (Debye)	0
I_A (amu-Å^2)	11.8576
I_B (amu-Å^2)	113.65118
I_C (amu-Å^2)	125.5088
Ray's asymmetry parameter κ	-0.978229

In the PGOPHER simulation, the spectra for an asymmetric molecule was selected and the spectroscopic parameters such as the v_{20} band origin, point group symmetry C_{2h}, the ground and excited state symmetry of A_g and B_u, values of A, B, C, dd_a, dd_b, dd_c were used as inputs to simulate the fine ro-vibrational spectra. Further, the experimental CRDS spectrum was overlaid on the simulated spectra and a least square fitting analysis was done to minimize the differences in the simulated spectra as compared to the experimental spectra. Thus, about ~924 ro-vibrational spectral lines of 1,3-butadiene were identified and assigned with the ro-vibrational parameters using PGOPHER.

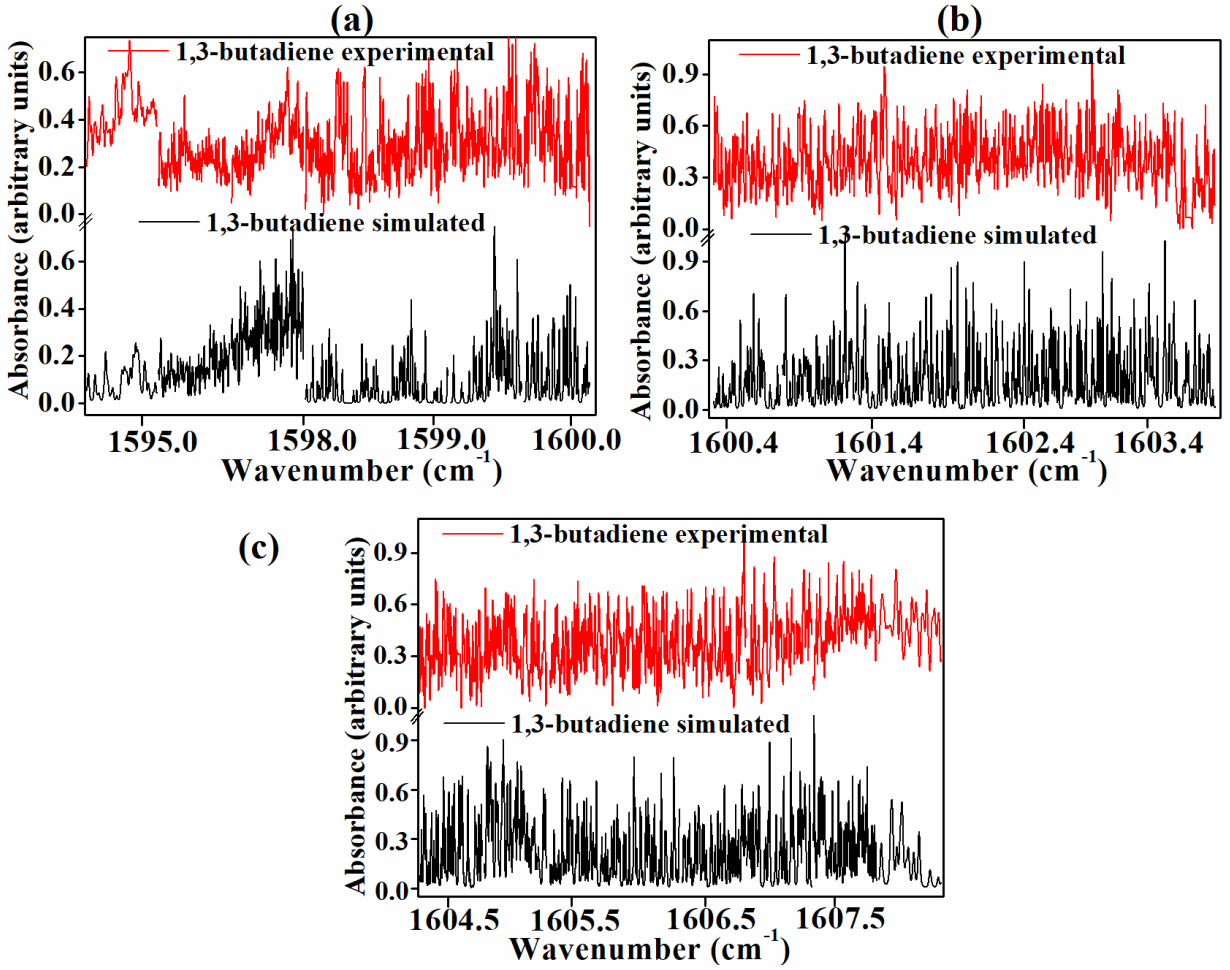

Figure 3.4 a), b) *and* ***c)*** *represent three different spectral regions (ranging from ~ 1594-1608 cm^{-1}) of 1,3-butadiene. The red data depicts the experimental spectra while the black data shows the simulated PGOPHER spectra [23].*

The complete list of the spectral line positions of experimental and simulated spectra along with the line assignments are provided in Appendix 1 (Table A1) at the end of the thesis. Figure 3.4a, b and c depict the comparison of the CRDS spectra and the PGOPHER simulated spectra of 1,3-butadiene where numerous high-resolution spectral lines can be seen in narrow regions of wavenumbers, thereby indicating the huge number of transitions in 1,3-butadiene molecule.

Subsequently, we plotted the residuals of the difference between the experimental and the simulated spectra as shown in Figure 3.5a and a good agreement was observed between the two spectra. From the spectral line assignments of J, K_a and K_c values of the ground and excited states, the nature of the bands was validated to be the A/B hybrid type (as mentioned in section 3.3) although the A band feature was more prominent.

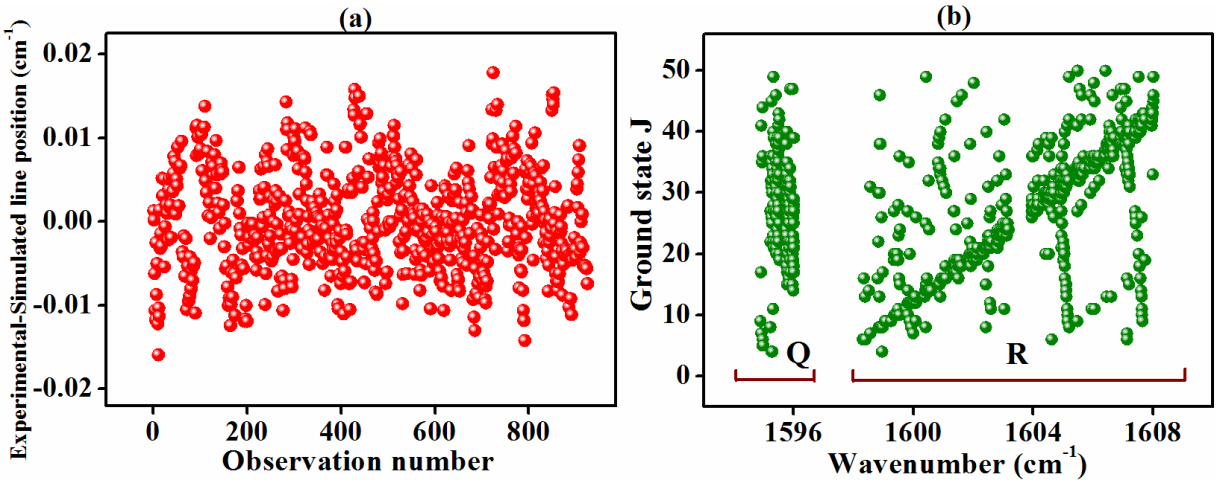

Figure 3.5 a) *shows a plot of the residuals of the difference between the experimental and simulated data for the observed spectral lines. A standard deviation (1σ) of 0.0059 cm^{-1} was observed for the residuals.* ***b)*** *Fortrat diagram depicting the variation of the J values with the wavenumber position of the spectral lines [23].*

Furthermore, we used the Fortrat diagram which is a plot of the J value versus the line position (wavenumber) of a particular transition line and helps in the representation of the ro-vibrational spectra. The Fortrat diagram is shown in Figure 3.5b which shows that the probed spectral lines in the region (~1594-1608 cm^{-1}) mainly belong to the Q ($\Delta J=0$) and R ($\Delta J=+1$) branches of the ro-vibrational spectra where values of J up to 50 have been investigated. Also, multiple J values for some spectral lines were seen as few line positions consisted of more than one transitions due to the congested nature of the spectra, thus having multiple assignments for certain lines.

We further intended to identify a spectral region for selective detection of 1,3-butadiene. Subsequently, we carried out a HITRAN simulation and identified a region (1604.39-1604.56 cm^{-1}) within the 1,3-butadiene spectra which was relatively interference-free from the spectra of other molecular species. The region is shown in Figure 3.6a with the experimental and PGOPHER simulated spectra of 1,3-butadiene along with the HITRAN simulation for spectra of other molecules such as H_2O, CO_2, NO_2, CH_4, NH_3, N_2O etc. in the region. As observed from Figure 3.6a, other molecules have insignificant absorption in this region and hence this region can be suitably utilized for the selective detection of 1,3-butadiene.

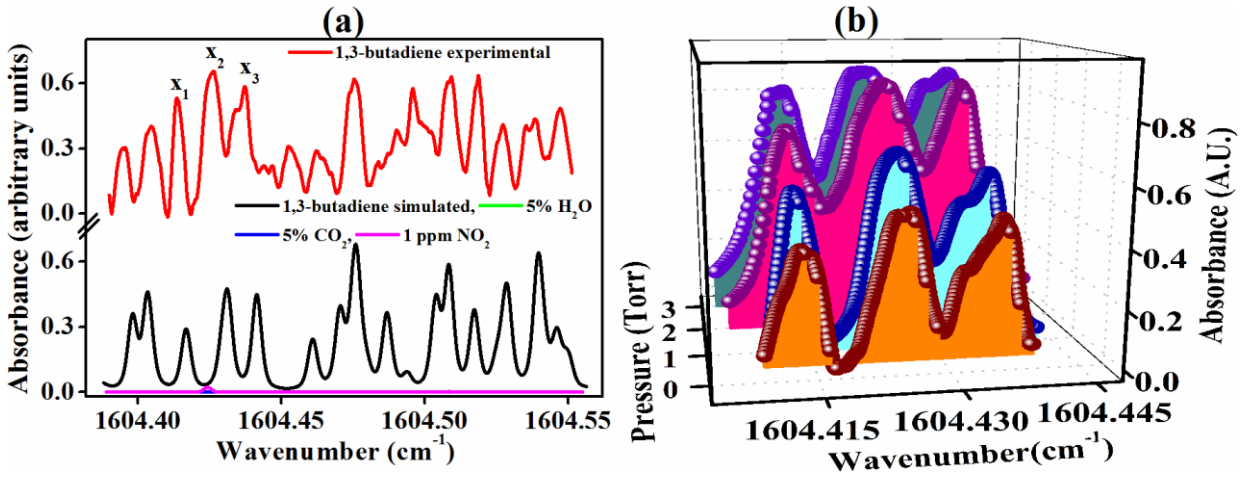

Figure 3.6 a) *shows the selected interference-free region within the 1,3-butadiene spectra wherein the red and the black data correspond to the experimental and the PGOPHER simulated spectra of 1,3-butadiene, respectively. The graph also contains the HITRAN simulation of various other molecular spectra present in the region.* x_1*,* x_2 *and* x_3 *refer to the three 1,3-butadiene peaks with details described in Table 3.2.* ***b)*** *CRDS spectra of* x_1*,* x_2 *and* x_3 *peaks of 1,3-butadiene at different pressures [23]. A. U. depicts arbitrary units.*

Moreover, we analysed three particular spectral lines of 1,3-butadiene in a narrow range of ~ 0.17 cm^{-1} and evaluated the absorption cross-sections of these lines by inserting 1,3-butadiene at different pressures in the ring-down cavity. The peak details are provided in Table 3.2 while the spectra at different pressures are provided in Figure 3.6b. It is to be noted that the multiple assignments refer to more than one transition for a particular spectral line. Moreover, the detection limit for 1,3-butadiene in the present setup was evaluated to be ~197 ppbv for the spectral peak at 1604.4254 cm^{-1} at a pressure of 25 Torr.

Table 3.2 *Spectroscopic details of peaks x_1, x_2 and x_3 of 1,3-butadiene in the interference-free region. The Δ values refer to the difference of the excited and ground state while J″, K_a″ and K_c″ values refer to the ground state quantum numbers [23].*

Peak No.	**Centre wavenumber of transition line (cm^{-1})**	**Wavelength dependent absorption cross-section (cm^2 $molecule^{-1}$)**	**Assignment $^{\Delta Ka}\Delta J_{\Delta Kc}$ (J", Ka", Kc")**
x_1	1604.4136	5.12×10^{-20}	$^{Q}R_R$ (30,14,16), $^{Q}R_R$ (30,14,17), $^{R}P_P$ (20,5,15)
x_2	1604.4254	9.29×10^{-20}	$^{P}R_R$ (30,1,30), $^{R}Q_P$ (39,2,38)
x_3	1604.4361	5.88×10^{-20}	$^{Q}R_R$ (29,8,22), $^{Q}R_R$ (29,8,21)

We eventually made a comparison between the available HITRAN 16 database [13] with a resolution of ~0.06 cm^{-1} and the present study with ~ 0.001 cm^{-1} spectral resolution (Figure 3.7) [23]. It is evident from Figure 3.7 that the present study provided resolved spectra with separated ro-vibrational spectral lines. Thus, the resolved spectra of 1,3-butadiene would not only enable better assessment of its spectroscopic parameters but would also assist in studying other higher conjugated molecules. Moreover, the CRDS analysis of the spectra in the interference-free region would allow selective and high-sensitive detection of 1,3-butadiene in the future.

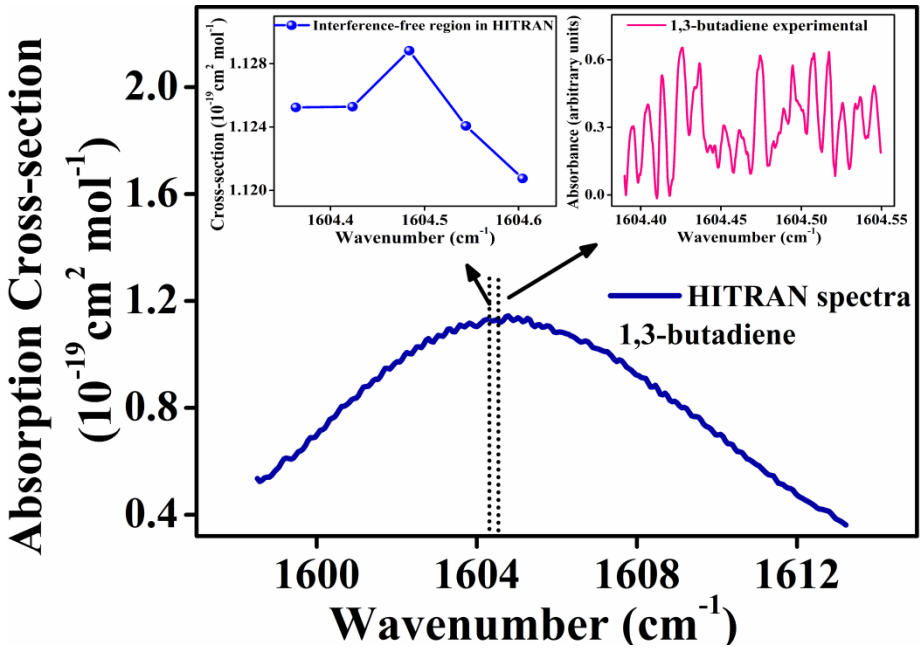

Figure 3.7 *The blue curve represents the HITRAN data in the region around 6.2 µm. The insets show a comparison of the HITRAN 16 database with the present CRDS based study depicting the resolved CRDS spectra [23].*

3.6 Conclusion

In this chapter, the application of the QCL-CRDS system at 6.2 µm for high-resolution analysis of the ro-vibrational spectra of a bigger molecule, 1,3-butadiene was discussed. Here, the narrow linewidth of the QCL and the high-sensitive nature of CRDS made such high-resolution spectral study practicable. The CRDS spectra of ~ 924 transition lines of 1,3-butadiene were identified and the relevant spectroscopic parameters for the vibrational band near 1596 cm^{-1} were calculated using Gaussian 16. Further, to simulate the high-resolution spectra, PGOPHER simulation was carried out by using input parameters from Gaussian. The experimental spectra were compared to the simulated spectra and spectral assignments were made for the spectral peaks. An interference-free region was also identified for sensitive and specific detection of 1,3-butadiene in real samples. Therefore, this study would serve as a prototypical study and

might open up ways for the spectroscopic analysis of higher conjugate molecules and other molecules with similar C=C anti-symmetric stretching vibration.

3.7 References

[1] Doyle M., K. G. Sexton, H. Jeffries, K. Bridge and I. Jaspers. "Effects of 1, 3-Butadiene, Isoprene, and Their Photochemical Degradation Products on Human Lung Cells." *Environmental health perspectives* 112, (2004**)**: 1488.

[2] Morrow, N. L. "The Industrial Production and Use of 1, 3-Butadiene." *Environmental health perspectives* 86, (1990**):** 7.

[3] Duffy B. L. and P. F. Nelson. "Exposure to Emissions of 1,3-Butadiene and Benzene in the Cabins of Moving Motor Vehicles and Buses in Sydney, Australia." *Atmospheric Environment* 31, (1997): 3877.

[4] Prazeller P., T. Karl, A. Jordan, R. Holzinger, A. Hansel and W. Lindinger. "Quantification of Passive Smoking Using Proton-Transfer-Reaction Mass Spectrometry." *International journal of mass spectrometry* 178, (1998): L1.

[5] Duffy, B. L. and P. F. Nelson. "Exposure to emissions of 1, 3-butadiene and benzene in the cabins of moving motor vehicles and buses in Sydney, Australia." *Atmospheric Environment* 31, no. 23 (1997): 3877-3885.

[6] Kim, Y. M., S. Harrad and R. M. Harrison. "Concentrations and sources of VOCs in urban domestic and public microenvironments." *Environmental science & technology* 35, no. 6 (2001): 997-1004.

[7] Gordon, S. M., L. A. Wallace, M. C. Brinkman, P. J. Callahan and D. V. Kenny. "Volatile organic compounds as breath biomarkers for active and passive smoking." *Environmental health perspectives* 110, no. 7 (2002): 689-698.

[8] Panchenko, Y. N. "A Partial Vibrational Reassignment of 1, 3-Butadiene." *Spectrochimica Acta Part A: Molecular Spectroscopy* 31, **(**1975): 1201.

[9] Yukio F., T. Hideo, H. Issei and T. Mitsuo. "Molecular Force Fields of s-Trans-1,3-Butadiene and The Second Stable Conformer." *Bulletin of the Chemical Society of Japan* 56, (1983): 392.

[10] Harward Sr C. N., R. E. Baren and M. E. Parrish. "Determination of Molecular Parameters for 1,3-Butadiene and Propylene Using Infrared Tunable Diode Laser Absorption Spectroscopy." *Spectrochimica Acta Part A: Molecular and Biomolecular Spectroscopy* 60**, (**2004): 3421.

[11] Craig N. C. and R. L. Sams. "An Investigation of the Rotamers of Butadiene by High-Resolution Infrared Spectroscopy." *The Journal of Physical Chemistry A* 112, (2008):12637.

[12] Craig N. C., J. L. Davis, K. A. Hanson, M. C. Moore, K. J. Weidenbaum and M. Lock. "Analysis of The Rotational Structure in Bands in the High-Resolution Infrared Spectra of Butadiene and Butadiene-2,3-D_2: Refinement in Assignments of Fundamentals." *Journal of molecular structure* 695, (2004): 59.

[13] Gordon I. E., L. S. Rothman, C. Hill, R. V. Kochanov, Y. Tan, P. F. Bernath, M. Birk, V. Boudon, A. Campargue, K. V. Chance *et al.* "The HITRAN2016 Molecular Spectroscopic Database." *Journal of Quantitative Spectroscopy and Radiative Transfer* 203, (2017): 3.

[14] Harris, D. C. and M. D. Bertolucci. *Symmetry and spectroscopy: an introduction to vibrational and electronic spectroscopy*. Courier Corporation, (1989).

[15] Townes, C. H. and A. L. Schawlow. *Microwave spectroscopy*. Courier Corporation, (2013).

[16] Frisch, M. J., G. W. Trucks, H. B. Schlegel, G. E. Scuseria, M. A. Robb, J. R. Cheeseman, G. Scalmani, V. Barone, G. A. Petersson, H. Nakatsuji *et al.*, Gaussian, Inc., Wallingford CT, (2016).

[17] Dennington, R., T. A. Keith and J. M. Millam. Semichem Inc., Shawnee Mission, KS, (2016).

[18] Western, C. M. University of Bristol Research Data Repository , doi:10.5523/bris.160i6ixoo4kir1jxvawfws047m (accessed June 2018).

[19] Western, C. M. "PGOPHER: A program for simulating rotational, vibrational and electronic spectra." *Journal of Quantitative Spectroscopy and Radiative Transfer* 186, (2017): 221-242.

[20] Western, C. M. and B. E. Billinghurst. "Automatic Assignment And Fitting of Spectra with PGOPHER." *Physical Chemistry Chemical Physics* 19, (2017): 10222.

[21] Becke, A. D. "Density-Functional Thermochemistry. III. The Role of Exact Exchange." *The Journal of chemical physics* 98, no. 7 (1993**):** 5648-5652.

[22] Binning Jr, R. C. and L. A. Curtiss. "Compact Contracted Basis Sets for Third-Row Atoms: Ga–Kr." *Journal of Computational Chemistry* 11, no. 10 (1990): 1206-1216.

[23] Maithani, S., A. Maity and M. Pradhan. "High-resolution spectral analysis of hybrid A/B-type band of 1, 3-butadiene at 6.2 μm using an EC-QCL coupled with cavity ring-down spectroscopy." *Chemical Physics* 522, (2019): 123-128.

Chapter 4

Study of deuterated isotopes of water and their fractionations in the gas-phase at 7.8 μm using QCL based CRDS system

4.1 Introduction

Water is one of the most essential molecules since it is vital for life. It also finds use in agricultural, industrial and daily activities of humans. Due to its vast applications, there is continuous research to understand its physical and chemical properties. Conversely, the study of water isotopes provides a different perspective in understanding their behaviour. Specifically, the investigation of deuterated isotopes of water (which contain at least one deuterium atom instead of hydrogen) helps to study the atmospheric chemistry [1, 2], build climatic models and obtain paleoclimatic information [3] through their measurements in oceans, glaciers etc. The measurement of D/H ratios in water in astrophysical environments helps to understand water formation and exchange reactions occurring in molecular clouds, comets and in atmospheres of other planets [4-6]. Even with a low natural abundance of 2.4197×10^{-8} [7], the doubly deuterated isotope of water (D_2O) is artificially produced in high isotopic purities (>99.8%) for its utilization in heavy water nuclear reactors as a coolant and moderator for slowing down fast neutrons [8, 9]. In such reactors, the leakage of D_2O can act as an indicator of radioactive contamination of the surroundings and so the reactors are monitored for such leakage events. Furthermore, D_2O is utilized in infrared analysis where it is used as a

substitute solvent in place of H_2O, to avoid the strong absorption and overlap of H_2O with a sample [10].

If we look at the chemistry of the isotopes themselves, in an isotopic mixture of H_2O and D_2O, the atoms H and D rapidly interchange to form another molecule HDO (equation 4.1) and an equilibrium is reached among the molecules involved in this exchange reaction [11-13].

$$H_2O + D_2O \leftrightarrow 2HDO \qquad (4.1)$$

The resultant concentration of the components at equilibrium depends on the relative fractions of the two isotopes, H_2O and D_2O. Thus, HDO does not exist in isolation but in a mixture of its parent isotopes. So, if one wants to know the total deuterium content in a deuterium enriched sample, both these isotopes (D_2O and HDO) need to be analyzed. Moreover, other deuterated species such as $HD^{18}O$ and $HD^{17}O$ with different oxygen isotopes also exist, whose role and fractionation chemistry in the above exchange reaction is not clear. Table 4.1 provides the natural abundances of different water isotopes [7].

Table 4.1 *List of water isotopologues with their respective natural abundances [7].*

Isotope	Mass (amu)	Natural abundance
$H_2{}^{16}O$	18	0.997317
$H_2{}^{18}O$	20	0.002000
$H_2{}^{17}O$	19	3.71884×10^{-4}
$HD^{16}O$	19	3.10693×10^{-4}
$HD^{18}O$	21	6.23003×10^{-7}
$HD^{17}O$	20	1.15853×10^{-7}
$D_2{}^{16}O$	20	2.41970×10^{-8}

It can be noted from Table 4.1 that the masses of few isotopes are similar and hence they cannot be separated using only mass-selective detection techniques. Although in the liquid state, the deuterium (D)-enriched isotopes of water have been studied using the FTIR technique [11,14], but the liquid state spectra of the isotopes has high overlapping among themselves which makes it difficult to evaluate the relative isotopic concentration, and thus requires careful analysis. On the other hand, infrared spectra can be performed in the gas-phase with high-resolution and high-sensitivity using cavity enhanced techniques such as CRDS. Moreover, studying the gas-phase spectra is not only beneficial for high-resolution spectroscopy but would also be effective in determining water isotopes in atmospheric samples.

In this chapter, the spectral analysis of deuterated water isotopes using a QCL based CRDS setup at 7.8 μm region has been discussed. Various interference-free spectral lines in the ν_2 bending vibration of D_2O were identified along with the lines of other deuterated isotopes such as $HD^{16}O$, $HD^{18}O$ and $HD^{17}O$. The normal modes of vibration in water are shown in Figure 4.1. These spectral lines were further utilized to study the H-D exchange reaction (equation 4.1) in the gas-phase. For the same reaction, the variation of the oxygen isotopes in the deuterated water was investigated and their relative fractionation chemistry was studied. The capability of the setup to determine trace concentrations of these isotopes was also demonstrated by measuring the isotopes in an isotopically diluted sample of water.

4.2 Vibrational spectroscopy of water isotopes

Water is a non-linear molecule and so it has 3N-6=3x3-6=3 normal modes of vibration, where N is the number of atoms. The vibrational modes of water isotopes are shown in Figure 4.1. Since water is also an asymmetric top molecule, its rotational transitions are assigned using the rotational

quantum numbers J, K_a and K_c as described in section 3.3 of chapter 3. In the work described in this chapter, the ν_2 bending vibration mode of the water isotopes has been probed.

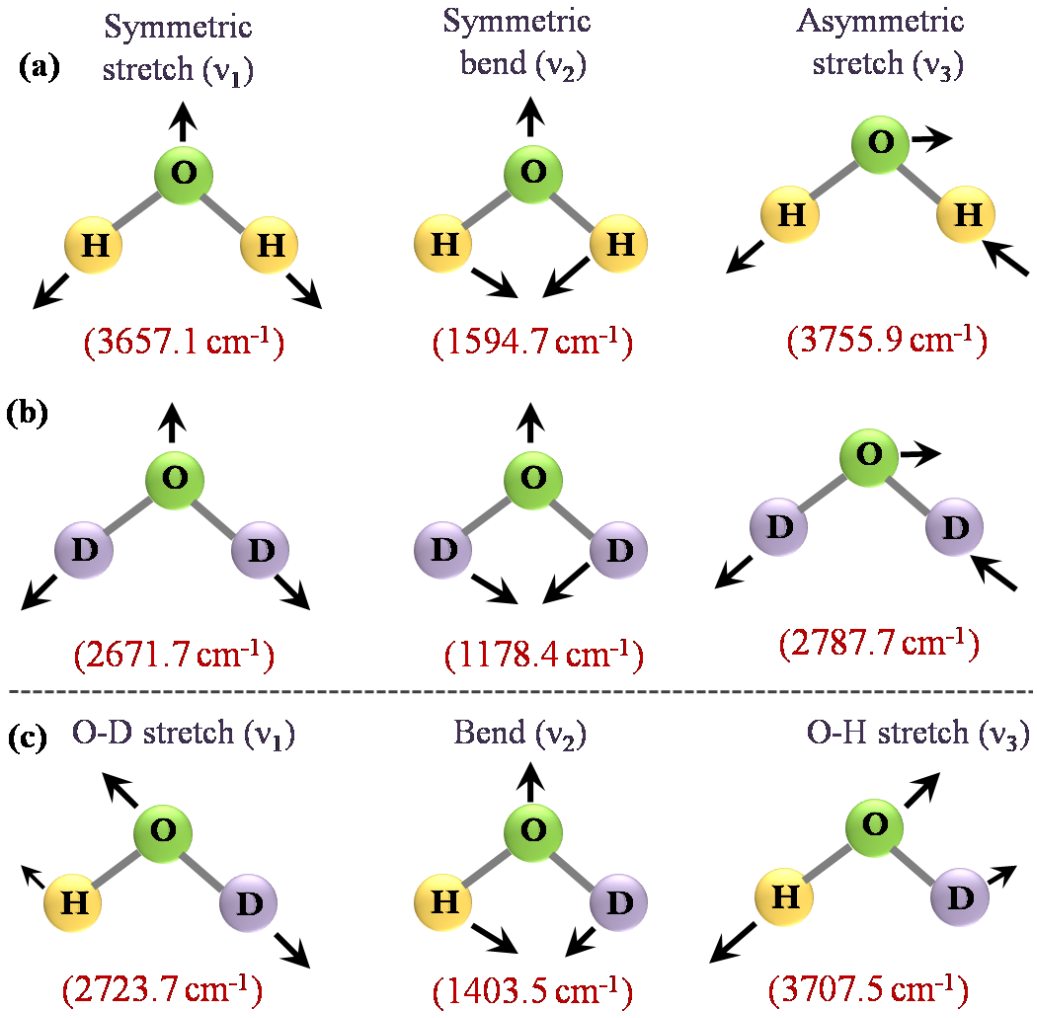

Figure 4.1 a), b) *and* ***c)*** *depict vibrational modes of H_2O, D_2O and HDO, respectively. The arrows indicate the direction of vibration whereas the numbers in brackets depict the band positions of the water isotopes in the gas-phase. Figure adapted from Ref. [15] while band positions were taken from Ref. [16].*

4.3 Experimental details

4.3.1 Setup description

To probe the D-enriched water isotopes, a QCL-CRDS setup was used with a similar arrangement as described in section 2.7 with the QCL operating around 7.8 μm. This different setup was utilized to access the absorption of water isotopes in the region of 7.8 μm. The complete details for the development of the setup have been described elsewhere [17]. The QCL (MHF-41078; Daylight Solutions, USA) used in this setup operated around 7.8 μm and had a MHF tuning range between 1257 cm^{-1}-1341 cm^{-1} with a narrow linewidth of ~0.0004 cm^{-1}. The rest of the experimental arrangement is similar to the description of section 2.7. In this system, the empty cavity ring-down time (τ_0) was 14.13 μs with 0.56% standard deviation (1σ) on averaging of 5 ring-down events [17]. The optical path length for this system was ~ 4.2 km while the finesse was F~26000. The minimum absorption coefficient for the system was evaluated to be α_{min}= 1.32×10^{-8} cm^{-1} while the noise equivalent absorption (NEA) coefficient of 4.17×10^{-9} cm^{-1} $Hz^{-1/2}$ was attained at a 100 Hz data acquisition rate of a single ring-down event.

4.3.2 Method and Materials

Although the setup had basic working design similar to the one described in section 2.7, additional arrangements were made for water isotopes measurement. A schematic diagram for the arrangement is provided in Figure 4.2. Since all the measurements were performed in the gas-phase, the liquid samples were evaporated in a chamber covered by a heating jacket and subsequently mixed with zero air (Air Liquide, UK) to avoid saturation of signal in the cavity due to pure sample. To introduce small quantities in microlitre range (0.2-1 μL) of the liquid sample, Hamilton's syringe was used. The sample was then channelled to the inlet of the cavity

and the cavity pressure was controlled using a pressure gauge. To avoid the condensation of the sample on the cavity walls and the mirror surface, the cavity was maintained at a temperature of 45^{0}C (318 K) (with ±0.01°C precision). The cavity and the sample chambers were purged thoroughly with zero air to remove the residues of the previous sample and the removal of the residues was ensured by observing the empty cavity ring-down time in the system, before inserting the next sample. High purity D_2O (99.9%) (DLM-4-100) was obtained from Cambridge Isotope Laboratories, Inc., USA whereas Milli-Q water (H_2O) was used to prepare D_2O mixtures in H_2O.

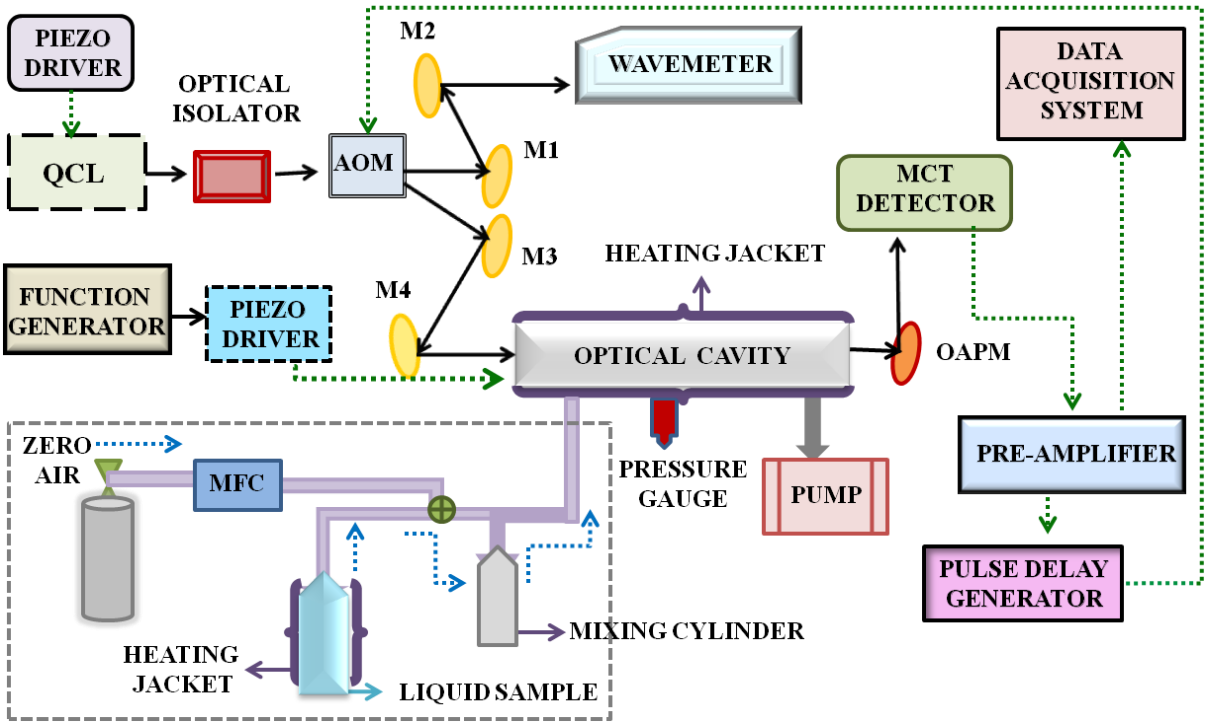

Figure 4.2 *Schematic diagram of the experimental arrangement for measurement of water isotopes [18]. The dotted box indicates the sample mixing arrangement.*

4.3.3 Water Vapour Isotope Analyser (WVIA)

In this work, besides the QCL-CRDS setup, a commercial, high-precision water vapour isotope analyser (WVIA) (Model no. IWA-45EP, ABB LGR USA) was also used for parallel measurement and validation of the $HD^{16}O$ isotope. The working of WVIA is based on another variant of the cavity enhanced absorption spectroscopy (CEAS) technique i.e. the off-axis integrated cavity output spectroscopy (OA-ICOS). In OA-ICOS, the light is incident on the optical cavity in an off-axis direction such that after some passes the light retraces its path again. Hence, the optical path length enhancement is achieved here but with difference in cavity alignment. Moreover, in ICOS the wavenumber is scanned across the absorption spectra and the time integrated intensity is noted as the output. The WVIA utilized the water absorption in the near-infrared region of 1.38 μm and provided isotope ratio (δD value) of the $HD^{16}O$, as described by equation 4.2.

$$\delta D\,(‰) = \left[\frac{\left(\frac{HD^{16}O}{H_2{}^{16}O} \right)_{sample}}{\left(\frac{HD^{16}O}{H_2{}^{16}O} \right)_{standard}} - 1 \right] \times 1000\ ‰ \qquad (4.2)$$

where $(HD^{16}O/H_2{}^{16}O)_{standard}$ =3.1152 x 10^{-4} is the $HD^{16}O$ abundance of Vienna Standard Mean Ocean Water (VSMOW) [18, 19]. For δD measurements, the precision of WVIA was 0.2‰. From the δD values, the concentration (in ppmv) of $HD^{16}O$ was evaluated using the total $H_2{}^{16}O$ concentration.

4.4 Results and discussion

We initially exploited the water isotope absorption in the 7.8 μm region to explore the interference-free transition lines of $D_2{}^{16}O$ molecule in the gas-phase, using the QCL-CRDS setup at 7.8 μm [18]. We experimentally probed eight such transition lines in the region between 1263 cm^{-1}-1279 cm^{-1} as shown in Figure 4.3. These 8 transitions occurred due to the ν_2 bending mode of $D_2{}^{16}O$, where five lines belonged to the fundamental band (010←000) while three lines were hot band transitions (020←010). The experiments were performed at 318 K temperature to prevent the condensation of vapour inside the cavity walls and mirror surfaces while the sample pressures were kept below 25 Torr to minimize the effects of pressure broadening. The experimental details and the line assignments are provided in Table 4.2 along with the comparison of experimental and HITRAN [7] simulated line positions. It is noteworthy of mention here that the experimental temperature was 318 K whereas the HITRAN simulations provide the line position at a reference temperature of 296 K. Although, the experimental and simulated are fairly matched with each other, there is a slight shift towards the lower wavenumber for experimental line positions. This might be the effect of the pressure-induced line position shift which is temperature dependent since the experimental and simulated temperatures are different. From Table 4.2 it can be observed that the spectral lines possess a wide range of absorption cross-sections which can be utilized for the measurement of a broad range of $D_2{}^{16}O$ concentrations. Moreover, the interference-free nature of these lines would allow the selective detection of $D_2{}^{16}O$ in a real sample mixture.

We further selected the $D_2{}^{16}O$ spectral line with the highest line intensity (absorption cross-section) at 1278.1371 cm^{-1} for high-sensitive sensing of $D_2{}^{16}O$ in real samples. For this, we prepared low concentrations (of ~ ppmv order) by mixing zero air with $D_2{}^{16}O$ vapour generated by evaporating different quantities of liquid $D_2{}^{16}O$. The resultant sample mixture was inserted into the cavity at different pressures from 0.1 to 5 Torr.

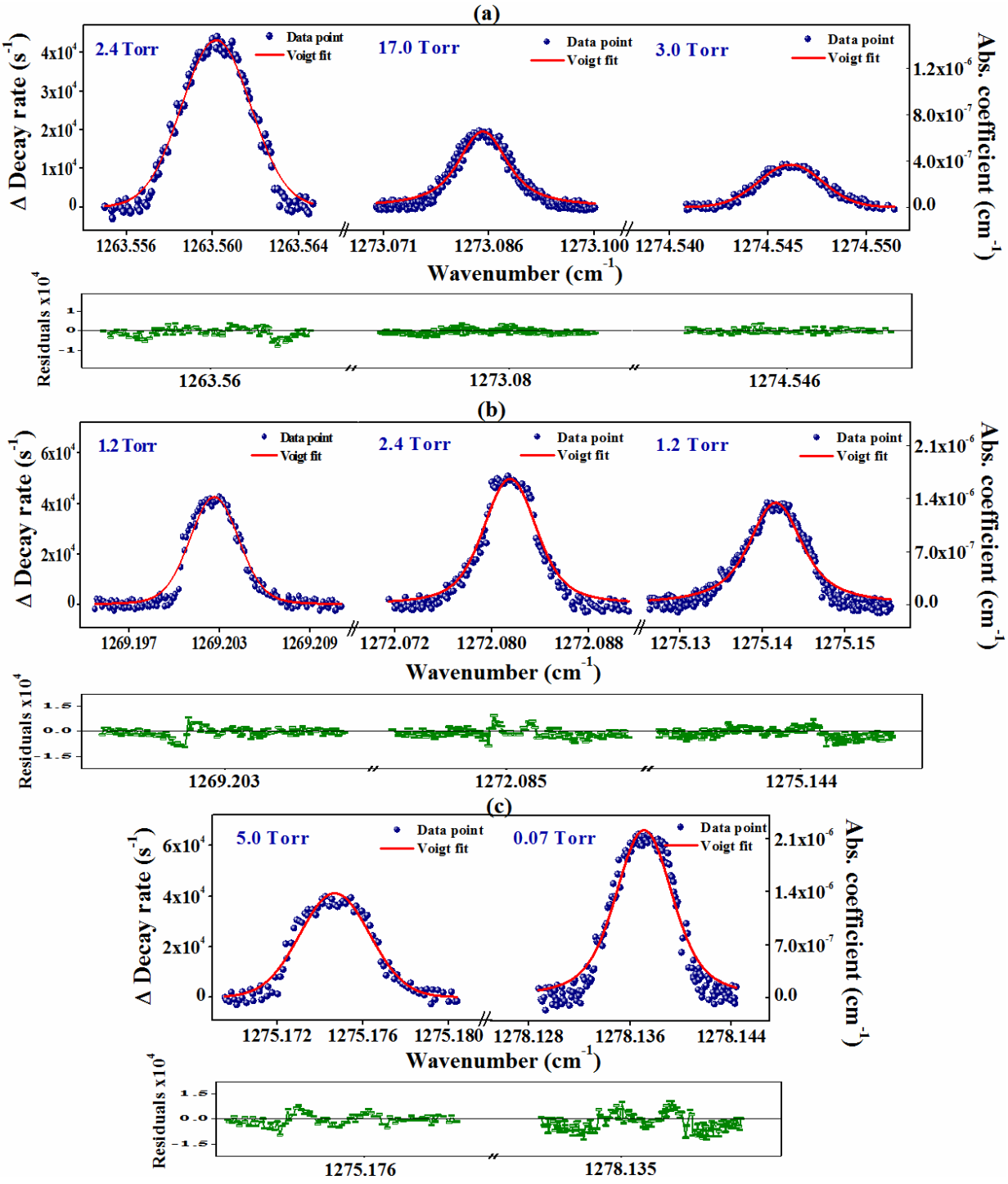

Figure 4.3 *The experimental CRDS spectra of $D_2{}^{16}O$ in the gas-phase.* ***a)*** *depicts the hot band transitions while* ***b)*** *and* ***c)*** *are the fundamental transitions lines of $D_2{}^{16}O$. The data points are fitted using Voigt profiles. The y-scale on the right shows the equivalent value of absorption coefficient α. The working pressure for each line measurement is given with the peaks while the fitting residuals are given below each spectrum [18].*

Table 4.2 *Experimental line positions and absorption cross-sections (HITRAN) of $D_2{}^{16}O$ transition lines. The first 3 belong to hot-band while the rest are the fundamental ν_2 transition lines. The upper and ground states are indicated using prime and double primes, respectively. J is the total angular momentum quantum number while K_a and K_c depict the projections of J onto the 'a' and 'c' axes of the molecule, respectively [18].*

Sl. No	**Isotopic Species**	**Experimental line centre (cm^{-1}) T= 318 K**	**HITRAN line centre (cm^{-1}) at T= 296 K**	**HITRAN absorption cross-section ($cm^2\ mol^{-1}\ cm^{-1}$) at T= 296 K**	**Assignments ($\nu_1'\ \nu_2'\ \nu_3'$)← ($\nu_1''\nu_2''\ \nu_3''$), $^{\Delta Ka}\Delta J_{\Delta Kc}$ (J'', K_a'',K_c'')**
1	$D_2{}^{16}O$	1263.5601 ± 0.002	1263.5785	6.872×10^{-23}	(020) ← (010), $^{P}R_{R}$ (8,2,7)
2	$D_2{}^{16}O$	1273.0845 ± 0.002	1273.0984	4.277×10^{-24}	(020) ← (010), $^{P}R_{R}$ (10,4,7)
3	$D_2{}^{16}O$	1274.5461 ± 0.001	1274.5498	4.372×10^{-24}	(020) ← (010), $^{Q}Q_{P}$ (11,1,11)
4	$D_2{}^{16}O$	1269.2026 ± 0.001	1269.2136	2.477×10^{-20}	(010) ← (000), $^{Q}R_{R}$ (8,1,8)
5	$D_2{}^{16}O$	1272.0813 ± 0.001	1272.1028	1.045×10^{-22}	(010) ← (000), $^{P}R_{T}$ (12,6,6)
6	$D_2{}^{16}O$	1275.1416 ± 0.002	1275.1617	2.116×10^{-22}	(010) ← (000), $^{R}Q_{P}$ (13,2,11)
7	$D_2{}^{16}O$	1275.1747 ± 0.001	1275.1893	9.240×10^{-23}	(010) ← (000), $^{T}Q_{N}$ (3,0,3)
8	$D_2{}^{16}O$	1278.1371 ± 0.001	1278.1542	3.618×10^{-20}	(010) ← (000), $^{P}R_{R}$ (9,1,9)

The measured gas-phase concentrations were plotted against the amount of liquid $D_2{}^{16}O$ used and a linear correlation was observed as depicted in Figure 4.4, which validated the direct correlation between the liquid and the gas-phase observations. For this spectral line of $D_2{}^{16}O$ at 1278.1371 cm^{-1}, the minimum detection limit of the setup was ~ 1.66 ppbv at a pressure of 25 Torr.

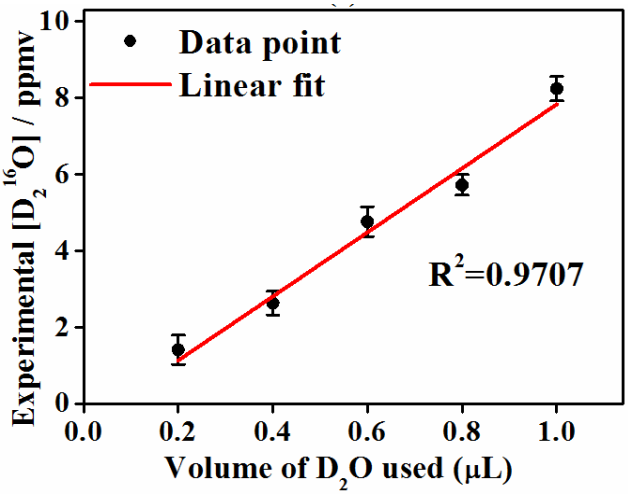

Figure 4.4 *The experimental gas-phase measurements of $D_2{}^{16}O$ plotted against the initial quantity of liquid $D_2{}^{16}O$ used. The data points are fitted with linear regression fit [18].*

Subsequently, we explored the absorption spectra of other deuterated water isotopes containing different isotopic oxygen such as $HD^{16}O$, $HD^{17}O$ and $HD^{18}O$. Low concentration mixtures of H_2O and D_2O were prepared so as to form the above mentioned isotopologues of HDO. We also identified a spectral line of $H_2{}^{18}O$ for comparison with $HD^{18}O$ which will be described later. Table 4.3 provides the experimental and HITRAN simulated spectroscopic parameters of the different water isotopologues where the assignments were obtained from the HITRAN simulation. The absorption cross-sections in Table 4.3 are given at 296 K and 318 K as the HITRAN simulations provide the cross-section values at the reference temperature of 296 K but the value at another temperature (here 318 K) can be evaluated

using equation 4.3. Since the experiments were performed at 318 K, the cross-sectional values are calculated for 318 K.

Table 4.3 *Experimental and simulated line positions and HITRAN absorption cross-sections at reference and experimental temperatures for water isotopologues. The line assignments (HITRAN) follow similar notation to Table 4.2 [18].*

Peak No.	**Isotopic Species**	**Experimental line centre (cm^{-1}) at T=318 K**	**HITRAN Simulated line centre (cm^{-1}) at T=296 K**	**HITRAN simulated absorption cross-section (cm^2 mol^{-1} cm^{-1}) at T=296 K**	**HITRAN simulated absorption cross-section (cm^2 mol^{-1} cm^{-1}) at T=318 K**	**Assignments $(v_1' v_2' v_3') \leftarrow (v_1'' v_2'' v_3'')$, ${}^{\Delta K_a}\Delta J_{\Delta K_c}$ (J'', K_a'', K_c'')**
1	$D_2{}^{16}O$	1278.1371 ± 0.001	1278.1542	3.618×10^{-20}	3.808×10^{-20}	(010) ← (000), ${}^{P}R_R$ (9,1,9)
2	$D_2{}^{16}O$	1272.0813 ± 0.001	1272.1028	1.045×10^{-22}	1.443×10^{-22}	(010) ← (000), ${}^{P}R_T$ (12,6,6)
3	$HD^{16}O$	1285.1360 ± 0.001	1285.1590	3.273×10^{-21}	3.963×10^{-21}	(010) ← (000), ${}^{P}Q_R$ (10,1,9)
4	$H_2{}^{18}O$	1261.5643 ± 0.001	1261.5774	5.500×10^{-22}	7.018×10^{-22}	(010) ← (000), ${}^{P}P_R$ (8,3,5)
5	$HD^{18}O$	1275.0972 ± 0.001	1275.1101	1.445×10^{-20}	1.601×10^{-20}	(010) ← (000), ${}^{Q}P_P$ (9,1,9)
6	$HD^{17}O$	1270.4994 ± 0.001	1270.5123	3.524×10^{-20}	3.487×10^{-20}	(010) ← (000), ${}^{P}P_P$ (4,3,2)
7	$HD^{16}O$	1278.6339 ± 0.001	1278.6471	3.012×10^{-22}	3.965×10^{-22}	(010) ← (000), ${}^{R}P_P$ (11,2,9)

Since the spectroscopic parameters in HITRAN are simulated for a reference temperature of 296 K, the following equation (4.3) can be utilized to evaluate the absorption cross-section at a temperature T.

$$S(T) = S(T_0)\frac{Q(T_0)\exp\left(-\frac{hcE''}{kT}\right)\left(1-\exp\left(-\frac{hc\,\nu_c}{kT}\right)\right)}{Q(T)\exp\left(-\frac{hcE''}{kT_0}\right)\left(1-\exp\left(-\frac{hc\,\nu_c}{kT_0}\right)\right)} \qquad (4.3)$$

Here, S is the line integrated absorption cross-section of the spectral line, T and T_0 represent the working temperature (318 K) and the reference temperature (296 K), respectively, Q refers to the total internal partition function, E'' is the energy of the lower transition state, ν_c depicts the transition line position, and h, c and k refer to Planck's constant, speed of light and Boltzmann's constant, respectively [18, 20].

Next, we carried out a HITRAN simulation [7] to examine the interference-free nature of the spectral regions of the water isotopes provided in Table 4.3. The simulations are provided in Figure 4.5a and b. Since the sample mixtures contain water it might cause a continuum effect on the spectra due to the strong absorption of water in the mid-infrared region. Thus, to verify whether the water continuum affects the spectra, we measured laboratory air containing ~ 1% (10,000 ppmv) water at 15 Torr pressure and compared it with the empty-cavity spectra as shown in Figure 4.5c. No interference due to the water continuum was observed as the lab air spectra did not vary with respect to the empty-cavity value. However, at very high pressures and concentrations the water continuum might have an effect. Although Figure 4.5c shows one region, similar behaviour was found for other spectral regions as well. Further, we utilized a commercial water vapour isotope analyzer (WVIA), described in section 4.3.3, which was capable of measuring the $HD^{16}O$ isotope, to validate the $HD^{16}O$ measurements with those obtained using the QCL-CRDS setup.

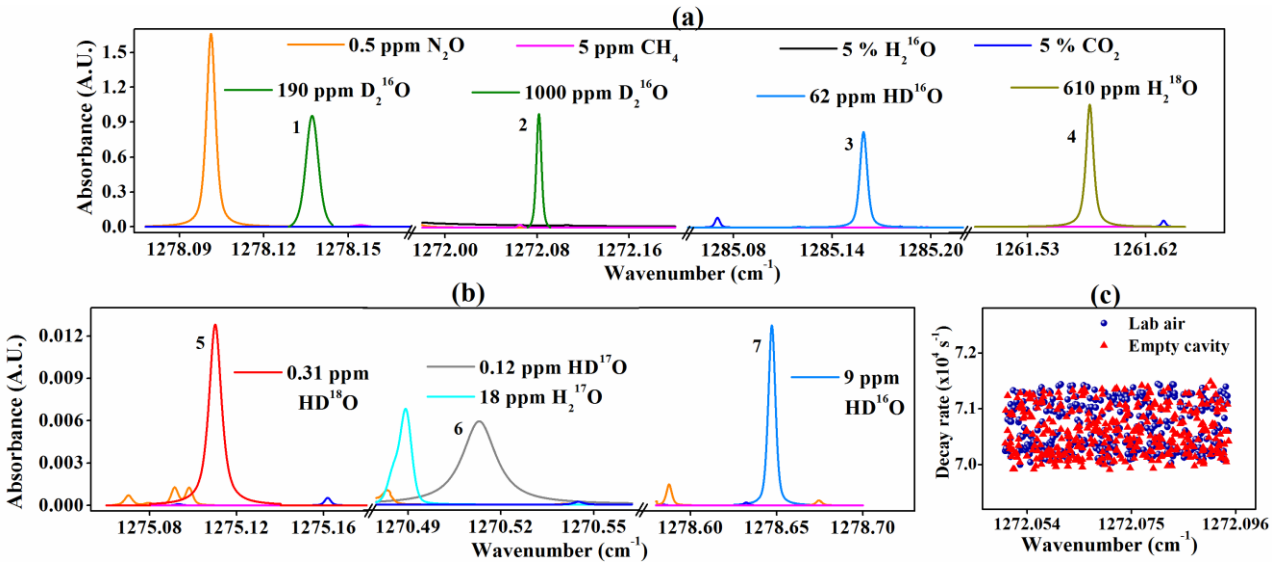

Figure 4.5 a) *and* ***b)*** *show the HITRAN simulations for regions around the spectral lines of water isotopologues illustrating the interference-free nature of these regions. The simulations were done with several trace molecules and only those are shown whose spectra were nearby. The peaks 1-7 refer to the peak numbers in Table 4.3. A.U. refers to arbitrary units.* ***c)*** *Comparison of lab air and empty cavity spectra showing the absence of water continuum effect on the spectral region for 1% water vapour[18].*

Figure 4.6 shows the comparison of the $HD^{16}O$ values obtained using the CRDS system and the WVIA. The graph shows well-matched and linearly correlated values from both the systems. It is to be noted that the pressure for the $HD^{16}O$ samples in CRDS were kept about 5 to 15 Torr whereas the concentrations were maintained in the ppmv range in accordance with the measurement range of the WVIA. Nevertheless, the minimum detection limits in CRDS system for singly deuterated isotopologues of water, $HD^{16}O$, $HD^{17}O$, $HD^{18}O$ in the gas-phase were evaluated as 16.5 ppbv, 1.8 ppbv, and 3.8 ppbv, respectively at the respective wavenumbers of 1285.1360 cm^{-1}, 1270.4994 cm^{-1} and 1275.0972 cm^{-1}, at a pressure of 25 Torr. For ^{18}O content of light water, i.e. $H_2{}^{18}O$ the detection limit was 89.1 ppbv at 1261.5643 cm^{-1} and 25 Torr pressure.

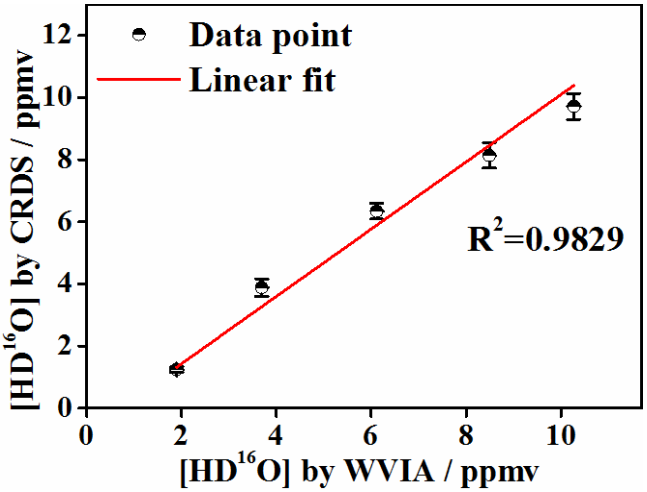

Figure 4.6 *Comparison of the $HD^{16}O$ values obtained from CRDS and WVIA systems. [$HD^{16}O$] represents the concentration of $HD^{16}O$ [18].*

Thus, the above ro-vibrational spectroscopic study of the water isotopes was performed to identify the potential spectral lines and ensure the high-sensitive and selective detection capability of the QCL-CRDS system. Using the above spectral information, we then proceeded for high-sensitive detection of these isotopes. We prepared a much diluted mixture containing 0.01% D_2O in water to assess the trace concentration of the four deuterated water isotopologues. The spectra for the measurements are shown in Figure 4.7.

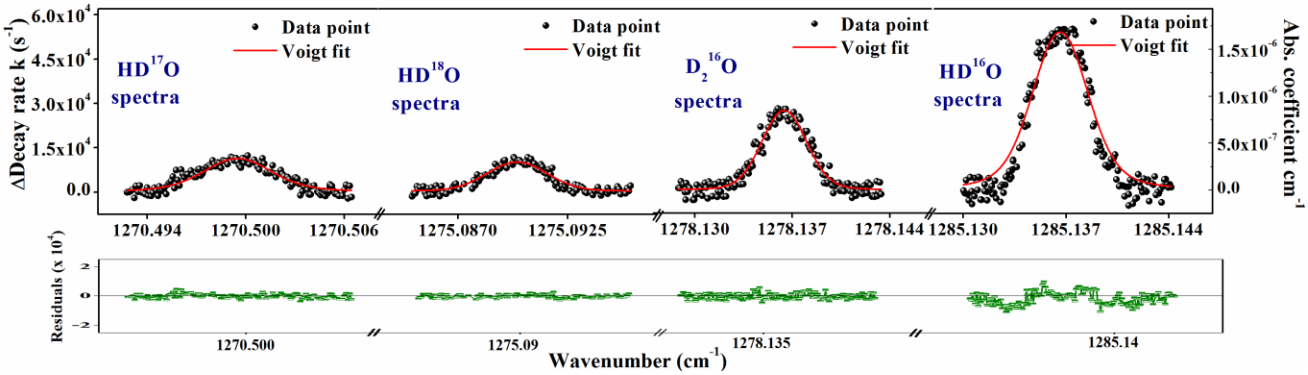

Figure 4.7 *CRDS spectra for four water isotopologues in a diluted sample of D_2O in water, in a small wavenumber range of ~ 15 cm^{-1}. The green data points below each curve show the residuals from the Voigt fit of the data points [18].*

The measurement pressures ranged from 0.1 to 8 Torr depending on the absorption cross-section of the line and the concentration of that particular isotope. For higher absorption cross-section and high concentrations, the pressure needs to be lowered to avoid saturation of the CRDS signal. The measured concentrations for $D_2{}^{16}O$, $HD^{16}O$, $HD^{18}O$ and $HD^{17}O$ in the diluted sample were 4.45 ± 0.19 ppmv, 765.50 ± 9.70 ppmv, 3.38 ± 1.40 ppmv and 279 ± 12 ppbv, respectively. This demonstrates the ability of the CRDS setup for sensing trace quantities of these deuterated isotopes in real life applications such as detecting leakage in a heavy water reactor or for detecting isotopic impurity in chemical samples.

We next exploited the spectral lines of water isotopologues to explore their isotopic fractionation (relative abundances of the isotopes) chemistry in the H-D exchange reaction between D_2O and H_2O. When D_2O and H_2O are mixed, the H and D atoms rapidly exchange to give a mixture of H_2O, HDO, and D_2O. Now, the proportion H_2O:HDO:D_2O depends on the initial mixing fractions of D_2O and H_2O and at equilibrium the components follow the relation (equation 4.4) [11]:

$$K = \frac{[HDO]^2}{[H_2O][D_2O]} \qquad (4.4)$$

Here, K is the equilibrium constant of the reaction and [H_2O], [D_2O] and [HDO] depict the concentrations of H_2O, D_2O and HDO, respectively. Solutions with different fractions of D_2O in H_2O were prepared and evaporated completely to keep the same fractionation in the vapour state. The mixtures were measured in the QCL-CRDS setup and the resultant concentration profiles of $D_2{}^{16}O$ and $HD^{16}O$ were obtained as illustrated in Figure 4.8a. For these measurements, we used the spectral line at 1272.0813 cm^{-1} (Table 4.3) for $D_2{}^{16}O$ and the line at 1285.1360 cm^{-1} for $HD^{16}O$ for their suitable cross-sections to measure the required range of concentrations. It is to be noted that the general terms 'HDO' and 'D_2O' are used when referring to the general samples containing all oxygen isotopes such as in

liquid samples while 'HD^{16}O' and 'D$_2$^{16}O' are used when referring to particular isotope which is measured using a spectral line of that isotope.

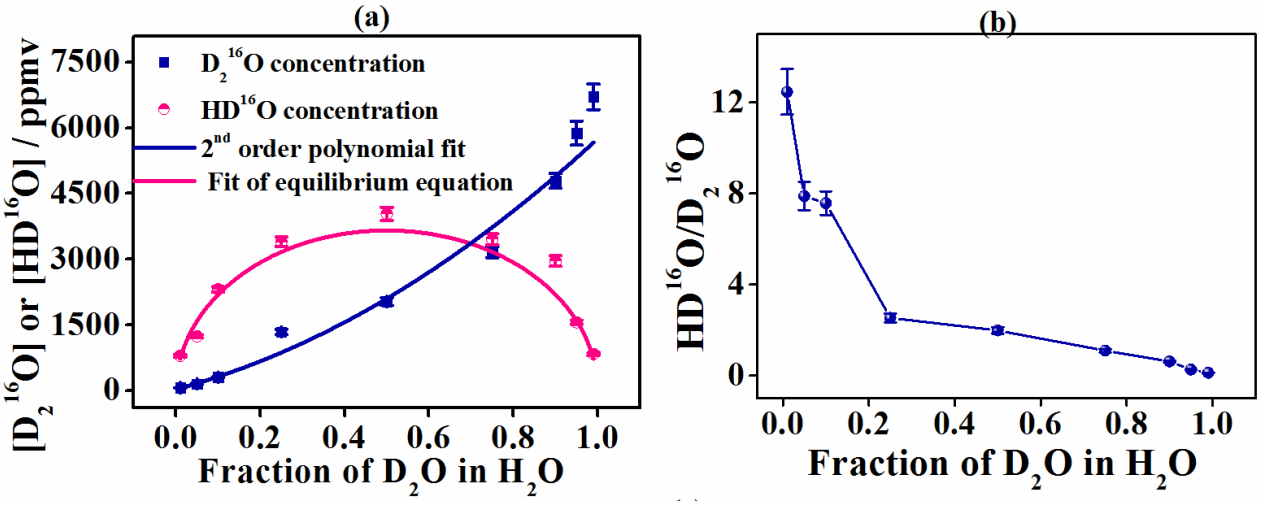

Figure 4.8 a) *Experimental concentration profiles of gas-phase D$_2$^{16}O and HD^{16}O obtained from mixing different fractions of D$_2$O in H$_2$O. The D$_2$^{16}O profile is fitted with a 2nd order polynomial while HD^{16}O profile is fitted using equation 4.4.* ***b)*** *Fractionation of HD^{16}O with respect to D$_2$^{16}O for different fractions of D$_2$O in H$_2$O [18].*

From Figure 4.8a, it is evident that with the increase in the fraction of D_2O in H_2O, the gas-phase concentration of $D_2{}^{16}O$ increases non-linearly while that of $HD^{16}O$ follows a symmetric profile about the maximum value at 1:1 fraction of D_2O:H_2O. Moreover, the experimental results validated the theoretically simulated calculations reported earlier [12], where the $D_2{}^{16}O$ profile followed a quadratic nature and the $HD^{16}O$ profile followed the equation 4.4 with the value of K=3.82 [12, 21] at 45^{0}C temperature. Hence, the experimental data in Figure 4.8a were fitted with a quadratic polynomial and with equation 4.4 for $D_2{}^{16}O$ and $HD^{16}O$, respectively. Interestingly, when the fractionation of $HD^{16}O$ concentration was calculated with respect to $D_2{}^{16}O$ concentrations (i.e. $HD^{16}O/D_2{}^{16}O$), we observed that the fractionation of $HD^{16}O$ concentration was comparatively

higher for the lesser initial proportions of D_2O in the mixture (Figure 4.8b). As the initial concentration of D_2O changed from 10% to 50%, the D_2O-to-HDO conversion efficiency decreased from about 40% to 25%. It is worthy of note that different isotopes of a molecule with different neutrons might act as distinct species with respect to the colligative properties of their mixtures [22]. The result in Figure 4.8b also indicates that D_2O and H_2O behave as distinct species where D_2O possibly prefers to form clusters so that the D_2O molecules are held together in the D_2O-H_2O mixture. Thus, for higher fractions of D_2O in H_2O, the efficiency of HDO conversion is decreased. This observation highlighted a novel aspect of the H-D exchange reaction which can be explored in future to understand the clustering between different water isotopic species.

Another significant observation from Figure 4.8a can be made. It is known that the measurement of HDO is used for detecting leak of D_2O from heavy water nuclear reactors [23], due to the formation of HDO from D_2O and H_2O (water vapour) from the surroundings. However, from Figure 4.8a it is clear that since HDO profile is symmetric, even for large values of initial D_2O, the resultant HDO value would indicate a lesser D_2O concentration, which would be erroneous.

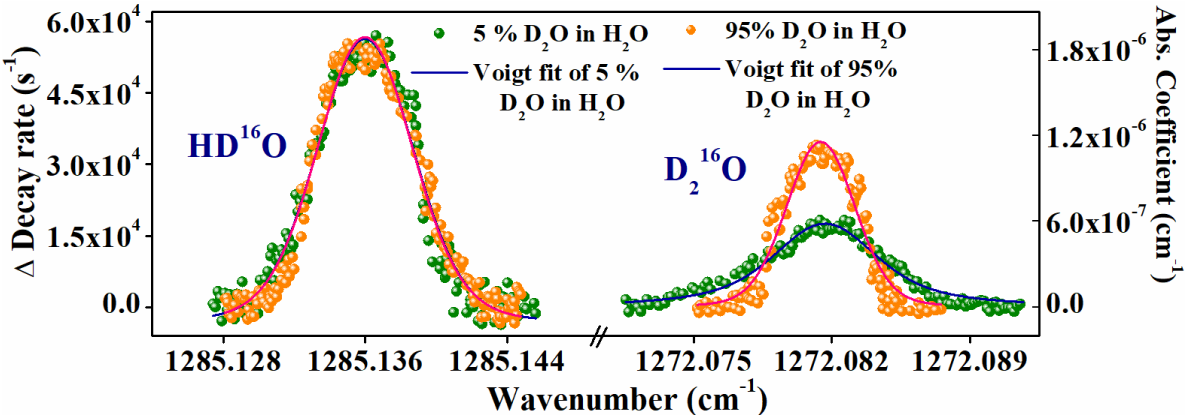

Figure 4.9 *Experimental CRDS spectra of $HD^{16}O$ and $D_2{}^{16}O$ for 5% and 95% mixture of D_2O in H_2O. The curves demonstrate the importance of measuring both the isotopes to assess the D_2O content in a sample [18].*

This scenario is illustrated using Figure 4.9 where the symmetric concentration of $HD^{16}O$ at 5% and 95% mixture (D_2O in H_2O) is indistinguishable but the $D_2{}^{16}O$ curve indicates the difference in the D_2O levels. Thus, in order to assess the accurate concentration of D_2O or the total deuterium content in a sample, it is essential to measure both the D_2O and the HDO isotopes.

Finally, we investigated the behaviour of different isotopes of oxygen in the H-D exchange reaction. As the reaction proceeds, both D_2O and H_2O in the mixture provide the ^{18}O and ^{17}O isotopes to form $HD^{18}O$ and $HD^{17}O$. It is important to note that the concentrations of $HD^{18}O$ and $HD^{17}O$ would depend on the initial abundances of the ^{18}O and ^{17}O isotopes in D_2O and H_2O (reactants). In addition, we also utilized the spectral line of $H_2{}^{18}O$ at 1261.5643 cm^{-1} for comparison with $HD^{18}O$. The concentration profiles of $HD^{18}O$, $HD^{17}O$ and $H_2{}^{18}O$ are shown in Figure 4.10. The concentration of $H_2{}^{18}O$ decreases as the fraction of H_2O decreases and the trend is similar to that expected from $H_2{}^{16}O$. On the other hand, simultaneous enhancement of the $HD^{18}O$ isotope is seen till equal ratio of D_2O:H_2O (1:1) since one of its precursor molecules i.e. $H_2{}^{18}O$ is reduced and is converted to $HD^{18}O$.

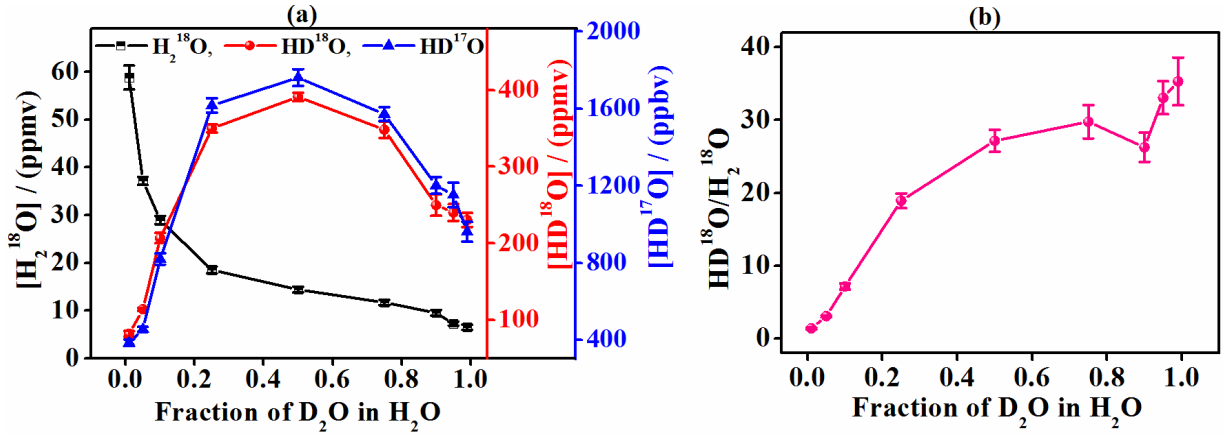

Figure 4.10 a) *Concentration profiles for different oxygen isotopologues of water. The y-axes in left and right are coloured and scaled according to the particular isotope profile.* ***b)*** *Fractionation of $HD^{18}O$ with respect to $H_2{}^{18}O$ for various fractions of D_2O in H_2O [18].*

Beyond the maximum value at 1:1 ratio, the $HD^{18}O$ levels decrease further. The trend of $HD^{17}O$ concentration profile is similar to that of $HD^{18}O$. However, in comparison to the symmetric profile of $HD^{16}O$ (Figure 4.8a), there is asymmetry in the concentration profiles of $HD^{18}O$ and $HD^{17}O$ (Figure 4.10a). This asymmetry is possibly due to the 'kinetic isotope effect (KIE)' wherein mass dependent reaction rates are utilized to process and purify D_2O from natural water. Since the masses of $HD^{18}O$ (21 amu) and $HD^{17}O$ (20 amu) are similar or greater than the mass of $D_2{}^{16}O$ (20 amu), the KIE dependent conversion is lesser for $HD^{17}O$ (20 amu) and $HD^{18}O$ (21 amu) in comparison to $HD^{16}O$ (19 amu). Hence, higher concentrations of $HD^{18}O$ and $HD^{17}O$ were possibly present in D_2O than in H_2O and introduced the asymmetry in the curve (Figure 4.10a).

Subsequently, to investigate the role of different oxygen isotopes in H-D exchange reaction, we evaluated the fractionation of $HD^{18}O$ with respect to $H_2{}^{18}O$ in the D_2O-H_2O mixture (Figure 4.10b). The trend for $HD^{18}O/H_2{}^{18}O$ was vastly different from the fractionation of $HD^{16}O/D_2{}^{16}O$, as the fraction of D_2O in H_2O increased. The profile of $HD^{18}O/H_2{}^{18}O$ increased sharply in contrast to the sharp decrease of the $HD^{16}O/D_2{}^{16}O$ profile as fraction of D_2O increased. It has been shown in an earlier study [24] that the size of the first shell local hydrogen-bonded tetrahedron is lower for $H_2{}^{18}O$ owing to lesser quantum translational motions of $H_2{}^{18}O$ as compared to $H_2{}^{16}O$ [24], which possibly promotes the H-D exchange for $H_2{}^{18}O$ and hence the enhanced formation of $HD^{18}O$. It is also speculated that since $D_2{}^{16}O$ and $H_2{}^{18}O$ have the same mass, $H_2{}^{18}O$ being in the environment of $D_2{}^{16}O$, it would facilitate the H-D exchange between $H_2{}^{18}O$ and $D_2{}^{16}O$ resulting in greater amount of $HD^{18}O$. However, the underlying mechanisms of the H-D exchange reaction involving the ^{18}O isotope can be better understood by using enriched ^{18}O isotopes in initial D_2O and H_2O mixture. Nevertheless, the current study provided a high-sensitive and isotope-selective approach to monitor deuterated water isotopologues in the gas-phase along with the investigation of the fractionation of different isotopes in the H-D exchange reaction of water.

4.5 Conclusion

In this chapter, the spectroscopic investigation of deuterated water isotopologues has been performed using a QCL-CRDS system at 7.8 μm region. The gas-phase interference-free spectral lines of $D_2{}^{16}O$ and other water isotopes such as $H_2{}^{18}O$, $HD^{16}O$, $HD^{18}O$ and $HD^{17}O$ were validated using the CRDS system. In parallel, the $HD^{16}O$ concentrations were also validated using a water vapour isotope analyzer utilizing the ICOS technique. The capability of the system was also assessed for determining trace concentrations of the water isotopes. Such trace detection can be used in real life applications to detect leaks in heavy water reactors and D_2O production facilities along with impurity detection in chemical analysis. Eventually, the fractionation chemistry of various isotopes involved in the H-D exchange reaction was examined. Although, there are gaps in understanding the governing mechanisms for the fractionation among the isotopes, more detailed studies using enriched isotopic species can be performed to get a complete picture.

4.6 References

[1] Kuang, Z., G. C. Toon, P. O. Wennberg and Y. L. Yung. "Measured HDO/H2O ratios across the tropical tropopause." *Geophysical research letters* 30, no. 7 (2003).

[2] Randel, W. J., E. Moyer, M. Park, E. Jensen, P. Bernath, K. Walker and C. Boone. "Global variations of HDO and HDO/H2O ratios in the upper troposphere and lower stratosphere derived from ACE-FTS satellite measurements." *Journal of Geophysical Research: Atmospheres* 117, no. D6 (2012).

[3] Sturm, C., Q. Zhang and D. Noone. "An introduction to stable water isotopes in climate models: benefits of forward proxy modelling for paleoclimatology." *Climate of the Past* 6, no. 1 (2010): 115-129.

[4] Webster, C. R. and P. R. Mahaffy. "Determining the local abundance of Martian methane and its' 13C/12C and D/H isotopic ratios for comparison with related gas and soil analysis on the 2011 Mars Science Laboratory (MSL) mission." *Planetary and Space Science* 59, no. 2-3 (2011): 271-283.

[5] Furuya, K., E. F. Van Dishoeck and Y. Aikawa. "Reconstructing the history of water ice formation from HDO/H_2O and D_2O/HDO ratios in protostellar cores." *Astronomy & Astrophysics 586*, (2016): A127.

[6] Robert, F., D. Gautier and B. Dubrulle. "The solar system D/H ratio: Observations and theories." In *From dust to terrestrial planets;* Benz W., Kallenbach R., Lugmair G.W. (Eds), Springer, Dordrecht, Vol. 9, (2000): 201-224.

[7] Gordon, I. E., L. S. Rothman, C. Hill, R. V. Kochanov, Y. Tan, P. F. Bernath, M. Birk *et al.* "The HITRAN2016 molecular spectroscopic database." *Journal of Quantitative Spectroscopy and Radiative Transfer* 203, (2017): 3-69.

[8] Mushtaq, A. "Producing radioisotopes in power reactors." *Journal of Radioanalytical and Nuclear Chemistry* 292, no. 2 (2011): 793-802.

[9] Kim, T. S., H. Park, K. Ko, G. Lim, Y. H. Cha, J. Han and D. Y. Jeong. "Laser-based sensor for a coolant leak detection in a nuclear reactor." *Applied Physics B* 100, no. 2 (2010): 437-442.

[10] Manning, M. C. "Use of infrared spectroscopy to monitor protein structure and stability." *Expert review of proteomics* 2, no. 5 (2005): 731-743.

[11] Libnau, F. O., A. A. Christy and O. M. Kvalheim. "Determination of the equilibrium constant and resolution of the HOD spectrum by alternating least-squares and infrared analysis." *Applied Spectroscopy* 49, no. 10 (1995): 1431-1437.

[12] Katsir, Y., Y. Shapira, Y. Mastai, R. Dimova and E. Ben-Jacob. "Entropic Effects and Slow Kinetics Revealed in Titrations of D2O−H2O Solutions with Different D/H Ratios." *The Journal of Physical Chemistry B* 114, no. 17 (2010): 5755-5763.

[13] Cappa, C. D., J. D. Smith, W. S. Drisdell, R. J. Saykally and R. C. Cohen. "Interpreting the H/D isotope fractionation of liquid water during evaporation without condensation." *The Journal of Physical Chemistry C* 111, no. 19 (2007): 7011-7020.

[14] Max, J. J. and C. Chapados. "Isotope effects in liquid water by infrared spectroscopy." *The Journal of chemical physics* 116, no. 11 (2002): 4626-4642.

[15] Bagchi, B. "Dynamics of Water: Molecular Motions and Hydrogen-Bond-Breaking Kinetics." Chapter. In *Water in Biological and Chemical Processes: From Structure and Dynamics to Function*, 27–60. Cambridge Molecular Science. Cambridge: Cambridge University Press, 2013. doi:10.1017/CBO9781139583947.005.

[16] Zarei, A., S. Klumbach and H. Keppler. "The Relative Raman Scattering Cross Sections of H2O and D2O, with Implications for In Situ Studies of Isotope Fractionation." *ACS Earth and Space Chemistry* 2, no. 9 (2018): 925-934.

[17] Maity, A., M. Pal, G. D. Banik, S. Maithani and M. Pradhan. "Cavity ring-down spectroscopy using an EC-QCL operating at 7.5 μm for direct monitoring of methane isotopes in air." *Laser Physics Letters* 14, no. 11 (2017): 115701.

[18] Maithani, S., B. Panda, A. Maity and M. Pradhan. "Gas-Phase Isotopic Fractionation Study of Singly and Doubly Deuterated Isotopologues of Water in the H–D Exchange Reaction by Cavity Ring-Down Spectroscopy." *The Journal of Physical Chemistry A* 124, no. 6 (2020): 1104-1111.

[19] Scheepmaker, R. A., C. Frankenberg, N. M. Deutscher, M. Schneider, S. Barthlott, T. Blumenstock, O. E. Garcia, F. Hase, N. Jones, E. Mahieu *et al.* "Validation of SCIAMACHY HDO/H_2O measurements using the TCCON and NDACC-MUSICA networks." *Atmospheric Measurement Techniques* 8, (2015): 1799–1818.

[20] Šimečková, M., D. Jacquemart, L. S. Rothman, R. R. Gamache and A. Goldman. "Einstein A-coefficients and statistical weights for molecular absorption transitions in

the HITRAN database." *Journal of Quantitative Spectroscopy and Radiative Transfer* 98, no. 1 (2006): 130-155

[21] Simonson, J. M. "The enthalpy of the isotope-exchange reaction: H2O + D2O = 2HDO at temperatures to 673 K and at pressures to 40 MPa." *The Journal of Chemical Thermodynamics* 22, no. 8 (1990): 739-749.

[22] Kiyosawa, K. "Freezing Point of Mixtures of $H_2{}^{16}O$ with $H_2{}^{17}O$ and Those of Aqueous CD_3CH2OH and $CH_3{}^{13}CH2OH$ Solutions." *Journal of solution chemistry* 33, no. 4 (2004): 323-328.

[23] Gupta, A., P. J. Singh, D. Y. Gaikwad, D. V. Udupa, A. Topkar and N. K. Sahoo. "Instrumentation and signal processing for the detection of heavy water using off axis–integrated cavity output spectroscopy technique." *Review of Scientific Instruments* 89, no. 2 (2018): 023110.

[24] Hart, R. T., C. J. Benmore, J. Neuefeind, S. Kohara, B. Tomberli and P. A. Egelstaff. "Temperature Dependence of Isotopic Quantum Effects in Water." *Physical review letters* 94, (2005): 047801-4.

Chapter 5

Development of an evanescent wave based cavity enhanced absorption spectroscopy (EW-CEAS) setup to study interfacial kinetics of condensed phase molecules

5.1 Introduction

Till now, the development and applications of the CEAS technique for gas-phase spectroscopy have been discussed. In this chapter, the development and application of the CEAS technique in combination with the concept of evanescent wave (EW) has been described to study molecules in the condensed phase. As described in detail in section 1.6, EW is an exponentially decaying near-field wave that is generally produced at the interface of the two media using the total internal reflection (TIR) condition. Since this wave lies in close vicinity to the surface in sub-wavelength region, it can be utilized to study surface phenomena. The extent of the EW in the second medium is expressed quantitatively as the penetration depth, as given by equation 1.18 in section 1.6. The surface sensitivity of EW can be exploited by the perturbation of the EW wherein an absorber or scatterer interacts with the EW causing the light to propagate in the second medium. Since the light is drawn from the incident beam, the change in the reflected light can be monitored for surface

sensitive detection. However, EW is not directly utilized due to the difficulty of measuring a small signal against the large background intensity fluctuations of the source laser intensity. Hence, various methods are used to enhance the detection capability of EW as described in section 1.6 before. Since the ring-down time is measured in some variants of CEAS (such as in CRDS) it makes the technique independent of the background source fluctuations. Thus, in EW-CEAS, not only the background noise is eliminated but the multi-pass nature largely increases the signal to noise ratio, which allows even minute disturbances in EW to be observed accurately. Moreover, due to the repeated generation of EW at the same position on the prism top, the spatial resolution of the technique is enhanced as compared to fibre optic based techniques and ATR spectroscopy where EW is generated at different positions.

Surface based molecular interactions are interesting to study as molecular dynamics on surfaces are different from those in a bulk medium. Applications of surface studies include investigation of thin-film behaviour [1,2], molecular adsorption, nanoparticles and self-assembled monolayers on surfaces [3,4], inspecting the efficacy of functionalized surfaces [5] and so forth. In the past few years, there has been growing need for surface based chemical sensors for environmental, biomedical and impurity sensing in everyday samples. To examine the response times of such sensors and the behaviour of molecules on surfaces, it is essential to study interfacial kinetics of molecules and develop new methodologies to analyze these phenomena.

Metal nanoparticles (NPs) would be ideal probe particles for EW-CEAS, since they possess strong plasmon resonance bands in the visible light region and their nanometre sizes would enable strong scattering in the near-field region of EW whose penetration depth extends to only a few hundred nanometres for visible light. Among the metal NPs, gold (Au) and silver (Ag) are quite frequently used in sensing biomolecules [6] as nanoparticles get coated by a layer of proteins when exposed to the

proteins and the layer is called protein-corona, which induces shifts and alterations in shape of their plasmon bands. Then again, these variations depend on the pH, ionic strength, temperature of the medium [6,7] which vary to different extents in real biosamples and are time-dependent in nature. Hence, it is essential to investigate the individual effects of these factors to understand the protein-nanoparticle interactions on surfaces.

In this chapter, the development and extensive characterization of an EW-CRDS setup have been described. The EW was generated using TIR on the top of a right-angled prism which was kept inside the optical cavity. The setup was utilized to study the surface adsorption due to the aggregation of Au and Ag nanoparticles (NPs) caused by changing the ionic strength of the solution. The aggregation of NPs was further validated by capturing the images of the surface coverage. We also illustrated a comparison between a single pass EW system and the EW-CRDS technique demonstrating the high-sensitivity of the developed system. We eventually investigated the effect of a protein-corona of urease (protein) on the aggregation of NPs. Thus, the development and utilization of the CEAS technique to study aggregation of NPs are demonstrated, which can be used for characterization of NP based sensors in the future.

5.2 Development of the EW-CRDS setup: Experimental details

The schematic diagram of the developed experimental setup [8] is shown in Figure 5.1. The laser source is a continuous wave diode laser (18040565-CNI Optoelectronics Co.) emitting at a wavelength of 643.9 ± 1.8 nm. The laser spectra and the linewidth (3.6 nm) were obtained using a spectrometer (CCS-200/M, Thorlabs) which shows a nearly single mode Gaussian profile as shown in Figure 5.2a [8]. The laser was pulsed by means of a pulse generator (TGP-110-TTi). To prevent the back reflection of light towards the laser from the optics in the system, a combination of a polarizer (LPVISE100-A, Thorlabs) and a quarter wave plate (AQWP05M-

600, Thorlabs) was used which acted as an optical isolator. The polarizer caused the incoming light to be linearly polarized while the quarter wave plate (QWP) was placed with its axis 45^0 with respect to the polarizer axis which caused the output light from it to be circularly polarized. The back reflected light from mirror M_1 would be oppositely circularly polarized (phase change of π) and hence after passing again from the QWP would be linearly polarized but at 90^0 with respect to the initial direction. Thus, it would be blocked by the polarizer from going back towards the laser. The laser light was further incident on an open, linear optical cavity composed of two high-reflectivity plano-concave mirrors (R>99.98% for 400-800 nm, 149645 Layertec, Radius of curvature = 1 m) with a right-angled prism (N-BK7, PS908L-A Thorlabs) in the centre. The prism had anti-reflection coatings on its inclined surfaces to reduce reflection losses. In this setup, the output signal was collected below the second inclined surface of the prism rather than at the conventional position after the second mirror. At this position the signal intensity was high which improved the overall signal to noise ratio in the system.

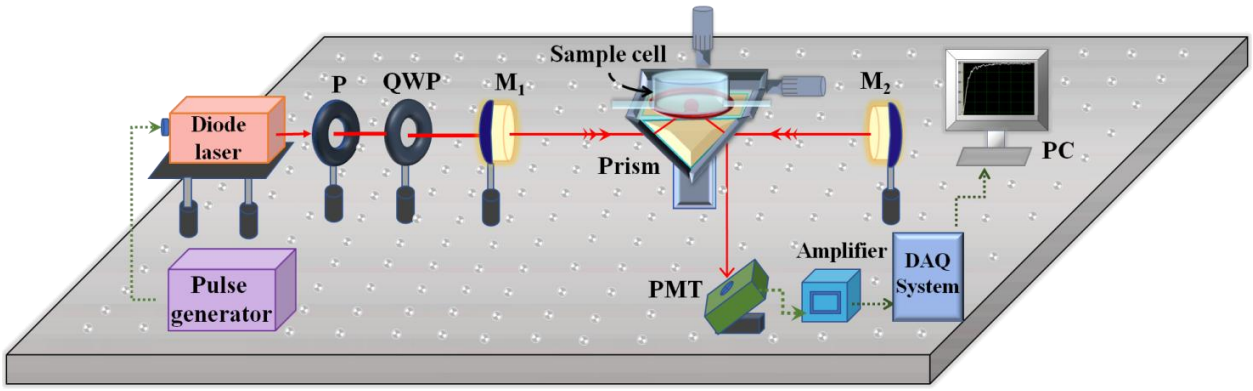

Figure 5.1 *Schematic diagram of the EW-CRDS setup. P and QWP refer to polarizer and quarter wave plate, respectively while M_1 and M_2 are the high-reflectivity mirrors. DAQ and PC refer to data acquisition and personal computer, respectively. The prism is held using a stage while a sample cell holds the liquid sample on the prism surface.*

A fast response photomultiplier tube (PMT) (R4632, Hamamatsu) with a rise time of ~ 2.2 ns was used to collect the signal and the resulting signal current was converted to an amplified voltage signal using a transimpedence amplifier (C9663, Hamamatsu). A high-speed data acquisition card (5122 PCI National Instruments, 14-bit, 100 MHz bandwidth) was used for data acquisition and a custom-written LabVIEW (Version 2015) program was utilized for data analysis.

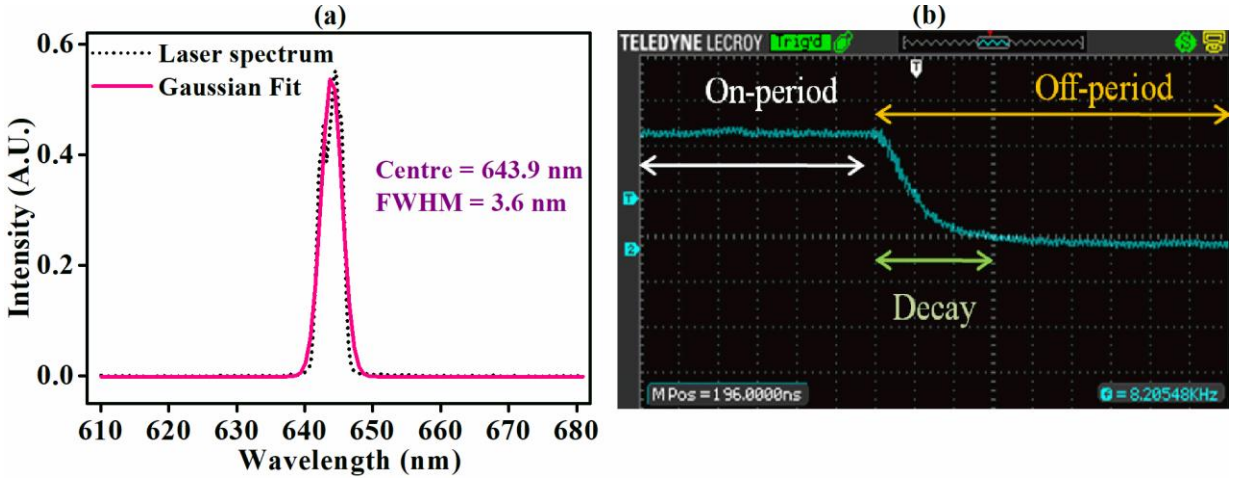

Figure 5.2 a) *Spectra of the diode laser showing the centre wavelength and the laser linewidth. The spectrum is fitted using a Gaussian function [8].* ***b)*** *An oscilloscope image of the ring-down decay from the laser pulse showing the on-period, off-period and the ring-down decay.*

Since the optical cavity was linear with the position of the right-angled prism (refractive index n ~ 1.514 at ~ 644 nm) aligned along the cavity's central axis, the incidence angle on the prism base was ~ 72.8°. This configuration satisfied the TIR condition for the present study as the critical angle for prism-water interface is ~ 61.4° and it can be utilized for higher refractive index liquids as well. With this configuration of incident angle and the incidence wavelength, the penetration depth (d_p) of the EW was ~ 180 nm at the prism-water interface.

The number of passes inside the cavity was increased due to the repeated reflections from the high-reflectivity mirrors and the build-up of resonance during the on-period of the laser pulse. Since the laser was pulsed, the ring-down was achieved by observing the fall time of the laser pulse during the off-period (~ 125 μs). An oscilloscope picture of a typical ring-down decay from pulsed laser is shown in Figure 5.2b. It is important to note that the specifications of the laser pulse need to be selected such that the fall time of the laser pulse itself (few nanoseconds, here < 4 ns) should be far lesser than the decay time of light in the cavity. Similarly, the response time of the PMT and the amplifier were also selected to be < 3 ns so that the inherent instrumental response times should not interfere with the ring-down decay time.

Since the measurements in the current study were made in the solution phase, the baseline ring-down time (τ_0) was calculated for water on top of the prism. To assess the effect of cavity length (L) on the baseline ring-down time (τ_0), we varied the length L and monitored the resultant τ_0. The variation is shown in Figure 5.3a along with the corresponding number of cavity modes (N) inside a single laser mode. As the cavity length increases, the FSR (c/2L) between the cavity modes reduces which allows more cavity modes (N) into a single laser mode and hence increases the mode-coupling and the ring-down time. N was calculated by dividing the FWHM of the laser (~2.6 x 10^{12} Hz) by the free spectral range (FSR=c/2L) for different values of L. Since several thousand modes were covered by the laser linewidth, additional mode matching components were not required. It is evident from the trend in Figure 5.3a that τ_0 increases with the cavity length and therefore for the current setup we created an optical cavity of ~ 120 cm length to obtain a high value of τ_0. For this particular length, the value of N was ~ 20810 while the g-parameters were $g_1=g_2=-0.2$ (symmetric cavity) and their product $g_1.g_2=0.04$ showed the cavity to be stable. Moreover, the linearity between L and τ_0 also shows that the prism and the open environment do not induce much non-linearity in this relation.

Furthermore, the effect of the laser pulse parameters such as modulation frequency (Figure 5.3b) and duty cycle (Figure 5.3c) were also investigated.

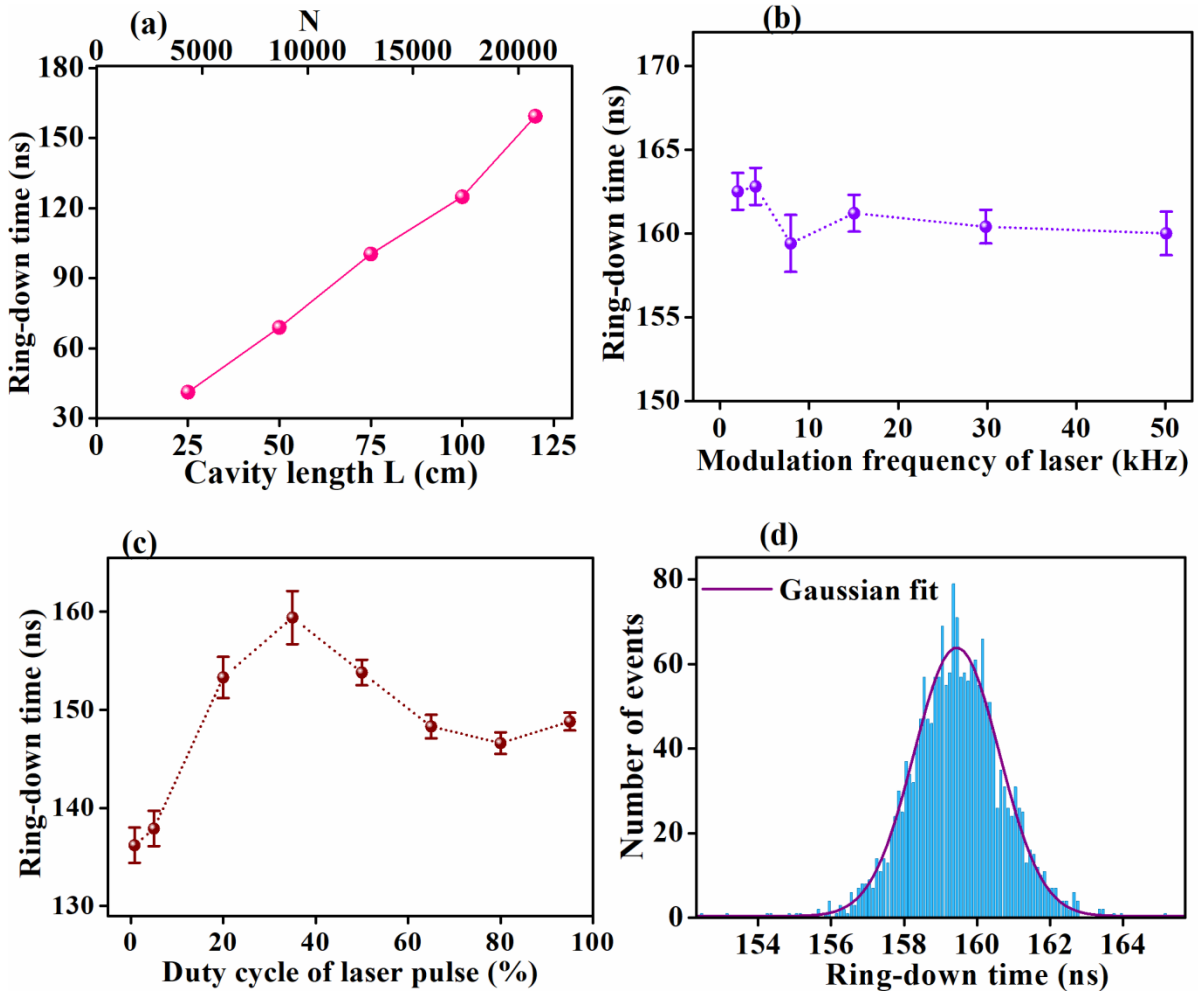

Figure 5.3 a) *Profile of ring-down time (τ_0) with variation in cavity length and the corresponding number of cavity modes covered by a single laser mode (N).* ***b)*** *and* ***c)*** *depict the change in τ_0 with modulation frequency and duty cycle of the pulse, respectively.* ***d)*** *Distribution of the baseline ring-down time where the data followed a Gaussian profile [8].*

It is to note that the duty cycle is the part of the time period when the pulse is in on-state. It was observed that τ_0 did not change considerably with the modulation frequency (inverse of the time period) of the laser pulse. Since τ_0 is in a range of ~ 140-160 ns, the total time period of the pulse ~ 1 ms to 20 µs (modulation frequency of ~ 1 kHz to 50 kHz) is far greater than τ_0 and hence does not significantly affect its value. However, τ_0 varies quite interestingly with change in the duty cycle as it increases till ~ 40% but decreases beyond that. When duty cycle is less (< 40%), the laser output power is also low which decreases the value of τ_0 while for greater duty cycles >40%, the pulse gets lower off-period time which seems to adversely impact τ_0. Thus, we selected the optimized pulse parameters of 4 kHz modulation frequency and a 50% duty cycle (~ 53 mW of laser power) to obtain an optimum τ_0 and low standard deviation.

Using the optimized parameters for the setup, the distribution of τ_0 was observed for 15 minutes as shown in Figure 5.3d. The data followed a uniform Gaussian distribution which indicated that there were no considerable drifts in τ_0 and therefore the setup can be used for investigating molecular kinetics. From Figure 5.3d the baseline ring-down time τ_0 (mean value) of 159.4 ns was attained with a standard deviation of 0.8% on averaging 80 ring-down events. The corresponding optical path length was ~ 47 m which indicated ~ 40 trips of light between the mirrors. Further, the stability of the cavity was assessed using Allan variance [9] analysis as given in Figure 5.4. The Allan variance has been described earlier in section 2.7.2. Initially, with successive data averaging with time, the Allan variance decreased linearly indicating the presence of white noise. Further on, the variance increased owing to various fluctuations in the system. An optimum integration time of ~308 s was obtained for the current setup.

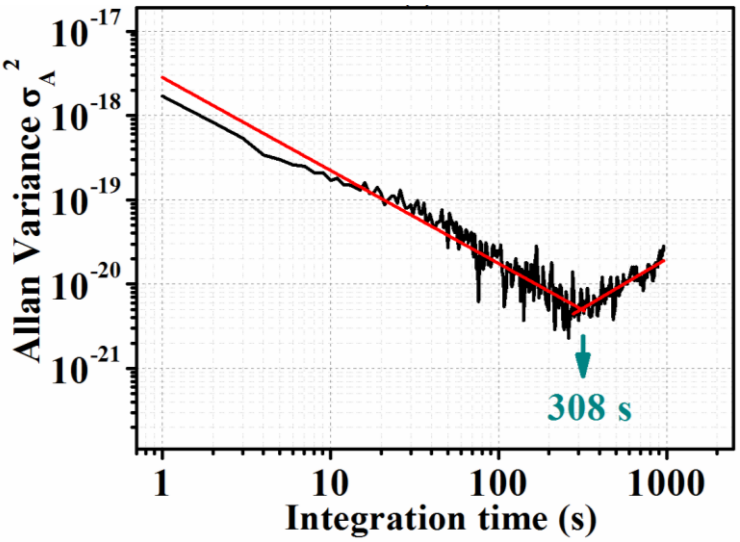

Figure 5.4 *Analysis of the baseline ring-down time using Allan variance technique [8].*

For the current system, the minimum absorption coefficient α_{min} (equation 2.8) was evaluated to be 1.67 x 10^{-6} cm^{-1} while the noise equivalent absorption (NEA) (equation 2.9) of 3.34 x 10^{-7} cm^{-1} $Hz^{-1/2}$ was observed at a data acquisition rate of 50 Hz after averaging. The absorbance or extinction (A) due to a sample can be evaluated by using the ring-down time with the sample (τ) and the baseline ring-down time (τ_0) using equation 5.1 [10].

$$A = \frac{L}{2.303c}\left(\frac{1}{\tau} - \frac{1}{\tau_0}\right) \qquad (5.1)$$

Here, L and c are the cavity length and the speed of light, respectively.

5.3 Material and methods

40 nm diameter Au (741981) and 40 nm diameter Ag (795968) NPs (nanospheres), bought from Sigma Aldrich, were used in the current study. The Au NPs were citrate-capped, while Ag-40 nm were stabilized using PVP (polyvinylpyrrolidone) and dispersed in water. The manufacturer supplied concentrations of the NPs are given in Table 5.1. Urease enzyme (Jack-Bean, U1500) was purchased from Sigma Aldrich and Sodium Chloride (NaCl) (1.93606.0521) was procured from Merck. Millipore water was used as the baseline solvent and also for dilution of other solutions. The prepared solution of urease enzyme was filtered using a 0.22 µm syringe filter unit (Millex-GP, Merck) before use. To clean the prism before and after every experiment, water, ethanol and acetone were applied by drop and drag method. The prism was regarded as clean when the baseline ring-down time was restored. The solutions were injected on a glass sample cell placed on top of the prism. All the experiments were conducted at room temperature.

5.4 Results and discussion

Firstly, we assessed the capability of the developed EW-CRDS setup for the measurement of interfacial dynamics by observing the time-dependent surface extinction of solutions of 40 nm Au and 40 nm Ag NPs aggregated in presence of NaCl. NPs are generally capped with small, charged molecules to stabilize them and prevent the NPs from attaching together and aggregating. But, changes in the environment of NPs can cause destabilization of the NPs. For instance, in a solution of NPs, when the ionic strength is increased by adding salt, the NPs start destabilizing and aggregating, beyond a certain concentration of salt [11]. Consequently, we monitored the aggregation kinetics of the Au NPs using NaCl for different concentrations of Au NPs (Figure 5.5a) and NaCl (Figure 5.5b). From Figure 5.5a, it is clear that only bare Au NP solution does not cause any

change in extinction. In other words, Au NPs did not adsorb on the prism surface so the extinction does not change with time. This is likely due to the electrostatic repulsion between the negatively charged Si-OH surface of the prism and the citrate (negatively charged) capped Au NPs.

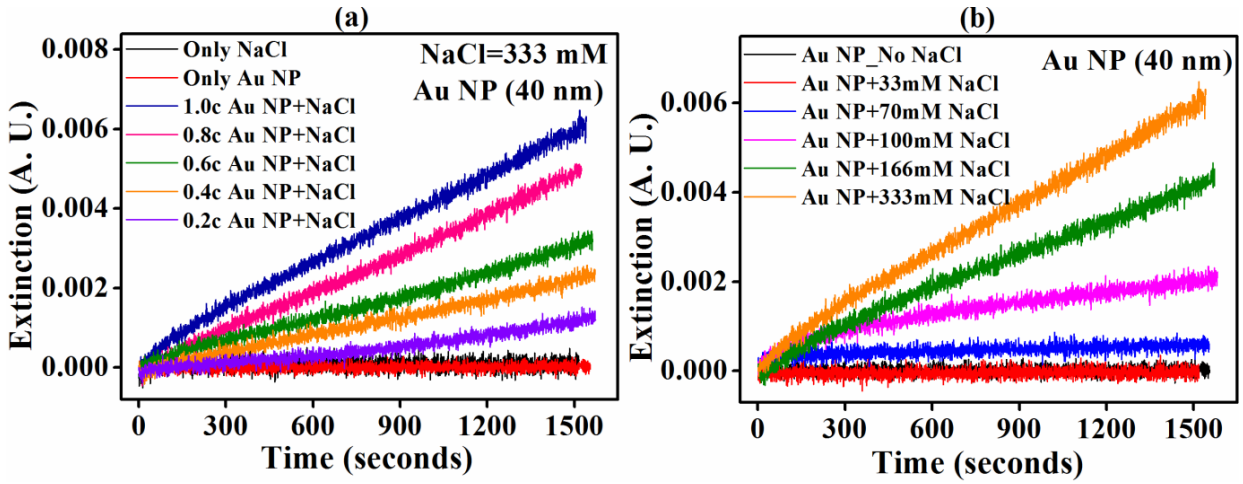

Figure 5.5 a) *Surface extinction kinetics for various concentrations of Au NPs aggregated using NaCl. Here 'c=119.5 picomolar (pM)' is the concentration of Au NPs given in Table 5.1.* ***b)*** *Variation of NaCl concentration on the extinction kinetics of Au NPs on the prism surface [8].*

Moreover, no change in extinction was seen for only NaCl solution even for the highest concentration of NaCl used in the study, signifying that these bulk solutions individually have no considerable effect on the prism surface and so the interfacial extinction does not change even after several minutes. In contrast, with the addition of NaCl to the Au NPs, aggregation of the NPs occurs and the aggregates adsorb on the prism surface which increases the surface extinction. It shows that aggregation increases the affinity of the NPs towards the surface. It was also observed that the rates of change in extinction were linear with an increase in the NP concentrations (Figure 5.6). Thus, higher concentration of NPs increases the aggregation rate which in turn increases the rate of the observed extinction. Moreover, higher formation of aggregates would also enable more

sedimentation on the prism surface. Table 5.1 provides a list of the values of the extinction rates and the corresponding concentrations of NPs.

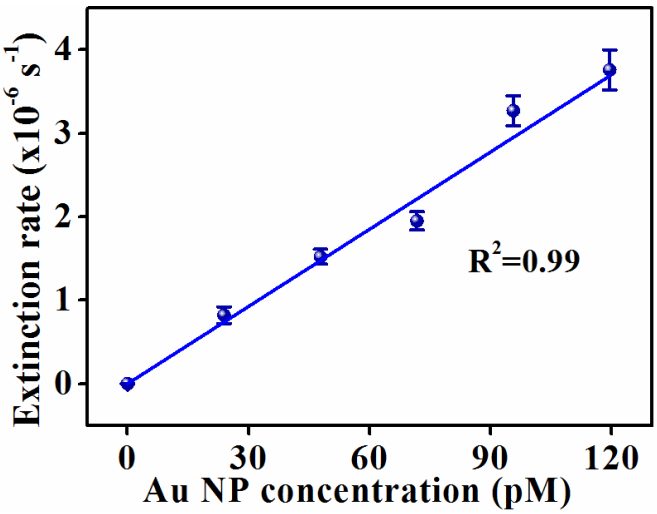

Figure 5.6 *Variation of the surface extinction rate with change in the Au NP concentration. The data has been fitted using a linear regression analysis [8].*

It was worthy of note that a part of the results mentioned above were in contradiction to another work by Fisk *et al.* [12] wherein the adsorption of bare (only) Au NPs on the prism surface was shown, whereas we observed no surface adsorption of the bare Au NPs. This contradiction may have resulted from the difference in the experimental conditions in the two studies. In the work of Fisk *et al.* [12] the sample solutions were continuously flowed on the prism surface which might have enhanced the adsorption probability of the NPs, especially on the crevices and rough surface features on the prism. On the other hand, we employed static solutions on the prism surface. Furthermore, we utilized commercial NPs for the experiment while they synthesized the Au NPs which could have caused different surface charges on the NPs and therefore the different adsorption characteristics on the prism surface.

Table 5.1 *Surface extinction rates due to the aggregated Au and Ag NPs and their corresponding concentrations [8].*

S. No.	Nanoparticle Sample	Nanoparticle Concentration (picomolar, pM)	NaCl Concentration (millimolar, mM)	Extinction rate (s^{-1})
1	Au – 40 nm	23.9	333	$(0.82 \pm 0.10) \times 10^{-6}$
2	Au – 40 nm	47.8	333	$(1.52 \pm 0.09) \times 10^{-6}$
3	Au – 40 nm	71.7	333	$(1.95 \pm 0.11) \times 10^{-6}$
4	Au – 40 nm	95.6	333	$(3.27 \pm 0.30) \times 10^{-6}$
5	Au – 40 nm	119.5	333	$(3.76 \pm 0.24) \times 10^{-6}$
6	Au – 40 nm	119.5	166	$(2.65 \pm 0.16) \times 10^{-6}$
7	Au – 40 nm	119.5	100	$(0.97 \pm 0.11) \times 10^{-6}$
8	Au – 40 nm	119.5	70	$(0.19 \pm 0.06) \times 10^{-6}$
9	Au – 40 nm	119.5	33	$(0.03 \pm 0.01) \times 10^{-6}$
10	Ag – 40 nm	2.36	333	$(0.42 \pm 0.03) \times 10^{-6}$
11	Ag – 40 nm	7.08	333	$(0.79 \pm 0.04) \times 10^{-6}$
12	Ag – 40 nm	9.44	333	$(0.85 \pm 0.07) \times 10^{-6}$
13	Ag – 40 nm	11.8	333	$(0.90 \pm 0.08) \times 10^{-6}$

Similarly, the salt (NaCl)-induced aggregation kinetics for the 40 nm Ag NPs was also observed (Figure 5.7a). Here also, no adsorption or change in extinction was observed for bare Ag NPs which was most likely due to the repulsion between the negative charge on the PVP-capped Ag NPs and the Si-OH of the prism surface. On addition of salt, the extinction linearly increases with time while the extinction rates are not linear with increase in the concentration of Ag NPs (Figure 5.7b).

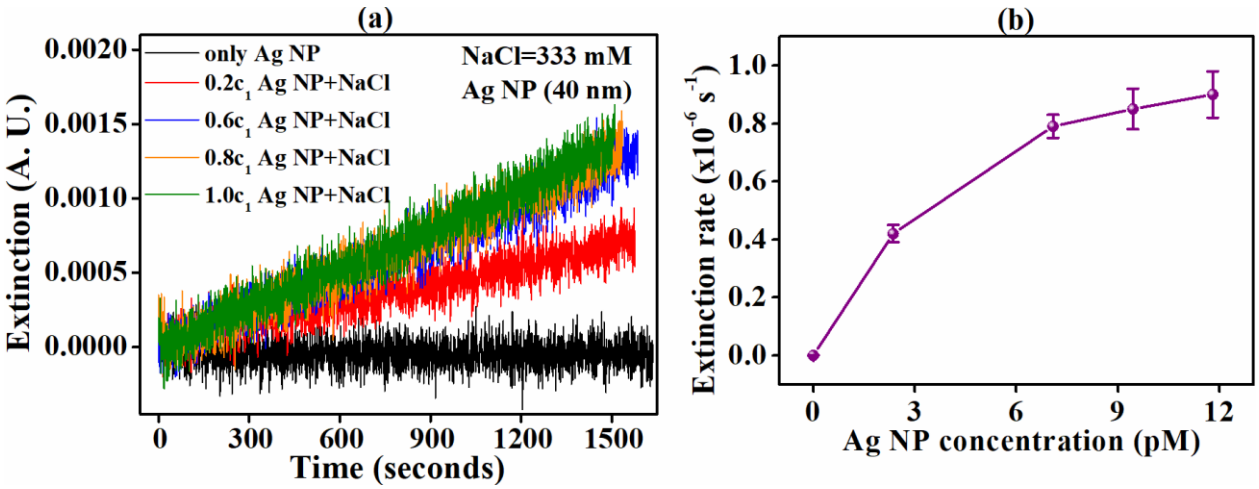

Figure 5.7 a) *Surface extinction kinetics for salt-induced aggregation of Ag NPs. Here 'c_1=11.8 pM' is the concentration of Ag NPs provided in Table 5.1.* ***b)*** *Variation in the extinction rates with increase in the concentration of Ag NPs which shows a non-linear relation between the two [8].*

It was speculated that since Ag NPs do not have strong absorption in our working region around 644 nm (the plasmon band of Ag NPs is around 400 nm), there is not much increase in extinction as the concentration of NPs is increased and the extinction might be dominated by the scattering of Ag NPs alone [13]. In contrast, Au NPs possess stronger absorption and scattering near this region (its plasmon band being near 540 nm) which might attribute to its linear behaviour in extinction rate (Figure 5.6). Thus, from the above results the capability of the EW-CRDS system to probe interfacial kinetics was demonstrated.

We further aimed to investigate the effect of urease enzyme (protein) on the salt-induced aggregation kinetics of the NPs. It is well known that on exposure to proteins, the NPs are covered by a protein layer which is termed as 'protein corona' and this leads to variations in the properties of NPs such as their plasmon bands [7]. The changes in the plasmonic properties due to protein corona are utilized in NP-based biomolecule sensors. Therefore, we wanted to explore the changes in the surface behaviour of NPs due to the protein corona. Moreover, the urease enzyme was the first enzyme to be crystallized [14] and is found in various plants, microbes, fungi and bacteria. It plays a significant role in the environment [15] and is linked to gastrointestinal diseases such as stomach ulcer and stomach cancer [16, 17]. Also, it is easily available from a plant based source (Jack-urease) and so it was used as the model enzyme in our work.

To prepare the protein-corona, the NPs were incubated with 4.5 μM urease for 24 hours at 4^0C temperature. Salt was added to the solutions with protein-corona and the aggregation kinetics were monitored (Figure 5.8a). It was observed that solely urease solution with NaCl has no affinity towards the prism surface, thus no variation in the extinction takes place. In contrast, a solution of the urease-corona with Au NPs even without the salt showed increase in the extinction and was saturated quickly, thus indicating a slight affinity induced by the urease-corona on the Au NPs. This result agrees with observations in other works where it has been shown that NPs aggregate to a certain extent on exposure to proteins [18] and the proteins also form few aggregates themselves in presence of NPs [19]. Thus, such aggregates might adsorb on the prism to give a slight rise in the extinction. However, in our experiments, the protein solution was filtered prior to use (using 0.22 μm filter) so that the protein aggregates were not present initially in the solution, but might have formed by interaction with NPs. Conversely, the extinction for NaCl-added (333 mM) urease-corona of Au NPs is greater in comparison to without NaCl case but is quite lower than due to the NaCl-induced aggregation of bare Au NPs. This shows that the protein-corona layer around the Au NPs shields or

reduces the access of NaCl to the NPs, thus causing a lower extinction in comparison to bare Au NPs.

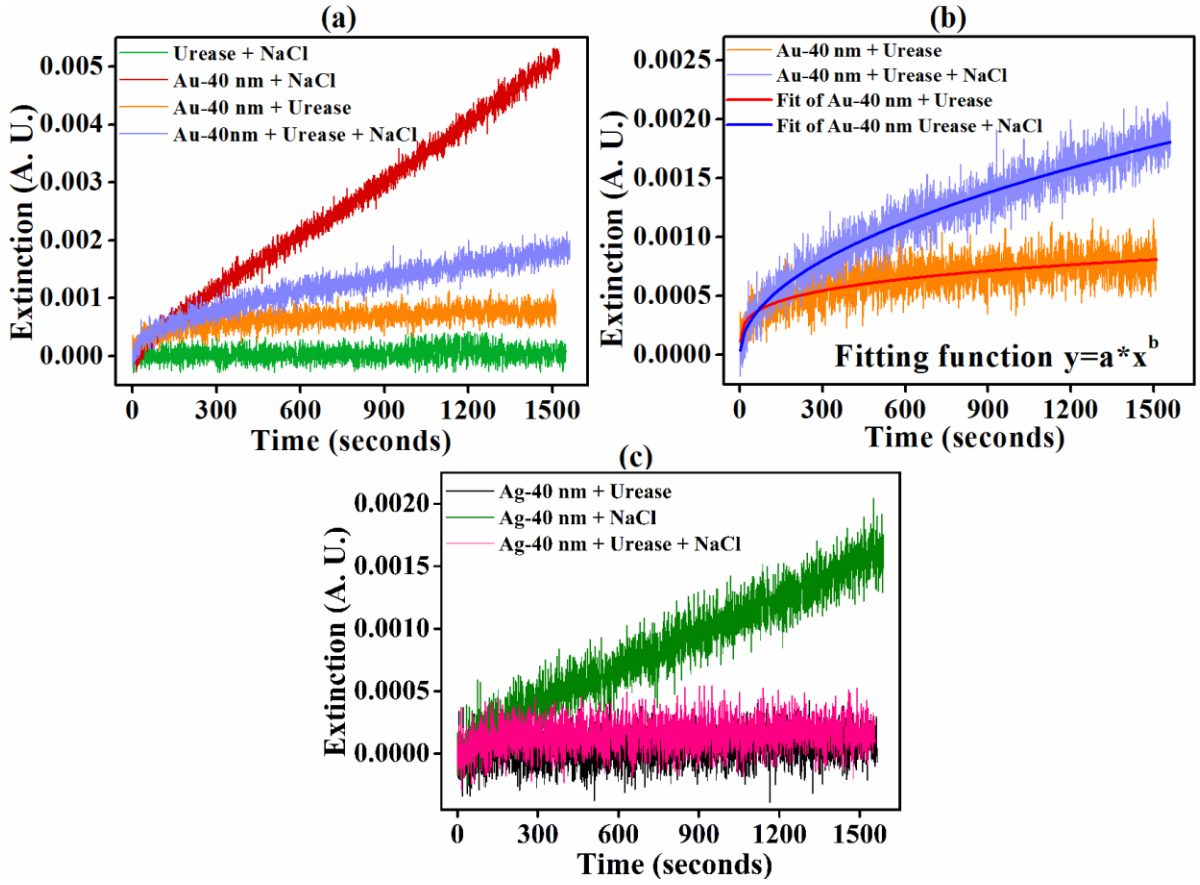

Figure 5.8 a) *Surface extinction for salt-induced aggregation of urease-corona of Au NPs. The graph shows a comparison for aggregation with and without the protein-corona on Au NPs [8].* ***b)*** *Fitting of the extinction data for urease-corona of Au NPs, in the absence and presence of NaCl.* ***c)*** *NaCl-induced aggregation for urease-corona of Ag NPs.*

To understand this behaviour further, we fitted the extinction data for urease-corona of Au NPs with power law functions (Figure 5.8b) and obtained the values of exponents of b=0.49 and b=0.24 for urease-corona in presence and absence of NaCl, respectively. Interestingly, the exponent

index of 0.49 is near to the value of attachment efficiency α ~ 0.53 for diffusion limited cluster aggregation (DLCA) of gold colloids [20]. In DLCA, the average size of the aggregated cluster R_{avg} is proportional to t^{α}, where 't' is the cluster formation time and 'α' shows how fast the aggregation takes place. DLCA is also characterized by open type cluster formation with low fractal dimensions [20]. Hence, on comparing the current results for protein-corona of Au NPs and the DLCA of gold colloids, it can be supposed that the urease-corona of Au NPs follow the DLCA aggregation kinetics. However, salt added urease-corona of Ag NPs showed negligible change in extinction (Figure 5.8c) which was lesser than that of bare Ag NPs with salt. This also denotes the restricted access of salt to the Ag NPs due to the urease-corona. Therefore, by monitoring the surface extinction using the EW-CRDS system, we examined the salt-induced aggregation kinetics of Au and Ag NPs and their respective behaviour with the protein-corona of urease enzyme. It is supposed that such studies would assist in the characterization of surface based biosensors.

To compare the performance of the present setup with a single pass EW based system, we measured the salt-induced aggregation of Au NPs in both the systems. In the single pass EW system, no high-reflectivity mirrors were used and the light was incident directly on the prism to generate the EW and the output reflected intensity was monitored using the PMT. The comparison for both the arrangements is shown in Figure 5.9. It is observed that the single pass EW system was not able to measure the kinetics due to insufficient signal to noise ratio while the surface kinetics can be sensitively monitored using the EW-CRDS technique.

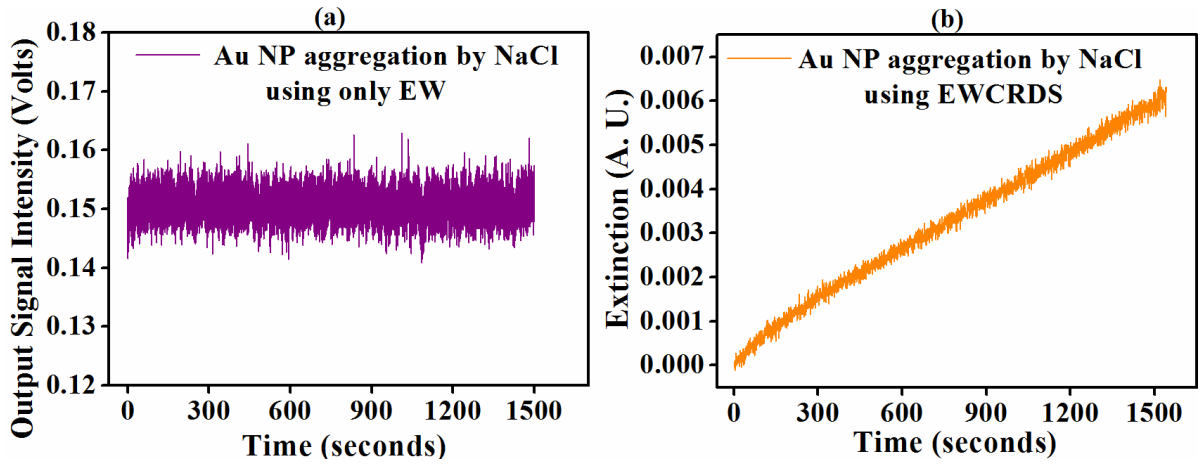

Figure 5.9 a) *and* ***b)*** *provide a comparison of single pass EW and EW-CRDS setups, respectively, in monitoring the salt-induced aggregation of Au NPs [8]. A. U. depicts arbitrary units.*

Eventually, we observed the progress of the surface adsorption for the NP aggregates by capturing digital images of the prism surface at various time intervals (Figure 5.10). The images show the scattered light due to the interaction of the NP aggregates with the EW. The scattered light intensity was found to increase with time as the aggregates formed multiple layers on the prism surface. Although this was a qualitative approach to observe the surface adsorption, high-resolution imaging techniques along with imaging detection can be utilized to monitor such kinetics quantitatively.

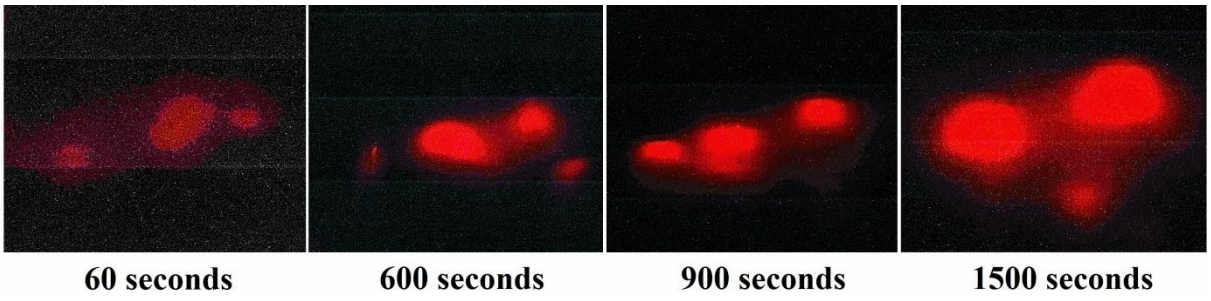

Figure 5.10 *Images of the prism surface for various time intervals as the salt-induced aggregation of the Au NPs progresses. The images illustrate the data provided in Figure 5.9b [8].*

5.5 Conclusion

In this chapter, the development of an EW based CRDS setup was described along with detailed characterization of the setup parameters. This simple and high-sensitive system was used for direct monitoring of condensed phase molecules wherein the surface kinetics behaviour of Au and Ag NPs, aggregated using salt, were observed. The system was further utilized to study the effect of protein-corona of urease enzyme on the NPs. The study helped to provide an estimation of surface adsorption of such aggregates which can be further applied to characterize surface based sensors. We also used an alternative approach of preliminary surface imaging to demonstrate the prospect of observing such phenomena through imaging techniques.

5.6 References

[1] Serghei, A., M. Tress and F. Kremer. "The glass transition of thin polymer films in relation to the interfacial dynamics." *The Journal of chemical physics* 131, no. 15 (2009): 154904.

[2] Hannon, T. E., S. Chah and R. N. Zare. "Evanescent-wave cavity ring-down investigation of polymer/solvent interactions." *The Journal of Physical Chemistry B,* 109, no. 15 (2005): 7435-7442.

[3] Mazurenka, M., S. M. Hamilton, P. R. Unwin and S. R. Mackenzie. "In-situ measurement of colloidal gold adsorption on functionalized silica surfaces." *The Journal of Physical Chemistry C* 112, no. 16 (2008): 6462-6468.

[4] Olivier, A., F. Meyer, J. -M. Raquez, P. Damman and P. Dubois. "Surface-initiated controlled polymerization as a convenient method for designing functional polymer brushes: From self-assembled monolayers to patterned surfaces." *Progress in polymer science* 37, no. 1 (2012): 157-181.

[5] Sui, G., J. Wang, C. C. Lee, W. Lu, S. P. Lee, J. V. Leyton, A. M. Wu and H. R. Tseng. "Solution-phase surface modification in intact poly (dimethylsiloxane) microfluidic channels." *Analytical chemistry* 78, no. 15 (2006): 5543-5551.

[6] Doria, G., J. Conde, B. Veigas, L. Giestas, C. Almeida, M. Assunção, J. Rosa and P. V. Baptista. "Noble metal nanoparticles for biosensing applications." *Sensors* 12, no. 2 (2012): 1657-1687.

[7] Rahman, M., S. Laurent, N. Tawil, L. Yahia and M. Mahmoudi. "Nanoparticle and protein corona." In *Protein-nanoparticle interactions*, pp. 21-44. Springer, Berlin, Heidelberg, (2013).

[8] Maithani, S., A. Maity and M. Pradhan. "A prototype evanescent wave-coupled cavity ring-down spectrometer for probing real-time aggregation kinetics of gold and silver nanoparticles." *Analytical Chemistry* 92, no. 5 (2020): 3998-4005.

[9] Werle, P., R. Mucke and F. Slemr. "The limits of signal averaging in atmospheric trace-gas monitoring by tunable diode-laser absorption spectroscopy (TDLAS)." *Applied Physics B* 57, (1993): 131-139.

[10] Martin, W. B., S. B. Mirov, D. V. Martyshkin, R. Venugopalan and A. M. Shaw. "Hemoglobin adsorption isotherm at the silica-water interface with evanescent wave cavity ring-down spectroscopy." *Journal of biomedical optics* 10, no. 2 (2005): 024025.

[11] Trinh, L. T. T., A. L. Kjøniksen, K. Zhu, K. D. Knudsen, S. Volden, W. R. Glomm and B. Nyström. "Slow salt-induced aggregation of citrate-covered silver particles in aqueous solutions of cellulose derivatives." *Colloid and Polymer Science* 287, no. 12 (2009): 1391.

[12] Fisk, J. D., M. Rooth and A. M. Shaw. "Gold Nanoparticle Adsorption and Aggregation Kinetics at the Silica− Water Interface." *The Journal of Physical Chemistry C* 111, no. 6 (2007)**:** 2588-2594.

[13] Solati, E. and D. Dorranian. "Comparison between silver and gold nanoparticles prepared by pulsed laser ablation in distilled water." *Journal of Cluster Science* 26, no. 3 (2015): 727-742.

[14] Sumner, J. B. "The isolation and crystallization of the enzyme urease." *Journal of Biological Chemistry* 69, (1926): 435-441.

[15] Mobley, H. L. and R. P. Hausinger. "Microbial ureases: significance, regulation, and molecular characterization." *Microbiology and Molecular Biology Reviews* 53, no. 1 (1989)**:** 85-108.

[16] Maity, A., M. Pal, S. Maithani, B. Ghosh, S. Chaudhuri and M. Pradhan. "Molecular hydrogen in human breath: a new strategy for selectively diagnosing peptic ulcer disease, non-ulcerous dyspepsia and *Helicobacter pylori* infection." *Journal of Breath research* 10, no. 3 (2016): 036007

[17] Qin, Y. and J. M. S. Cabral. "Kinetic studies of the urease-catalyzed hydrolysis of urea in a buffer-free system." *Applied biochemistry and biotechnology* 49, no. 3 (1994): 217-240.

[18] Lacerda, S. H. De Paoli., J. J. Park, C. Meuse, D. Pristinski, M. L. Becker, A. Karim and J. F. Douglas. "Interaction of gold nanoparticles with common human blood proteins." *ACS Nano* 4, no. 1 (2009)**:** 365-379.

[19] Zhang, D., O. Neumann, H. Wang, V. M. Yuwono, A. Barhoumi, M. Perham, J. D. Hartgerink, P. Wittung-Stafshede and N. J. Halas. "Gold nanoparticles can induce the formation of protein-based aggregates at physiological pH." *Nano Letters* 9, no. 2 (2009)**:** 666-671.

[20] Lin, M. Y., H. M. Lindsay, D. A. Weitz, R. C. Ball, R. Klein and P. Meakin. "Universality in colloid aggregation." *Nature* 339, no. 6223 (1989): 360.

Chapter 6

Investigation of isotope-selective activation of urease enzyme using off-axis cavity enhanced absorption spectroscopy

6.1 Introduction

In this chapter, a different type of application of the CEAS technique will be discussed. Here, the isotope-selectivity of an enzyme (urease) towards gaseous carbon-dioxide (CO_2) molecule is explored. Urease is a dinuclear nickel (II) containing metalloenzyme [1] which was the first enzyme to be isolated in crystalline form [2]. Urease is found in soil microbes and is secreted by various bacteria, fungi, pathogens and so on. Not only it affects the nitrogen transformations in the environment [3] but the urease activity of certain pathogens also helps in the diagnosis of diseases caused by them [4]. For instance, the *Helicobacter Pylori (H. Pylori)* bacteria which causes peptic ulcer and stomach cancer in humans, secretes the urease enzyme whose activity is utilized to diagnose the presence of bacteria in the stomach. Moreover, urease is well known for its specific action on urea to hydrolyse it into ammonium carbamate [$H_2NCO_2NH_4$] which rapidly gets converted to give carbon dioxide and ammonia as the final products (Equation 6.1).

$$\underset{\text{Urea}}{H_2N-CO-NH_2} + H_2O \xrightarrow{\text{Urease}} CO_2 + 2NH_3 \qquad (6.1)$$

As an assay, urease is frequently utilized for the determination of urea in biological fluids [4] and in several other environments. Considering the relevance and utility of the urease mediated urea hydrolysis, many works have been done to study the reaction kinetics [5], action of buffers [6], effect of temperature [7], isotope effect [8,9] and so on. However, the mechanism of urease activation and the aspects of the urea hydrolysis reaction from the viewpoint of isotopic variation have not been completely understood. Furthermore, it was shown in a past study [10] that urease is activated by dissolved carbon dioxide (d-CO_2) which has a potential link to the bi-nickel metal centres in urease and also plays an active role in its catalysis mechanism [11]. Thus, CO_2 being both the product of the reaction and the activator of the catalyst, makes the overall mechanism more complex. To separate out the roles of CO_2 molecule as an activator and the product, ^{13}C-isotopic enrichments of the carbon atom in both urea and CO_2 were utilized in the current study. Also, the effect of isotopic variations of the substrate urea on the urease activity was not explored earlier. This study additionally provided the opportunity to explore the extent of possible selectivity of the urease enzyme, if any, towards the CO_2 isotopes involved.

Therefore, in the current study, the response of the urease activity in an isotopically enriched CO_2 environment was investigated. The measurement of gaseous CO_2 isotopes was performed using an off-axis integrated cavity output spectroscopy (off-axis ICOS) technique which is another variant of the CEAS technique. The results revealed a distinctive affinity of urease enzyme towards the $^{12}CO_2$ isotope in comparison to the $^{13}CO_2$ isotope. We extended this idea by varying the proportions of the two isotopes in the substrate urea to observe their combined effect. The isotope-specific activity was also shown to be consistent in buffer mediums. Thus, we unfolded an interesting isotopic dependence of the activity of urease enzyme on both the substrate and the reaction environment.

6.2 Experimental details

6.2.1 CO_2 isotopes measurement using the ICOS technique

The gaseous $^{12}CO_2$ and $^{13}CO_2$ isotopes were measured using a commercial CO_2 isotope analyzer (CCIA 36-EP, Los Gatos Research LGR, USA) employing the off-axis ICOS technique [12-14]. In the ICOS based analyzer, two high-reflectivity mirrors (R~99.98%) in a ~ 59 cm of cavity length were employed to create the optical cavity which provided an optical path length of ~ 3 km for high-sensitive CO_2 isotopes measurements. The system utilized a continuous wave distributed feedback (cw-DFB) laser in the near-infrared region of ~ 2.05 μm. The spectral lines of $^{12}CO_2$ and $^{13}CO_2$ at 4874.448 cm^{-1} and 4874.086 cm^{-1}, respectively in the ro-vibrational combination band $(2,0^0,1)\leftarrow(0,0^0,0)$ of CO_2 were utilized for the measurement. The rotational assignments of $^{12}CO_2$ and $^{13}CO_2$ were R(28) and P(16), respectively where R and P refer to the rotational notation of $\Delta J(J'')$ as used in earlier chapters. The cavity pressure was maintained at ~ 30 Torr by a diaphragm pump and various valves in the system. The cavity was purged using pure nitrogen (N_2) after every measurement to remove the residues of the previous measurement. The instrument provided the concentrations of $^{12}CO_2$ and $^{13}CO_2$ isotopes along with the delta (δ) value of their isotope ratio with a precision of ±0.15‰. The isotope ratios were calculated in accordance with equation 1.1. The precision of the instrument was determined using certified calibration standards with known δ values (Cambridge Isotope Laboratory, CIL, US, $\delta^{13}C$ =-22.8‰, -13.22‰ and -7.33‰) of CO_2 in air [13].

6.2.2 Materials

Jack-bean urease enzyme (E.C. 3.5.1.5) was procured from Sigma Aldrich while ^{13}C-enriched urea (^{13}C-Urea, 99%) (CCLM-311-GMP) was purchased from Cambridge Isotopic Laboratories, Inc., USA. The prepared solution of

urease enzyme was filtered using a 0.22 µm syringe filter unit (Millex-GP, Merck) before use. Other chemicals and ACS grade ^{12}C-enriched urea were obtained from Sigma Aldrich. The aqueous solutions were prepared using Milli-Q water.

6.2.3 Method

The solutions of urea and urease were prepared as aqueous solutions except when mentioned otherwise. Sealed round-bottomed flasks were used to perform the reactions and the space above the solutions was the headspace which served as the gaseous environment for the reaction. The flasks were thoroughly purged with pure N_2 before each experiment to remove the residual CO_2. To provide the CO_2 environment, the gas was injected into the flask. The reaction was considered to be completed at 60 minutes as validated by Berthelot's experiment [15], which is a standard reaction to detect product NH_3 in the urea-urease reaction. After 60 minutes, phosphoric acid (H_3PO_4) was added to the solution to acidify the solution and extract the dissolved CO_2 into the headspace. The headspace CO_2 was subsequently collected and measured in the ICOS based CO_2 isotope analyzer. Another flask containing only urease solution and equivalent headspace CO_2 concentration was used as a blank flask. To obtain the net evolved CO_2 concentration from the reactions, the CO_2 from the blank flask was subtracted from the concentration of CO_2 obtained from the reactions. All experiments were conducted at room temperature.

6.3 Results and discussion

To explore the effect of the gaseous CO_2 environment on the hydrolysis reaction, the urea (4 mM)-urease (1 µM) reaction was carried out in different headspace $^{12}CO_2$ concentrations (with ~1.1% natural abundance of $^{13}CO_2$) beginning with CO_2-free N_2 environment. In the headspace, the total

pressure of the gaseous environment was kept around the atmospheric pressure and only the concentration of the CO_2 was varied. Additionally, to understand the different roles of CO_2 in the hydrolysis reaction, we performed the reaction using ^{12}C and ^{13}C-enriched urea substrates. We first examined the ^{13}C-urea hydrolysis (Figure 6.1a) where it was observed that on increasing the headspace $^{12}CO_2$ concentration the product $^{13}CO_2$ from the reaction also increased, while the $^{12}CO_2$ initially provided in headspace was increasingly absorbed i.e. the final headspace $^{12}CO_2$ concentration was decreased. This indicated that the intake of $^{12}CO_2$ was linked with an enhancement in the urease activity which resulted in the increased formation of the product $^{13}CO_2$. In contrast, such observations cannot be made with ^{12}C-urea hydrolysis as the reaction product and the headspace species ($^{12}CO_2$) are the same.

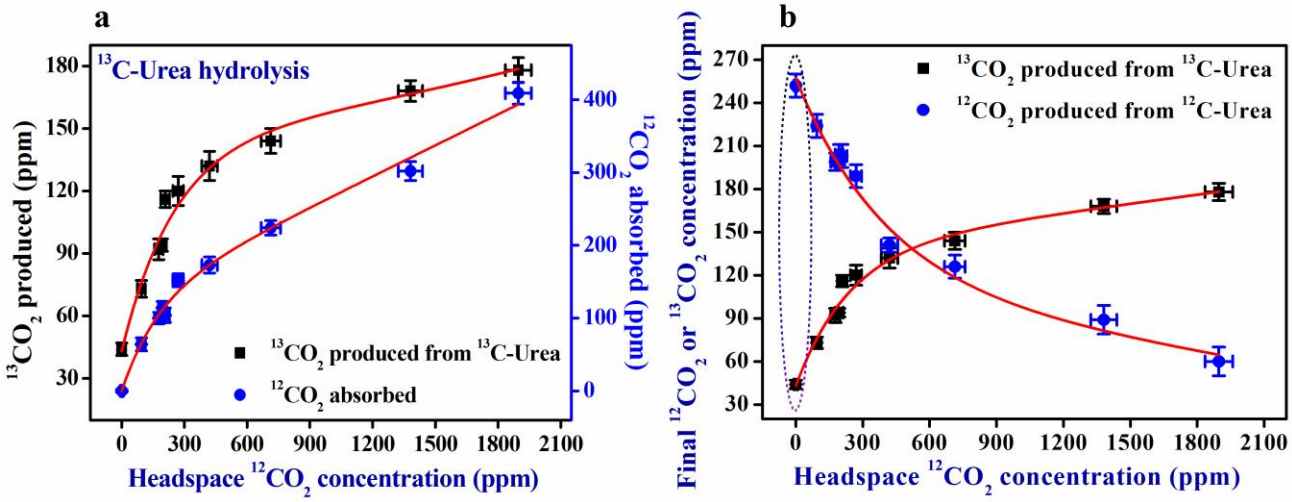

Figure 6.1 a) *Variation of the product $^{13}CO_2$ from ^{13}C-urea hydrolysis with increase in the headspace $^{12}CO_2$ concentration. The product $^{13}CO_2$ increases while the headspace $^{12}CO_2$ is increasingly absorbed.* ***b)*** *Variation of product $^{12}CO_2$ and $^{13}CO_2$ from ^{12}C and ^{13}C-urea hydrolysis, respectively. The error bars depict the standard deviation for the data points [14].*

Nevertheless, we compared the results of ^{12}C and ^{13}C-urea hydrolysis (Figure 6.1b) and found an interesting point. In a CO_2-free pure N_2

environment, the $^{13}CO_2$ product was lowest while the $^{12}CO_2$ from ^{12}C-urea hydrolysis was the highest (Figure 6.1b). This showed that with negligible $^{12}CO_2$ in the headspace, the urease activity diminishes in ^{13}C-urea hydrolysis and so the product formation of $^{13}CO_2$ is reduced. On the other hand, in ^{12}C-urea hydrolysis, the *in-situ* product $^{12}CO_2$ itself activates the urease enzyme and thus the product formation is not hindered in spite of a CO_2-free headspace. However, the product $^{12}CO_2$ from ^{12}C-urea hydrolysis decreases markedly with increase in the headspace $^{12}CO_2$ concentration. This is likely due to the excess partial pressure of $^{12}CO_2$ in the headspace and the over-saturation of urease enzyme due to excess $^{12}CO_2$.

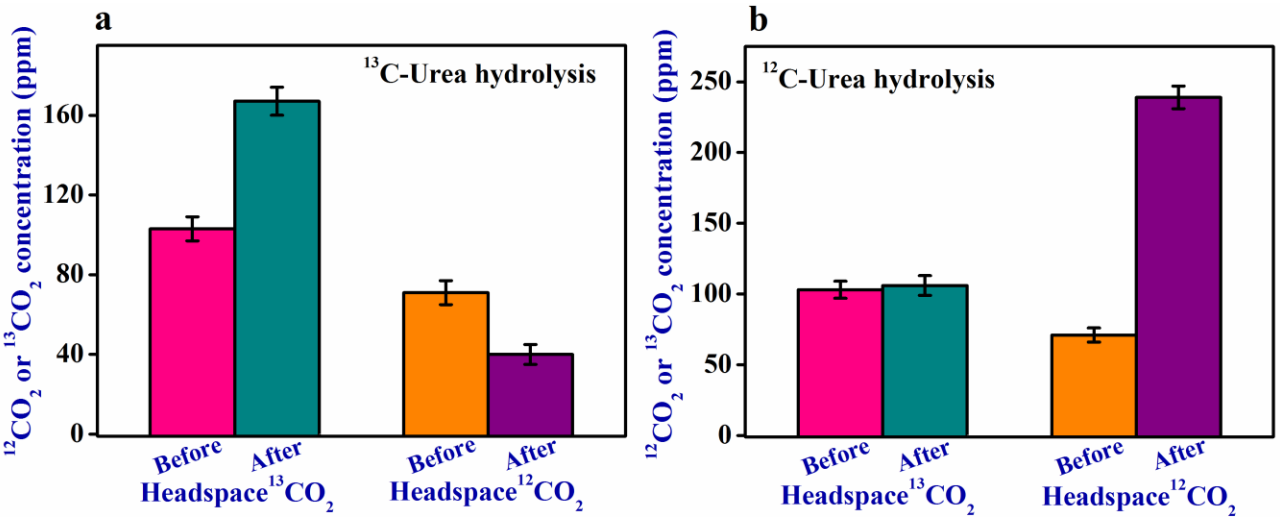

Figure 6.2 a) *and* ***b)*** *Variation of the headspace $^{13}CO_2$ and $^{12}CO_2$ concentration before and after the reaction in ^{13}C and ^{12}C urea hydrolysis, respectively. While $^{12}CO_2$ is absorbed in the reaction medium, there is no change or absorption of $^{13}CO_2$ indicating an isotope-selective intake of CO_2 by urease [14].*

Further, to investigate the effect of $^{13}CO_2$ environment on the urease activity, about 60% isotopically enriched $^{13}CO_2$ (103 ppmv out of 174 ppmv total CO_2) was provided in the headspace and the concentrations of the headspace $^{12}CO_2$ and $^{13}CO_2$ were monitored before and after the reaction. It was observed that for ^{13}C-urea hydrolysis, the headspace $^{13}CO_2$ increased

due to the product $^{13}CO_2$ formation but the $^{12}CO_2$ was absorbed (Figure 6.2a). However, interestingly in ^{12}C-urea hydrolysis, no absorption of $^{13}CO_2$ was seen while $^{12}CO_2$ product was increased after the reaction (Figure 6.2b). This observation revealed isotope-specific affinity of the urease enzyme towards the $^{12}CO_2$ for its activation. This observation is also summarized in a schematic diagram as shown in Figure 6.3.

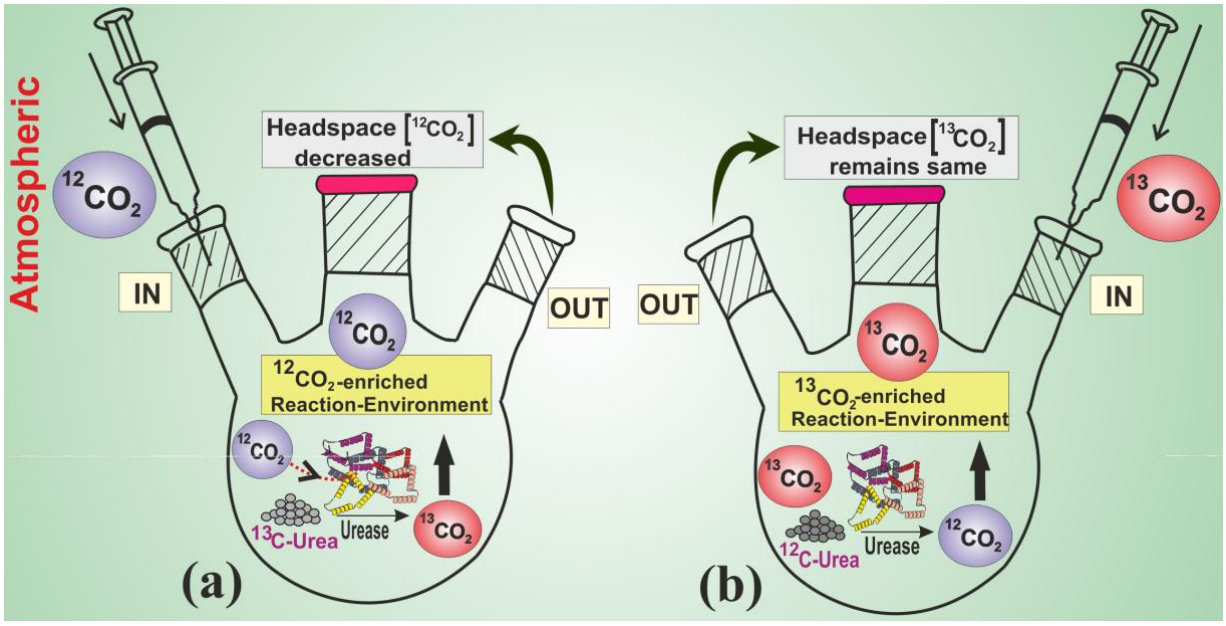

Figure 6.3 a) *and* ***b)*** *Schematic diagrams depicting the ^{13}C and ^{12}C-urea hydrolysis reactions in round-bottomed flasks. The headspace CO_2 is injected into the flask and subsequently extracted after the reaction. The $^{12}CO_2$ is decreased (or absorbed) while $^{13}CO_2$ concentration remains the same [14].*

Next, to investigate the effect of the isotopically enriched substrate urea on the urease mediated hydrolysis reaction, we prepared different proportions (^{12}C:^{13}C) of the isotopes in the urea keeping the headspace $^{12}CO_2$ concentration (~360 ppmv) fixed. It is worthy of note that 360 ppmv is the typical concentration of CO_2 in the atmosphere so it would help in comparing urease-urea reactions taking place in normal atmospheric conditions. The solutions were prepared by using different proportions of

the urea isotopes while keeping the total urea concentration (4 mM) same as before. The product $^{13}CO_2$ values from the different proportions of urea are shown in Figure 6.4a.

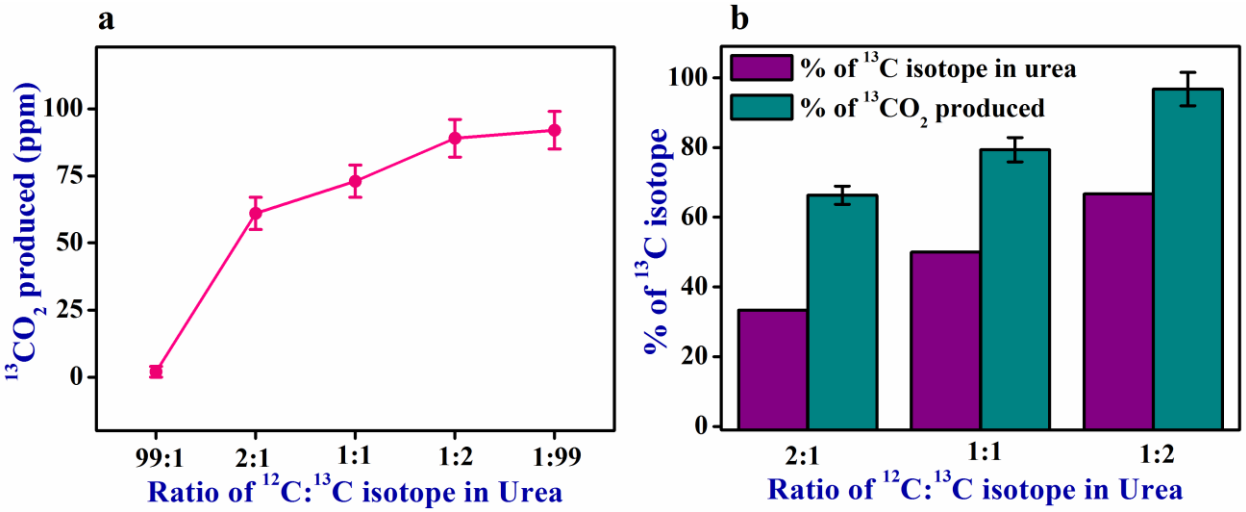

Figure 6.4 a) *$^{13}CO_2$ production from various isotopic compositions of substrate urea for a fixed headspace CO_2 concentration.* ***b)*** *Comparison of percentage of $^{13}CO_2$ evolved in the urease-urea reaction to the ^{13}C-enrichment present in the substrate urea [14].*

It was found that the product $^{13}CO_2$ from hydrolysis of ^{12}C:^{13}C=1:2 proportion of urea was very close to that of ^{12}C:^{13}C=1:99 isotopic-composition (Figure 6.4a). However, the initial ^{13}C-enrichment of the ^{12}C:^{13}C=1:2 substrate urea was considerably less than that of ^{12}C:^{13}C=1:99 composition of urea. This result shows that the *in-situ* product $^{12}CO_2$ produced in the hydrolysis of ^{12}C:^{13}C=1:2 urea itself provided further activation for urease which enhanced the product $^{13}CO_2$. On the other hand, the ^{12}C:^{13}C=1:99 composition was not effectively hydrolyzed due to negligible amount of *in-situ* $^{12}CO_2$ formed in the reaction. To further understand the role of *in-situ* $^{12}CO_2$, we normalized the product $^{13}CO_2$ generated from the various isotopic-compositions of urea (i.e. ^{12}C:^{13}C=2:1, 1:1 and 1:2) by the $^{13}CO_2$ generated from ^{12}C:^{13}C=1:99 (Figure 6.4b). It was

observed for all the three compositions, the percentage of product $^{13}CO_2$ generated was higher than the percentage of isotopic ^{13}C-enrichment initially present in the substrate urea. This shows that the *in-situ* $^{12}CO_2$ plays a role in these compositions to enhance the product $^{13}CO_2$ formation. Moreover, it also signifies the inadequate hydrolysis of ^{12}C:^{13}C=1:99 composition of urea with negligible *in-situ* $^{12}CO_2$ produced from the reaction. Thus, it shows that even the *in-situ* $^{12}CO_2$ from the hydrolysis interacts with the urease enzyme to enhance its activity and the activation is isotope-specific to the $^{12}CO_2$ isotope of CO_2.

Furthermore, we examined the effect of changing urease and urea concentrations on the activation of urease enzyme keeping the headspace CO_2 concentration (~ 360 ppmv) fixed. It was found that with increase in the ^{12}C or ^{13}C-urea concentration (with urease fixed at 1 µM), the product $^{12}CO_2$ or $^{13}CO_2$ concentration gradually increased with increase in urea concentration from 100 µM to 5mM (Figure 6.5a). But, after 5 mM of urea the product formation started to decline due to the substrate inhibition effect where the excess quantity of a substrate decreases the overall yield of the reaction.

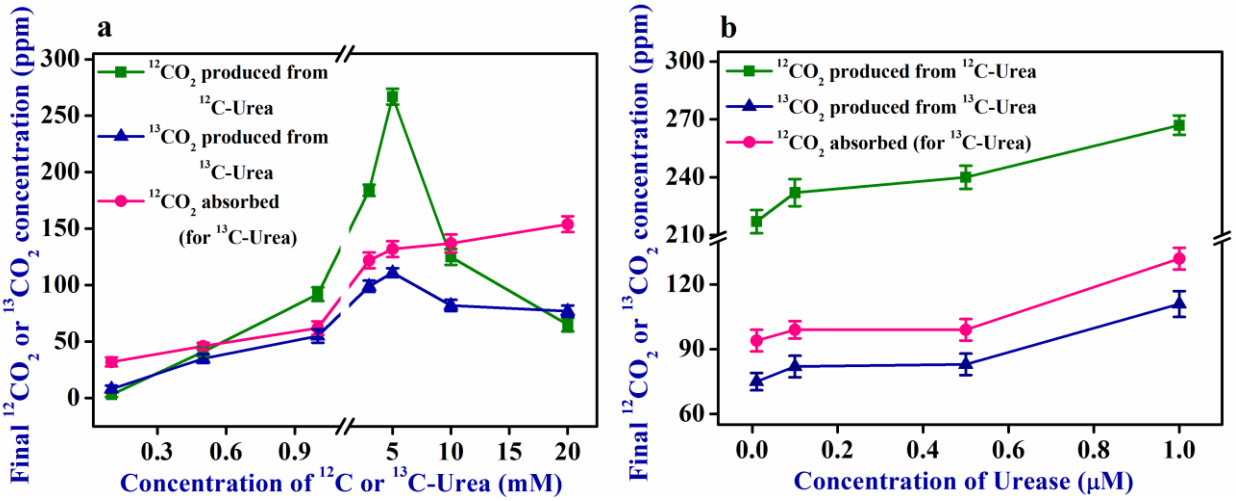

Figure 6.5 a) *Variation of the product $^{12}CO_2$ or $^{13}CO_2$ with increase in the ^{12}C or ^{13}C-urea concentration.* ***b)*** *Variation of the product $^{12}CO_2$ or $^{13}CO_2$ with increase in urease concentration [14].*

Conversely, with increase of the urease concentration (with urea fixed at 4 mM), the product CO_2 did not increase significantly, thereby suggesting that the urease enzyme has a steady catalytic activity for a range of urease concentrations (Figure 6.5b). Eventually, we examined the effect of buffer medium on the isotope-selective activation of urease to eliminate the possible effect that CO_2 might have on the pH of the medium. It is worthy of note that the above experiments were performed using aqueous solutions of urea and urease so as to minimize the urease inhibition due to buffer ions [16]. Figure 6.6 depicts the product $^{12}CO_2$ or $^{13}CO_2$ produced from the hydrolysis reaction of ^{12}C or ^{13}C-urea with change in the headspace $^{12}CO_2$ concentration, in Tris-hydrochloride (pH 7.4) and phosphate (pH 7.0) buffer mediums. The profiles in Figure 6.6 are similar to those in Figure 6.1b, thus indicating that the phenomena of urease activation by $^{12}CO_2$ still occurs in buffer mediums.

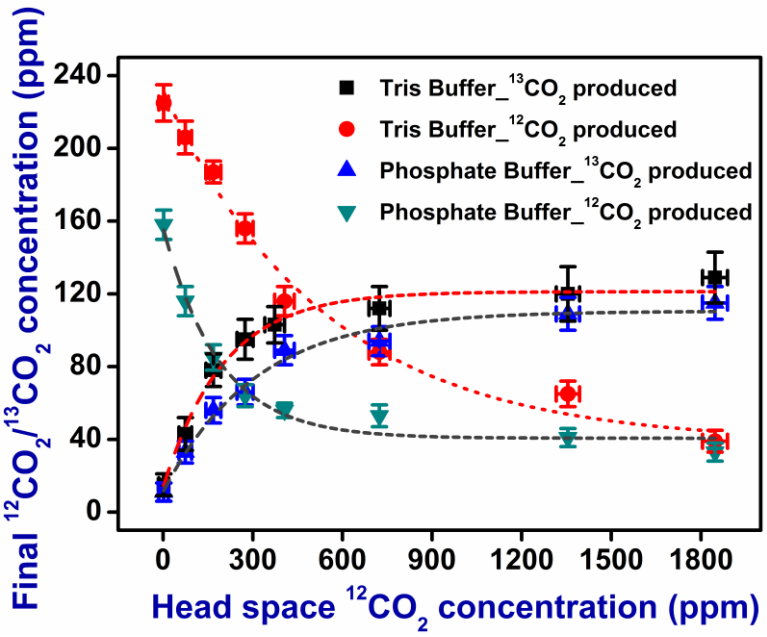

Figure 6.6 *Concentration profiles of $^{12}CO_2$ or $^{13}CO_2$ produced from the urea-urease reaction with change in the headspace $^{12}CO_2$ concentration, for Tris and phosphate buffer mediums [14].*

However, the product concentrations are reduced in comparison to those in the aqueous medium due to the inhibitory effect of buffer ions. Thus, it can be inferred from the above experimental observations that the urease enzyme exhibits an isotope-specific activation by $^{12}CO_2$ in comparison to $^{13}CO_2$. This activation not only depends on the reaction environment but also on the *in-situ* availability of $^{12}CO_2$ and the isotopic compositions of the substrate urea. In a past study [17], it has been shown that CO_2 acts as a ligand in urease-urea reaction. Thus, the preference towards $^{12}CO_2$ might be due to the lower interaction energy offered by $^{12}CO_2$ molecule as compared to $^{13}CO_2$. However, better understanding of this phenomenon can be achieved through quantum mechanical calculations of interaction energy for the binding of the two CO_2 isotopes to the urease enzyme.

6.4 Conclusion

In this chapter, an application of the ICOS technique was described wherein the response of urease enzyme towards different isotopes of CO_2 was explored in the urea hydrolysis reaction. The results demonstrated the isotope-selective catalytic activation of the urease enzyme where the $^{12}CO_2$ isotope is strongly preferred for activation as opposed to the $^{13}CO_2$ isotope. This activation depended on the reaction environment, the isotopic-compositions of urea and the *in-situ* $^{12}CO_2$ availability in the reaction. The dependence on urea and urease concentrations as well as buffer dependence was investigated. Although, the current study provides evidence for the distinct isotope-specificity of urease, the detailed mechanisms for this phenomenon are yet to be explored. It is also supposed that this phenomenon would assist in field applications where the urea-urease reaction is utilized.

6.5 References

[1] Dixon, N. E., T. C. Gazzola, R. L. Blakeley and B. Zermer. "Jack bean urease (EC 3.5.1.5). A metalloenzyme. A simple biological role for nickel?" *Journal of the American Chemical Society* 97, no. 14 (1975)**:** 4131-4133.

[2] Sumner, J. B. "The isolation and crystallization of the enzyme urease." *Journal of Biological Chemistry* 69, (1926): 435-441.

[3] Mobley, H. L. and R. P. Hausinger. "Microbial ureases: significance, regulation, and molecular characterization." *Microbiology and Molecular Biology Reviews* 53, no. 1 (1989): 85-108.

[4] Fawcett, J. K. and J. E. Scott. "A rapid and precise method for the determination of urea." *Journal of clinical pathology* 13, no. 2 (1960): 156-159.

[5] Huang, T. C. and D. H. Chen. "Kinetic study of urease-catalysed urea hydrolysis." *Journal of Chemical Technology and Biotechnology* 52, no. 4 (1991): 433-444.

[6] Jespersen, N. D. "Thermochemical study of the hydrolysis of urea by urease." *Journal of the American Chemical Society* 97, no. 7 (1975): 1662-1667.

[7] Krajewska, B., R. van Eldik and M. Brindell. "Temperature-and pressure-dependent stopped-flow kinetic studies of jack bean urease. Implications for the catalytic mechanism." *JBIC Journal of Biological Inorganic Chemistry* 17, no. 7 (2012): 1123-1134.

[8] Lynn, K. R. and Peter E. Yankwich. "13C Kinetic isotope effects in the urease-catalyzed hydrolysis of urea I. Temperature dependence." *Biochimica et biophysica acta* 56, (1962): 512-530.

[9] Lynn, K. R. and Peter E. Yankwich. "13C kinetic isotope effects in the urease-catalyzed hydrolysis of urea: II. Influences of reaction variables other than temperature." *Biochimica et Biophysica Acta (BBA)-Specialized Section on Enzymological Subjects* 81, no. 3 (1964): 533-547.

[10] Park, I. S. and R. P. Hausinger. "Requirement of carbon dioxide for in vitro assembly of the urease nickel metallocenter." *Science* 267, no. 5201 (1995): 1156.

[11] Dixon, N. E., P. W. Riddles, C. Gazzola, R. L. Blakeley and B. Zerner. "Jack bean urease (EC 3.5. 1.5). V. On the mechanism of action of urease on urea, formamide,

acetamide, N-methylurea, and related compounds." *Canadian journal of biochemistry* 58, no. 12 (1980): 1335-1344.

[12] Crosson, E. R., K. N. Ricci, B. A. Richman, F. C. Chilese, T. G. Owano, R. A. Provencal, M. W. Todd *et al.* "Stable isotope ratios using cavity ring-down spectroscopy: determination of 13C/12C for carbon dioxide in human breath." *Analytical Chemistry* 74, no. 9 (2002): 2003-2007.

[13] Maity, A., S. Som, C. Ghosh, G. D. Banik, S. B. Daschakraborty, S. Ghosh, S. Chaudhuri and M. Pradhan. "Oxygen-18 stable isotope of exhaled breath CO2 as a non-invasive marker of *Helicobacter pylori* infection." *Journal of Analytical Atomic Spectrometry* 29, no. 12 (2014): 2251-2255.

[14] Maithani, S., M. Pal, A. Maity and M. Pradhan. "Isotope selective activation: a new insight into the catalytic activity of urease." *RSC advances* 7, no. 50 (2017): 31372-31376.

[15] Harfmann, R. G. and S. R. Crouch. "Kinetic study of Berthelot reaction steps in the absence and presence of coupling reagents." *Talanta* 36, no. 1-2 (1989): 261-269.

[16] Qin, Y. and J. M. S. Cabral. "Kinetic studies of the urease-catalyzed hydrolysis of urea in a buffer-free system." *Applied biochemistry and biotechnology* 49, no. 3 (1994): 217-240.

[17] Walther, D., M. Ruben and S. Rau. "Carbon dioxide and metal centres: from reactions inspired by nature to reactions in compressed carbon dioxide as solvent." *Coordination Chemistry Reviews* 182, no. 1 (1999): 67-100.

Chapter 7

An isotopic investigation of preferential coordination between $^{12}CO_2$ and urease enzyme and its application to ^{13}C-UBT

7.1 Introduction

In the preceding chapter, the isotope-specific activation of the urease enzyme by $^{12}CO_2$ was discussed. In this chapter, we describe a study in which we explored the isotopic preferential coordination between urease and the substrate urea by observing the response of the urease enzyme towards different forms of CO_2 during urea hydrolysis. As mentioned in the previous chapter, urease is binuclear Ni (II) containing metalloenzyme where the Ni (II) acts as an active site. This Ni (II) centre also coordinates with the substrate urea during the urea hydrolysis reaction to produce bicarbonate (HCO_3^-) and ammonium (NH_4^+) ions [1,2] in the solution which in dissolved form represent the CO_2 and NH_3 molecules. It has been shown in the past studies [3,4], that the binding between the urease apoenzyme (inactive form of enzyme) and the Ni^{2+} ions is mediated by CO_2 for the catalytic activity of urease. But, the in-depth mechanisms governing the hydrolysis reaction and the urease activation are not clear [1]. Moreover, it is known that bicarbonate ion (HCO_3^-), the product of urea hydrolysis, exists in various forms (i.e. H_2CO_3, CO_2, CO_3^{2-}) depending on the pH of the reaction medium [5]. Thus, it can be conjectured that using isotopically different forms of HCO_3^- ions can help in understanding the

form of ligand which binds to urease enzyme. Furthermore, the urea-urease reaction is utilized in various enzymatic assays to detect urea in biological fluids such as blood, urine etc. [6,7]. But, many biological fluids contain bicarbonate ions which might affect the catalytic activity of urease enzyme and might also affect the quantitative estimation of the urea present in the sample. Thus, it is crucial to understand the role of bicarbonate ions upon the activity of urease and its effect on urea-urease reaction. Moreover, the urease activity of various pathogens is crucial for the diagnosis of the diseases caused by them [8].

Helicobacter Pylori (*H. pylori*) is one such pathogen that infects the human stomach and is responsible for gastritis, peptic ulcer and stomach cancer [8,9]. It survives in the acidic environment of the stomach on account of its urease secretion which hydrolyses the gastric juice urea to produce ammonia, thereby neutralizing the surroundings for its survival. The conventional method for the diagnosis of *H. pylori* infection is endoscopy and biopsy based rapid urease test (RUT). This conventional method is invasive and carries a risk of cross-infection. However, the ^{13}C-UBT (^{13}C-Urea Breath Test) is an alternative non-invasive test which includes ingesting ^{13}C-enriched urea that is hydrolyzed by the urease secreted by *H. Pylori* in the stomach [10-12]. The exhaled breath $^{13}CO_2$ produced from hydrolysis is utilized to assess the presence of the bacteria in the stomach, where an individual harbouring the bacteria would exhale more $^{13}CO_2$ in comparison to a non-infected individual. Thus, the ^{13}C-UBT is a non-invasive, robust alternative method which is preferable to children, pregnant women and elderly people. Hence, an improvement in sensitivity of ^{13}C-UBT would ensure better and large-scale diagnostic applicability of the method. Thus, one of the aims in this study was to examine the effect of urease activation in *in-vivo* condition using ^{13}C-UBT.

In this study, we utilized the ICOS technique to investigate the roles of isotopically enriched bicarbonate ions on the urease catalyzed hydrolysis of urea. We validated that the activation of urease enzyme by the bicarbonate

ions is an isotope-specific phenomenon. Furthermore, we studied the influence of different pH environments upon the bicarbonate mediated urease activation which revealed the specific species responsible for the activation of urease enzyme and provided an insight on the preferential coordination between the $^{12}CO_2$ isotope and urease. Eventually, the *in-vitro* results were validated in an *in-vivo* environment utilizing the ^{13}C-UBT which was shown to increase the sensitivity of ^{13}C-UBT for non-invasive diagnosis of *H. pylori* infection.

7.2 Experimental details

7.2.1 Materials

^{13}C-labelled urea (^{13}C-urea, 99%) (CCLM-311-GMP) was obtained from Cambridge Isotopic Laboratories, Inc., USA. Jack-bean urease enzyme (E.C. 3.5.1.5) and ^{13}C-enriched sodium bicarbonate ($NaH^{13}CO_3$, 99%) (372382) were procured from Sigma Aldrich. ^{12}C-enriched urea (99% ^{12}C) was purchased from Sisco Research Laboratories (21113) while other chemicals were bought from Sigma Aldrich and were used without further purification. Milli-Q water was used to prepare the aqueous solutions.

7.2.2 Method for *in-vitro* experiment

The reactions were performed in sealed round-bottomed flasks which were thoroughly purged with nitrogen (N_2) to remove any residue of air or previous measurement. The reactions were carried out in CO_2-free N_2 headspace environment and the solution volume was optimized to ensure a measurable CO_2 output. Sodium bicarbonate was used to provide bicarbonate ions in the solutions. Similar to the method mentioned in chapter 6, the hydrolysis reaction was terminated after 60 minutes by adding H_3PO_4 to extract the CO_2 into the headspace area. The headspace

gas was collected and measured in the ICOS-based CO_2 isotope analyzer. Here, the blank flask contained the urease and sodium bicarbonate solution, and the net concentration of CO_2 from the reactions were considered after subtracting the CO_2 values from the blank flask. The experiments were conducted at room temperature whereas a standard pH meter (ecphtutor-ds) was used to measure the pH of the solutions.

7.2.3 Method for human breath collection

The group for human breath analysis study consisted of 20 subjects (age within 25-60 years) with different gastrointestinal disorders like gastritis, peptic ulcer and non-ulcerous dyspepsia. The subjects were sorted as *H. pylori* positive (n=12) and *H. pylori* negative (n=8) depending on the results of the "gold-standard" tests i.e. endoscopy and biopsy-based rapid urea test (RUT) and the ^{13}C-UBT. The results for both the tests were same for all the participants in the study. Moreover, written consents were taken from all the individuals participating in the study. The Ethics Committee Review Board of AMRI Hospital, Salt Lake, Kolkata, India (Study no.: AMRI/ETHICS/2013/1) and the administration of S. N. Bose Centre, Kolkata, India, (Ref. no.: SNB/PER-2-6001/13-14/1769) approved the protocol of the ^{13}C-UBT study.

The ^{13}C-UBT was performed within 1-2 days of the endoscopy test. In the breath test, a baseline breath sample from the individuals was taken after an overnight fasting, using a breath collection bag (QUINTRON, USA, SL No.QT00892). Next, a test meal of 75 mg of ^{13}C-enriched urea in 50 ml water was administered to the subjects and their breath samples were taken at 15 minutes intervals up to 90 minutes. The next day, the individuals took the ^{13}C-UBT where along with the ^{13}C-urea, ^{12}C-sodium bicarbonate (100 mg) [13] was provided as the test meal and the remaining procedure was kept the same as ^{13}C-UBT. The breath samples were analyzed for $^{12}CO_2$ and $^{13}CO_2$ isotopes using the ICOS technique.

7.2.4 Measurement

The gaseous $^{12}CO_2$ and $^{13}CO_2$ isotopes were measured using the CO_2 isotope analyzer based on the ICOS technique, described in section 6.2.1 in the previous chapter.

The $^{12}CO_2$ and $^{13}CO_2$ concentrations from reactions were stated in parts per million by volume (ppmv) whereas the $^{13}C/^{12}C$ isotope ratios for breath analysis were expressed in the $\delta^{13}C$ notation (in per mil, ‰) as described in equation 7.1. The breath values were expressed in isotope ratios to nullify the effect of absolute exhaled CO_2 concentrations which vary from one individual to another.

$$\delta^{13}C(‰) = \frac{\left(\frac{^{13}C}{^{12}C}\right)_{sample} - \left(\frac{^{13}C}{^{12}C}\right)_{standard}}{\left(\frac{^{13}C}{^{12}C}\right)_{standard}} \times 1000 \qquad (7.1)$$

where $(^{13}C/^{12}C)_{Standard}$ = 0.0112372 is the international standard Pee-Dee Belemnite value. The $\delta^{13}C$ values were measured with a precision of 0.15‰. The ^{13}C-enrichment in the exhaled breath samples at time 't' was evaluated using delta over baseline (DOB) notation where the enhancement in exhaled $^{13}CO_2$ is measured with respect to the baseline value at time t=0 minute (equation 7.2).

$$\delta_{DOB}{}^{13}C‰ = \left(\delta^{13}C‰\right)_{t=t_{min}} - \left(\delta^{13}C‰\right)_{t=0_{min}} \qquad (7.2)$$

where the $\delta^{13}C$ value before urea ingestion is considered to be at $\delta^{13}C$‰ at t=0 min. An individual was considered as *H. Pylori* positive if the $\delta_{DOB}{}^{13}C$ value was ≥ 3.0‰ [10,11] and negative if it was less than 3.0‰. Now, the

rate of $^{13}CO_2$ produced from the ingested urea, denoted as the ^{13}C-post dose recovery (^{13}C-PDR) was calculated using equation 7.3 [10,14]:

$$^{13}C-PDR(\%/hour)=\frac{\delta_{DOB}{}^{13}C\times\left(\frac{^{13}C}{^{12}C}\right)_{standard}\times10^{-3}\times V_{CO_2}}{\left(\frac{D}{M_t}\right)\times\left(p\times\frac{n}{100}\right)}\times100 \qquad (7.3)$$

where V_{CO2} is the rate of CO_2 produced per hour, D is the dose of the administered test meal (here 75 mg), M_t is molecular weight of the substrate meal (M_t of ^{13}C-urea=61.05 gm mol^{-1}), p is ^{13}C atom excess (isotope enrichment in %) which was 99% in the present case and n is the number of labelled carbon positions (1 in ^{13}C-urea). The V_{CO2} was evaluated using the basic metabolic rate (BMR) of an individual. The total ^{13}C-labelled substrate metabolised at a given period of time i.e. the cumulative post-dose recovery (c-PDR) was determined by taking integral [14] of the ^{13}C-PDR values for the time-period. This gave the value of the ^{13}C-urea hydrolyzed in ^{13}C-UBT.

7.3 Results and discussion

Initially, to assess the role of HCO_3^- ions in the activation of urease, we performed the ^{12}C and ^{13}C-urea hydrolysis reactions in presence of $NaH^{12}CO_3$ (2 mM) in the reaction solution. The reactions were carried out in Tris buffer (pH 7.0) medium at room temperature and atmospheric pressure was maintained in the flask [15]. Figure 7.1a and b depict the profiles of the reaction products $^{12}CO_2$ and $^{13}CO_2$ from hydrolysis of different concentrations of ^{12}C and ^{13}C-urea in presence of 1 μM urease. It was observed that in absence of any bicarbonate ions, the product yield of ^{13}C-urea was lesser than that of ^{12}C-urea. This shows a preference of the active site of urease enzyme towards ^{12}C-urea hydrolysis. In contrast, on

addition of $NaH^{12}CO_3$, the yield ($^{13}CO_2$) of ^{13}C-urea enhanced while that of ^{12}C-urea diminished considerably in comparison to the non-bicarbonate case. Since $H^{12}CO_3^-$ ion (from $NaH^{12}CO_3$) is known to acquire the form of $^{12}CO_2$ at a pH of 7.0, it is inferred that $H^{12}CO_3^-/^{12}CO_2$ helps to increase the activity of urease through better coordination between the urease active site and ^{13}C-urea, which enhances the overall yield of ^{13}C-urea hydrolysis. Moreover, in case of ^{12}C-urea hydrolysis in presence of $NaH^{12}CO_3$, the $^{12}CO_2$ from the $H^{12}CO_3^-$ ions possibly saturates the active site of urease in addition to the $^{12}CO_2$ being produced from the reaction and thus shifts the equilibrium to the other side of the reaction and decreases the reaction yield due to common ion effect.

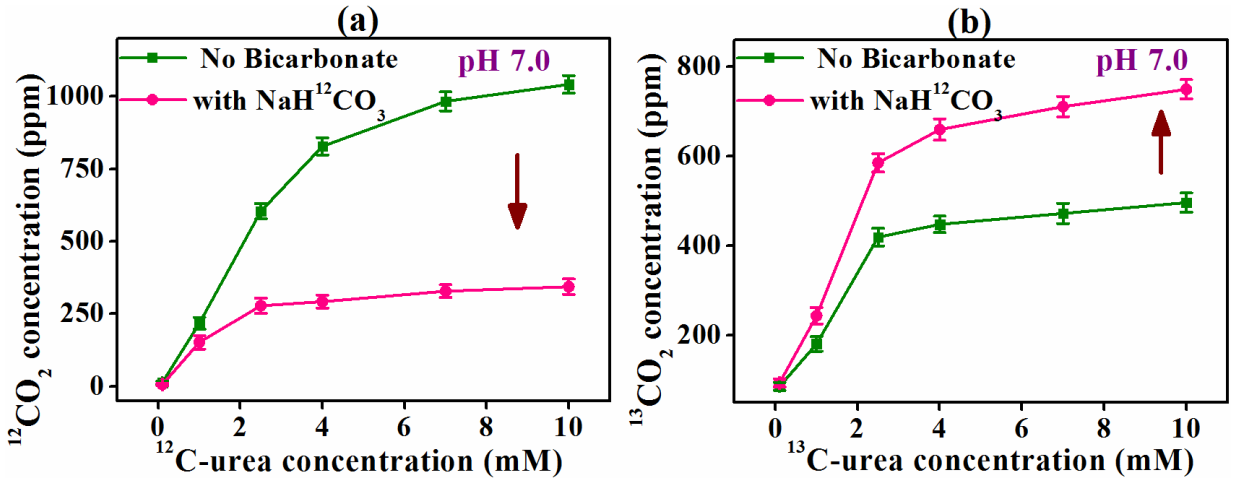

Figure 7.1 a) *and* ***b)*** *Hydrolysis yields of different concentrations of ^{12}C and ^{13}C-urea, respectively showing the effect of $NaH^{12}CO_3$ on the hydrolysis products. The error bars indicate the standard deviation (1 SD) [15].*

We further examined the effect of $NaH^{13}CO_3$ on the hydrolysis of ^{12}C and ^{13}C-urea with similar urease concentration (Figure 7.2a and b) in the Tris buffer medium of pH 7.0. Here, the $NaH^{13}CO_3$ would convert to $^{13}CO_2$ at a pH of 7.0. From Figure 7.2a, it is interesting to observe that the product yield $^{12}CO_2$ from ^{12}C-urea hydrolysis in presence of $NaH^{13}CO_3$ was more in comparison to that with $NaH^{12}CO_3$ in the medium, which indicates that

$NaH^{13}CO_3$ does not cause saturation and the urease site is more accessible to the ^{12}C-urea in absence of external $H^{12}CO_3^-$ ions. Still, the product concentration with $NaH^{13}CO_3$ is lesser than the non-bicarbonate case indicating that $H^{13}CO_3^-$ ions negatively affect the coordination between the ^{12}C-urea and urease which is also evident from the highly diminished yield of ^{13}C-urea in presence of $NaH^{13}CO_3$ (Figure 7.2b).

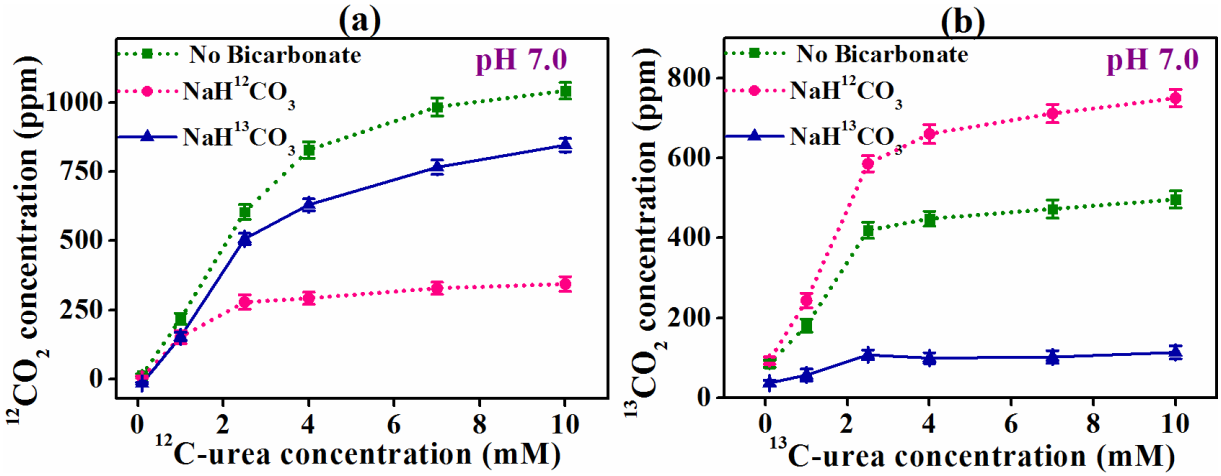

Figure 7.2 a) *and* ***b)*** *Hydrolysis of different concentrations of ^{12}C and ^{13}C-urea, respectively, in presence of $NaH^{12}CO_3$ and $NaH^{13}CO_3$ showing the negative effect of $NaH^{13}CO_3$ upon the product yield [15].*

The above results further validate the preferential response of the urease enzyme towards $^{12}CO_2$ isotope of CO_2. It has been discussed in past studies [1,3,4], that $^{12}CO_2$ in the form of carbamate binds to the active Ni (II) site of urease in a bidentate (with two oxygen linked to the two metal atoms) manner and forms a Ni-CO_2 complex which leads to the activation of the enzyme. Our experimental studies show that $^{13}CO_2$ does not seem to increase the urease activity but in turn induces a negative effect on the urea hydrolysis reaction, which indicates an improper coordination of $^{13}CO_2$ to the urease active site leading to a decrease in the overall reaction yield. Thus, such strong isotopic preference cannot occur solely due to the classical isotope effect where the isotope mass ratio causes different

response towards the isotopes. It is speculated that since $^{13}CO_2$ possesses a non-zero nuclear spin, the magnetic isotope effect [16] may also play a significant role in the isotope-specific preference of urease. The schemes for the reactions in the above results are shown in Scheme 7.1 and 7.2.

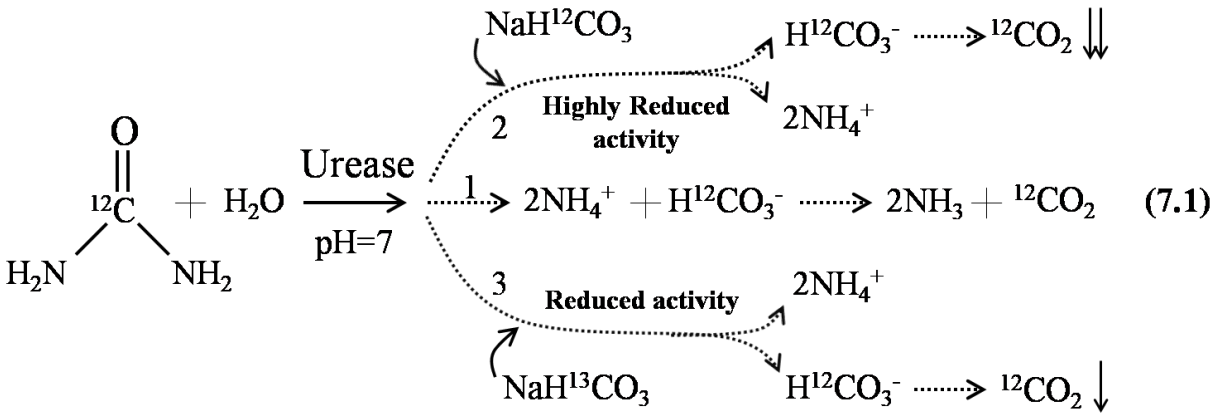

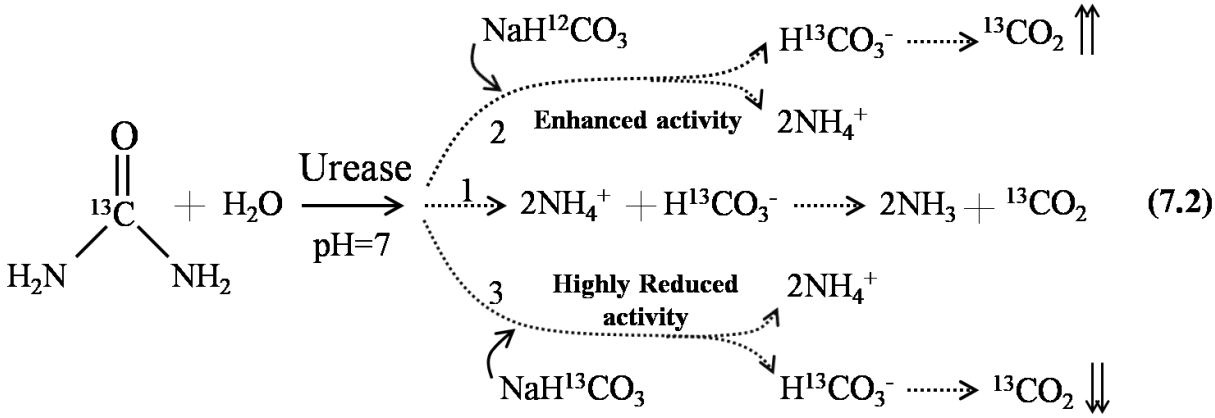

***Schemes 7.1** and **7.2** Reactions depicting the effect of different isotopes of bicarbonate ions on the hydrolysis of ^{12}C and ^{13}C-urea by urease [15].*

As mentioned before, HCO_3^- ions take different forms in different pH mediums. Next, to assess the role of different forms of HCO_3^- ions in the activation of urease, we performed the urease-urea reaction at different pH mediums using Tris buffer at pH 8.5 and Phosphate buffer at pH 4.2. Thus, it would allow the comparison of the forms of HCO_3^- ions i.e. H_2CO_3, CO_2 and CO_3^{2-} at pH mediums of 4.2, 7.0 and 8.5, respectively.

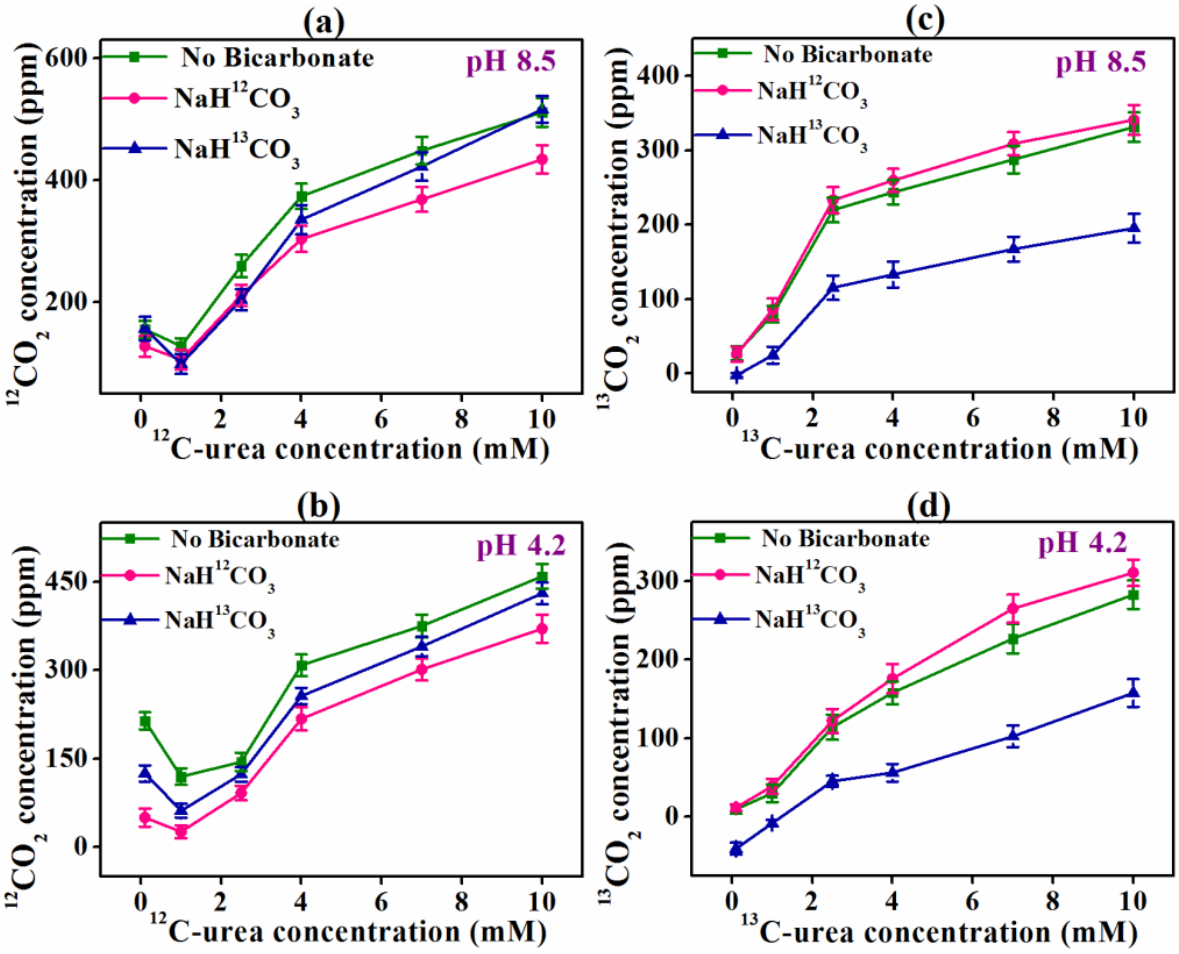

Figure 7.3 a) *and* ***b)*** *depict the* ^{12}*C-urea hydrolysis at pH mediums 8.5 and 4.2, respectively, with and without the* HCO_3^- *ions. The product profiles show negligible difference in presence and absence of* HCO_3^- *ions.* ***c)*** *and* ***d)*** *depict the* ^{13}*C-urea hydrolysis at pH mediums 8.5 and 4.2, respectively, with and without the* HCO_3^- *ions. While there is no significant difference in absence and presence of* $H^{12}CO_3^-$ *ions, the products are diminished in presence of* $H^{13}CO_3^-$ *ions [15].*

Figure 7.3a and b depict the product yield for ^{12}C-urea hydrolysis at pH mediums 8.5 and 4.2, respectively, in presence and absence of ^{12}C and ^{13}C-bicarbonate ions. For both the cases (pH 8.5 and 4.2), the reaction yields were significantly lower than that for pH 7.0 while addition of $H^{12}CO_3^-$ or $H^{13}CO_3^-$ ions did not have any considerable effect on the product yields. Similar results were observed for ^{13}C-urea hydrolysis at pH mediums 8.5 and 4.2 (Figure 7.3c and d), with the exception that in presence of $H^{13}CO_3^-$ ions the product yield was lesser in comparison to that with $H^{12}CO_3^-$ ions or in absence of any HCO_3^- ions. Since no effect is observed on the urease activity with HCO_3^- ions at pH 8.5 and 4.2, it is inferred that the forms of HCO_3^- ions at these pH (H_2CO_3, CO_3^{2-}) do not interact with urease to alter its activity. Thus, only the $^{12}CO_2$ isotope is involved with an increase in urease activation while $^{13}CO_2$ induces a negative effect or a hindrance to the urease activation. The results for different pH mediums are illustrated using phase diagrams (Figure 7.4a and b) where the extent of the forms of HCO_3^- ions are shown with change in the pH of the solution.

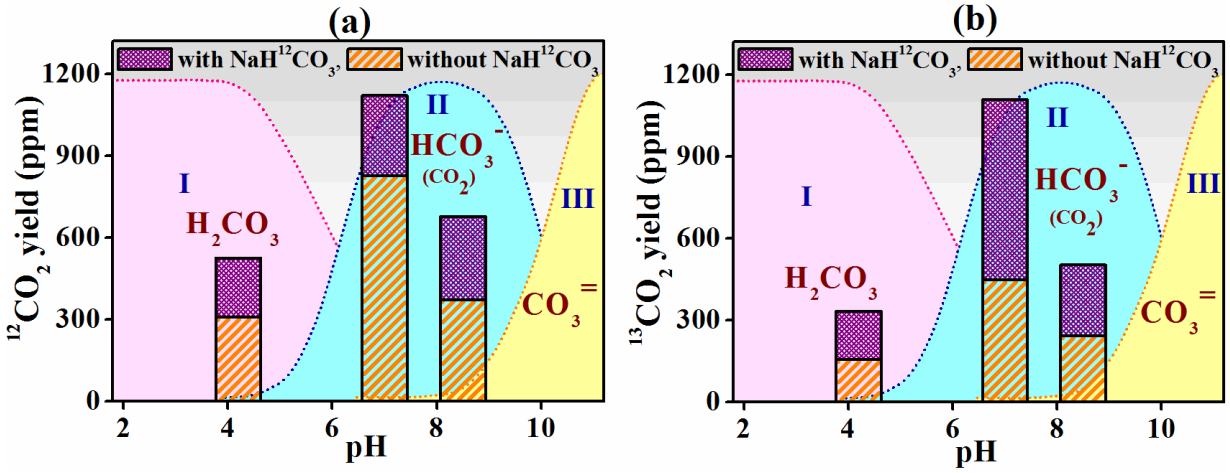

Figure 7.4 a) *and* ***b)*** *depict the product yield of ^{12}C and ^{13}C-urea hydrolysis at different pH mediums. The regions I, II and III depict the range of pH within which the each form of HCO_3^- ions, exists. The partitions in the bar graphs show the product yields in presence and absence of $H^{12}CO_3^-$ ions, which are significantly manifested at pH 7.0 showing the role of $^{12}CO_2$ in altering the urease activity [15].*

Furthermore, we examined the effect of varying the HCO_3^- ion concentration on the product yield from urea (4 mM) hydrolysis for Tris buffer medium at pH 7.0. The reaction yield of ^{12}C-urea decreased with increase of $H^{12}CO_3^-$ or $H^{13}CO_3^-$ ion concentration (Figure 7.5a). On the other hand, the yield of ^{13}C-urea hydrolysis showed two opposite trends for the two isotopes of HCO_3^- ions (Figure 7.5b) where the yield enhanced with increase in $H^{12}CO_3^-$ ions and decreased continuously with increase in concentration of $H^{13}CO_3^-$ ions. This further validated the enhancing role of $^{12}CO_2$ and the negative effect of $^{13}CO_2$ on the urease-mediated urea hydrolysis. Thus, the *in-vitro* study with HCO_3^- ions provided a better understanding of the isotope-specific urease activation which can be utilized in enzymatic assays and can also help in paving the way to explore the isotopic response of other enzymes towards various ligands.

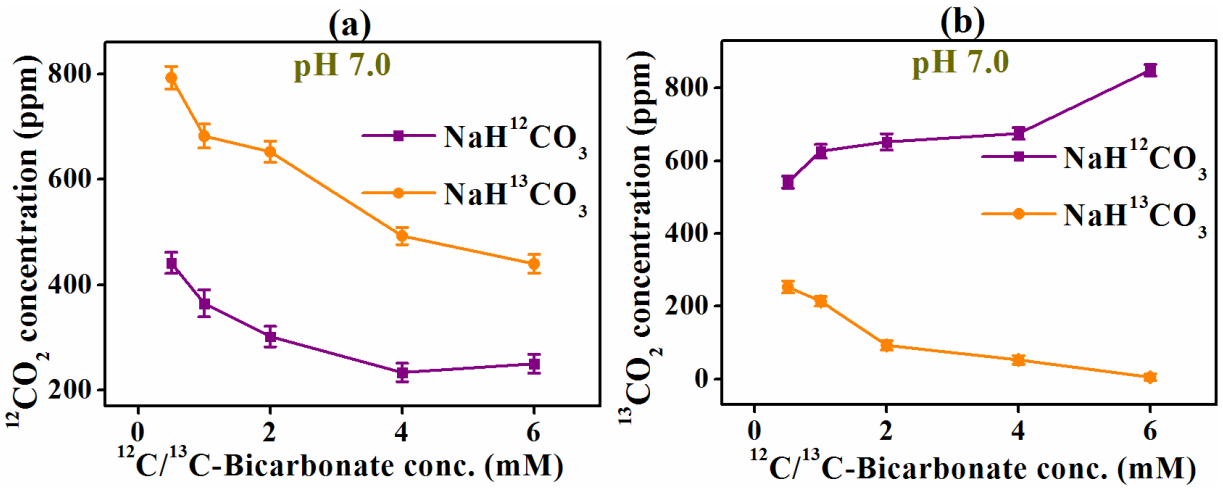

Figure 7.5 a) *and* ***b)*** *show the variation of the reaction yields for ^{12}C and ^{13}C-urea hydrolysis with change in the HCO_3^- ion concentration. While ^{12}C-urea yield decreases with increase in HCO_3^- ion concentration of both isotopes, the trend is different for ^{13}C-urea which increases for $H^{12}CO_3^-$ and decreases for $H^{13}CO_3^-$ ion concentration [15].*

Eventually, we aimed to apply the *in-vitro* observations in the *in-vivo* environment using the urease activity of the *H. Pylori* bacteria in human stomach. To achieve this, we utilized the ^{13}C-UBT in which ^{13}C-enriched urea is orally administered to an individual to determine whether they suffer from *H. Pylori* bacterial infection in the stomach or not. Since urease enzyme is secreted by *H. Pylori*, the urease will react with the ingested urea to produce $^{13}CO_2$, which can be detected in the exhaled human breath while the $^{13}CO_2$ generation will be negligible in the absence of *H. Pylori* infection. The individuals underwent ^{13}C-UBT with and without $NaH^{12}CO_3$ along with ^{13}C-urea. The solution was provided in water (pH~ 7) and the pH at empty stomach is usually in a range of ~5-7 so the overall pH would be near ~7. The time kinetics for ^{13}C-hydrolyzed in ^{13}C-UBT of *H. Pylori* positive and *H. Pylori* negative individuals are shown in Figure 7.6a. The evaluation method of ^{13}C-urea hydrolyzed is provided in section 7.2.4.

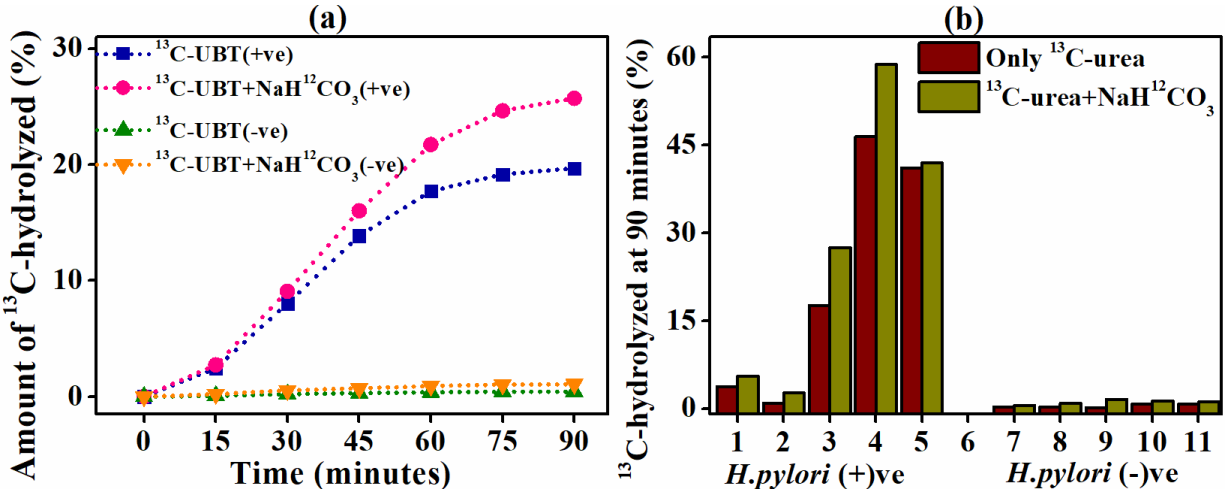

Figure 7.6 a) *Kinetics of ^{13}C-urea hydrolyzed from exhaled $^{13}CO_2$, for H. Pylori positive and negative individuals. An enhancement is observed for ^{13}C-UBT in presence of $NaH^{12}CO_3$ showing a better utilization of the ingested ^{13}C-urea [15].* ***b)*** *Total ^{13}C-urea hydrolyzed at 90 minutes for H. Pylori positive and negative patients showing enhancement in ^{13}C-urea utilization for positive individuals in presence of bicarbonate ions.*

It was observed that the ^{13}C-urea was hydrolyzed more in presence of $NaH^{12}CO_3$ for *H. Pylori* infected (positive) subjects while no significant difference was observed for non-infected (negative) individuals. The total ^{13}C-urea hydrolyzed at 90 minutes for various *H. Pylori* positive and *H. Pylori* negative individuals are shown in Figure 7.6b, where an enhancement is obtained with $NaH^{12}CO_3$ for *H. Pylori* infected patients. These observations validated the previous *in-vitro* result shown in Figure 7.1b and indicated better utilization of the ingested ^{13}C-urea in presence of $NaH^{12}CO_3$. More importantly, the enhanced product would increase the sensitivity of the ^{13}C-UBT for better diagnosis of *H. Pylori* infection. Thus, the proposed new methodology for ^{13}C-UBT possesses the potential for a more sensitive approach towards diagnosing *H. Pylori* infection in humans.

7.4 Conclusion

In the work described in this chapter, we have explored the effect of isotopically varied bicarbonate ions in urease catalysed hydrolysis of urea, through *in-vitro* and *in-vivo* investigations. Initially, we demonstrated the isotope-selective nature of urease activation by $H^{12}CO_3^-$ ions, during the urease-urea reaction using the high-sensitive ICOS technique. We further identified the particular form of bicarbonate ions (i.e. $^{12}CO_2$) responsible for the activation of urease by studying the effect of bicarbonate ions at different pH mediums. Thus, the study helped to take a step towards understanding the interaction of urease enzyme with ligands during urea hydrolysis. It is presumed that such isotopic preference with ligands might be observed in other enzyme–ligand systems and thus remains an open question. We eventually applied these results to the *in-vivo* environment using the urease activity of *H. Pylori* bacteria in human stomach through ^{13}C-UBT. The *in-vivo* results were consistent with the *in-vitro* results which implied enhanced sensitivity of the ^{13}C-UBT through activation of urease in *in-vivo* environment and would open new possibilities for application of this work in future.

7.5 References

[1] Walther, D., M. Ruben and S. Rau. "Carbon dioxide and metal centres: from reactions inspired by nature to reactions in compressed carbon dioxide as solvent." *Coordination Chemistry Reviews* 182, no. 1 (1999): 67-100.

[2] Krajewska, B., R. van Eldik and M. Brindell. "Temperature-and pressure-dependent stopped-flow kinetic studies of jack bean urease. Implications for the catalytic mechanism." *JBIC Journal of Biological Inorganic Chemistry* 17, no. 7 (2012): 1123-1134.

[3] Park, I. S. and R. P. Hausinger. "Requirement of carbon dioxide for in vitro assembly of the urease nickel metallocenter." *Science* 267, no. 5201 (1995): 1156.

[4] Hong, S., J. M. Kuo, L. S. Mullins and F. M. Raushel. "CO_2 Is Required for the Assembly of the Binuclear Metal Center of Phosphotriesterase." *Journal of the American Chemical Society* 117, (1995): 7580-7581.

[5] Butler J. N. in Carbon Dioxide Equilibria and Their Applications (Addison-Wesley, Reading, MA, 1982).

[6] Qin, Y. and J. M. S. Cabral. "Review Properties and Applications of Urease." *Biocatalysis and Biotransformation* 20, no. 1 (2002): 1-14.

[7] Singh, M., N. Verma, A. K. Garg and N. Redhu. "Review: Urea biosensors." *Sensors and Actuators B: Chemical* 134, no. 1 (2008): 345-351.

[8] Mobley, H. L. and R. P. Hausinger. "Microbial ureases: significance, regulation, and molecular characterization." *Microbiology and Molecular Biology Reviews* 53, no. 1 (1989): 85-108.

[9] Maity A., M. Pal, S. Maithani, B. Ghosh, S. Chaudhuri and M. Pradhan, "Molecular hydrogen in human breath: a new strategy for selectively diagnosing peptic ulcer disease, non-ulcerous dyspepsia and *Helicobacter pylori* infection." *Journal of Breath Research* 10, no. 3 (2016), 036007.

[10] Som S., A. Maity, G. D. Banik, C. Ghosh, S. Chaudhuri, S. B. Daschakraborty, S. Ghosh and M. Pradhan. "Excretion kinetics of 13C-urea breath test: influences of endogenous CO2 production and dose recovery on the diagnostic accuracy of *Helicobacter pylori* infection." *Analytical and bioanalytical chemistry* 406, no. 22 (2014): 5405-5412.

[11] Maity, A., G. D. Banik, C. Ghosh, S. Som, S. Chaudhuri, S. B. Daschakraborty, S. Ghosh, B. Ghosh, A. K. Raychaudhuri and M. Pradhan. "Residual gas analyzer mass spectrometry for human breath analysis: a new tool for the non-invasive diagnosis of *Helicobacter pylori* infection." *Journal of breath research* 8, (2014): 016005.

[12] Gisbert, J. P. and J. M. Pajares. "13C-urea breath test in the diagnosis of *Helicobacter pylori* infection—a critical review." *Alimentary pharmacology & therapeutics* 20, (2004): 1001–1017.

[13] Modak, A. S. "Stable isotope breath tests in clinical medicine: a review." *Journal of breath research* 1, no. 1 (2007): 014003.

[14] Dill S., J. J. Payne-James, J. J. Misiewicz, G. K. Grimble, D. McSwiggan, K. Pathak, A. J. Wood, C. M. Scrimgeour and M. J. Rennie. "Evaluation of 13C-urea breath test in the detection of *Helicobacter pylori* and in monitoring the effect of tripotassium dicitratobismuthate in non-ulcer dyspepsia." *Gut* 31, no. 11 (1990): 1237-1241.

[15] Maithani S., A. Maity, M. Pal, S. Bhattacharya, G. D. Banik, C. Ghosh, S. Chaudhuri and M. Pradhan. "Isotopic evidences of the preferential coordination between 12CO2 and urease enzyme." *Chemical Physics* 520, (2019): 21-26.

[16] Buchachenko, A. L. Magnetic isotope effect: Nuclear spin control of chemical reactions." *The Journal of Physical Chemistry A* 105, no. 44 (2001): 9995-10011.

Chapter 8

Summary

and

Future perspectives

8.1 Summary of the thesis

The works in this thesis involved the development and implementation of different variants of the CEAS (CRDS, EW-CRDS and ICOS) technique for spectroscopic study and applications of trace sensing of gaseous and condensed-phase molecules. Firstly, the development and characterization of a QCL based CRDS system in the mid-infrared region of ~ 6.2 μm has been described for high-resolution spectroscopic analysis of ten transition lines of NH_3 molecule. The ability of the system to detect ppbv levels of NH_3 in real samples was demonstrated along with a preliminary study involving the breath analysis of NH_3 in diabetic individuals with signs of kidney malfunction. The same system was utilized to study the high-resolution (~0.001 cm^{-1}) spectra of a larger molecule 1,3-butadiene and ~ 924 spectral lines in the ν_{20} fundamental band were identified. Further, calculations using Gaussian were performed to evaluate the spectroscopic parameters and subsequently PGOPHER simulation was used to simulate the high-resolution ro-vibrational spectra of 1,3-butadiene in the 6.2 μm region. The experimental and the simulated data were compared and ~ 924 lines were spectroscopically assigned. We also identified a narrow region

in 1,3-butadiene spectra free from the spectral interference of other molecules which can be utilized for high-sensitive and selective sensing of 1,3-butadiene in real samples.

We then utilized another CRDS setup with QCL around the 7.8 μm region to study the deuterated isotopes of water in the gas-phase. High-resolution spectra of these isotopes were measured using CRDS and compared to the HITRAN simulated values. Trace levels (~ ppbv) of these deuterated water isotopologues were measured which demonstrated the high-sensitive detection ability of the system. Further, the gas-phase profiles and fractionations of different deuterated isotopes of water were explored in the exchange reaction between D_2O and H_2O. It was inferred that measuring multiple isotopes can serve to accurately detect the deuterium content in real samples such as leaks in heavy water reactors and also provide an assessment of the relative fractionations of the various isotopes in real life systems.

We next discussed the development and characterization of an EW based CRDS setup using a diode laser in the visible region (~ 644 nm) for high-sensitive analysis of condensed phase molecules. The setup combined the high surface-sensitivity of the EW with CRDS technique and was employed to study the interfacial dynamics of salt-induced aggregation of gold and silver nanoparticles. We further demonstrated the effect of protein binding on the aggregation by performing the measurements of urease-corona on the nanoparticles. Thus, such high-sensitive surface analysis could be useful for characterization of biosensors and to monitor surface adsorption of particles and trace molecular species.

We finally utilized a commercial spectrometer based on ICOS technique working in the near-infrared region around 2.05 μm, to measure the isotopes of CO_2 and study the isotope-specific role of CO_2 in the urease catalyzed urea hydrolysis. We studied the product yield of CO_2 produced from isotopically different (^{12}C and ^{13}C) urea substrates and found the

urease activation to be isotopically dependent on $^{12}CO_2$. We further investigated the isotope-specific activation using isotopically-enriched bicarbonate ions in the reaction and explored the roles of the different forms of bicarbonate ions, thus providing a new insight into the catalytic activation of urease. The isotope-specific urease activity was validated in the *in-vivo* environment through ^{13}C-UBT and the sensitivity of the ^{13}C-UBT was shown to be enhanced, thus paving the way for application of this phenomenon to real field problems.

8.2 Future perspectives

In this section, improvements and future prospects of the studies described in this thesis will be discussed.

8.2.1 Study of nuclear spin using the QCL-CRDS systems

The QCL-CRDS setups allow the high-resolution and high-sensitive detection of spectral lines of molecules. Such high-resolution investigation possesses the potential to identify and separate splitting of transition lines (hyperfine splitting) due to nuclear spin and can lead to the determination of related spectroscopic parameters. Symmetric molecules which have identical nuclei cause different combinations of the spins of the nuclei and result in different total spins for the molecule. These are known as nuclear spin isomers of the molecule [1,2]. For example, in hydrogen molecule (H_2) the combination of spins of the two hydrogen nuclei give total nuclear spins of 0 (para) and 1 (ortho). Oftentimes, different isotopes of a molecule also show different nuclear spins, which can be studied. Many molecules and their isotopes whose spectra lie in the region of the QCLs at 6.2 μm and 7.8 μm such as CH_4, D_2O, NH_3, NO_2 etc. can be studied for nuclear spin related spectroscopy.

8.2.2 Improvements and future prospects for the EW-CRDS system

The EW-CRDS setup described in chapter 5 can be improved to obtain better sensitivity. For instance, the ring-down time can be increased by using mirrors with higher reflectivities and the prism size can be reduced to minimize the losses in the cavity. Further, EW-CRDS can be combined with the surface plasmon resonance (SPR) technique (section 1.6.2) by coating a thin film (of nanometre order) of noble metal (such as gold) on the prism surface that can enhance the strength of the EW. Alternately, thin films of noble metal nanoparticles can be suitably coated on the prism to exploit the local SPR sensing of the nanoparticles. However, caution is required for coating the prism as it would also add to the cavity losses. Similarly, various chemical coatings on the prism can be applied which can interact with only a certain chemical species for specific trace molecule detection.

8.2.3 Future possibilities for isotope-specific behaviour of enzymes

In chapters 6 and 7, we discussed the isotope-specific activation of urease enzyme by $^{12}CO_2$ and described its utility in a real-life application. However, this phenomenon also needs to be studied through quantum mechanical simulations to identify the cause for such strong preference for a particular isotope of a ligand ($^{12}CO_2$), by an enzyme. If possible, other experimental techniques such as ^{13}C-nuclear magnetic resonance (NMR) spectroscopy can be used to study this reaction system. Furthermore, this phenomenon can be explored for other enzyme-ligand systems to study the in-depth mechanism of this behaviour which could lead to useful applications in biochemistry.

8.2.4 Future prospects in the field of breath analysis

In chapter 2, a preliminary breath analysis study was described for the measurement of NH_3 in diabetic patients with signs of kidney malfunction where NH_3 levels were enhanced for such patients in comparison to non-diabetic individuals. However, the study had very few participants and a large scale study can be performed with more individuals at different stages in the kidney disease to explore if these stages can be differentiated. Although NH_3 is a well-known biomarker for kidney failure, still early stages of kidney disease are not diagnosed due to asymptomatic nature of the earlier stages. Thus, by examining diabetic individuals which are more prone to kidney malfunction, kidney failure can be prevented and the malfunction can be treated in early stages.

In chapter 7, another breath analysis study was performed to demonstrate the increase in sensitivity of the ^{13}C-UBT. This study can be elaborated with more participants to quantify the enhancement achieved in sensitivity. Moreover, the ^{13}C-urea in ^{13}C-UBT is expensive and it may be possible to suitably reduce the test meal amount and using the bicarbonate simultaneously to retain the current sensitivity of the test, which might reduce the overall cost of the test.

8.3 References

[1] Chapovsky, P. L. "Laser detection of nuclear spin isomers of ethylene molecules." *Quantum Electronics* 49, no. 7 (2019): 623.

[2] Miani, A. and J. Tennyson. "Can ortho–para transitions for water be observed?" *The Journal of chemical physics* 120, no. 6 (2004): 2732-2739.

Appendix 1

Table A1. *Experimental CRDS and PGOPHER simulated spectral line positions for the ν_{20} band of 1,3-butadiene. J", K_a" and K_c" refer to ground state rotational quantum numbers whereas J', K_a' and K_c' refer to the excited state rotational quantum numbers.*

Experimental	Simulated	Experimental – Simulated (Residue)	J"	K_a"	K_c"	J'	K_a'	K_c'
1594.8953	1594.8940	0.0013	9	0	9	8	1	8
1594.9071	1594.9069	0.0002	17	3	14	18	2	17
1594.9214	1594.9277	-0.0062	7	1	6	7	0	7
1594.9214	1594.9320	-0.0106	41	4	37	40	5	36
1594.9483	1594.9601	-0.0117	35	5	30	36	4	33
1594.9617	1594.9642	-0.0025	5	1	4	4	1	3
1594.9617	1594.9704	-0.0087	44	6	39	45	5	40
1594.9617	1594.9667	-0.0050	5	4	2	4	4	1
1594.9617	1594.9667	-0.0050	5	4	1	4	4	0
1594.9745	1594.9867	-0.0122	6	1	5	6	0	6
1594.9745	1594.9904	-0.0159	5	2	3	4	2	2
1594.9745	1594.9848	-0.0103	36	3	34	35	4	31
1594.9921	1595.0035	-0.0113	5	0	5	4	0	4
1595.2264	1595.2249	0.0014	8	0	8	7	1	7
1595.2264	1595.2296	-0.0032	27	4	23	28	3	26
1595.2264	1595.2278	-0.0014	36	5	31	37	4	34
1595.2264	1595.2293	-0.0029	22	22	0	22	22	1
1595.2264	1595.2293	-0.0029	22	22	1	22	22	0
1595.2495	1595.2443	0.0052	36	2	35	35	3	32
1595.2495	1595.2464	0.0031	27	21	6	27	21	7
1595.2495	1595.2464	0.0031	27	21	7	27	21	6
1595.2495	1595.2444	0.0051	32	20	13	32	20	12
1595.2495	1595.2444	0.0051	32	20	12	32	20	13
1595.2645	1595.2699	-0.0054	45	6	40	46	5	41
1595.2645	1595.2651	-0.0006	4	3	2	3	3	1
1595.2645	1595.2651	-0.0006	4	3	1	3	3	0
1595.2645	1595.2625	0.0020	26	21	6	26	21	5
1595.2645	1595.2625	0.0020	26	21	5	26	21	6
1595.2645	1595.2635	0.0010	31	20	12	31	20	11

1595.2645	1595.2635	0.0010	31	20	11	31	20	12
1595.2645	1595.2668	-0.0022	35	19	16	35	19	17
1595.2645	1595.2668	-0.0022	35	19	17	35	19	16
1595.2801	1595.2761	0.0039	4	2	3	3	2	2
1595.2801	1595.2749	0.0051	4	2	2	3	2	1
1595.2801	1595.2783	0.0017	32	2	31	31	3	28
1595.2801	1595.2780	0.0020	25	21	4	25	21	5
1595.2801	1595.2780	0.0020	25	21	5	25	21	4
1595.2801	1595.2820	-0.0019	30	20	11	30	20	10
1595.2801	1595.2820	-0.0019	30	20	10	30	20	11
1595.2912	1595.2858	0.0054	4	0	4	3	0	3
1595.2912	1595.2876	0.0036	34	19	16	34	19	15
1595.2912	1595.2876	0.0036	34	19	15	34	19	16
1595.3151	1595.3094	0.0058	11	2	9	12	1	12
1595.3151	1595.3073	0.0078	23	21	3	23	21	2
1595.3151	1595.3073	0.0078	23	21	2	23	21	3
1595.3151	1595.3079	0.0072	33	19	14	33	19	15
1595.3151	1595.3079	0.0072	33	19	15	33	19	14
1595.3261	1595.3252	0.0009	40	4	36	39	5	35
1595.3261	1595.3210	0.0051	22	21	1	22	21	2
1595.3261	1595.3210	0.0051	22	21	2	22	21	1
1595.3261	1595.3218	0.0043	49	5	45	48	6	42
1595.3261	1595.3172	0.0089	28	20	9	28	20	8
1595.3261	1595.3172	0.0089	28	20	8	28	20	9
1595.3261	1595.3242	0.0019	36	18	19	36	18	18
1595.3261	1595.3242	0.0019	36	18	18	36	18	19
1595.3406	1595.3341	0.0064	21	21	1	21	21	0
1595.3406	1595.3341	0.0064	21	21	0	21	21	1
1595.3406	1595.3339	0.0067	27	20	8	27	20	7
1595.3406	1595.3339	0.0067	27	20	7	27	20	8
1595.3406	1595.3309	0.0096	39	17	23	39	17	22
1595.3406	1595.3309	0.0096	39	17	22	39	17	23
1595.4048	1595.4085	-0.0036	22	20	2	22	20	3
1595.4048	1595.4085	-0.0036	22	20	3	22	20	2
1595.4048	1595.4090	-0.0042	46	6	40	47	5	43
1595.4048	1595.4065	-0.0017	32	18	14	32	18	15
1595.4048	1595.4065	-0.0017	32	18	15	32	18	14
1595.4151	1595.4216	-0.0065	21	20	1	21	20	2
1595.4151	1595.4216	-0.0065	21	20	2	21	20	1
1595.4151	1595.4171	-0.0020	27	19	8	27	19	9
1595.4151	1595.4171	-0.0020	27	19	9	27	19	8
1595.4151	1595.4256	-0.0105	31	18	14	31	18	13
1595.4151	1595.4256	-0.0105	31	18	13	31	18	14

1595.4151	1595.4204	-0.0053	35	17	18	35	17	19
1595.4151	1595.4204	-0.0053	35	17	19	35	17	18
1595.4151	1595.4246	-0.0095	38	16	23	38	16	22
1595.4151	1595.4246	-0.0095	38	16	22	38	16	23
1595.4252	1595.4341	-0.0089	20	20	1	20	20	0
1595.4252	1595.4341	-0.0089	20	20	0	20	20	1
1595.4252	1595.4294	-0.0042	30	2	29	29	3	26
1595.4252	1595.4332	-0.0080	26	19	7	26	19	8
1595.4252	1595.4332	-0.0080	26	19	8	26	19	7
1595.4566	1595.4624	-0.0058	34	3	32	33	4	29
1595.4566	1595.4636	-0.0070	24	19	6	24	19	5
1595.4566	1595.4636	-0.0070	24	19	5	24	19	6
1595.4566	1595.4620	-0.0053	29	18	12	29	18	11
1595.4566	1595.4620	-0.0053	29	18	11	29	18	12
1595.4566	1595.4615	-0.0049	33	17	16	33	17	17
1595.4566	1595.4615	-0.0049	33	17	17	33	17	16
1595.4566	1595.4675	-0.0109	39	15	24	39	15	25
1595.4566	1595.4675	-0.0109	39	15	25	39	15	24
1595.4894	1595.4782	0.0112	28	4	24	29	3	27
1595.4894	1595.4815	0.0079	36	5	32	37	4	33
1595.4894	1595.4779	0.0115	23	19	4	23	19	5
1595.4894	1595.4779	0.0115	23	19	5	23	19	4
1595.4894	1595.4793	0.0101	28	18	11	28	18	10
1595.4894	1595.4793	0.0101	28	18	10	28	18	11
1595.4894	1595.4812	0.0082	32	17	15	32	17	16
1595.4894	1595.4812	0.0082	32	17	16	32	17	15
1595.4894	1595.4812	0.0082	41	14	28	41	14	27
1595.4894	1595.4812	0.0082	41	14	27	41	14	28
1595.5020	1595.4934	0.0087	37	5	32	38	4	35
1595.5020	1595.4916	0.0104	22	19	3	22	19	4
1595.5020	1595.4916	0.0104	22	19	4	22	19	3
1595.5020	1595.4960	0.0061	27	18	9	27	18	10
1595.5020	1595.4960	0.0061	27	18	10	27	18	9
1595.5020	1595.4908	0.0113	35	16	20	35	16	19
1595.5020	1595.4908	0.0113	35	16	19	35	16	20
1595.5020	1595.4908	0.0113	38	15	23	38	15	24
1595.5020	1595.4908	0.0113	38	15	24	38	15	23
1595.5020	1595.4882	0.0138	43	13	31	43	13	30
1595.5222	1595.5173	0.0049	20	19	2	20	19	1
1595.5222	1595.5173	0.0049	20	19	1	20	19	2
1595.5222	1595.5188	0.0035	30	17	13	30	17	14
1595.5222	1595.5188	0.0035	30	17	14	30	17	13
1595.5222	1595.5138	0.0084	42	13	30	42	13	29

1595.5222	1595.5138	0.0084	42	13	29	42	13	30
1595.5299	1595.5292	0.0007	19	19	1	19	19	0
1595.5299	1595.5292	0.0007	19	19	0	19	19	1
1595.5299	1595.5276	0.0023	25	18	8	25	18	7
1595.5299	1595.5276	0.0023	25	18	7	25	18	8
1595.5299	1595.5319	-0.0020	33	16	18	33	16	17
1595.5299	1595.5319	-0.0020	33	16	17	33	16	18
1595.5299	1595.5294	0.0005	39	14	26	39	14	25
1595.5299	1595.5294	0.0005	39	14	25	39	14	26
1595.7603	1595.7532	0.0071	19	16	3	19	16	4
1595.7603	1595.7532	0.0071	19	16	4	19	16	3
1595.7603	1595.7537	0.0066	24	15	9	24	15	10
1595.7603	1595.7537	0.0066	24	15	10	24	15	9
1595.7603	1595.7563	0.0040	38	5	33	39	4	36
1595.7603	1595.7523	0.0080	28	14	14	28	14	15
1595.7603	1595.7523	0.0080	28	14	15	28	14	14
1595.7603	1595.7563	0.0040	31	13	19	31	13	18
1595.7603	1595.7563	0.0040	31	13	18	31	13	19
1595.7603	1595.7507	0.0097	34	12	22	34	12	23
1595.7702	1595.7645	0.0056	18	16	2	18	16	3
1595.7702	1595.7645	0.0056	18	16	3	18	16	2
1595.7702	1595.7680	0.0022	23	15	8	23	15	9
1595.7702	1595.7680	0.0022	23	15	9	23	15	8
1595.7702	1595.7690	0.0011	27	14	14	27	14	13
1595.7702	1595.7690	0.0011	27	14	13	27	14	14
1595.7702	1595.7709	-0.0008	33	12	21	33	12	22
1595.7702	1595.7709	-0.0008	33	12	22	33	12	21
1595.7810	1595.7753	0.0057	17	16	2	17	16	1
1595.7810	1595.7753	0.0057	17	16	1	17	16	2
1595.7810	1595.7740	0.0070	40	4	37	39	5	34
1595.7810	1595.7748	0.0062	30	13	17	30	13	18
1595.7810	1595.7748	0.0062	30	13	18	30	13	17
1595.7810	1595.7750	0.0059	15	2	13	16	1	16
1595.7810	1595.7789	0.0020	35	11	25	35	11	24
1595.7810	1595.7789	0.0020	35	11	24	35	11	25
1595.8044	1595.8074	-0.0030	20	15	5	20	15	6
1595.8044	1595.8074	-0.0030	20	15	6	20	15	5
1595.8044	1595.8045	-0.0002	27	2	26	26	3	23
1595.8044	1595.8099	-0.0056	28	13	16	28	13	15
1595.8044	1595.8099	-0.0056	28	13	15	28	13	16
1595.8044	1595.8097	-0.0053	31	12	19	31	12	20
1595.8044	1595.8097	-0.0053	31	12	20	31	12	19
1595.8336	1595.8414	-0.0078	17	15	2	17	15	3

1595.8336	1595.8414	-0.0078	17	15	3	17	15	2
1595.8336	1595.8436	-0.0100	22	14	8	22	14	9
1595.8336	1595.8436	-0.0100	22	14	9	22	14	8
1595.8336	1595.8427	-0.0091	26	13	14	26	13	13
1595.8336	1595.8427	-0.0091	26	13	13	26	13	14
1595.8336	1595.8460	-0.0124	29	12	18	29	12	17
1595.8336	1595.8460	-0.0124	29	12	17	29	12	18
1595.8336	1595.8435	-0.0099	16	2	14	17	1	17
1595.8336	1595.8397	-0.0061	32	11	22	32	11	21
1595.8521	1595.8611	-0.0090	15	15	1	15	15	0
1595.8521	1595.8611	-0.0090	15	15	0	15	15	1
1595.8521	1595.8567	-0.0046	21	14	7	21	14	8
1595.8521	1595.8567	-0.0046	21	14	8	21	14	7
1595.8521	1595.8582	-0.0062	25	13	13	25	13	12
1595.8521	1595.8582	-0.0062	25	13	12	25	13	13
1595.8521	1595.8633	-0.0112	28	12	17	28	12	16
1595.8521	1595.8633	-0.0112	28	12	16	28	12	17
1595.8521	1595.8588	-0.0067	31	11	21	31	11	20
1595.8521	1595.8588	-0.0067	31	11	20	31	11	21
1595.8837	1595.8812	0.0025	19	14	6	19	14	5
1595.8837	1595.8812	0.0025	19	14	5	19	14	6
1595.8837	1595.8800	0.0037	27	12	16	27	12	15
1595.8837	1595.8800	0.0037	27	12	15	27	12	16
1595.8837	1595.8772	0.0065	30	11	19	30	11	20
1595.8837	1595.8772	0.0065	30	11	20	30	11	19
1595.8837	1595.8827	0.0010	47	6	42	48	5	43
1595.8837	1595.8846	-0.0008	32	10	23	32	10	22
1595.8837	1595.8846	-0.0008	32	10	22	32	10	23
1595.8837	1595.8853	-0.0016	34	9	26	34	9	25
1595.8980	1595.9032	-0.0052	17	14	4	17	14	3
1595.8980	1595.9032	-0.0052	17	14	3	17	14	4
1595.8980	1595.9012	-0.0032	22	13	9	22	13	10
1595.8980	1595.9012	-0.0032	22	13	10	22	13	9
1595.8980	1595.9036	-0.0056	31	10	22	31	10	21
1595.8980	1595.9036	-0.0056	31	10	21	31	10	22
1595.9686	1595.9805	-0.0119	15	13	3	15	13	2
1595.9686	1595.9805	-0.0119	15	13	2	15	13	3
1595.9686	1595.9802	-0.0116	20	12	8	20	12	9
1595.9686	1595.9802	-0.0116	20	12	9	20	12	8
1595.9686	1595.9786	-0.0100	47	5	43	46	6	40
1595.9686	1595.9805	-0.0119	29	9	21	29	9	20
1595.9686	1595.9805	-0.0119	29	9	20	29	9	21
1595.9893	1595.9895	-0.0002	14	13	2	14	13	1

1595.9893	1595.9895	-0.0002	14	13	1	14	13	2
1595.9893	1595.9921	-0.0028	19	12	7	19	12	8
1595.9893	1595.9921	-0.0028	19	12	8	19	12	7
1595.9893	1595.9912	-0.0019	21	2	19	20	3	18
1595.9893	1595.9899	-0.0006	23	11	12	23	11	13
1595.9893	1595.9899	-0.0006	23	11	13	23	11	12
1595.9893	1595.9900	-0.0007	26	10	17	26	10	16
1595.9893	1595.9900	-0.0007	26	10	16	26	10	17
1596.0033	1596.0034	-0.0002	18	12	7	18	12	6
1596.0033	1596.0034	-0.0002	18	12	6	18	12	7
1596.0033	1596.0036	-0.0003	22	11	12	22	11	11
1596.0033	1596.0036	-0.0003	22	11	11	22	11	12
1596.0033	1596.0055	-0.0022	25	10	16	25	10	15
1596.0033	1596.0055	-0.0022	25	10	15	25	10	16
1596.0125	1596.0142	-0.0016	17	12	6	17	12	5
1596.0125	1596.0142	-0.0016	17	12	5	17	12	6
1596.0125	1596.0167	-0.0042	21	11	10	21	11	11
1596.0125	1596.0167	-0.0042	21	11	11	21	11	10
1596.0125	1596.0183	-0.0058	28	4	25	29	3	26
1596.0125	1596.0162	-0.0036	39	5	34	40	4	37
1596.0125	1596.0145	-0.0019	27	9	19	27	9	18
1596.0125	1596.0145	-0.0019	27	9	18	27	9	19
1596.0125	1596.0169	-0.0043	29	8	22	29	8	21
1596.0125	1596.0169	-0.0043	29	8	21	29	8	22
1598.3135	1598.3097	0.0037	6	1	6	7	1	7
1598.3135	1598.3108	0.0027	6	5	2	7	5	3
1598.3135	1598.3108	0.0027	6	5	1	7	5	2
1598.3364	1598.3301	0.0063	6	4	3	7	4	4
1598.3364	1598.3301	0.0063	6	4	2	7	4	3
1598.3364	1598.3336	0.0028	6	1	5	5	2	4
1598.3449	1598.3454	-0.0005	6	3	4	7	3	5
1598.3449	1598.3455	-0.0006	6	3	3	7	3	4
1598.3449	1598.3444	0.0005	16	2	15	17	1	16
1598.3607	1598.3568	0.0039	6	0	6	7	0	7
1598.3607	1598.3542	0.0066	6	2	5	7	2	6
1598.3829	1598.3788	0.0041	13	0	13	13	1	12
1598.4001	1598.4101	-0.0099	6	1	5	7	1	6
1598.5145	1598.5066	0.0080	14	0	14	14	1	13
1598.5596	1598.5658	-0.0062	31	4	28	30	5	25
1598.5596	1598.5637	-0.0041	7	6	2	8	6	3
1598.5596	1598.5637	-0.0041	7	6	1	8	6	2
1598.8101	1598.8028	0.0072	16	0	16	16	1	15
1598.8324	1598.8237	0.0087	22	3	20	21	4	17

1598.8324	1598.8258	0.0066	30	4	26	29	5	25
1598.8428	1598.8455	-0.0027	8	1	8	9	1	9
1598.8640	1598.8632	0.0008	8	5	4	9	5	5
1598.8640	1598.8632	0.0008	8	5	3	9	5	4
1598.8640	1598.8609	0.0030	13	2	11	12	3	10
1598.8740	1598.8757	-0.0017	30	4	27	29	5	24
1598.8740	1598.8784	-0.0044	38	5	33	37	6	32
1598.8740	1598.8787	-0.0047	46	6	40	45	7	39
1598.8828	1598.8828	-0.0000	8	4	5	9	4	6
1598.8828	1598.8828	-0.0000	8	4	4	9	4	5
1598.8828	1598.8870	-0.0042	46	6	41	45	7	38
1598.9012	1598.9012	0.0000	8	0	8	9	0	9
1598.9012	1598.8984	0.0028	8	3	6	9	3	7
1598.9012	1598.8987	0.0025	8	3	5	9	3	6
1598.9012	1598.8992	0.0020	38	5	34	37	6	31
1598.9263	1598.9195	0.0068	8	2	6	9	2	7
1598.9374	1598.9336	0.0037	26	3	24	27	2	25
1598.9552	1598.9588	-0.0036	4	0	4	5	1	5
1598.9743	1598.9720	0.0024	17	0	17	17	1	16
1598.9743	1598.9746	-0.0003	8	1	7	9	1	8
1599.0466	1599.0549	-0.0083	9	8	1	10	8	2
1599.0466	1599.0549	-0.0083	9	8	2	10	8	3
1599.0835	1599.0870	-0.0034	9	7	2	10	7	3
1599.0835	1599.0870	-0.0034	9	7	3	10	7	4
1599.2587	1599.2555	0.0031	9	1	8	10	1	9
1599.3490	1599.3522	-0.0032	19	0	19	19	1	18
1599.3490	1599.3557	-0.0067	27	3	25	28	2	26
1599.3490	1599.3506	-0.0015	20	3	17	19	4	16
1599.3585	1599.3617	-0.0032	10	7	4	11	7	5
1599.3585	1599.3617	-0.0032	10	7	3	11	7	4
1599.3713	1599.3778	-0.0065	10	1	10	11	1	11
1599.3790	1599.3896	-0.0106	10	6	5	11	6	6
1599.3790	1599.3896	-0.0106	10	6	4	11	6	5
1599.4064	1599.4134	-0.0070	10	5	6	11	5	7
1599.4064	1599.4134	-0.0070	10	5	5	11	5	6
1599.4064	1599.4144	-0.0080	20	3	18	19	4	15
1599.4358	1599.4333	0.0025	10	4	7	11	4	8
1599.4358	1599.4333	0.0025	10	4	6	11	4	7
1599.4612	1599.4469	0.0143	20	1	19	20	2	18
1599.4612	1599.4502	0.0110	19	1	18	19	2	17
1599.4612	1599.4527	0.0086	10	2	9	11	2	10
1599.4612	1599.4494	0.0118	10	3	8	11	3	9
1599.4612	1599.4503	0.0110	10	3	7	11	3	8

1599.4935	1599.4928	0.0007	19	2	18	20	1	19
1599.4935	1599.4927	0.0008	28	4	25	27	5	22
1599.4935	1599.4923	0.0012	11	2	9	10	3	8
1599.5079	1599.5100	-0.0021	23	1	22	23	2	21
1599.5170	1599.5196	-0.0026	16	1	15	16	2	14
1599.5350	1599.5355	-0.0006	10	1	9	11	1	10
1599.5350	1599.5343	0.0007	36	5	32	35	6	29
1599.5510	1599.5580	-0.0069	24	1	23	24	2	22
1599.5510	1599.5588	-0.0078	15	1	14	15	2	13
1599.7583	1599.7593	-0.0010	11	2	9	12	2	10
1599.7583	1599.7628	-0.0045	11	1	10	11	2	9
1599.8000	1599.7920	0.0079	27	1	26	27	2	25
1599.8098	1599.7997	0.0101	27	4	24	26	5	21
1599.8098	1599.8001	0.0096	12	10	3	13	10	4
1599.8098	1599.8001	0.0096	12	10	2	13	10	3
1599.8098	1599.7986	0.0111	10	2	8	9	3	7
1599.8189	1599.8200	-0.0011	14	1	14	15	0	15
1599.8189	1599.8188	0.0001	10	1	9	10	2	8
1599.8487	1599.8408	0.0080	12	9	3	13	9	4
1599.8487	1599.8408	0.0080	12	9	4	13	9	5
1599.8487	1599.8404	0.0084	35	5	30	34	6	29
1599.8805	1599.8742	0.0063	9	1	8	9	2	7
1599.8805	1599.8796	0.0009	20	2	19	21	1	20
1599.8805	1599.8772	0.0033	12	8	5	13	8	6
1599.8805	1599.8772	0.0033	12	8	4	13	8	5
1599.9073	1599.9065	0.0008	12	1	12	13	1	13
1599.9073	1599.9094	-0.0020	12	7	6	13	7	7
1599.9073	1599.9094	-0.0020	12	7	5	13	7	6
1599.9343	1599.9375	-0.0032	12	6	7	13	6	8
1599.9343	1599.9375	-0.0032	12	6	6	13	6	7
1599.9257	1599.9276	-0.0019	8	1	7	8	2	6
1599.9692	1599.9615	0.0076	12	5	8	13	5	9
1599.9692	1599.9615	0.0076	12	5	7	13	5	8
1599.9777	1599.9699	0.0078	12	0	12	13	0	13
1599.9893	1599.9818	0.0075	12	4	9	13	4	10
1599.9893	1599.9819	0.0075	12	4	8	13	4	9
1599.9893	1599.9781	0.0112	7	1	6	7	2	5
1600.0029	1599.9970	0.0059	12	2	11	13	2	12
1600.0029	1599.9984	0.0045	12	3	10	13	3	11
1600.0029	1600.0004	0.0025	12	3	9	13	3	10
1600.0361	1600.0398	-0.0037	12	2	10	13	2	11
1600.0898	1600.0925	-0.0027	12	1	11	13	1	12
1600.0898	1600.0891	0.0006	26	4	22	25	5	21

1600.0795	1600.0805	-0.0010	9	0	9	10	1	10
1600.0679	1600.0730	-0.0051	13	10	4	14	10	5
1600.0679	1600.0730	-0.0051	13	10	3	14	10	4
1600.3801	1600.3693	0.0108	13	1	12	14	1	13
1600.3964	1600.3860	0.0104	14	9	6	15	9	7
1600.3964	1600.3860	0.0104	14	9	5	15	9	6
1600.4118	1600.4134	-0.0016	8	1	8	8	2	7
1600.4118	1600.4100	0.0018	25	4	22	24	5	19
1600.4249	1600.4225	0.0024	14	8	7	15	8	8
1600.4249	1600.4225	0.0024	15	8	7	14	8	6
1600.4249	1600.4274	-0.0025	49	5	45	50	4	46
1600.4323	1600.4316	0.0007	14	1	14	15	1	15
1600.4555	1600.4538	0.0017	16	1	16	17	0	17
1600.4555	1600.4548	0.0006	14	7	8	15	7	9
1600.4555	1600.4548	0.0006	14	7	7	15	7	8
1600.4809	1600.4831	-0.0022	14	6	9	15	6	10
1600.4809	1600.4831	-0.0022	14	6	8	15	6	9
1600.5081	1600.5070	0.0011	32	1	31	32	2	30
1600.5081	1600.5075	0.0006	14	5	10	15	5	11
1600.5081	1600.5075	0.0006	14	5	9	15	5	10
1600.5264	1600.5284	-0.0020	14	4	11	15	4	12
1600.5264	1600.5285	-0.0021	14	4	10	15	4	11
1600.5264	1600.5260	0.0004	24	0	24	24	1	23
1600.5487	1600.5455	0.0033	14	3	12	15	3	13
1600.5487	1600.5495	-0.0008	14	3	11	15	3	12
1600.5982	1600.6017	-0.0036	14	2	12	15	2	13
1600.8261	1600.8258	0.0003	35	2	33	35	3	32
1600.8261	1600.8269	-0.0008	38	2	36	38	3	35
1600.8261	1600.8237	0.0024	15	3	12	16	3	13
1600.8556	1600.8561	-0.0005	34	2	32	34	3	31
1600.8556	1600.8607	-0.0050	39	2	37	39	3	36
1600.8818	1600.8830	-0.0012	15	2	13	16	2	14
1600.8991	1600.9000	-0.0009	33	2	31	33	3	30
1600.8991	1600.9034	-0.0043	13	0	13	14	1	14
1600.9042	1600.9124	-0.0082	40	2	38	40	3	37
1600.9042	1600.9083	-0.0041	34	1	33	34	2	32
1600.9281	1600.9290	-0.0008	16	9	7	17	9	8
1600.9281	1600.9290	-0.0008	16	9	8	17	9	9
1600.9619	1600.9563	0.0056	32	2	30	32	3	29
1600.9619	1600.9531	0.0089	16	1	16	17	1	17
1600.9711	1600.9656	0.0055	16	8	9	17	8	10
1600.9711	1600.9656	0.0055	16	8	8	17	8	9
1601.0246	1601.0237	0.0008	31	2	29	31	3	28

1601.0246	1601.0266	-0.0020	16	6	11	17	6	12
1601.0246	1601.0266	-0.0020	16	6	10	17	6	11
1601.0473	1601.0514	-0.0040	16	5	12	17	5	13
1601.0473	1601.0514	-0.0041	16	5	11	17	5	12
1601.0687	1601.0753	-0.0065	16	2	15	17	2	16
1601.0687	1601.0725	-0.0038	18	1	18	19	0	19
1601.0687	1601.0730	-0.0043	16	4	13	17	4	14
1601.0687	1601.0732	-0.0045	16	4	12	17	4	13
1601.0687	1601.0714	-0.0026	42	2	40	42	3	39
1601.0976	1601.1009	-0.0034	30	2	28	30	3	27
1601.0976	1601.0979	-0.0003	16	3	13	17	3	14
1601.3470	1601.3425	0.0045	17	2	16	18	2	17
1601.3470	1601.3446	0.0024	17	4	14	18	4	15
1601.3470	1601.3450	0.0009	27	0	27	27	1	26
1601.3587	1601.3620	-0.0033	17	3	15	18	3	16
1601.3733	1601.3753	-0.0020	19	1	19	20	0	20
1601.3733	1601.3760	-0.0026	27	2	25	27	3	24
1601.3733	1601.3720	0.0014	17	3	14	18	3	15
1601.3733	1601.3701	0.0032	36	1	35	36	2	34
1601.4184	1601.4283	-0.0099	24	2	23	25	1	24
1601.4184	1601.4288	-0.0104	18	10	8	19	10	9
1601.4184	1601.4288	-0.0104	18	10	9	19	10	10
1601.4390	1601.4453	-0.0063	17	2	15	18	2	16
1601.4514	1601.4533	-0.0020	45	2	43	45	3	42
1601.4514	1601.4525	-0.0011	19	1	19	19	2	18
1601.5028	1601.5102	-0.0074	16	0	16	17	1	17
1601.5028	1601.5064	-0.0036	18	8	11	19	8	12
1601.5028	1601.5064	-0.0036	18	8	10	19	8	11
1601.4878	1601.4926	-0.0048	19	14	5	20	14	6
1601.4878	1601.4926	-0.0048	19	14	6	20	14	7
1601.5159	1601.5224	-0.0065	18	0	18	19	0	19
1601.5281	1601.5391	-0.0110	18	7	12	19	7	13
1601.5281	1601.5391	-0.0110	18	7	11	19	7	12
1601.5444	1601.5504	-0.0059	19	13	7	20	13	8
1601.5444	1601.5504	-0.0059	19	13	6	20	13	7
1601.5769	1601.5679	0.0089	18	6	13	19	6	14
1601.5769	1601.5679	0.0089	18	6	12	19	6	13
1601.6148	1601.6158	-0.0010	18	4	15	19	4	16
1601.6148	1601.6163	-0.0015	18	4	14	19	4	15
1601.6148	1601.6191	-0.0042	46	2	44	46	3	43
1601.7798	1601.7762	0.0035	19	0	19	20	0	20
1601.7798	1601.7760	0.0038	19	8	12	20	8	13
1601.7798	1601.7760	0.0038	19	8	11	20	8	12

1601.8013	1601.8088	-0.0074	19	7	13	20	7	14
1601.8013	1601.8088	-0.0074	19	7	12	20	7	13
1601.8013	1601.8119	-0.0105	25	2	24	26	1	25
1601.8306	1601.8378	-0.0072	19	6	14	20	6	15
1601.8306	1601.8378	-0.0072	19	6	13	20	6	14
1601.8670	1601.8634	0.0035	19	5	15	20	5	16
1601.8670	1601.8635	0.0035	19	5	14	20	5	15
1601.8778	1601.8741	0.0038	19	2	18	20	2	19
1601.8778	1601.8726	0.0052	20	12	9	21	12	10
1601.8778	1601.8726	0.0052	20	12	8	21	12	9
1601.8999	1601.8865	0.0134	19	4	16	20	4	17
1601.8999	1601.8872	0.0127	19	4	15	20	4	16
1601.8999	1601.8841	0.0158	22	2	20	22	3	19
1601.8999	1601.8851	0.0148	38	1	37	38	2	36
1601.9173	1601.9202	-0.0029	19	3	16	20	3	17
1601.9173	1601.9207	-0.0034	18	0	18	19	1	19
1601.9173	1601.9207	-0.0034	29	0	29	29	1	28
1601.9173	1601.9219	-0.0047	20	11	9	21	11	10
1601.9173	1601.9219	-0.0047	20	11	10	21	11	11
1601.9731	1601.9674	0.0057	21	1	21	22	0	22
1601.9731	1601.9671	0.0060	20	10	11	21	10	12
1601.9731	1601.9671	0.0060	20	10	10	21	10	11
1602.0181	1602.0031	0.0150	19	1	18	20	1	19
1602.0181	1602.0065	0.0116	19	2	17	20	2	18
1602.0181	1602.0064	0.0117	48	2	46	48	3	45
1602.0181	1602.0081	0.0101	20	9	11	21	9	12
1602.0181	1602.0081	0.0101	20	9	12	21	9	13
1602.0491	1602.0450	0.0041	20	8	13	21	8	14
1602.0491	1602.0450	0.0041	20	8	12	21	8	13
1602.0755	1602.0779	-0.0025	20	7	14	21	7	15
1602.0755	1602.0779	-0.0025	20	7	13	21	7	14
1602.1259	1602.1292	-0.0033	19	0	19	20	1	20
1602.1259	1602.1331	-0.0072	20	5	16	21	5	17
1602.1259	1602.1332	-0.0073	20	5	15	21	5	16
1602.1358	1602.1384	-0.0025	20	2	19	21	2	20
1602.1358	1602.1408	-0.0050	21	12	10	22	12	11
1602.1358	1602.1408	-0.0050	21	12	9	22	12	10
1602.3264	1602.3134	0.0129	21	8	14	22	8	15
1602.3264	1602.3134	0.0129	21	8	13	22	8	14
1602.3406	1602.3403	0.0003	20	0	20	21	1	21
1602.3518	1602.3465	0.0053	21	7	15	22	7	16
1602.3518	1602.3465	0.0053	21	7	14	22	7	15
1602.3835	1602.3760	0.0075	21	6	16	22	6	17

1602.3835	1602.3760	0.0075	21	6	15	22	6	16
1602.4016	1602.4017	-0.0001	21	2	20	22	2	21
1602.4016	1602.4024	-0.0008	21	5	17	22	5	18
1602.4016	1602.4024	-0.0008	21	5	16	22	5	17
1602.4227	1602.4265	-0.0038	21	4	18	22	4	19
1602.4227	1602.4279	-0.0052	21	4	17	22	4	18
1602.4227	1602.4259	-0.0032	15	2	13	15	3	12
1602.4227	1602.4247	-0.0020	8	1	7	9	2	8
1602.4435	1602.4424	0.0011	21	3	19	22	3	20
1602.4435	1602.4434	0.0001	40	1	39	40	2	38
1602.4651	1602.4689	-0.0038	21	3	18	22	3	19
1602.4973	1602.5031	-0.0058	22	10	12	23	10	13
1602.4973	1602.5031	-0.0058	22	10	13	23	10	14
1602.4973	1602.5057	-0.0084	31	0	31	31	1	30
1602.4973	1602.5020	-0.0047	23	15	8	24	15	9
1602.4973	1602.5020	-0.0047	23	15	9	24	15	10
1602.4973	1602.5060	-0.0087	18	4	14	17	5	13
1602.4868	1602.4954	-0.0086	22	1	22	23	1	23
1602.5343	1602.5319	0.0024	22	0	22	23	0	23
1602.5343	1602.5355	-0.0012	21	1	20	22	1	21
1602.5508	1602.5414	0.0094	23	1	23	24	0	24
1602.5508	1602.5442	0.0065	22	9	14	23	9	15
1602.5508	1602.5442	0.0065	22	9	13	23	9	14
1602.5508	1602.5409	0.0099	26	1	26	26	2	25
1602.5611	1602.5541	0.0070	21	0	21	22	1	22
1602.5611	1602.5533	0.0078	12	2	10	12	3	9
1602.5735	1602.5653	0.0082	21	2	19	22	2	20
1602.5735	1602.5689	0.0046	27	2	26	28	1	27
1602.5867	1602.5813	0.0053	22	8	15	23	8	16
1602.5867	1602.5813	0.0053	22	8	14	23	8	15
1602.5867	1602.5831	0.0036	11	2	9	11	3	8
1602.6213	1602.6146	0.0067	22	7	16	23	7	17
1602.6213	1602.6146	0.0067	22	7	15	23	7	16
1602.7983	1602.7991	-0.0008	22	1	21	23	1	22
1602.7983	1602.7993	-0.0010	32	0	32	32	1	31
1602.8054	1602.8128	-0.0074	21	2	20	21	3	19
1602.8054	1602.8115	-0.0061	23	9	15	24	9	16
1602.8054	1602.8115	-0.0061	23	9	14	24	9	15
1602.8160	1602.8220	-0.0060	24	1	24	25	0	25
1602.8519	1602.8492	0.0026	22	2	21	22	3	20
1602.8519	1602.8487	0.0032	23	8	16	24	8	17
1602.8519	1602.8487	0.0032	23	8	15	24	8	16
1602.8664	1602.8664	0.0000	36	2	34	35	3	33

1602.8815	1602.8821	-0.0006	23	7	17	24	7	18
1602.8815	1602.8821	-0.0006	23	7	16	24	7	17
1602.8949	1602.8909	0.0040	23	2	22	23	3	21
1602.8949	1602.8883	0.0066	24	13	11	25	13	12
1602.8949	1602.8883	0.0066	24	13	12	25	13	13
1602.9121	1602.9121	-0.0000	23	6	18	24	6	19
1602.9121	1602.9121	-0.0001	23	6	17	24	6	18
1602.9330	1602.9252	0.0078	23	2	22	24	2	23
1602.9496	1602.9394	0.0103	23	5	19	24	5	20
1602.9496	1602.9394	0.0102	23	5	18	24	5	19
1602.9496	1602.9382	0.0115	24	2	23	24	3	22
1602.9496	1602.9407	0.0089	28	2	27	29	1	28
1602.9496	1602.9420	0.0076	24	12	12	25	12	13
1602.9496	1602.9420	0.0076	24	12	13	25	12	14
1602.9719	1602.9647	0.0072	23	4	20	24	4	21
1602.9719	1602.9673	0.0046	23	4	19	24	4	20
1602.9968	1602.9902	0.0067	23	0	23	24	1	24
1602.9968	1602.9912	0.0056	25	2	24	25	3	23
1602.9968	1602.9915	0.0053	24	11	14	25	11	15
1602.9968	1602.9915	0.0053	24	11	13	25	11	14
1603.0345	1603.0318	0.0027	24	0	24	25	0	25
1603.0345	1603.0368	-0.0024	24	10	15	25	10	16
1603.0345	1603.0368	-0.0024	24	10	14	25	10	15
1603.0345	1603.0338	0.0007	42	1	41	42	2	40
1603.0345	1603.0382	-0.0037	11	1	10	12	2	11
1603.0246	1603.0186	0.0060	23	3	20	24	3	21
1603.0795	1603.0782	0.0014	24	9	16	25	9	17
1603.0795	1603.0782	0.0014	24	9	15	25	9	16
1603.0889	1603.0986	-0.0098	25	1	25	26	0	26
1603.0889	1603.0952	-0.0063	29	1	29	29	2	28
1603.0889	1603.0924	-0.0035	33	0	33	33	1	32
1603.1188	1603.1205	-0.0018	23	2	21	24	2	22
1603.1188	1603.1158	0.0030	27	2	26	27	3	25
1603.1188	1603.1155	0.0032	24	8	17	25	8	18
1603.1188	1603.1155	0.0032	24	8	16	25	8	17
1603.1479	1603.1491	-0.0012	24	7	18	25	7	19
1603.1479	1603.1491	-0.0012	24	7	17	25	7	18
1603.1479	1603.1542	-0.0062	25	13	12	26	13	13
1603.1479	1603.1542	-0.0062	25	13	13	26	13	14
1603.1796	1603.1794	0.0001	24	6	19	25	6	20
1603.1796	1603.1794	0.0001	24	6	18	25	6	19
1603.9513	1603.9445	0.0068	26	2	24	27	2	25
1603.9513	1603.9470	0.0043	27	7	21	28	7	22

1603.9513	1603.9470	0.0043	27	7	20	28	7	21
1603.9513	1603.9483	0.0030	29	13	17	28	13	16
1603.9513	1603.9483	0.0030	28	13	15	29	13	16
1603.9677	1603.9596	0.0081	27	2	26	28	2	27
1603.9677	1603.9613	0.0064	36	0	36	36	1	35
1603.9791	1603.9783	0.0008	27	6	22	28	6	23
1603.9791	1603.9783	0.0008	27	6	21	28	6	22
1604.0090	1604.0066	0.0024	28	1	28	29	1	29
1604.0090	1604.0078	0.0012	27	5	23	28	5	24
1604.0090	1604.0081	0.0009	27	5	22	28	5	23
1604.0090	1604.0086	0.0004	36	2	35	36	3	34
1604.0180	1604.0243	-0.0063	28	0	28	29	0	29
1604.0180	1604.0214	-0.0034	31	2	30	32	1	31
1604.0841	1604.0887	-0.0045	27	1	26	28	1	27
1604.1291	1604.1235	0.0056	28	0	28	29	1	29
1604.1291	1604.1217	0.0074	27	3	24	28	3	25
1604.1382	1604.1394	-0.0011	28	9	20	29	9	21
1604.1382	1604.1394	-0.0011	28	9	19	29	9	20
1604.1382	1604.1423	-0.0040	37	2	36	37	3	35
1604.1553	1604.1561	-0.0009	32	3	29	32	4	28
1604.1553	1604.1538	0.0015	29	14	16	30	14	17
1604.1553	1604.1538	0.0015	29	14	15	30	14	16
1604.1626	1604.1708	-0.0082	29	1	29	30	0	30
1604.1716	1604.1774	-0.0058	28	8	21	29	8	22
1604.1716	1604.1774	-0.0058	28	8	20	29	8	21
1604.1845	1604.1909	-0.0064	38	3	36	39	2	37
1604.3409	1604.3409	0.0000	28	1	27	29	1	28
1604.3524	1604.3560	-0.0035	29	0	29	30	1	30
1604.3691	1604.3676	0.0015	30	3	27	30	4	26
1604.3691	1604.3683	0.0008	32	2	31	33	1	32
1604.4136	1604.4167	-0.0031	30	14	16	31	14	17
1604.4136	1604.4167	-0.0031	30	14	17	31	14	18
1604.4136	1604.4172	-0.0036	20	5	15	19	6	14
1604.4254	1604.4315	-0.0061	30	1	30	31	0	31
1604.4254	1604.4295	-0.0041	39	2	38	39	3	37
1604.4361	1604.4415	-0.0054	29	8	22	30	8	23
1604.4361	1604.4415	-0.0054	29	8	21	30	8	22
1604.4619	1604.4610	0.0009	29	3	26	29	4	25
1604.4750	1604.4763	-0.0013	29	7	23	30	7	24
1604.4750	1604.4763	-0.0013	29	7	22	30	7	23
1604.4750	1604.4748	0.0001	30	13	17	31	13	18
1604.4750	1604.4748	0.0001	30	13	18	31	13	19
1604.4981	1604.5039	-0.0059	30	1	30	31	1	31

1604.4981	1604.5085	-0.0104	29	6	24	30	6	25
1604.4981	1604.5085	-0.0104	29	6	23	30	6	24
1604.5082	1604.5039	0.0043	30	1	30	31	1	31
1604.5082	1604.5085	-0.0003	29	6	24	30	6	25
1604.5082	1604.5085	-0.0003	29	6	23	30	6	24
1604.5158	1604.5173	-0.0016	30	0	30	31	0	31
1604.5240	1604.5289	-0.0049	20	1	19	21	2	20
1604.5240	1604.5288	-0.0048	30	12	19	31	12	20
1604.5240	1604.5288	-0.0048	30	12	18	31	12	19
1604.5240	1604.5273	-0.0033	38	0	38	38	1	37
1604.5240	1604.5250	-0.0010	28	6	22	27	7	21
1604.5240	1604.5251	-0.0010	28	6	23	27	7	20
1604.5386	1604.5393	-0.0006	29	5	25	30	5	26
1604.5386	1604.5399	-0.0012	29	5	24	30	5	25
1604.5386	1604.5418	-0.0032	36	1	36	36	2	35
1604.5921	1604.5898	0.0023	30	0	30	31	1	31
1604.5921	1604.5912	0.0008	29	1	28	30	1	29
1604.6202	1604.6232	-0.0030	27	3	24	27	4	23
1604.6202	1604.6246	-0.0044	30	10	21	31	10	22
1604.6202	1604.6246	-0.0044	30	10	20	31	10	21
1604.6202	1604.6261	-0.0059	39	3	37	40	2	38
1604.6202	1604.6273	-0.0071	6	2	4	7	3	5
1604.6723	1604.6747	-0.0024	29	3	26	30	3	27
1604.6723	1604.6791	-0.0067	31	14	17	32	14	18
1604.6723	1604.6791	-0.0067	31	14	18	32	14	19
1604.6904	1604.6897	0.0006	31	1	31	32	0	32
1604.6904	1604.6926	-0.0023	26	3	23	26	4	22
1604.6974	1604.7051	-0.0077	30	8	23	31	8	24
1604.6974	1604.7051	-0.0077	30	8	22	31	8	23
1604.6974	1604.7079	-0.0106	33	2	32	34	1	33
1604.9301	1604.9298	0.0002	29	3	27	29	4	26
1604.9301	1604.9258	0.0043	30	3	28	30	4	27
1604.9301	1604.9262	0.0039	32	3	30	32	4	29
1604.9301	1604.9314	-0.0014	33	3	31	33	4	30
1604.9301	1604.9295	0.0006	31	9	23	32	9	24
1604.9301	1604.9295	0.0006	31	9	22	32	9	23
1604.9435	1604.9458	-0.0023	32	1	32	33	0	33
1604.9435	1604.9448	-0.0013	27	3	25	27	4	24
1604.9435	1604.9405	0.0029	34	3	32	34	4	31
1604.9435	1604.9403	0.0031	21	3	18	21	4	17
1604.9435	1604.9435	-0.0001	23	1	22	24	2	23
1604.9635	1604.9665	-0.0029	25	3	23	25	4	22
1604.9635	1604.9681	-0.0046	31	8	24	32	8	25

1604.9635	1604.9681	-0.0046	31	8	23	32	8	24
1604.9635	1604.9718	-0.0082	36	3	34	36	4	33
1605.0060	1605.0083	-0.0023	32	0	32	33	0	33
1605.0060	1605.0036	0.0025	31	7	25	32	7	26
1605.0060	1605.0036	0.0025	31	7	24	32	7	25
1605.0060	1605.0061	-0.0001	22	3	20	22	4	19
1605.0060	1605.0030	0.0031	19	3	16	19	4	15
1605.0258	1605.0229	0.0029	30	2	28	31	2	29
1605.0258	1605.0201	0.0057	21	3	19	21	4	18
1605.0258	1605.0226	0.0032	38	3	36	38	4	35
1605.0405	1605.0367	0.0038	31	6	26	32	6	27
1605.0405	1605.0367	0.0038	31	6	25	32	6	26
1605.0405	1605.0401	0.0004	34	2	33	35	1	34
1605.0405	1605.0342	0.0064	20	3	18	20	4	17
1605.0545	1605.0608	-0.0063	32	0	32	33	1	33
1605.0545	1605.0616	-0.0071	18	3	16	18	4	15
1605.0545	1605.0567	-0.0022	40	3	38	41	2	39
1605.0621	1605.0690	-0.0069	31	5	27	32	5	28
1605.0621	1605.0701	-0.0080	31	5	26	32	5	27
1605.0621	1605.0703	-0.0083	16	3	13	16	4	12
1605.1011	1605.0989	0.0023	15	3	13	15	4	12
1605.1011	1605.1022	-0.0010	14	3	11	14	4	10
1605.1011	1605.1033	-0.0021	32	11	22	33	11	23
1605.1011	1605.1033	-0.0021	32	11	21	33	11	22
1605.1121	1605.1166	-0.0044	31	4	27	32	4	28
1605.1121	1605.1151	-0.0029	13	3	10	13	4	9
1605.1364	1605.1413	-0.0049	41	3	39	41	4	38
1605.1364	1605.1362	0.0002	11	3	8	11	4	7
1605.1364	1605.1381	-0.0017	11	3	9	11	4	8
1605.1364	1605.1397	-0.0033	33	15	19	34	15	20
1605.1364	1605.1397	-0.0033	33	15	18	34	15	19
1605.1469	1605.1494	-0.0025	32	10	23	33	10	24
1605.1469	1605.1494	-0.0025	32	10	22	33	10	23
1605.1469	1605.1447	0.0022	10	3	7	10	4	6
1605.1469	1605.1458	0.0011	10	3	8	10	4	7
1605.1469	1605.1521	-0.0052	9	3	6	9	4	5
1605.1979	1605.1918	0.0061	32	9	24	33	9	25
1605.1979	1605.1918	0.0061	32	9	23	33	9	24
1605.1979	1605.1932	0.0047	42	3	40	42	4	39
1605.1979	1605.1888	0.0091	49	1	48	49	2	47
1605.1979	1605.1940	0.0039	8	2	7	9	3	6
1605.4096	1605.4110	-0.0014	33	10	24	34	10	25
1605.4096	1605.4110	-0.0014	33	10	23	34	10	24

1605.4012	1605.4002	0.0010	34	15	20	35	15	21
1605.4012	1605.4002	0.0010	34	15	19	35	15	20
1605.4549	1605.4519	0.0030	34	1	34	35	0	35
1605.4549	1605.4535	0.0014	33	9	25	34	9	26
1605.4549	1605.4535	0.0014	33	9	24	34	9	25
1605.4702	1605.4795	-0.0093	33	2	32	34	2	33
1605.4702	1605.4794	-0.0092	27	1	26	28	2	27
1605.4702	1605.4816	-0.0114	41	3	39	42	2	40
1605.4702	1605.4743	-0.0041	9	2	8	10	3	7
1605.4840	1605.4971	-0.0130	34	0	34	35	0	35
1605.4840	1605.4897	-0.0056	34	1	34	35	1	35
1605.4840	1605.4926	-0.0086	33	8	26	34	8	27
1605.4840	1605.4926	-0.0086	33	8	25	34	8	26
1605.4840	1605.4925	-0.0085	50	1	49	50	2	48
1605.5033	1605.5042	-0.0008	32	3	29	33	3	30
1605.5136	1605.5210	-0.0074	34	13	22	35	13	23
1605.5136	1605.5210	-0.0074	34	13	21	35	13	22
1605.5136	1605.5228	-0.0091	35	17	18	36	17	19
1605.5136	1605.5228	-0.0091	35	17	19	36	17	20
1605.5222	1605.5288	-0.0066	33	7	27	34	7	28
1605.5222	1605.5288	-0.0066	33	7	26	34	7	27
1605.5318	1605.5348	-0.0031	34	0	34	35	1	35
1605.5530	1605.5522	0.0008	32	2	30	33	2	31
1605.5530	1605.5544	-0.0014	47	3	45	47	4	44
1605.5610	1605.5630	-0.0020	33	6	28	34	6	29
1605.5610	1605.5631	-0.0021	33	6	27	34	6	28
1605.5693	1605.5764	-0.0071	33	1	32	34	1	33
1605.5693	1605.5753	-0.0060	34	12	22	35	12	23
1605.5693	1605.5753	-0.0060	34	12	23	35	12	24
1605.5923	1605.5969	-0.0046	33	5	29	34	5	30
1605.5923	1605.5988	-0.0065	33	5	28	34	5	29
1605.6005	1605.6098	-0.0093	33	3	31	34	3	32
1605.6060	1605.6157	-0.0097	28	1	27	29	2	28
1605.6185	1605.6262	-0.0077	33	4	30	34	4	31
1605.6185	1605.6256	-0.0071	34	11	24	35	11	25
1605.6185	1605.6256	-0.0071	34	11	23	35	11	24
1605.6185	1605.6233	-0.0048	46	2	45	46	3	44
1605.6185	1605.6209	-0.0024	42	0	42	42	1	41
1605.6559	1605.6536	0.0022	33	4	29	34	4	30
1605.6842	1605.6823	0.0019	36	2	35	37	1	36
1605.7152	1605.7147	0.0004	34	9	26	35	9	27
1605.7152	1605.7147	0.0004	34	9	25	35	9	26
1605.8913	1605.8892	0.0021	34	4	31	35	4	32

1605.8913	1605.8859	0.0053	35	11	25	36	11	26
1605.8913	1605.8859	0.0053	35	11	24	36	11	25
1605.9100	1605.8966	0.0134	30	1	29	31	2	30
1605.9100	1605.9007	0.0093	46	4	42	46	5	41
1605.9100	1605.9001	0.0099	42	3	40	43	2	41
1605.9100	1605.8922	0.0178	42	1	42	42	2	41
1605.9215	1605.9224	-0.0009	34	4	30	35	4	31
1605.9390	1605.9325	0.0065	35	10	26	36	10	27
1605.9390	1605.9325	0.0065	35	10	25	36	10	26
1605.9480	1605.9513	-0.0033	36	1	36	37	0	37
1605.9480	1605.9512	-0.0033	11	2	9	12	3	10
1606.0239	1606.0107	0.0133	36	0	36	37	1	37
1606.0239	1606.0150	0.0089	35	8	28	36	8	29
1606.0239	1606.0150	0.0089	35	8	27	36	8	28
1606.0239	1606.0099	0.0140	48	2	47	48	3	46
1606.0457	1606.0425	0.0032	31	1	30	32	2	31
1606.0457	1606.0448	0.0009	45	4	41	45	5	40
1606.0457	1606.0392	0.0065	11	2	10	12	3	9
1606.0457	1606.0407	0.0050	36	13	23	37	13	24
1606.0457	1606.0407	0.0050	36	13	24	37	13	25
1606.0587	1606.0553	0.0035	34	3	31	35	3	32
1606.0587	1606.0520	0.0067	35	7	29	36	7	30
1606.0587	1606.0520	0.0067	35	7	28	36	7	29
1606.0649	1606.0610	0.0039	35	1	34	36	1	35
1606.0969	1606.0875	0.0093	35	6	30	36	6	31
1606.0969	1606.0877	0.0092	35	6	29	36	6	30
1606.1292	1606.1245	0.0047	35	3	33	36	3	34
1606.1292	1606.1231	0.0061	35	5	31	36	5	32
1606.1292	1606.1262	0.0030	35	5	30	36	5	31
1606.1545	1606.1516	0.0029	35	4	32	36	4	33
1606.1487	1606.1457	0.0030	36	11	26	37	11	27
1606.1487	1606.1457	0.0030	36	11	25	37	11	26
1606.1999	1606.1915	0.0085	35	4	31	36	4	32
1606.1999	1606.1928	0.0072	32	1	31	33	2	32
1606.1999	1606.1924	0.0075	36	10	27	37	10	28
1606.1999	1606.1924	0.0075	36	10	26	37	10	27
1606.3767	1606.3802	-0.0035	36	3	34	37	3	35
1606.4025	1606.4049	-0.0024	37	11	27	38	11	28
1606.4025	1606.4049	-0.0024	37	11	26	38	11	27
1606.4130	1606.4133	-0.0004	36	4	33	37	4	34
1606.4130	1606.4126	0.0004	50	2	49	50	3	48
1606.4500	1606.4449	0.0051	38	1	38	39	0	39
1606.4500	1606.4455	0.0045	13	2	11	14	3	12

1606.4717	1606.4680	0.0036	38	0	38	39	0	39
1606.4717	1606.4641	0.0076	38	1	38	39	1	39
1606.4717	1606.4722	-0.0005	37	2	36	38	2	37
1606.5054	1606.4951	0.0102	37	9	29	38	9	30
1606.5054	1606.4951	0.0102	37	9	28	38	9	29
1606.5054	1606.4995	0.0058	38	14	24	39	14	25
1606.5054	1606.4995	0.0058	38	14	25	39	14	26
1606.5170	1606.5083	0.0087	34	1	33	35	2	34
1606.5434	1606.5354	0.0081	37	8	30	38	8	31
1606.5434	1606.5354	0.0081	37	8	29	38	8	30
1606.5434	1606.5320	0.0114	41	4	37	41	5	36
1606.5500	1606.5418	0.0082	37	1	36	38	1	37
1606.5567	1606.5582	-0.0015	38	13	26	39	13	27
1606.5567	1606.5582	-0.0015	38	13	25	39	13	26
1606.5567	1606.5567	-0.0000	40	17	24	39	17	23
1606.5567	1606.5567	-0.0000	39	17	22	40	17	23
1606.5841	1606.5881	-0.0040	36	2	34	37	2	35
1606.5841	1606.5920	-0.0079	39	2	38	40	1	39
1606.6071	1606.6102	-0.0031	37	6	32	38	6	33
1606.6071	1606.6104	-0.0034	37	6	31	38	6	32
1606.6071	1606.6128	-0.0058	38	12	27	39	12	28
1606.6071	1606.6128	-0.0058	38	12	26	39	12	27
1606.6071	1606.6131	-0.0060	13	2	12	14	3	11
1606.6314	1606.6348	-0.0034	37	3	35	38	3	36
1606.6314	1606.6320	-0.0006	40	4	36	40	5	35
1606.6393	1606.6475	-0.0082	37	5	33	38	5	34
1606.6419	1606.6525	-0.0106	37	5	32	38	5	33
1606.6517	1606.6636	-0.0118	38	11	28	39	11	29
1606.6517	1606.6636	-0.0118	38	11	27	39	11	28
1606.6517	1606.6659	-0.0142	46	0	46	46	1	45
1606.6802	1606.6743	0.0059	37	4	34	38	4	35
1606.6802	1606.6739	0.0063	36	2	35	35	1	34
1606.6880	1606.6898	-0.0019	39	1	39	40	0	40
1606.7133	1606.7093	0.0039	39	0	39	40	0	40
1606.7133	1606.7060	0.0073	39	1	39	40	1	40
1606.7133	1606.7106	0.0027	39	10	30	38	10	29
1606.7133	1606.7106	0.0027	39	10	29	38	10	28
1606.9264	1606.9226	0.0038	44	4	41	44	5	40
1606.9264	1606.9217	0.0047	39	11	29	40	11	30
1606.9264	1606.9217	0.0047	39	11	28	40	11	29
1606.9264	1606.9206	0.0058	47	0	47	47	1	46
1606.9405	1606.9336	0.0069	40	1	40	41	0	41
1606.9405	1606.9346	0.0059	38	4	35	39	4	36

1606.9566	1606.9501	0.0066	40	0	40	41	0	41
1606.9566	1606.9472	0.0094	40	1	40	41	1	41
1606.9633	1606.9637	-0.0003	40	0	40	41	1	41
1606.9633	1606.9626	0.0007	40	2	39	39	2	38
1606.9633	1606.9680	-0.0046	42	4	39	42	5	38
1607.0049	1607.0004	0.0045	38	4	34	39	4	35
1607.0595	1607.0537	0.0058	39	8	32	40	8	33
1607.0595	1607.0537	0.0058	39	8	31	40	8	32
1607.0595	1607.0489	0.0106	39	4	36	39	5	35
1607.0595	1607.0541	0.0055	47	1	47	47	2	46
1607.0801	1607.0785	0.0016	34	4	30	34	5	29
1607.0801	1607.0781	0.0021	38	4	35	38	5	34
1607.0945	1607.0938	0.0007	38	2	36	39	2	37
1607.0945	1607.0926	0.0020	39	7	33	40	7	34
1607.0945	1607.0926	0.0019	39	7	32	40	7	33
1607.1103	1607.1078	0.0025	37	4	34	37	5	33
1607.1103	1607.1092	0.0010	45	3	43	46	2	44
1607.1346	1607.1311	0.0035	39	6	34	40	6	35
1607.1346	1607.1315	0.0031	39	6	33	40	6	34
1607.1346	1607.1321	0.0025	33	4	29	33	5	28
1607.1346	1607.1298	0.0047	16	2	14	17	3	15
1607.1346	1607.1282	0.0064	40	12	28	41	12	29
1607.1346	1607.1282	0.0064	40	12	29	41	12	30
1607.1346	1607.1327	0.0019	7	4	4	6	3	3
1607.1346	1607.1327	0.0018	6	3	4	7	4	3
1607.1445	1607.1408	0.0037	39	3	37	40	3	38
1607.1445	1607.1378	0.0067	36	4	33	36	5	32
1607.1676	1607.1701	-0.0025	39	5	35	40	5	36
1607.1676	1607.1664	0.0012	41	2	40	42	1	41
1607.1676	1607.1679	-0.0003	35	4	32	35	5	31
1607.1765	1607.1764	0.0002	41	1	41	42	0	42
1607.1765	1607.1779	-0.0013	39	5	34	40	5	35
1607.1765	1607.1809	-0.0044	32	4	28	32	5	27
1607.1765	1607.1793	-0.0027	40	11	30	41	11	31
1607.1765	1607.1793	-0.0027	40	11	29	41	11	30
1607.1981	1607.2016	-0.0035	41	0	41	42	1	42
1607.1981	1607.2065	-0.0083	40	2	39	41	2	40
1607.1981	1607.2034	-0.0052	38	1	37	39	2	38
1607.1981	1607.1979	0.0002	34	4	31	34	5	30
1607.1981	1607.2006	-0.0025	15	2	14	16	3	13
1607.2259	1607.2256	0.0003	31	4	27	31	5	26
1607.2259	1607.2276	-0.0017	33	4	30	33	5	29
1607.2259	1607.2267	-0.0008	40	10	31	41	10	32

1607.2259	1607.2267	-0.0008	40	10	30	41	10	31
1607.4054	1607.3921	0.0133	40	3	38	41	3	39
1607.4054	1607.3902	0.0152	39	1	38	40	2	39
1607.4054	1607.3908	0.0146	40	6	35	41	6	36
1607.4054	1607.3914	0.0140	40	6	34	41	6	35
1607.4054	1607.3901	0.0154	27	4	24	27	5	23
1607.4179	1607.4181	-0.0002	42	1	42	43	0	43
1607.4179	1607.4167	0.0011	39	3	36	40	3	37
1607.4179	1607.4137	0.0042	26	4	23	26	5	22
1607.4235	1607.4297	-0.0062	42	0	42	43	0	43
1607.4235	1607.4277	-0.0042	42	1	42	43	1	43
1607.4235	1607.4306	-0.0071	40	5	36	41	5	37
1607.4235	1607.4248	-0.0012	25	4	21	25	5	20
1607.5211	1607.5292	-0.0082	20	4	16	20	5	15
1607.5211	1607.5283	-0.0072	41	9	33	42	9	34
1607.5211	1607.5283	-0.0072	41	9	32	42	9	33
1607.5211	1607.5272	-0.0062	42	14	29	43	14	30
1607.5211	1607.5272	-0.0062	42	14	28	43	14	29
1607.5211	1607.5225	-0.0014	49	1	49	49	2	48
1607.4725	1607.4717	0.0008	23	4	19	23	5	18
1607.5402	1607.5415	-0.0012	40	4	36	41	4	37
1607.5402	1607.5408	-0.0006	18	2	16	19	3	17
1607.5579	1607.5605	-0.0026	18	4	14	18	5	13
1607.5579	1607.5614	-0.0035	18	4	15	18	5	14
1607.5823	1607.5911	-0.0088	40	2	38	41	2	39
1607.5823	1607.5870	-0.0047	16	4	12	16	5	11
1607.5823	1607.5874	-0.0051	16	4	13	16	5	12
1607.5823	1607.5862	-0.0040	42	13	30	43	13	31
1607.5823	1607.5862	-0.0040	42	13	29	43	13	30
1607.6060	1607.6100	-0.0040	41	7	35	42	7	36
1607.6060	1607.6100	-0.0040	41	7	34	42	7	35
1607.6060	1607.6093	-0.0033	14	4	10	14	5	9
1607.6060	1607.6095	-0.0035	14	4	11	14	5	10
1607.6208	1607.6191	0.0017	13	4	9	13	5	8
1607.6208	1607.6192	0.0017	13	4	10	13	5	9
1607.6208	1607.6189	0.0019	26	7	19	25	8	18
1607.6208	1607.6189	0.0019	26	7	20	25	8	17
1607.6321	1607.6423	-0.0102	41	3	39	42	3	40
1607.6321	1607.6360	-0.0039	11	4	7	11	5	6
1607.6321	1607.6360	-0.0039	11	4	8	11	5	7
1607.6321	1607.6414	-0.0092	42	12	31	43	12	32
1607.6321	1607.6414	-0.0092	42	12	30	43	12	31
1607.6321	1607.6432	-0.0111	10	4	6	10	5	5

1607.6321	1607.6432	-0.0111	10	4	7	10	5	6
1607.6464	1607.6502	-0.0038	41	6	36	42	6	37
1607.6464	1607.6509	-0.0046	41	6	35	42	6	36
1607.6464	1607.6497	-0.0033	9	4	5	9	5	4
1607.6464	1607.6497	-0.0033	9	4	6	9	5	5
1607.6651	1607.6687	-0.0036	43	0	43	44	0	44
1607.6651	1607.6669	-0.0019	43	1	43	44	1	44
1607.6734	1607.6767	-0.0033	43	0	43	44	1	44
1607.7154	1607.7187	-0.0033	43	2	42	44	1	43
1607.7154	1607.7197	-0.0043	43	15	29	44	15	30
1607.7154	1607.7197	-0.0043	43	15	28	44	15	29
1607.7360	1607.7321	0.0039	42	1	41	43	1	42
1607.7360	1607.7315	0.0045	19	2	17	20	3	18
1607.9343	1607.9326	0.0017	43	2	42	44	2	43
1607.9577	1607.9518	0.0059	41	3	38	42	3	39
1607.9577	1607.9503	0.0074	42	5	38	43	5	39
1607.9577	1607.9486	0.0091	43	11	33	44	11	34
1607.9577	1607.9486	0.0091	43	11	32	44	11	33
1607.9649	1607.9686	-0.0037	43	1	42	44	1	43
1607.9649	1607.9674	-0.0025	42	4	39	43	4	40
1607.9649	1607.9649	0.0000	42	5	37	43	5	38
1607.9754	1607.9784	-0.0030	42	1	41	43	2	42
1607.9754	1607.9745	0.0009	44	15	29	45	15	30
1607.9754	1607.9745	0.0009	44	15	30	45	15	31
1607.9846	1607.9876	-0.0031	44	2	43	45	1	44
1607.9914	1607.9967	-0.0053	43	10	34	44	10	35
1607.9914	1607.9967	-0.0053	43	10	33	44	10	34
1607.9914	1607.9965	-0.0052	33	8	25	32	9	24
1607.9914	1607.9965	-0.0052	33	8	26	32	9	23
1608.0095	1608.0148	-0.0053	45	18	28	46	18	29
1608.0095	1608.0148	-0.0053	45	18	27	46	18	28
1608.0095	1608.0151	-0.0056	49	10	39	48	11	38
1608.0095	1608.0151	-0.0056	49	10	40	48	11	37
1608.0095	1608.0169	-0.0074	46	21	25	47	21	26
1608.0095	1608.0169	-0.0074	46	21	26	47	21	27